Electrically Conductive Scaffolds for Peripheral Nerve Repair

A thesis submitted to The University of Manchester
for the degree of Doctor of Philosophy
in the Faculty of Science and Engineering

2020

Adrián Magaz Molina

School of Natural Sciences
Department of Materials

Blank page

Contents

Chapter 4 *Modulation of neuronal cell affinity on PEDOT–PSS non-woven silk scaffolds for neural tissue engineering* 113

Chapter 5 ***Neuronal cell growth and differentiation on biosynthetic reflectin functionalised silk fibrous scaffolds*** **.. 145**

Word count: 40,880

Blank page

List of figures

Chapter 2

Chapter 3

Chapter 4

Chapter 5

List of tables

Chapter 2

Chapter 4

Blank page

List of abbreviations

ATR, Attenuated total reflectance

BCA, Bicinchoninic acid

BMP, Bone morphogenetic protein

BSA, Bovine serum albumin

CNF, ciliary neurotrophic factor

CV, Coverslip

DAPI, 4′,6-diamidino-2-phenylindole dihydrochloride

DC, Direct current

DI, Deionised

DLS, Dynamic light scattering

DMEM, Dulbecco's modified Eagles medium

DMSO, Dimethyl sulfoxide

DRG, Dorsal root ganglia

dsDNA, Double-stranded deoxyribonucleic acid

ECM, Extracellular Matrix

EDC, 1-ethyl-3-(dimethylaminopropyl) carbodiimide hydrochloride

ES, Electrical stimulation

FBS, Foetal bovine serum

FDA, Food and Drug administration

FSD, Fourier self-deconvolution

(FE)SEM, Field emission scanning electron microscope

FTIR, Fourier Transform infrared spectroscopy

GAP, Growth associated protein

GDNF, Glial derived nerve growth factor

GO, Graphene oxide

HAT, Hypoxanthine-aminopterin-thymidine

HFIP, Hexafluoro-2-propanol

HG, High glucose

ICC, Immunocytochemistry

IKVAV, Ile-Lys-Val-Ala-Val

IL-6, Interleukin 6

LIF, Leukaemia inhibitory factor

MWNT, Multi-walled carbon nanotube

NBF, Neutral buffered formalin

NGF, Nerve growth factor

NGC, Nerve guidance conduit

NHS, N-hydroxysuccinimide

PANI, Polyaniline

PBS, Phosphate buffered saline

PCB, Polycarbazole

PCL, Poly(ε-caprolactone)

PEDOT–PSS, Poly(3,4-ethylenedioxythiophene)-polystyrene sulfonate

PGP, Protein gene product.

PLA, Polylactic acid

PLCL, Poly(L-lactide-co-ε-caprolactone)

PNI, Peripheral nerve injury

PPy, Polypyrrole

PVDF, Poly(vinylidene fluoride)

PVDF-TrFE, Poly(vinylidene fluoride–trifluoroethylene)

rGO, Reduced graphene oxide

RGD, Arg-Gly-Asp

RNA, Ribonucleic acid

RSF, Regenerated silk fibroin

RSP, Regenerated silk spidroin

RT, Room temperature

SBS, Solution blow spinning

SD, Standard deviation

SDS-PAGE, Sodium dodecyl sulfate polyacrylamide gel electrophoresis

SF, Silk fibroin

SP, Silk spidroin

SWNT, Single-walled carbon nanotube

TCP, Tissue culture plastic

TFA, Trifluoroacetic acid

UV, Ultraviolet

XRD, X-ray diffraction

YIGSR, Tyr–Ile–Gly–Ser–Arg

Blank page

Abstract

Tissue repair and regeneration is a complex physiological process that requires multiple biological and physico-chemical cues acting together. Electrical regimes are particularly effective in controlling the cellular response of electrically sensitive tissues such as nerve, highlighting the need to develop new electroconductive/active microenvironments. This thesis describes the development of electroconductive/active micro/nano- fibrous scaffolds based on *Bombyx mori* silk fibroin (SF) for neural tissue engineering applications. Composites based on the incorporation of graphene oxide (GO) at controlled loadings (1 to 10% wt.) followed by *in situ* post-reduction into reduced GO (rGO) were first explored, but the electrical conductivity achieved was limited. On the other hand, functionalisation with poly(3,4-ethylenedioxythiophene)-polystyrene sulfonate (PEDOT–PSS) led to much higher conductance, readily tuned in terms of the coating concentration or by treating it with dimethyl sulfoxide (DMSO). Decoration of silk with intrinsically conductive recombinant reflectin, reported among the highest proton conductors in nature and involved in cephalopod brain neurogenesis, was also investigated. Experimental work was conducted to characterise the physico-chemical properties of the developed scaffolds. *In vitro* studies with neuroma NG108-15 cells showed that cellular viability was maintained in all scaffold groups, while metabolic activity and proliferation were greatly promoted from the early stages of the cell culture. Furthermore, these families of electroconductive/active scaffolds supported cell differentiation with neurite sprouting. Neurite outgrowth was observed after 5 days of culture, with neurite extensions up to 150-250 μm. The data reported here suggests that these electroconductive/active microenvironments may be beneficial and could potentially outperform unmodified silk scaffolds. Overall, the study conducted here provides useful information about the combined use of silk and various electroconductive/active moieties that could be useful for the regeneration and repair process of peripheral nerves, and hint at the potential of using these electroconductive/active scaffolds in combination with exogenous electrical regimes to allow direct delivery of electrical signals and trigger the controlled release of therapeutics to the site of interest.

Blank page

Declaration

The author declares that no portion of the work referred to in the thesis has been submitted in support of an application for another degree or qualification of this or any other university or other institute of learning.

Copyright statement

I. The author of this thesis (including any appendices and/or schedules to this thesis) owns certain copyright or related rights in it (the “Copyright”) and s/he has given The University of Manchester certain rights to use such Copyright, including for administrative purposes.

II. Copies of this thesis, either in full or in extracts and whether in hard or electronic copy, may be made only in accordance with the Copyright, Designs and Patents Act 1988 (as amended) and regulations issued under it or, where appropriate, in accordance with licensing agreements which the University has from time to time. This page must form part of any such copies made.

III. The ownership of certain Copyright, patents, designs, trademarks and other intellectual property (the “Intellectual Property”) and any reproductions of copyright works in the thesis, for example graphs and tables (“Reproductions”), which may be described in this thesis, may not be owned by the author and may be owned by third parties. Such Intellectual Property and Reproductions cannot and must not be made available for use without the prior written permission of the owner(s) of the relevant Intellectual Property and/or Reproductions.

IV. Further information on the conditions under which disclosure, publication and commercialisation of this thesis, the Copyright and any Intellectual Property and/or Reproductions described in it may take place is available in the University IP Policy (see http://documents.manchester.ac.uk/DocuInfo.aspx?DocID=24420), in any relevant Thesis restriction declarations deposited in the University Library, The University Library’s regulations (see http://www.library.manchester.ac.uk/about/regulations/) and in The University’s policy on Presentation of Theses.

Acknowledgements

First and foremost, I would like to thank my supervisor Dr. Jonny J. Blaker, who made it possible for me to start this exciting journey into a PhD between Manchester and Singapore. His patience and generosity with his time and knowledge, even while I was in a faraway time zone, meant I always had someone to turn to for guidance and to keep me on track. I would also like to thank my co-supervisor at Manchester, Prof. Julie E. Gough, for her continuous support, encouragement and guidance with the cell studies. I would also like to express my gratitude to Dr. Xu Li, for welcoming me into his research group at A*STAR in Singapore and hosting me in his lab for two years. Their trust and faith in me inspired me to try my best, and their motivation kept me going.

This work would have not been possible without the encouragement and help from all members of the Biomaterials research group at Manchester, along with all the people that supported me in the lab during my secondment in Singapore. Special thanks to the lab technicians and experimental officers. Everyone helped me in some way, and for that I am very grateful.

I would also like to thank Dr. Adam J. Reid’s, Prof. Sarah Cartmell’s, Prof. Eriko Takano’s and Prof. Nigel S. Scrutton’s labs at The University of Manchester, and Dr. John G. Hardy’s at Lancaster University, for contributing resources and help for this research.

Many thanks to all my family and friends – without their support, I would have not been able to come this far.

This work was primarily funded by the Faculty of Science and Engineering (FSE) and the Faculty of Biology, Medicine and Health (FBMH) at The University of Manchester, along with an Engineering and Physical Sciences Research Council (EPSRC) Doctoral Training Programme (DTP) (EP/N509565/1, studentship 1786315) and support by the Agency for Science, Technology and Research (A*STAR) in Singapore via the A*STAR Research Attachment Programme (ARAP).

Blank page

About the author

Adrián Magaz Molina

A brief summary of the author's main academic achievements during this Doctoral Thesis follows.

List of peer-reviewed publications

(1) **Magaz A,** Spencer BF, Hardy JG, Li X, Gough JE, Blaker JJ. "Modulation of neuronal cell affinity on electroconductive PEDOT–PSS modified silk fibroin non-woven scaffolds". *ACS Biomaterials Science & Engineering*. 2020;6(12):6906–16. (I.F 4.2)

(2) **Magaz A**, Li X, Gough JE, Blaker JJ. "Graphene oxide and electroactive reduced graphene oxide-based composite fibrous scaffolds for engineering excitable nerve tissue". *Materials Science and Engineering: C*. 2021;19: 111632. (I.F 5.9)

(3) **Magaz A**, Ashton MD, Hathoutd RM, Li X, Hardy JG, Blaker JJ. "Electroresponsive silk-based biohybrid composites for electrochemically controlled growth factor delivery". *Pharmaceutics*. 2020;12(8):742. (I.F 4.4)

(4) Roberts AD, Lee JSM, **Magaz A**, Smith MW, Dennis M, Scrutton NG, Blaker JJ. "Hierarchically porous silk/activated-carbon composite fibres for adsorption and repellence of volatile organic compounds". *Molecules*. 2020;25(5):1207. (I.F. 3.3)

(5) **Magaz A**, Roberts AD, Faraji S, Nascimento TRL, Medeiros ES, Zhang W, Greenhalgh R, Mautner A, Li X, Blaker JJ. "Porous, aligned and biomimetic fibres of regenerated silk fibroin produced by solution blow spinning". *Biomacromolecules.* 2018;19(12):4542–53. (I.F. 6.1)

(6) **Magaz A**, Faroni A, Reid JA, Gough EJ, Li X, Blaker JJ. "Bioactive silk-based nerve guidance conduits for augmenting peripheral nerve repair". *Advanced Healthcare Materials*. 2018;7(23):1800308. (I.F. 7.37)

(7) Tandon B, **Magaz A**, Balint R, Blaker JJ, Cartmell SH. “Electroactive biomaterials: Vehicles for controlled delivery of therapeutic agents for drug delivery and tissue regeneration”. *Advanced Drug Delivery Reviews*. 2018;129:148–68. (I.F. 13.30)

Publications in preparation

(1) **Magaz A**, Wolde-Michael E, Heyes DJ, Takano E, Scrutton NG, Li X, Gough JE, Blaker JJ. “Neuronal cell growth and differentiation on conductive biosynthetic reflectin functionalized silk fibrous scaffolds”

Conferences. Oral presentations

(1) **Magaz A**, Wolde-Michael E, Takano E, Scrutton NS, Li X, Blaker JJ. Surface functionalized electroconductive silk fibres for nerve tissue engineering. *Oral presentation*. 10th International Conference on Materials for Advanced Technologies, Singapore (2019)

(2) Blaker JJ, Periklis P, Greenhalgh RD, **Magaz A**, Li X. Hierarchical and gradient nanofibre constructs for tissue regeneration. *Oral presentation*. 10th International Conference on Materials for Advanced Technologies, Singapore (2019)

(3) Phamornnak C, **Magaz A**, Li X, Blaker JJ, Cartmell SH. Engineering nerve tissue with silk:graphene oxide fibres. *Oral presentation*. TERMIS EU, Greece (2019)

(4) Blaker JJ, **Magaz A**, Ambler W, Greenhalgh RD, Medeiros E, Tirelli N, Li X. Solution blow spinning of sol-gel inorganic/polypeptide fibres. *Oral presentation*. 9th International Conference on Materials for Advanced Technologies, Singapore (2017)

Conferences. Poster presentations

(1) **Magaz A**, Phamornnak C, Li X, Cartmell SH, Blaker JJ. Design and fabrication of conductive silk-based fibres for peripheral nerve regeneration.

Poster presentation. 10th International Conference on Materials for Advanced Technologies, Singapore (2019)

(2) **Magaz A,** Phamornnak C, Li X, Cartmell SH, Blaker JJ. Electroconductive silk-based fibres for peripheral nerve regeneration. *Poster presentation*. Scandinavian Society for Biomaterials Conference, Finland (2019)

(3) **Magaz A**, Roberts AD, Blaker JJ, Li X. Solution blow spinning of regenerated silk fibroin sub-micron fibres. *Poster presentation*. Sheffield Silk Conference, UK (2017)

(4) **Magaz A**, Faraji S, Roberts AD, Blaker JJ, Li X. Solution blow spinning of silk nanofibres towards peripheral nerve regeneration. *Poster presentation*. A*STAR–UK Partner Universities Conference, UK (2017)

(5) Faraji S & Finnigan W, **Magaz A**, Breitling R, Scrutton N, Takano E, Blaker JJ. Tough recombinant spider silk/graphene multifunctional nanofibres for wearable personal protection. *Poster presentation*. Ministry of Defence, Science and Technology Laboratory Conference, UK (2017)

Awards

(1) Fully-funded PhD studentship by the Faculty of Science and Engineering (FSE) and the Faculty of Biology, Medicine and Health (FBMH) at The University of Manchester, supported by the Engineering and Physical Sciences Research Council (EPSRC) Doctoral Training Programme (DTP) (2016-2020).

(2) A*STAR Research Attachment Programme (ARAP). Scholarship to undertake two years at the Agency for Science Technology and Research (A*STAR) Institutes in Singapore (2017-2019).

Other peer-reviewed publications

(1) Wu L, **Magaz A**, Huo S, Darbyshire A, Loizidou M, Emberton M, Birchall M, Song W. "Human airway-like multilayered tissue on 3D-TIPS printed

thermoresponsive elastomer/collagen hybrid scaffolds”. *Acta Biomaterialia*. 2020. 113, 177-195. (I.F. 7.24)

(2) Wu L, **Magaz A**, Darbyshire A, Howkins A, Reynolds A, Boyd IW, Song H, Song JH, Loizidou M, Emberton M, Birchall M, Song W. “Thermoresponsive stiffness softening of hierarchically porous nanohybrid membranes promotes niches for mesenchymal stem cell differentiation”. *Advanced Healthcare Materials*. 2019. 8(10), 1801556. (I.F. 7.37)

(3) Wu L, **Magaz A**, Maughan E, Oliver N, Darbyshire A, Loizidou M, Emberton M, Birchall M, Song W. “Cellular responses to thermoresponsive stiffness memory elastomer nanohybrid scaffolds by 3D-TIPS”. *Acta Biomaterialia*. 2018. 85, 157-171. (I.F. 7.24)

(4) Wu L, **Magaz A**, Wang T, Liu C, Loizidou M, Emberton M, Birchall M, Song W. “Stiffness memory of 3D-printed elastomer nanohybrid scaffolds regulates chondrogenesis and osteogenesis of human mesenchymal stem cells”. *Biomaterials*. 2018. 186, 64-79. (I.F. 10.32)

Other conferences

(1) Mohmad-Saberi SE, **Magaz A**, Wu L, Oliver N, Derbyshire A, Kasimatis M, Cousins BG, Song W. 3D printing biodegradable polyurethane nanocomposite scaffold for heart valve regeneration. *Poster presentation*. 28th Annual Conference of the European Society for Biomaterials, Greece (2017)

(2) Mohmad-Saberi SE, **Magaz A**, Derbyshire A, Cousins BG, Song W. Development of 3D printed biodegradable polyurethane nanohybrid scaffold for heart valve regeneration. *Oral presentation*. 5th TERMIS World Congress, Japan (2018)

Chapter 1
Introduction

1.1 Overview

Regeneration of the nervous system is a complex biological process with a large personal, social and economic burden. The gold standard approach for repairing nerve injuries depends upon the type of nerve. Nerve damage to the peripheral nervous system occurs in about 3-10% of trauma patients, with one million surgical reconstruction procedures performed annually between Europe and the US [1,2]. Unlike the central nervous system, peripheral nerves are capable of self-regeneration by extending and reconnecting with the nerve stump, typically when the injuries are small (e.g. less than 5 mm nerve gap) [3,4]. In severe cases when the nerve gap is too large, the axon is unable to reach across and the connection is terminated. When the injury consists of nerve gaps of more than 5 mm in length, suturing of the two stumps is the standard method. If more severe but less than 3 cm in length, autologous nerve grafting is the gold standard. Several limitations are known, though, such as donor site morbidity and lack of donor nerve, scar tissue invasion, or aberrant regeneration [5,6]. When the damage to the nerve tissue is even more extreme, allografts and vascularised/avascularised nerve grafts may be used [5]. Nevertheless, even in the most optimal scenario axonal regeneration may not necessarily result in full recovery of nerve functionality. Failure of the nerve to regenerate leads to loss of functional and structural support, reduction in the quality of life of the patient and an associated high social impact.

Regeneration of peripheral nerves primarily focuses on the development of alternatives to nerve autografts, such as the use of nerve guides and conduits to facilitate axonal growth [4,7]. While these approaches may overcome some of the limitations of autografts, there is no current solution available for a completely successful treatment. Current commercial nerve conduits do not offer the proper physical or spatial guidance; they take the form of hollow tubes with a single lumen and no internal substructure or stimulatory cues. Such a lack of relevant architectural features and stimulatory cues is the major drawback leading to differing biological responses compared with the original healthy tissue, since normal cellular behaviour requires spatial cues from the surrounding environment. Therefore, these conduits do not stimulate neuronal or Schwann cell adhesion, migration or differentiation for nerve repair purposes.

The use of growth factors, tissue engineered constructs and ‘smart’ biomaterials are alternatives being explored to enhance the repair and regeneration process. Many of these approaches focus on delivering stimulatory cues to promote the biological process. Electrical regimes in particular play an important role in the repair and regeneration process of many biological systems. Nerve tissues are electrically sensitive since neurons rely on sending electrical impulses to communicate between each other. Therefore, electrical regimes have been employed as a useful tool [8]. Electrical regimes can alter cellular process such as growth, proliferation, migration or differentiation [9], and have great potential in regenerative medicine applications. For this reason, the use of electroconductive/active biomaterials, capable of conducting electricity, are gathering increasing interest in the repair and regeneration process of peripheral nerves. By making nerve conduits that are electrically conductive, the wound healing response and regenerative process could be enhanced by conducting native pulses sent by the regenerating axon, or by providing means for direct stimulation to promote communication across the nerve gap. Direct exogenous electrical stimulation (ES) (e.g. electrotherapy) of cells and tissues has been explored by many research groups, but its translation into the clinic is challenging. Alternatively, a particularly interesting option that has been explored to a less extent is making use of endogenous electrical regimes (e.g. passive stimulation) provided by an electroconductive/active substrate to promote the cellular response.

Developing an electroconductive/active microenvironment as a standalone material is difficult. Instead, electroconductive/active moieties are employed with a host material. Silks are very attractive biological materials with a unique combination of properties in terms of strength, elasticity, toughness, slow degradation and aqueous processability [10] – properties that could be suitable for peripheral nerve repair. SF obtained from silkworm cocoons is inexpensive, readily available, and easily processed into films, fibres, sponges or hydrogels, with demonstrated success in many biomedical applications [10,11]. SF is not electroactive, but its (bio)functionality could be harnessed in combination with electroactive/conductive moieties for peripheral nerve tissue engineering.

1.2 Project aim and objectives

As highlighted in the overview, previous research has demonstrated that electrical regimes play a key role in the regeneration of electrically sensitive tissues such as nerve. In addition, silk is a promising host material to develop an electroconductive/active microenvironment towards peripheral nerve repair. Bearing this in mind, the central **hypothesis** tests that electroconductive/active micro/nano-fibrous scaffolds based on silk will promote neuronal cell behaviour to a greater extent compared with unmodified silk for the potential application of improving neuronal and Schwann cell growth during the nerve repair and regeneration process.

The main **aim** of this thesis is to explore the use of electroconductive/active *in vitro* models based on SF for peripheral nerve tissue engineering, in the absence of external direct ES. The specific **objectives** of this project and related experimental work objectives are as follows:

(1) Production of micro/nano- fibrous composites based on SF and an electroactive carbon-based nanomaterial (i.e. electron/ion charged carrier).
  - Comparison of unmodified silk scaffolds to composites containing different loadings of electroactive rGO in relation to GO.
    - To understand the effects of the carbon-based filler in terms of the physico-chemical properties of the scaffold, and their biological properties with the perspective of tissue engineering.
    - To understand the effects of the carbon-based filler with respect to conductivity, and to assess the influence of dry and wet conditions.
    - To understand the challenges, advantages and limitations of the endogenous electrical regime provided by a carbon-based nanomaterial.

        - To establish the correlations between the response of neuronal-like cells and the role of electron/ion conduction provided by a carbon-based nanomaterial.

(2) Production of micro/nano- fibrous silk scaffolds functionalised with an inherent conjugated polymer (i.e. electron/ion charged carrier).
    - Comparison of unmodified silk scaffolds to scaffolds functionalised with different concentrations of doped PEDOT–PSS.
        - To establish the correlations between the structure and conductive properties of the scaffolds regarding their functionalisation degree with a conjugated polymer, and to compare their physico-chemical and biological properties with the perspective of tissue engineering.
        - To assess the influence of dry and wet conditions with respect to the achieved conductance.
        - To understand the challenges, advantages and limitations of the endogenous electrical regime provided by a conjugated polymer in comparison to the use of an electroactive carbon-based filler.
        - To assess the biological response of the scaffolds with analogue neuronal-like cells, and to investigate the role of electron/ion conduction provided by a conjugated polymer.

(3) Production of micro/nano- fibrous silk scaffolds functionalised with an intrinsic conductive naturally occurring protein (i.e. proton/ion charged carrier).
    - Comparison of unmodified silk scaffolds to scaffolds functionalised with recombinant reflectin and its derivatives.
        - To establish the correlations between the structure and conductive properties of the scaffolds regarding their functionalisation with different reflectin isoforms, and to compare their physico-chemical and biological properties with the perspective of tissue engineering. To understand the challenges, advantages and limitations of the proposed strategy.

- To establish the correlations between proton/ion conduction with respect to the number of repeat motifs of a biosynthetic isoform.
- To assess the influence of reflectin functionalisation in regulating the neuronal cell response.

1.3 Thesis outline

The content of this thesis is structured based on the overall hypothesis and thematic objectives 1-3, and it has been split into three experimental chapters apart from this introductory chapter, the literature review chapter and the conclusions and future perspectives chapter. Each experimental chapter consists of an individual introduction, results and discussion of the experiments performed, and conclusions and suggestions for future work. In addition, author contribution statements are detailed at the beginning of each experimental chapter, along with a brief chapter synopsis to include details of the objectives achieved and their content. References have been included as a single section at the end of the thesis. Two appendices regarding avenues for future research have been included after the references section (**Appendix A** has been published in *Biomacromolecules,* 2018; **Appendix B** has been published in *Pharmaceutics,* 2020).

A detailed outline of each chapter follows:

- **Chapter 1** provides an overview of the field and the clinical relevance of the research, highlighting the aim and objectives of this study.
- **Chapter 2** includes a comprehensive literature review of the field and highlights the research opportunities of this study. A version of this chapter has been published in *Advanced Healthcare Materials* (September 2018), but it has been updated to include more recent contemporary studies.
- **Chapter 3** focuses on a comparative study of micro/nano- fibrous silk composites based on GO or rGO, and the role that electroactive rGO has on the neuronal cell response in comparison to GO containing composites. A version of this chapter has been published in *Materials Science and Engineering: C* (October 2020).

- **Chapter 4** focuses on optimising the conductivity of silk-based scaffolds by exploring surface functionalisation with doped PEDOT–PSS, along with the effects on neuronal cell behaviour with respect to PEDOT–PSS treatment with DMSO. A version of this chapter has been published in *ACS Biomaterials Science & Engineering* (November 2020).
- **Chapter 5** focuses on the use of a naturally occurring proton conductor as an alternative to electron/ion charged carriers provided by carbon-based nanomaterials and inherent conductive polymers. In particular, the role of reflectin, an intrinsic conductive protein involved in neurogenesis in cephalopods, is explored as an active material.
- **Chapter 6** includes a summary of the findings of this thesis and provides insight into several research avenues that could be further explored.

Chapter 2

Literature review

Note: A version of this chapter has been published as Magaz *et al*. “Bioactive silk-based nerve guidance conduits for augmenting peripheral nerve repair”. *Advanced Healthcare Materials.* 2018;7(23):1800308

2.1 Introduction

Peripheral nerve injury (PNI) is a common condition that for the injured patient results in impaired sensation and reduced motor function of the affected region alongside pain and cold intolerance [12]. As a result, the psychological well-being and ability to function in a daily life (e.g. employability, psychological distress and relationships) are affected [13,14]. Current treatment options are surgical only, insufficient even in the most optimal setting, with a large societal and economical cost [15]. Current standard practice for nerve gap repair is autologous nerve autografting, despite several deficiencies such as limited availability and harvesting of functioning nerve, donor site morbidity, time consuming surgeries or incomplete recovery [16].

Clinical use of nerve conduits remains limited due to a lack of good clinical data, relative expense, and inability to bridge large nerve defect gaps. Clinical evidence suggests that conduits are currently no better than autografts for small nerve gaps and should not be used in the presence of large nerve gaps. Novel approaches that consider the complex biology underlying PNI are required to physically support tissue growth and elicit desired cellular-specific responses. In particular, silk (**Figure 2.1**) is a relatively inexpensive biomaterial that has showed promise in the field of nerve tissue engineering and has gained prominence over the last few years due to its physico-chemical, mechanical and biological properties.

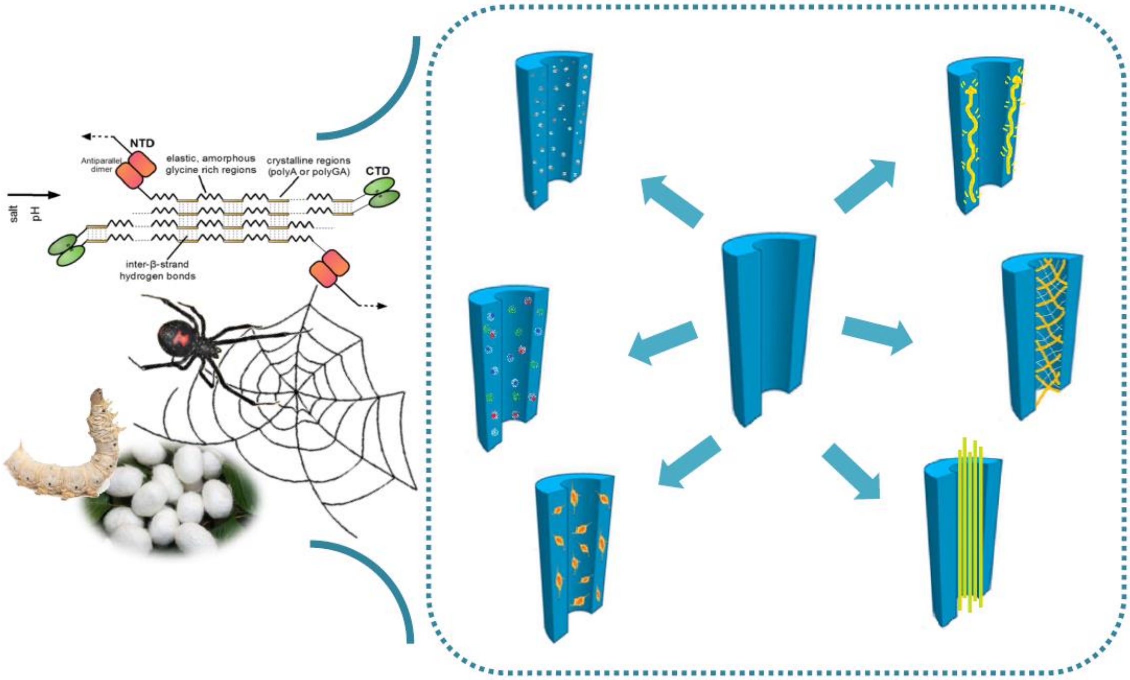

Figure 2.1 Schematics on the use of natural and synthetic recombinant SF and SP for peripheral nerve regeneration. On the left-hand side: synthetic recombinant silk expression, spider (black widow *Latrodectus hesperus*) silk, and silkworm (*Bombyx mori*) silk. Ideal property criteria of nerve conduit scaffolds on the right-hand side: suitable porosity to allow a vascular plexus within, mixture of neuronal and Schwann cells, and presence of biochemical and biophysical guidance cues (e.g. mimicking of the endoneurial-like structure, electroactivity, and growth factors)

2.2 Neurobiology and peripheral nerve repair

PNIs (**Table 2.1**) are common and disproportionately impact the young and working population. It is estimated that there are more than a million new cases of PNI worldwide each year, of which around 40% occur in Europe [17–19]. The aetiology of PNI is almost always trauma, yet this may also be iatrogenic or nerve sacrifice during tumour excision. PNI are not temporary but rather lifelong injuries: the percentage of people returning to work after upper extremity nerve trauma has been reported to be less than 60% a year [13], with affected prospects of returning to previous employment as 1 out of 20 patients tend to suffer from plexus injuries [14]. Despite best microsurgical interventions, functional restoration is always incomplete [20]. Long-term disability of the patient is therefore expected, with health and living expenses of an employed person to be estimated in around 50,000 EUR [15].

Table 2.1 Three main types of PNI can be described [21].

Injury type	**Degree**	**Outcome**
Neuropraxia	Mild	Structure of nerve remains intact: recovery can occur within days
Axonotmesis	Severe	Disruption of the axon, but distal connective tissue architecture remains intact: regeneration can occur within weeks to years
Neurotmesis	Critical	Complete disruption of the nerve and surrounding connective tissue: surgical intervention required for partial recovery

2.2.1 Structure and organisation of peripheral nerves

Peripheral nerves are cordlike structures consisting of bundles of hundreds or thousands of axons with a defined path, conveying impulses between the central nervous system and some other body region. They differ in length and diameter throughout the body and within populations [22–24].

2.2.1.1 Anatomy of peripheral nerves

Histologically speaking, peripheral nerves comprise three distinct layers **(Figure 2.2).** From inwards to outwards these are the epineurium, the perineurium and the endoneurium [4,25,26]:

- The epineurium is the outermost layer, surrounding the entire nerve trunk and mainly composed of bundles and fibrils of collagen type I and type III [26]. Some elastic fibers, fibroblasts and adipocytes are present as well. A vascular network within the epineurium accounts for nutrients supply and waste product removal.
- The perineurium is a protective elastic sheath rich in type I and type II collagen fibrils, and elastic fibers that are longitudinally and circumferentially arranged; proteoglycans and fibronectin are usually present in the basal lamina as well [4]. The perineurium surrounds fascicular bundles of longitudinally oriented axons.
- Each axon is encompassed by the so-called endoneurium, a basement membrane comprising loose connective tissue of type I and type II collagen

fibers longitudinally arranged, and a basal lamina of type IV collagen, fibronectin and heparin sulfate [25].

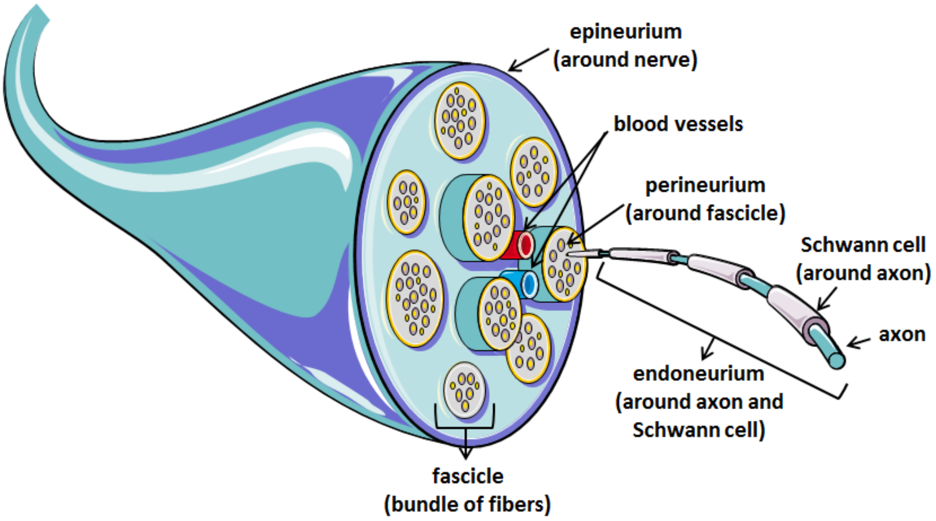

Figure 2.2 Structure of a peripheral nerve. The epineurium, perineurium and endoneurium, from outwards to inwards, make up the three main layers. Connective tissue of type I, type II and type IV collagen, fibronectin and proteoglycans, elastic fibers and heparin sulfate mainly comprise the various layers. *Adapted from Servier Medical Art.*

Axons vary vastly in width (e.g. 1-20 μm for the sciatic nerve), and are surrounded by a lipid and protective covering (i.e. myelin sheath) formed by several layers of Schwann cell membrane [27]. Some parts of the axons are not myelinated, forming gaps in between regular intervals (i.e. nodes of Ranvier, about 10 μm in length). These are important for how action potentials are propagated, jumping from one node to the other in the so-called saltatory conduction and leading up to faster conduction speeds. The outermost cytoplasmic nucleated Schwann cell layer covering the myelin sheath is the so-called neurolemma.

2.2.1.2 Cellular composition

Peripheral nerves are composed of two main cell types: neuron cells and neuroglia cells.

Neurons are the functional units of the nervous system, and similarly to muscle cells, they are electrically self-excitable. This means they are able to respond to a stimulus (i.e. any chemical change in the internal or external environment strong enough to initiate a nerve impulse) and convert it into an action potential (i.e. an electrical signal that propagates along the surface of the neuronal cell down its corresponding pathway) [4]. Neurons consist of two parts: a cell body and cell processes (either dendrites or axons). The cell body keeps a single nucleus with a prominent nucleolus, surrounded by a cytoplasm containing typical organelles. Dendrites are the input regions of neurons, while axons are the output portions that conduct nerve impulses away from the neuron to a dendrite, cell body of another neuron, or to an effector organ of the body. Neurons can be classified upon function into sensory afferent neurons, motor efferent neurons and interneurons [28].

Neuroglia cells are generally both smaller and more numerous than neurons, and do not generate or propagate nerve impulses [29]. Only one type of neuroglia cells is found in peripheral nerves: Schwann cells. Schwan cells are mainly responsible for producing myelin sheets around the axons of neurons, creating a growth-supportive milieu, and secreting and producing extracellular matrix (ECM). The ECM (**Table 2.2**) facilitates nerve regeneration of peripheral nerves by regulating axonal growth regeneration, and its interaction with Schwann cells is essential for the release of specific neurotrophic factors needed for neurite extension [30].

Table 2.2 Main components of the ECM of peripheral nerves.

ECM components	Function
Collagen	Major structural protein, with collagen type I accounting for around 90% of the tissue. Provides physical support for adhesion of Schwann cells and neurite extension [31–33]
Laminin	Modulates proliferation and survival of Schwann cells and their cytoskeleton dynamics [33]; being laminin a preferred surface to extend along [34]. Enhances axonal growth of some sensory neurons [35] compared with other ECM components [36–38]
Fibronectin	Predominantly located in the perineurium. Modulates Schwann cell motility and neurite outgrowth [39]
Glycoproteins and proteoglycans	Heparan, keratin, chondroitin and dermatan are involved in axonal growth regulation, Schwan cell proliferation and migration, and chemotaxis of neutrophils in nerve regeneration (e.g. nidogen) [40]. High levels of chondroitin sulfate negatively affect neurite extension after injury [41]

2.2.2 Nerve biology and current treatments

2.2.2.1 Natural nerve repair

Some functional recovery is possible whereby peripheral nerve axons are able to regenerate (e.g. neuropraxia and axonotmesis), however the probability of spontaneous recovery decreases as the level of injury increases (e.g. neurotmesis). Whether crushed or cut, a cascade of cellular events unfolds with extensive changes in the phenotype of injured neurons and Schwann cells distal to the injury that dictates neuronal survival and subsequent regeneration. The remaining surviving axons retract behind the injury front, while the distal segments undergo a process known as Wallerian degeneration (**Figure 2.3**). This process, starting 24–48h after injury, involves fragmentation of the axon and the surrounding myelin. Macrophages infiltrate and engulf the cellular debris during degeneration in a synergetic mechanism along with Schwann cells that aid to clear and prepare the injury site for regeneration. This process may last up to several months upon the length of injury [42]. In the most severe cases, the lack of guidance cues and the presence of fibrin deposition and dense scarring may create physical obstacles to regenerating axons.

Such regenerating process is mediated by several biochemical signals, where the usual flux of growth factors in the healthy state is hindered upon injury and primes the regenerative machinery [43]. During this process, the end bulbs of the axons sprout out sampling for survival and directional cues [44]. Some of these cues are provided by the presence of Schwann cells [45]. Following injury, Schwann cells lose their characteristic gene expression pattern [46] and activate a repair-related program, shifting from a myelinating phenotype into a regenerating status. This includes first an upregulation of surface proteins and several neurotrophic factors (e.g. nerve growth factor (NGF), leukaemia inhibitory factor (LIF), glial derived nerve growth factor (GDNF), growth associated protein GAP-43 and glial growth factor) [47]. Axonal elongation and survival of the injured neurons are promoted this way, and the activation of an innate immune response with an upregulation of cytokines follows [48]. This allows the recruitment of macrophages to the injured nerve that promote vascularisation at the distal site [49] and co-operate with Schwann cells to degrade myelin debris [50] that inhibit axonal growth. Macrophages are also attracted to the site by cytokines such as interleukin 6 (IL-6) or LIF, and act directly on neurons to promote axonal regeneration [48]. During this repair process, Schwann cells at the distal stump loose axonal contact and continue to proliferate and align longitudinally into solid tube-like structures. These are the so-called bands of Büngner, which along with trophic factors secreted by Schwann cells, serve as the track that enables guided axonal regeneration. However, axonal outgrowth rate is limited to 1-3 mm/day, and the fact that axons regenerate down the path does not determine a successful functional outcome [51].

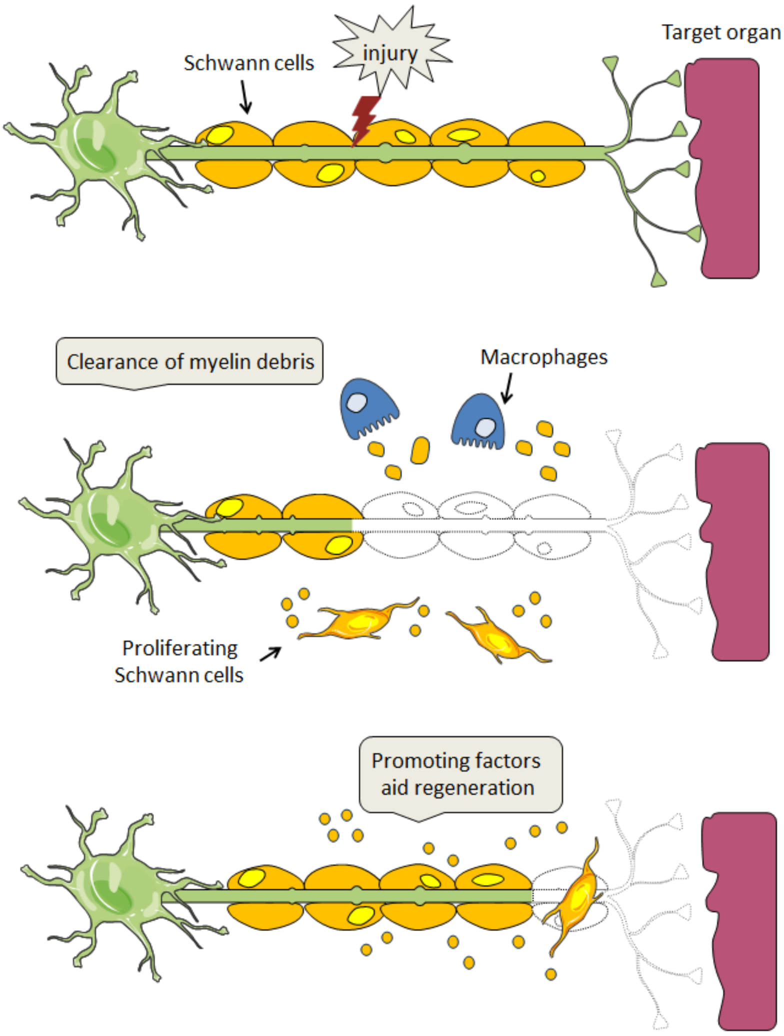

Figure 2.3 Regulation process in the regeneration of the peripheral nervous system. Schwann cells help macrophages remove myelin debris (i.e. Wallerian degeneration) and provide neurotrophic factors and physical support required to help the innate re-growth ability of the axons. Adapted from [52].

2.2.2.2 Current treatments for peripheral nerve repair

Several treatments for nerve reconstruction after segmental defects are currently available (**Table 2.3**) and have been previously reviewed [21,53]. However, where surgery is required, techniques have little changed over recent years, with many factors (i.e. age, time, extent of injury, and surgeon's skill) influencing the outcome.

Table 2.3 Available treatment options for PNIs.

Treatment	**Advantages**	**Disadvantages**
Primary repair, end suture	Most common approach for short nerve defects (i.e. <5 mm length) in which there is not too much tension [54,55]	Mismatching and misalignment of the fascicles and bundles is common. Scar tissue formation and compression of the axons may take place [56] Not practical for extended gap lengths: tension is generated and there is a reduction in blood supply to the damaged site
Nerve autograft	Gold standard technique for nerve defects with gaps up to 30 mm; tension-free and non-immunogenic	Donor site morbidity, availability and scar formation [57]. Need of a second surgery and loss of functionality. Sensory nerves are mainly used [58] but they may be inappropriate to replace injuries in a mixed nerve due to incorrect alignment, size disparity and morphogenic mismatches [59]
Nerve allograft	Temporary ECM for axon regeneration, tension-free	Long-term immunosuppression drugs, risk of infection and tumor formation
Entubulation	Alternative for nerve defects up to 30 mm; tension-free; relatively easy modification and may be patient specific and bespoke	Do not mimic ECM, hollow tubes with not subluminal structure. Performance has yet to surpass that of nerve autografts

When tensionless direct repair cannot be achieved, autografting is the benchmark. However, increased surgical times and donor site morbidities [56–59] have justified the search for better nerve conduit options.

2.2.2.3 Clinically approved nerve conduits

Several nerve conduits (entubulation) from natural and synthetic sources have been clinically [2] approved (**Table 2.4**).

Table 2.4 Clinically approved nerve conduits from natural and synthetic sources

Material	**Product**	**Type**	**Degradation rate**	**Maximum length**	**Inner diameter**
Processed human nerve allograft	Avance (AxoGen)	Conduit	3 to 4 months	70 mm	1 to 5 mm
Porcine small intestine submucosa ECM	AxoGuard Nerve Connector (AxoGen)	Conduit	3 to 4 months	10 mm	1.5 to 7 mm
	AxoGuard Nerve Protector (AxoGen)	Wrap	3 to 4 months	40 mm	2 to 10 mm
Collagen type I	NeuroMatrix/Neuroflex	Conduit	4 to 8 months	25 mm	2 to 6 mm
	NeuroMend	Wrap	4 to 8 months	25 mm	4 to 12 mm
	NeuraGen	Conduit	36 months	30 mm	1.5 to 7 mm
	NeuraWrap	Wrap	4 years	40 mm	-
Poly(L-lactide-co-ε-caprolactone (PLCL)	NeuroTube	Conduit	6 months	30 mm	2 to 8 mm
Poly(D,L-lactide-co-caprolactone)	NeuroLac	Conduit	16 months	25 mm	N/A
Poly(vinyl alcohol	Salubridge/Salutunnel	Wrap	Not degradable	40 mm	-

Based on data available from clinical studies in the literature, NeuroTube can provide positive functional recovery in 70% of patients achieving significant increase in myelination as well as improvement in sensation of transected nerve [60–68]. NeuroLac seems to be unsuitable due to inflexibility and collapse of the lumen because of stiffness and swelling [69–71], with a high incidence of complication including extrusion of the device [72]. Others, such as SaludBridge, are non-degradable and should be avoided due to chronic nerve compression and fibrosis. On the other hand, collagen-based nerve conduits such as NeuraGen could be an effective treatment option in 43% of the cases [73–76]; safety and effectiveness have been demonstrated in small nerve gap repair of non-critical nerve injuries. Rigidity of the tube and high cost of manufacturing, however, are some of their concerns [77]. AxoGen decellularised grafts, the only commercially-available decellularised allografts and most recent to be FDA approved (2010-2013) [1], have been successfully used for repair of human facial [78] and hand nerve defects [79] of 3 cm bridge length, and were able to restore sensation to near normal levels within 9 months of implantation. In rat models, they have been found superior to other currently available conduits such as NeuraGen but failed to conferred advantages over the use of an autograft [80].

While conduits of various lengths are available, this does not indicate that the maximum stated manufacturing lengths can be clinically addressed. Furthermore, direct comparison of the commercially available products is lacking; despite advances made, the clinical reality is that none of these conduits have been highly effective for nerve regeneration and none of these devices have been subjected to properly powered randomised controlled trials to conclude real effectiveness. Most clinical studies have targeted repair of sensory nerve defects, however, nerves with mixed motor and sensory fibres have not been well studied. Functional recovery is often poor (e.g. reduced motor function alongside pain and impaired sensation), and all of the commercial conduits have failed to meet the regenerative ability of the gold standard nerve autografting (likely due to the combination of ECM, Schwann cells and biological milieu). None can meet the clinical challenge to treat nerve defects in which there is a significant loss of tissue, with a generally accepted upper limit of 30 mm. None of them seek to address the biology of the regenerating nerve, and scar tissue formation is an issue. Current clinically approved conduits are mostly empty or filled with inner physiological solutions that provide no physical barrier. Furthermore, there are no topographical cues to direct growth within the lumen, nor delivery of culture cells or growth factors is facilitated this way.

2.2.3 Tissue engineering of the peripheral nerve: bioactive nerve conduits

Entubulation alone does not add further elements to the repair process, and rather than providing only a simple architecture, an active environment with further elements must be developed to control the interaction of cells with their surrounds and promote axonal regeneration. As such, tissue engineering has been widely proposed as a promising strategy to repair PNIs and serve as the gold standard of care in the future. It draws on principles from engineering and life sciences to restore and repair the tissue function by providing an appropriate physiological environment at the damaged site. One common approach is to grow cells *in vitro* on a three-dimensional (3D) scaffold to be later delivered to the desired site in the patient's body. An alternative is to implant a scaffold directly *in vivo* and make use of the host's environmental factors and the active cues of the scaffold to promote and direct tissue formation *in situ* [81–83]. However, the requirements of scaffolds for peripheral nerve repair are manifold due to the challenging injury-healing process of the tissue. For optimal nerve regeneration, the construct must maintain longitudinal strength in the repair to prevent loss of continuity. Schwann cell migration should be facilitated, and the tropic and trophic guidance cues that draw neurites to the distal nerve and reduce neuroma formation should be optimised while blocking the ingrowth of non-neural tissue that can impede regeneration [84]. The idea is therefore to develop a bioactive nerve conduit (**Figure 2.4**) that can mimic the elements of a nerve autograft required to promote regeneration – barrier function from the epineurium, physical integrity to maintain repair, directional guidance cues from the endoneurial tubes, mixture of immune compatible support cells, and availability of a vascular plexus within.

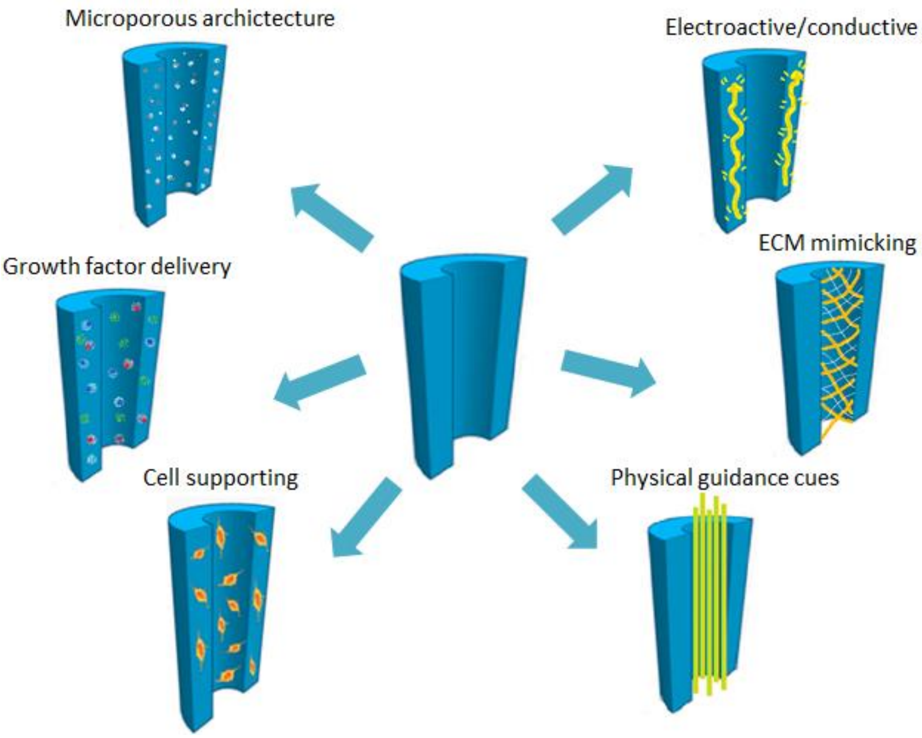

Figure 2.4 Property criteria for ideal bioactive scaffolds for tissue engineering of the peripheral nerve. Nerve conduits should maintain physical integrity to direct growth and exhibit desirable porosity for availability of a vascular plexus within, while keeping soft tissue out by maintaining the barrier function (e.g. epineurium). Nerve conduits should also provide appropriate biochemical and physical guidance cues required to stimulate regeneration across the nerve gap (e.g. mixture of immune compatible support cells, presence of growth factors, electroactive properties to facilitate electrical stimulation of cells and propagation of nerve action potentials, and presence of endoneurial-like tubes for mimicking the native tissue structure).

2.2.3.1 Use of synthetic and natural polymers: a biodynamic construct

A vast range of materials, both synthetic and of natural origin, have been well-investigated as potential candidates for tissue engineering nerve conduits.

Synthetic materials hold the promise that their properties can be easily tuned and controlled, however they lack the presence of biological sites for proteins to bind and cells to interact with, so there is an insufficient integration with the native tissue. As a result, their biological response has to be enhanced; yet the natural temporal and spatial complexity that the native ECM presents are poorly replicated. As previously reviewed [85–88], several synthetic polymers have been widely tested. However, they are limited to small diameter nerves and only small gap injuries can be bridged, and although some regeneration does occur, a poorly functional recovery is achieved and subsequent surgeries must follow. This is mainly due to poor mechanical properties, lack of cellular guidance, or concerns about the generated by-products and associated inflammatory responses. In addition, there is a lack of robust clinical data.

Natural materials have the advantage of conferring the needed biological sites for proteins to bind and biological cues for cell behaviour to be controlled. Natural scaffolds for peripheral nerve regeneration include the use of decellularised scaffolds for nerve guidance conduits (NGCs), glycosaminoglycans such as hyaluronan, polysaccharides such as chitosan and alginate, or fibrous protein gels such as collagen, laminin or gelatin [53,89]. Other than availability, the major drawback of decellularised scaffolds is the discrepancy in the decellularisation and post-processing technique that can result in the incomplete removal of cellular components and for damage to the microarchitecture; another problem being the fact that they may act as a nidus for disease transmission and immune responses. On the other hand, glycosaminoglycans, polysaccharides and protein gels do not generally present sufficient mechanical properties required to withstand compression and tend to swell and collapse over time in aqueous environments. Crosslinking agents may overcome this problem; however, the clinical use of most ECM components is limited since they are generally derived from animal or tumorigenic tissues.

No single material seems to hold dramatic benefit over any other in terms of nerve regeneration, and further active elements may need to be added to address the biology of the regenerating nerve. Indeed, to tackle the disadvantages of both synthetic and natural polymers alike, hybrid composites and co-polymer based systems have been used in the fabrication of NGCs to obtain tuneable ECM-like properties [90].

2.3 Silk for peripheral nerve regeneration

Technologies to aid nerve regeneration and to communicate with neurons are required from better biomaterial based bioactive conduits that can both physically support tissue growth and elicit desired cellular-specific responses.

2.3.1 Why silk is a suitable material for peripheral nerve repair

Substrates approved for current clinical use in peripheral nerve repair include collagen and synthetic polyester-based materials; however, their use has been limited due to the lack of good clinical data (e.g. there are no randomised controlled trials, and grading of outcomes by two-point discrimination is not standardised) [91], as well as their relative expense and inability to bridge large nerve gaps.

The use of silk, a natural occurring fibrous protein, has demonstrated great promise as an inexpensive biomaterial for nerve tissue engineering [92,93], useful for surgical implantation due to its physico-chemical, mechanical and biological characteristics. These have been covered in great detail by Guinea *et al*. [94] and Das *et al*. [95]. In brief, silk is an FDA approved material (e.g sutures for soft tissue repair) [96] from natural origin that possess many features that would suggest an ideal substrate in nerve repair. For instance, silk-based materials promote oxygen and water permeability [97,98], essential for transport of nutrients and other water-soluble metabolites. Silk has also been shown to support cell attachment and proliferation of neurons and Schwann cells [92], with no significant differences in cell phenotype or proliferation observed and no deleterious effect on their culture [99]. Silk also presents high biodegradation kinetics and solid physical strength with flexibility [11,100], desirable to avoid collapse of the conduit and to avoid second operations or long-term adverse effects of the implant. Relatively low inflammatory response and antigenicity are well-tested and reported compared with other biodegradable polymers [92,101–103]. In addition, silk can contain cell-friendly peptide sequences (e.g. RGD) upon the particular strain (i.e. breed, stock, or variety) [104,105], and silk proteins can be engineered to include designer peptide sequences [106] that can be more cell friendly/instructive towards nerve repair [107].

2.3.2 Use of purified silk and blended formulations in nerve repair

Silkworms and spiders are the two main sources of silk protein (i.e. silk fibroin, SF, and silk spidroin, SP, respectively). While their structural composition may vary in terms of amino acid sequences [108–110] and protein conformations [111,112], significant progress has been made towards developing adequate silk-based formulations that can be used in biomedical applications for NGCs.

2.3.2.1 From regenerated solutions to recombinant synthetic formulations

Most of the work conducted on silk towards peripheral nerve regeneration has been based on regenerated silk fibroin (RSF) solutions from *Bombyx mori*, and shown feasibility for use in nerve grafts due to appropriate cell-material interactions, cellular viability and proliferation [92,113]. However, the use of SP and regenerated silk spidroin (RSP) solutions, although limited, have been explored *in vitro* as well [114–116], and some of these spider silk-based conduits have been successfully translated into large animal models [117–119] in long distance nerve defects explored by Radtke *et al*. [117,120]. In one of these studies, a nerve conduit was produced from decellularised vein grafts filled with spider silk fibres to bridge a 6 cm tibial nerve defect in adult sheep [117]. Axons were shown to regenerate through the scaffold and were myelinated indicating Schwann cell migration; electrophysiological recordings in terms of the motor nerve conduction velocity and the amplitude of the compound motor action potential were comparable to those of an autologous experimental control [117]. The same strategy was used to characterise the *in vitro* regeneration on defects measuring up to 15 cm in length [120]; results indicated that these spider silk-based conduits were a favourable environment for Schwann cell attachment, proliferation and distribution independent of the construct length, over distances up to 15 cm *in vitro*.

Synthetic recombinant SF [121] and recombinant SP [122–131] proteins have been produced. These recombinant proteins reduce possible issues of batch-to-batch variations of natural silk proteins guaranteeing reproducible quality in the necessary protein quantities. Recombinant silks enables mass production issues to be overcome (i.e. spider silk) and to create specific genes with the appropriate sequences to tune specific properties [132], for example by introducing different binding peptides to have special functionalities. However, no silk gene has been cloned in its entirety and only partial sequences have been reported [133]. As consequence, recombinant spider silk studies *in vitro* and *in vivo* are limited [134–138], widely reviewed by Rising *et al*. and Widhe *et al*. in 2011-2012 [133,139]. The particular use of recombinant spider silk and recombinant SF formulations for peripheral nerve repair is barely found in the literature, which roots from the difficulty in producing recombinant silk proteins [140]. Mainly only *in vitro* studies have been performed [123,141–143] on the suitability of these synthetic recombinant proteins. For instance, films made out of rMaSp1 were shown to present a more suitable surface charge and substrate stiffness compared with that of rMaSp2 to support the growth of primary rat cortical neurons and promote axon extension and network connectivity *in vitro*; in addition, increased neural cell adhesion molecule expression at both mRNA and protein levels were exhibited [141], hypothesised to be in part due to the inherently positively charge nature of rMaSp1 at neutral pH. In a different study, Lewicka *et al*. showed that neural stem cells could proliferate on 4RepCT films and that they could mature into neurons when stimulated with bone morphogenetic protein [123]. Furthermore, in a study by Moisenovich *et al*. [143], a film scaffold based on a genetically engineered analogue of Nephila clavipes spidroin 1 (rS1/9) was shown to promote ingrowth of *de novo* vascularised connective tissue elements as well as ingrowth of nerve fibres when implanted into midline dorsal subcutaneous areas of adult mice.

2.3.2.2 Blended silk formulations in peripheral nerve repair

The mechanical properties of silk differ upon their manufacturing source and processability conditions [144]; a comprehensive up-to-date overview of these properties can be found in [145]. SF has been blended with various other polymers, which include both natural and synthetic molecules (**Table 2.5**). This enables facile tuning of its physico-chemical, mechanical and biological properties. Nevertheless, inter-study comparison between them is difficult in terms of scaffold fabrication and assessment criteria, and none so far have matched the outcome obtained with nerve autografts. One variable worth considering towards the future translation of a tissue engineered product from the lab to the clinic is the type of solvent the hybrid system can be processed in. Some solvents are very toxic, and the use of solvent-free green techniques would be more suitable (**Appendix A**).

Table 2.5 Silk-based composite blends used for peripheral nerve guides

Material	**Properties**	**Ratio (*)**	**Conduit type**	**Assessment**	**Outcome**
Chitosan	Antimicrobial and wound healing properties [146]. Similar structure to that of glycosaminoglycans in the ECM.	1:1; 3:7	Film conduit pre-seeded with adipose derived stem cells	10 mm gap, rat	Significant enhancement of nerve conductivity and functional recovery [147]
		1:1 ^{A}	Film conduit with lumen filled with SF fibres	10 mm gap, rat	Comparable morphological and electrophysiological results to a control nerve graft [148]
Collagen	Major component of the ECM; provides suitable surfaces for cell adhesion and migration	2:1	Film conduit pre-seeded with a co-culture of Schwann and adipose derived stem cells	10 mm gap, rat	Comparable morphological results to nerve autograft [149]
Tropoelastin	Improves cell adhesion, proliferation and migration [150]	1:0; 9:1; 3:1; 1:1; 1:3	Film	*In vitro*	Improved neurite extension and enhanced Schwann cell process length with increased tropoelastin content [151]
Poly(lactide-*co*-glycolide)	Good mechanical properties, appropriate degradation rate	1:1 ^{A}	Electrospun conduit (randomly aligned fibres)	Under rabbit skin	Mild inflammatory reaction [152]
		1:2 ^{A}	Electrospun conduit (aligned fibres)	10 mm gap, rat	Similar histology to nerve autograft [153]
PLCL	Good mechanical properties, appropriate degradation	1:3 ^{A}	Electrospun conduit (aligned fibres)	10 mm gap, rat	Significant low outcome compared with nerve autograft [154]
Polyacrilamide	Model of elasticity-cell interactions	1:1; 2:1; 4:1	Casted film	*In vitro*	*In situ* scaffolding but poor mechanical outcome [155]
Poly(p-dioxanone)	Strong wet-state strength and excellent toughness	1:1	Lyophilised conduit	*In vitro*	No *in vivo* studies [156]

*Ratio values are expressed in terms of SF:X (i.e. X being the other component) in (v/v) unless specified otherwise. A: (w/w)

2.4 Controlling the neuronal cell response

The attention has turned into the wall and lumen of conduits as a provision of a scaffold to ensure (1) directional neurite growth, Schwann cell migration and phenotypic expression, (2) maintenance of cells and (3) a reservoir for exogenous growth factors.

2.4.1 Cell-material interactions and topography

2.4.1.1 The role of contact guidance in nerve tissue repair

Connectivity of nerves is largely dependent on the directionality of the growing regenerating axons towards their genuine targets. If regenerating axons do not succeed in elongating appropriately, nerves will not mature, leading to their degradation and loss of function in the long term. In this regard, a way to lead neural axons and Schwann cells is by the presence of physical supports and guidance structures at the cellular level by creating highly ordered micro/nanostructured surface topographies (**Figure 2.5**) [157–160]; this is known as contact guidance theory.

Indeed, previous studies have demonstrated that neural cells respond to a range of linear guidance cues, and it has been shown that topographical cues in the form of channels and microgrooves enhance cellular alignment and neurite outgrowth [161,162]. For instance, Mobasseri *et al.* demonstrated comparable experimental outcomes between an autograft and a PCL/PLA conduit with inner lumen microstructured sloped wall-shaped grooves, being a potential alternative treatment [162].

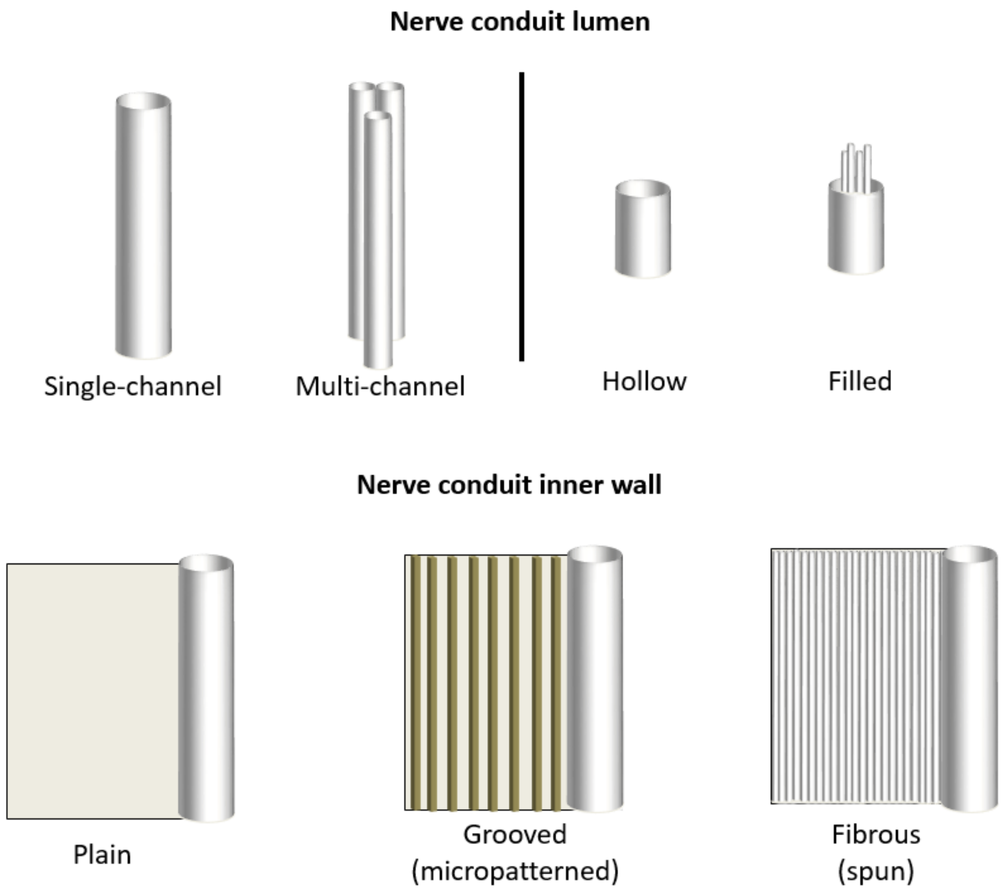

Figure 2.5 Physical support guidance structures in NGCs: lumen (e.g. single-channel vs multi-channel, hollow vs filled conduit) and inner wall (e.g. plain vs grooved vs fibrous).

Topographical cues in the form of aligned micro/nanofibres [154,163] have also been considered in peripheral nerve repair as oriented internal pathways to mimic endoneurial tubules and maximise the chance of target re-innervation by physically guiding neurons to grow. Aligned nano/microfibres (250 nm – 2 μm) present unique topographical properties that significantly enhance cell function, and act as cellular contact guidance by improving alignment [164–168] of the f-actin filaments (<25 nm) of the cytoskeleton of neural cells, their axons (1-20 μm), and the subsequent transition of Schwann cells towards the so-called bands of Büngner. Other than the fibre orientation, variations in the fibre diameter have also been reported to have a vital role in regulating proliferation and differentiation behaviours. For instance, it has been shown that higher degree of proliferation, differentiation and cell stretching along single fibre axis of neural stem progenitor cells occurred as the fibre diameter was decreased, with a lower degree of cellular aggregation [169]. In addition, a fibrous architecture can be designed to tune mechanical properties, as opposed to plain conduits for example.

2.4.1.2 Physical guidance cues in silk-based nerve conduits and their performance

Tubular constructs represent the major NGCs. In particular, hollow constructs present a suboptimal performance for large nerve gap defects, and many researchers have turned into the use of filled conduits to provide for an additional supporting structure in order to enhance their biological performance. While hydrogels may represent the simplest structural modification of a nerve conduit in terms of a luminary filler [170], they do not provide on their own the nano/microscale guidance architecture needed for axonal extension. The goal is not to recreate the architecture of nerves, but rather to provide the proper physical guidance cues as wall/luminary fillers to promote cells to rebuild the ECM and direct regeneration. However, control over the physical cues that tubular conduits can provide is limited by the availability of suitable fabrication techniques.

2.4.1.2.1 Macro-luminal cues in nerve conduits:

Injection moulding and metal wire dip-coating frameworks of SF solutions have been regarded as the simplest architectural modifications at the macroscale level. Indeed, several *in vivo* studies based on RSF are available on these techniques. For instance, a 6-month post-implantation study of a SF conduit filled with oriented SF filaments within the lumen was used to bridge a 10 mm sciatic nerve rat gap [93,171]. Results revealed low-to-non systemic inflammation, and neither electrophysiological nor morphological studies of the sensory and ventral motor neurons showed significant differences compared with the use of a nerve autograft; nevertheless, reversal of muscle atrophy due to denervation was less pronounced in the silk graft scaffold. Comparable performances to that of a nerve autograft and a collagen type I nerve guide in terms of inflammatory response, fibrotic formation and re-myelination capacity were also observed when a RSF casted conduit of empty lumen was used to bridge a 8 mm defect of a rat sciatic nerve [172]. Improved outcomes in terms of axonal growth and functional recovery have also been made possible by incorporating co-cultures of DRG and Schwann cells within the conduit for regenerating a 10 mm sciatic nerve defect in rats [173]. However, all these studies present a crude macro-luminal hollow structure.

The manufacture of RSF multichannel nerve conduits has been explored therefore as a way to provide control over another hierarchical level. The rationale behind is that a number of channels within the luminal space of the construct can help reduce axonal dispersion and aid controlling targeted axonal re-innervation when compared with a hollow NGC [174]. However, although multi-channel conduits can reduce axonal dispersion, a macroscale luminal cue on its own does not provide the required cell-material interactions needed for enhanced axonal pathfinding and Schwann cell migration. That is why spinning techniques for the hierarchical control over the inner structure of nerve conduits have recently gained traction [175] (**Figure 2.6**).

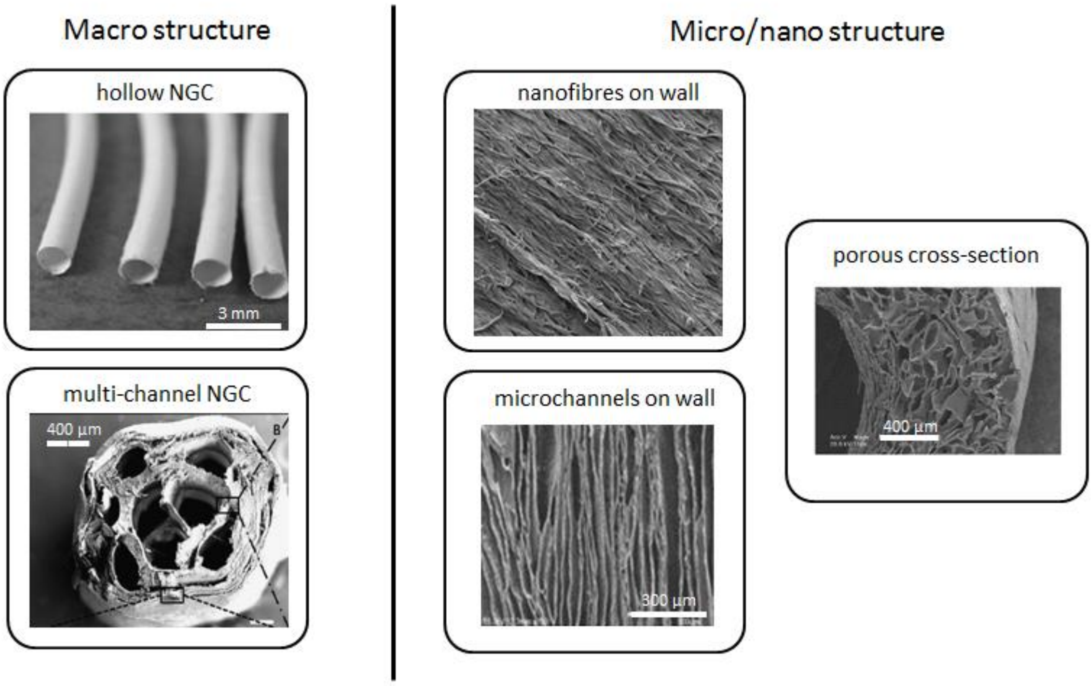

Figure 2.6 Physical guidance cues on SF-based NGCs: hollow vs multi-channel NGC, nanofibres vs microchannels on wall, microporosity. Reproduced with permission [93,175–177]. Copyright 2007, 2012, 2014 Elsevier, and 2013 Wolters Kluwer.

2.4.1.2.2 Micro-luminal cues in nerve conduits:

Microscale modifications of the luminal architecture have been made possible with the availability of more advanced fabrication techniques. Microscale guidance cues provide the ability to direct unidirectional alignment to enhance repair at the cellular level by influencing axonal pathfinding and increasing Schwann cell migration. For instance, in the late 90s the use of polyamide microfilaments (10-20 μm) showed success over small to large nerve gap defects [178,179], and can be used either on its own or as part of the luminal space. Interestingly, the number of filaments within the luminal space of the tubular construct was shown to influence repair success, with lower number of polyamide filaments needed for small gap repairs [178] and larger numbers of polyglycolic acid filaments capable of regenerating gaps up to 30 mm in dogs [180]. Although not many *in vivo* studies with RSF microfilaments have been performed [173,181], the use of advanced lyophilisation/freeze-drying and liquid-liquid phase separation techniques for the fabrication of unidirectional aligned porous microarchitectures have been investigated over SF scaffolds [93,149,176,182–185] as means to support unidirectional cell migration *in vitro*.

Interestingly, other than enhancing axonal growth and Schwann cell migration, microscale cues have shown to reduce the inflammatory response and limit foreign body reaction of the constructs [186]. In this regard, therapeutic strategies based on the incorporation of anti-inflammatory cytokines have been developed with SF to modulate macrophage phenotype from M1 towards M2 polarisation (i.e. decrease inflammation and encourage tissue repair) [187–189] and may be used to provide an enhanced regenerative response for neural repair [190].

2.4.1.2.3 Nano-luminal cues in nerve conduits:

Patterning at the nanoscale is now possible and may be applied towards nerve regeneration. Most studies on SF have been carried out so far on 2D substrates [191–193], as patterned nanostructures have yet to be engineered into tubular constructs. While grooves between 500 nm to 2 μm in width have been explored for better neural alignment compared with non-patterned substrates [194], studies have reported that a 2D surface patterning smaller than the size of a neural progenitor cell (<20 μm) leads to excellent cell alignment and maximises neurite length by restricting the number of neurites per cell, limiting the risk of off-target re-innervation [195]. This opens up the possibility of applying such patterning techniques for tubular constructs with nano/microscale structural modifications. However, what groove/fibre size is the most suitable for nerve repair remains under debate, with some research groups arguing that larger sizes perform much better in terms of the neuronal/Schwann cell response [196].

A wide range of fabrication techniques used in nerve scaffolding are currently available, recently reviewed by Wieringa *et al*. [197]. Most fibrous silk-based scaffolds for nerve repair to date have been based on electrospun structures [198]. Electrospinning is a simple and versatile low cost technique widely used to generate porous nerve conduits of aligned nano/microfibres [154,163]. For instance, electrospun RSF fibres in the range of 250-400 nm have been used as nanotopography patterns for hollow nerve conduits implanted *in vivo,* and have shown favourable motor function recovery comparable to that of a nerve autograft [177,199]. Improved regenerated outcome and functional recovery of the graft has also been proved in a 10 mm sciatic nerve defect gap in rats, with incorporation of bone-marrow derived mesenchymal stem cells that longitudinally aligned with the fibres (700 nm) axis as compared to RSF fibres alone [200]. The use of templating electrospinning by which microchannels are micropatterned with aligned sutures within three-dimensional electrospun constructs has been employed as a way to mimic the fascicular architecture and fibrous ECM found in native nerve [201]. However, issues with these electrospun scaffolds are the need to roll them up and combine them sometimes with multiple conduits – therefore sterilisation and handling may become problematic.

Techniques such as cell electrospinning [202], reviewed elsewhere [203], and more recently aerodynamically assisted bio-threading [204], have been used to incorporate cells directly into fibres. Whilst these methods allows the fabrication of continuous threads (50 to 350 μm) with a range of viable living cells types [204–207], there might be issues with increasing post-threading cell viability, optimizing mean thread diameter and avoiding non-continuous cellular populations within fibres; cells also cannot be allowed to become dehydrated during processing. To the authors' knowledge these techniques have not yet been applied to silk or for nerve tissue engineering; however, microfluidic spinning has been employed to generate silk-alginate fibres laden with L929 fibroblast cells [208]. Electrospinning and microfluidic spinning for functional biomedical fibres have recently been reviewed elsewhere [209].

Advances in materials science suggest that nanoscale cues will soon be fully incorporated into the next generation of nerve guidance constructs, and allow us to postulate that a combination of micro/nanoscale alignment within the walls and lumen of the conduit may allow for directed maximal neurite extension mediated solely by topographical cues.

2.4.2 Cell-loaded nerve conduits

While most silk-based conduits that have been tested *in vivo* are cell-free, other routes of investigation have focused on the addition of cells within the matrix to enhance the inner lumen of the constructs, making them more bioactive and facilitate regeneration. The regenerative potential of cell-based therapies alongside biomaterials may enhance nerve regeneration.

The key question is what cells are most appropriate to use. Autologous Schwann cells are the benchmark as they drive the normal regenerative process. They are immune competent and secrete a favourable cocktail of neurotrophic and tropic cues [210]. Schwann cells have been shown to increase the gap length that can be bridged compared with acellular constructs and allografts [211,212]. However, their isolation, harvest and culturing for expansion are costly and very time-consuming. Stem cells, on the other hand, present an alternative source to autologous Schwann cells without some of their associated limitations. The therapeutic potential of stem cells in nerve repair has been previously reviewed [213]. Bone-marrow derived mesenchymal stem cells can be harvested from an autologous source to reduce the risk of immune response and they have the potential to differentiate into a Schwann cell phenotype prior to transplantation. When differentiated, they can synthesise and secrete neurotrophins and they have been shown to upregulate myelin genes and protein expression *in vitro* [214]. Adipose derived stem cells have also been loaded into silk-based conduits. They can be easily harvested and isolated from the fat tissue, with faster proliferation rates and can be differentiated more readily *in vitro* prior to implantation to express Schwann cell phenotype markers [215]. However, maintenance of a Schwann cell-like phenotype in differentiated adipose derived stem cells requires the synergistic action of multiple growth factors [216]. While induced pluripotent and embryonic stem cells are another cell source of interest, to the authors' knowledge no studies on silk-based nerve conduits have been reported so far.

A summary of these cell types loaded into silk-based nerve conduits is presented in **Table 2.6**. While all these studies acclaim the effect of loading cells into the lumen of the scaffold, with a beneficial regenerative outcome superior to that in a cell-free control, inter-study comparison is challenging and none match the reproducibility obtained with nerve autografts. The material formulations, the scaffold fabrication technique and the physical guidance cues present are different, and they are evaluated within different defect gap lengths.

Table 2.6 Cell-loaded silk-based nerve conduits for peripheral nerve regeneration

Cell type	Pros / Cons	Conduit type	Assessment
Autologous Schwann cells	Phenotype (●●●) Immunity (●●●) Cost (●) Availability (●)	Isogenic veins filled with SP fibres	20 mm rat sciatic nerve [118]
		SF/chitosan film with conduit lumen filled with SF fibres	10 mm rat sciatic nerve [148]
		SF/collagen film conduit	10 mm rat sciatic nerve [149]
		SF film with lumen filled with 15 µm SF filaments	10 mm rat sciatic nerve [173]
Adipose derived stem cells	Phenotype (●●) Immunity (●●●) Cost (●●) Availability (●●●)	SF/chitosan film conduit	10 mm rat sciatic nerve [147]
Bone marrow derived stem cells	Phenotype (●●) Immunity (●●●) Cost (●●) Availability (●●)	SF film with conduit lumen filled with 15 µm SF filaments	10 mm rat sciatic nerve [181]

Phenotype (● different; ●●● very similar), likelihood to elicit an immune response (● quite likely; ●●● unlikely), cost (● high; ●●● low), and availability or ease of culture (● difficult; ●●● easy) for the various cell sources as compared with autologous Schwann cells

2.4.3 *Targeted therapeutics with proteins and growth factors*

A third route to make silk-based nerve conduits more bioactive is by incorporating elements that can reduce neuronal death and enhance cell function to promote tissue repair and regeneration following injury. Most of these therapies target covalent attachment of biochemical cues such as proteins, peptide sequences and growth factors [121,142,184,217–222] (**Figure 2.7**).

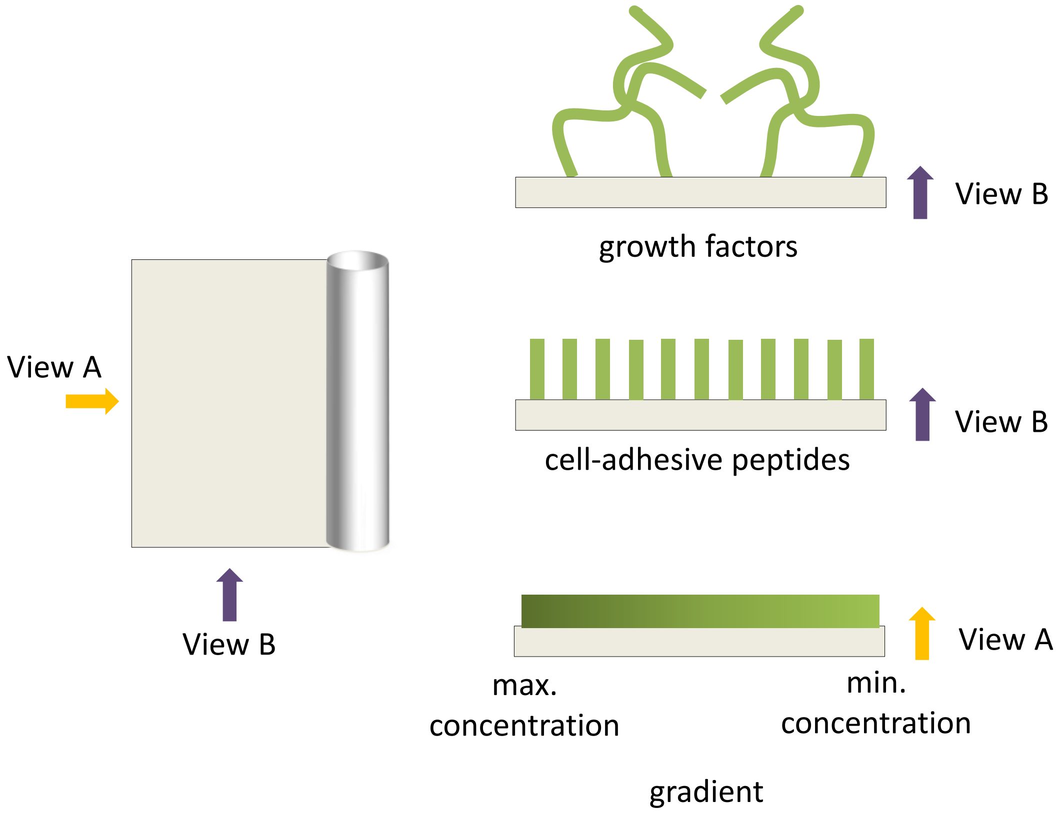

Figure 2.7 Surface engineered and peptide/growth factor release scaffold for nerve tissue engineering. The inner lumen of nerve conduits can be immobilised with cell specific ligands for cell adhesion and enhanced repair. These can be in the form of fixed growth factors (top image) or cell-adhesive peptides (middle image), or even as gradients (bottom image) longitudinally established along the inner lumen of the conduit with different growth factors/peptides and/or concentrations.

2.4.3.1 Modifications with proteins and peptide sequences

Development and repair of peripheral nerves are critically influenced by the presence of laminin and fibronectin, two basal laminal proteins found in peripheral nerves and closely associated with Schwann cells [223]. Laminin modulates proliferation and survival of Schwann cells and enhances axonal growth of some sensory neurons compared with other ECM components [33,36–38]; however, there remains no clear understanding of the signalling pathways involved. On the other hand, fibronectin is crucial in the migratory pathways of cells from the peripheral nervous system [224]; for instance, Schwann cell motility and neurite outgrowth are modulated by fibronectin [30,225]. Incorporation of fibronectin derived sequences by genetic engineering have been previously reported in recombinant SP and SF studies to further enhance their cell supportive ability [121,226], and it has been reported that covalent binding of these basal laminal proteins to SF may enhance nerve regeneration [184,217]. Elastin is another protein located in all three connective layers of peripheral nerves [227], and chimeric materials based on silk and elastin blocks have been engineered [228,229] for improved controlled delivery of therapeutics [230] in nerve tissue engineering applications by tuning the net charge of the protein [151,231]. Another chimeric material of interest is based on reflectins, proteins that possess unique self-assembling properties [232]. Reflectins have been detected during key stages of neurogenesis in cephalopods [233], and it has been shown that substrates based on reflectin A1 isoforms can facilitate neural progenitor stem cell growth *in vitro* [234,235].

Peptide sequences have also been investigated for improved outcomes in nerve tissue repair. The use of Arg-Gly-Asp (RGD), found in fibronectin, is well-known to improve cell attachment and differentiation by initiating specific internal signalling pathways [236,237]. Other sequences such as Ile-Lys-Val-Ala-Val (IKVAV) and Tyr-Ile-Gly-Ser-Arg (YIGSR), mainly found in laminin, are known to promote and facilitate neurite outgrowth and enhance attachment of migrating Schwann cells over the substrate [238–240]. Non-mulberry SF scaffolds containing cell-binding RGD motifs have been previously explored [218] and functionalised with IKVAV peptide sequences for neural tissue repair [219], which may serve as landmark for their use in peripheral nerve regeneration. Functionalisation of recombinant spider silk films with

RGD, IKVAV and YIGRSR cell binding peptides was also studied on Schwann cells by Widhe *et al*. [142]. Cells acquired a star-shaped morphology with long neurite-like outgrowths, however positive effects on both cell adhesion and survival were found with incorporation of IKVAV. Recombinant peptides based on the sequence of SF have also shown potential to support peripheral nerve regeneration [241]. For instance, in 2013 a new peptide compound known as SF16 was incorporated into a SF hydrogel-based scaffold and their outcome evaluated in a 10 mm rat sciatic nerve injury [107], with electrophysiological results showing improvement in amplitude recovery in the *in vivo* model.

In essence, data from these studies suggest that further structural modifications to silk-based tubular constructs can be undertaken by incorporating basal lamina proteins or peptide sequences that can significantly improve their regenerative capacity.

2.4.3.2 Addition of growth factors

Neurotrophic factors are naturally involved in survival, growth and differentiation of neural cells; they are predominantly produced by Schwann cells and play a homeostatic role in the neural cell turnover. Given their role in nerve injury and regeneration [242], their targeted delivery might be expected to reduce neuronal death, enhance regeneration and support the Schwann cell population. This has been demonstrated in experimental studies where several of these biomolecules have been incorporated alone or in combination into silk-based nerve conduits [119,175,183,220,221,243,244]. For instance, NGF was blended with a RSF solution and casted into a film conduit; *in vitro* testing reported the slow released of NGF – with their potency retained – over a period of 3 weeks, and significantly increased outgrowth of neurites [183]. In another study, co-delivery and bioactivity of GDNF and NGF were evaluated over a 4-week period by blending the growth factors with a SF solution that was electrospun into a conduit [220]; *in vitro* assays showed augmented axonal growth rate of sensory neurons and motor neurons of chicken embryos, with glial cells migrating in close association. In a similar study, NGF and GDNF were blended into a RSF based solution that was spin-coated into a nerve conduit [244]. Co-delivery of both growth factors over a 28 day period was reported to synergistically enhance neural cell activity compared with control [244]; however, the potency of the growth factors was not determined.

In vivo studies of loaded growth factors into RSF and RSP nerve conduits have also been explored. In 2014, NGF was blended with a RSP based solution and electrospun into a nerve conduit that was implanted to bridge a 20 mm rat sciatic nerve gap [119], and more recently, NGF and ciliary neurotrophic factor (CNF) were blended into an RSF solution that was electrospun into a multichannel nerve conduit [175]. While an overall improved outcome was demonstrated, results showed that much of the loaded factors' amount was not released over 10 days, and rapid degradation was observed after the first 3 days. In another work, an aligned electrospun RSF conduit was manufactured by loading brain-derived neurotrophic and vascular endothelial growth factors into an RSF solution [243]. *In vitro* assays demonstrated that the release of the factors was well maintained only up to 2 weeks, while *in vivo* results of the scaffolds implanted under the skin of adult mice revealed *de novo* innervation and vascularisation without chronic inflammatory response [243].

Although various *in vitro* and *in vivo* studies using several of these growth factors, alone or in combination, have shown promising results, there has not been a real effect on the clinical management of nerve injuries using any of these, and no trials are underway to the authors' knowledge. In addition, they may have unpredictable interactions: an oversupply of growth factors might be detrimental to regeneration, and for the cells to re-differentiate and re-myelinate, levels of growth factors might need to be gradually reducing in time. Repair of the neural tissue is regulated by a multistep process with multiple growth factors and cytokines that act in a concentrated and time-dependent fashion and whose actions may be contingent on a variety of different elements [53]. An ideal cocktail of factors may not be possible, and controlling their tethering attachment and temporal profile release remains challenging. As a consequence, the use of concentration gradients as guidance cues has recently received much attention [245–252].

2.4.3.3 Use of concentration gradients

The use of gradients avoids cell overdose (i.e. aberrant repair) and enhances long-term repair of the nerve by providing sustained delivery over longer periods of time, making sure cells receive a more appropriate timely exposure dose. Concentration gradients are currently being investigated in a wide variety of pattern shapes and distributions to direct cells [253]. For instance, a concentration gradient of NGF was immobilised in a poly(2-hydroxyethylmethacrylate) microporous gel and its release was maintained over an 8-day period to guide neurite outgrowth *in vitro* [245]. More recently, a spatially controlled multicomponent gradient of NGF and GDNF were immobilised in a 3D printed silicon/gelatin-methacrylate hydrogel conduit and their release was shown to be well-maintained over a 1-month period, although their stability were not determined [252]. Other than growth factors, peptides and protein molecules such as neurotrophins have been bound as well. For example, Shoichet *et al*. immobilised in 2006 for the first time well-defined concentration gradients of NGF and neurotrophin-3 in a cell-penetrable adhesive scaffold of poly(2-hydroxyethylmethacrylate) and poly(L-lysine) [247]. Since then, several gradient concentrations of ECM molecules have been explored, typically involving combinations of fibronectin and laminin, showing to promote axon extension along more intricate patterns [248–250,254]. For instance, surface-bound laminin and a gradient of a short peptide of laminin-1 containing the IKVAV sequence was shown to be sufficient in directing axonal growth [246].

Data from these studies suggest that similar strategies can be applied on silk substrates to further enhance response of silk-based nerve tubular guides [221,255]. However, directly embedding growth factors onto the surface of a nerve guide may not provide a suitable method for long-term delivery due to the growth factor’s short half-life *in vivo* [251]. In this regard, a concentration gradient of NGF on electrospun aligned RSF fibres was prepared by embedding the growth factor in the spinning solution, and their bioactivity assessed over a 5 day period [255]. It was observed that neurites extended about 209 μm per day in the presence of a four-step gradient, compared to about only 132 μm per day in a uniform growth factor concentration. Neurotropic growth factors have also been coaxially spun with SF at different concentrations, showing that the activity of the growth factors were well-maintained over long periods and that they enhanced differentiation of neural stem cells [222]. Other arrangements in the form of microparticle-based delivery systems [256] in combination with the use of gradients have also been explored [221]. For instance, GDNF-loaded silk microspheres were distributed either uniformly or in a gradient manner over a silk tube conduit implanted in a 15 mm rat sciatic nerve gap [221]. Results showed significantly increased density of nerve tissue in the GDNF treated groups compared with the empty microsphere-based conduit. In addition, significantly higher density of PGP 9.5 protein, a neuroendocrine marker, was reported in the middle-distal part of the conduit for the GDNF gradient scaffold compared with the GDNF uniformly distributed one [221]; increase in the density and number of regenerated axons resulted.

2.4.4 Exogenous and endogenous electrical regimes

2.4.4.1 Adequate electrical stimulation is pivotal for enhanced repair

Neuronal cells use ions to generate electricity, which is required for the nervous system to send signals throughout the body. These signals, travelling throughout nerves, are known as action potentials – waves of electrical depolarisation that propagate within the neuronal cell membrane. Furthermore, small electric potential gradients co-exist in healthy tissues. When the healthy tissue is injured, epithelial barriers are breached and the transepithelial potential differences are short-circuited to form an electric current that flows towards the compromised epithelium and establish laterally oriented electrical fields [257,258]. These are thought to be the result of passive ion leaking and play a role in the control and integration of multiple cell behaviours (e.g. proliferation, division, migration and nerve sprouting) [259].

Exogenous direct ES (active ES) attempts to mimic these endogenous electrical regimes, and since their basis to promote nerve regeneration back in 1952 [260], numerous studies have shown that ES can promote Schwann cell proliferation, neural cell differentiation, axonal growth and extension [261,262], and production of neurotrophic factors [263]. It has been suggested that redistribution of the cytoplasm in terms of cellular polarisation and organisation, changes in the ionic currents across the cell membrane, upregulation of gene expression or release of growth promoting molecules [264–268] are all influenced and regulated by extracellular electrical cues.

For instance, ES has been found to accelerate and increase neuronal expression of cytoskeletal proteins (e.g. actin and T-α1-tubulin) and growth-associated proteins (e.g. GAP-43) [269,270] with key roles in neuronal formation and repair [271].

Several electroconductive/active materials exist (**Table 2.7**), and they can be classified according to the mechanism of electrical conduction, differing upon the charge used as a carrier: (1) electrons (i.e. external electrical currents; electron mobility arising from the constitutive bonds between atoms or the presence of electroconductive moieties percolated in the matrix), ions (i.e. electrolytes from aqueous media, polyelectrolytes, ionic groups in the polymeric backbone or ionic groups appended to or complexed with conjugated polymers) and protons (i.e. molecules of bound water or amino acid side groups of protein-based materials) [272–274]. Conductive and piezoelectric substrates are well-known to allow direct delivery of ES to cells. However, induced ES may have a dual effect on tissue repair upon different parameters. For instance, the magnitude of the applied frequency was revealed to affect nerve fibre density, showing that a frequency of 2 Hz led to a significantly long duration, fast nerve conduction speed and large axonal densities compared with no stimulus and higher frequencies between 20 and 200 Hz [275]. Current intensities around 1 mA have also been reported to improve the number of axons and blood vessels compared to currents above 4 mA, suggesting that while an appropriate intensity accelerates nerve maturation, an excessive one might hinder its functional recovery [276,277]. Similarly, a short delay in the appliance of ES, between one to two weeks post-injury, has been demonstrated to enhance maturity of the neural components in sciatic rat nerve defects [278].

Table 2.7 Conductive polymers, piezoelectric materials and carbon-based fillers used in peripheral neuronal applications

Material	Type	Conductivity (S/cm)	Key findings in neural applications
Polypyrroles (PPy)	Conductive polymer	1×10^2 - 7.5×10^3	PPy films and fibre mats have shown significant increase in neurite length of PC12 neurons [279,280], while PPy composite nerve conduits have shown enhanced regeneration *in vivo* [281]
Polyanilines (PANI)	Conductive polymer	30 - 200	PANI-PPy nanofibres have shown to report 10-fold increase in density of viable neurons, with enhance growth and neurite extension [282]
Poly(3,4-ethylenedioxythiophene) (PEDOT)	Conductive polymer	1×10^3-1.7×10^5	PEDOT substrates have shown good viability and proliferation of neuroblastoma-derived cells *in vitro* [283,284]; no animal studies have been reported to the author's knowledge to date
Polycarbazoles (PCB)	Conductive polymer	More than 10^{-3}	Limited success has been reported on PCB. However, an aminopropyl carbazole derivative was reported to induced neurogenesis by increasing final cell division of neural stem cells [285]
Poly(vinylidene fluoride) (PVDF)	Piezoelectric polymer	Up to 6	Several neural related studies have been reported on PVDF [286,287]. For instance, PDVF membranes have exhibited significantly superior PC12 neural cell activity [288], and significantly higher levels of neurite outgrowth and differentiation of neuroblastoma cells [289,290] PDVF based nerve conduits implanted *in vivo* have shown significantly higher number of myelinating axons as compared to unpoled PDVF conduit as control [291]
Poly(vinylidene fluoride–trifluoroethylene) (PVDF-TrFE)	Piezoelectric polymer	Up to 6	PVDF-TrFe nerve conduits have shown improved neurite outgrowth in a sciatic nerve gap in adult rats [292], and addition of NGF and collagen gel as a filler has reported enhanced regenerative outcome [293]
Graphene	Carbon-based	Around 1×10^6	Higher degree of neural stem cell differentiation in 2D graphene substrates has been reported compared to glass surfaces [294]. Neurite outgrowth into organised interconnected neural networks on 2D graphene substrates has also been demonstrated [295], with an average of 30% increase in neural signalling and significantly more spontaneous calcium oscillations compared to control [296] Nanoparticles of GO have shown significantly higher embryonic stem cell differentiation into dopamine neurons compared to graphene nanoparticles and carbon nanotubes alone, and that the differentiation rate could be controlled by tuning their concentration [297]
Carbon nanotubes	Carbon-based	1×10^5 – 1×10^6	MWNTs may improve hippocampal neural signal transfer and support dendrite elongation and neurite extension [298], while manipulation of the carried charge may control outgrowth and branching of hippocampal neurons [299,300]. Embryonic rat-brain neurons grown on MWNTs coated with 4-hydroxynoneal have also exhibited extensive neurite branching [301]

2.4.4.2 Endogenous electrical regimes to stimulate electrically responsive cells

Incorporating electroactive moieties to the substrate can enhance the regenerative ability of the injured tissue. Exogenous ES could be a challenge in their translation to clinical applications, and studies have emerged showing that scaffolds incorporating electroconductive/active moieties (no need of exogenous ES, i.e. passive ES or inherent endogenous electrical regimes) can significantly enhance differentiation of stem cells when compared to their growth on the non-conductive counterpart [302]. For instance, it has been reported that a polylactide (PLA) based composite enhanced with an electroconductive/active moiety of aniline tetramer significantly promoted proliferation and osteogenesis of bone-marrow derived mesenchymal stem cells when compared to the PLA alone [302]. Enhancement of the biological response due to the incorporation of electroconductive/active moieties into the scaffold has also been reported in self-excitable cells such as cardiomyocytes [303–306]. These studies have reported that adding electrically active moieties, such as aniline, pyrrole, carbon-based fillers or gold particles, show a more extensive effect on the expression of cardiac genes involved in muscle contraction, relaxation and electrical coupling, as well as in cytoskeleton alignment, with or without ES. However, the effects of these electroconductive/active moieties on tissue repair are rarely studied. Although the exact mechanisms are not fully exploited, this is presumably through enhanced transmission of electrical signals between neighbouring cells. Conductive substrates can alter the local electrostatic charge of the scaffold modifying protein adsorption [307]; greater serum proteins are adsorbed on the scaffold, which in turn affects cell-material interactions by accelerating cell adhesion [308] and improving proliferation and migration [306,309]. The presence of these electroconductive/active moieties in the scaffolds also act as electrical binding sites to electrostatically attach the negative charged cell membrane, bringing the cells closer to the scaffold surface and establishing stronger attachment sites [308]. This in turn may assist in restoring certain conduction of action potentials in the damaged tissue, facilitating tissue growth and cell differentiation [306].

A similar effect of inherent electroconductive/active properties can be expected on other electrically responsive tissues such as nerve, to promote cellular proliferation and neurite growth and extension across the gap defect [280,307] with improvement of conduction velocities [263,310] and motor function [311]. Endogenous electric fields play a major role in regulating regeneration and embryonic development of tissues by a modulated cytokine secretion [312], and efforts to regulate cell function by exogenous ES may not be necessary.

2.4.4.3 Novel conductive properties of silk for neural tissue repair

Imparting conductive functionalities to silk is a promising approach, and there remains much scope for exploration (**Table 2.8**).

Conductive properties to biomedical applications of silk have been imparted by coating or *in situ* polymerisation of conductive polymers such as PPy [313–317], PANI [318–322], PEDOT [125,318] and their copolymers [323], incorporation of carbon-based materials such as graphene [324–327] and carbon nanotubes [184,193,328–330], by gold nanoparticles [311,331], or by silver plating coating [332]. In particular, some *in vitro* and *in vivo* studies using conductive silks for peripheral nerve repair have been explored. For example, conductive composite films of SF and single-walled carbon nanotubes (SWNTs) were fabricated for neural applications [193]. Results showed that the composite SF-SWNTs films exhibited an electrical conductivity of 2.8 S/cm at 0.3 V, just one order of magnitude lower than that of bare SWNTs. However, no major significant differences on viability of rat DRG neurons or their neurite length were exhibited with respect to SF alone during *in vitro* testing. In 2013, a NGC based on the incorporation of SWNTs, fibronectin and RSF was implanted into a 10 mm sciatic rat nerve defect [184]. The electrical conductivity of the substrate was found to be about 2.1×10^{-5} S/cm, while that for pure SF was reported to be around 1×10^{-17} S/cm (upper limit at 1×10^{-7} S/cm). Post-implantation results showed acceptable functional recovery. Although the nerve conduction velocity of the normal nerve was found to be significantly higher than that of the regenerated nerve using the conduit, they were within similar magnitudes, and the study suggested that the SF-SWNT-fibronectin conduit provided enough electrical conductivity compared to natural nerve [184]. Some studies have also been reported on conductive SF fibres to enhance the repair ability of peripheral nerve conduits, such as that reported by Xia and Liu in 2008 [318], in which fibres were coat-immersed in

PPy, PANI and PEDOT solutions, exhibiting electrical conductivities in the range of 5×10^{-3} to 3×10^{-1} S/cm; however, no cell culture studies were conducted. A peripheral nerve conduit fabricated by coating with PPy an electrospun mat of RSP and PCL exhibited electrical conductivities between 8.5×10^{-6} and 1.4×10^{-4} S/cm [333], and was effective at bridging a 20 mm sciatic nerve gap in rats, with exogenous ES promoting Schwann cell migration and axonal growth. Neural proliferation and differentiation via ES of a PPy coated SF film (electrical sheet resistance of around 124 kΩ/sq) was also enhanced [317], while spider silk-PPy films (conductivity around 16.7 S/cm) with topographical cues were reported to improve and direct DRG neurite outgrowth [119]. In a different study, the synergic effect of ES and NGF on neuronal growth was studied by coaxial electrospinning the growth factor in a PANI/RSF blended solution, with results showing that growth factor release from the nanofibre could be increased by direct ES [319]. *In vivo* studies with silk-based gold nanocomposite conduits have also been reported [311]. A high degree of functional neuro-muscular regeneration (in terms of nerve conduction velocity, compound muscle action and motor unit potentials) was shown with a silk-based gold nanocomposite conduit pre-seeded with Schwann cells to bridge a rat sciatic nerve, compared to those values observed in normal nerves [311]. Another material of interest to conjugate with silk for potential use in nerve repair is reflectin. Reflectins are intrinsic conductive proteins found in nature that function as effective proton conductors [334], and they have been shown *in vitro* to facilitate adhesion, proliferation, and differentiation of relatively difficult to culture neural progenitor stem cells [234,235].

Data from these studies suggest that silk proteins can be rendered electroconductive/active upon several methods, and that they may be used in a multi-step wise way to improve regenerative ability of bioactive nerve guides in a near future.

Table 2.8 Electroconductive/active silk in biomedical applications

Electroactive component	**Incorporation method**	**Scaffold fabrication**	**Application**
PPy	Blending	Casting	Undefined [313]
	Coat-immersion	Electrospinning	Undefined [314]
	In situ polymerisation	-	Nerve repair [318]
	In situ polymerisation	Electrospinning	Nerve repair [333]
	In situ polymerisation	Electrospinning	Nerve repair [119]
	In situ polymerisation	Casting	Nerve repair [317]
	In situ polymerisation	Casting	Undefined [315]
	In situ polymerisation	Casting	Undefined[316]
PANI	*In situ* polymerisation	Dispersion	Nerve repair [318]
	Blending	Electrospinning	Nerve repair [319]
	Blending	Electrospinning	Nerve repair[322]
	Blending	Electrospinning	Muscle repair [320]
	Blending	Phase-separation	Muscle repair[321]
PPy + PANI	*In situ* polymerisation	Salt leaching	Bone repair [323]
PEDOT	*In situ* polymerisation	-	Nerve repair [318]
	In situ polymerisation	Self-assembly	Undefined [125]
Graphene	Coat-immersion and *in situ* reduction	Electrospinning	Undefined [324]
	Coat-immersion	Electrospinning	Nerve repair [326]
	Blending	Electrospinning	Bone repair [325]
	Blending	Wet spinning	Undefined [327]
MWNTs	Blending	Wet spinning	Undefined [328]
		Electrospinning	Undefined [329]
	Coating	Extrusion	Undefined[330]
SWNTs	Wet-templating	Casting	Nerve repair [193]
			Nerve repair [184]
	Blending	Casting and freeze-drying	Undefined [325]
Pigmented melanin	Blending	Drop casting and electrospinning	Skeletal muscle repair [335]
Gold nanoparticles	Coating	Electrospinning	Nerve repair [311]
	Blending	Electrospinning	Undefined [331]
Silver plating	Coating	-	Antibacterial [332]

2.5 Current status, challenges and opportunities

Currently approved nerve conduits for peripheral nerve repair are generally hollow structures, and only a limited fraction of patients suffering from PNI have benefited from these due to their limited ability to bridge and repair gaps effectively. This highlights the fact that commercially available nerve conduits are currently only best for small injury defects, and tubular constructs with further elements (filled conduits, physical guidance cues, growth factors, conductivity amongst others) may show further improvement.

The complexity of nerves in terms of how they are injured and repaired is manifold and challenging. Silk is a popular material for use in tissue engineering of nerve conduits, and significant progress has been made towards their clinical translation. However, standardisation across animal studies in terms of gap defect length and proper use of controls would make it more efficient and allow for more accurate comparisons among studies. Correlation with the benchmark nerve autograft should also be a must to make these studies clinically more relevant.

The real impact of these upcoming tissue engineered NGCs will come when Schwann cell and neuronal cell behaviours can be radically altered to reduce axonal escape, and when the rate of regeneration across the injured site and out into the distal nerve stump is increased. To this regard, several strategies are being put into practice on how to shape more bioactive silk-based nerve conduit guides for enhanced repair. Recombinant and synthetic biology approaches have gained traction in recent years to overcome any mass production difficulties and tune specific functionalities; however, only partial gene sequences have been reported, and the complete removal of endotoxins, a common by-product from gram negative bacteria, remains an issue [132]. On the other hand, advances in the field have identified both structural and biochemical cues to enhance the repair capacity of nerve conduits. Various approaches of how silk can be modified in terms of blends, physical guidance cues and incorporation or tethering of growth factors, proteins and peptide sequences have been reviewed, opening up new opportunities in the use of combined functionalities for nerve repair. Indeed, cell-free and neurotrophic factor-free silk-based conduits are generally outperformed by cell-loaded or their neurotrophic factor-loaded counterparts, demonstrating that the use of biochemical cues could provide a significant improvement over currently available treatments. Related challenges are the elucidation of the impact of neurotrophic growth factors onto the silk scaffold including dose and long-term effect, and whether the same benefits of cell-loaded constructs could be achieved by neurotrophic factors in cell-free silk-based nerve conduit scaffolds. However, what growth factors to use and how/when to release them are still ongoing questions. The strategy of concentration gradients and tandem delivery of neurotrophic factors has been considered; however, this may incur in significant costs and further research is required to fully exploit their potential in silk-based materials to optimise their cost-benefit balance. Another issue is that incorporation of biomolecules does not allow extreme temperature ranges or extremely aggressive chemical conditions during processing, which may be a challenge to overcome in the scaffold fabrication process. Looking at different immobilisation and embedding routes of such biomolecules to control protein adhesion and release kinetics is another window of opportunity. Nevertheless, all these therapies have yet to be clinically proven and approved by regulatory agencies for use in nerve repair.

There is a significant scope in the application of electroconductive/active moieties within scaffolds as passive electrical stimulators, and could be a promising approach to aid in nerve regeneration [311]. Studies have showed that silk can be rendered electroconductive/active [119,313,314,318,319,324,325,328,332,333,335]; however, despite the inspiring progress made in the field, such active scaffolds have been barely studied. More research needs directing at assessing the suitability of electrically conductive/active silk-based scaffolds for tissue engineering (i.e. issues over degradability and toxicity) and their impact in peripheral nerve repair and/or in combination with other chemical factors. In particular, inclusion of carbon-based moieties seems promising, not only to enable novel conductive functionalities but also to further tailor the cell-material interactions of the construct based on their high surface area to volume ratio. Much of the work has focused on assessing the effects upon direct ES (active ES, exogenous electrical regimes), yet the effects of introducing electroactive moieties into the scaffolds (passive ES, endogenous electrical regimes) have not been fully investigated. This opens up opportunities for the usefulness of electrically conductive/active scaffolds in increasing the repair process of the damaged nerve tissue by amplifying cell to cell communication and modulating growth and cell differentiation without the need of an exogenous stimulus [302–309].

In summary, while there is significant research ongoing in the field of silk for peripheral nerve repair and new technologies are continuously emerging, increased efforts on novel strategies would promote development of silk-based scaffolds that can address the biology of the regenerating nerve. In addition, increased research to overcome the existing regulatory barriers associated with translating a silk-based nerve conduit into the clinic is required before a tissue engineering nerve conduit approach can replace the benchmark of nerve autografts. However, it should be noted that the injured site is only one of the many elements of the neurobiology of the injury and repair process of nerve, and further strategies should be addressed for patients to regain full restoration of nerve functionality (i.e. rehabilitation therapy).

Chapter 3

Graphene oxide and electroactive reduced graphene oxide-based composite fibrous scaffolds for engineering excitable nerve tissue

Note: A version of this chapter has been published as Magaz *et al*. "Graphene oxide and electroactive reduced graphene oxide-based composite fibrous scaffolds for engineering excitable nerve tissue". *Materials Science and Engineering: C.* 2021;19: 111632

Adrián Magaz[1,2], **Xu Li**[2,3], **Julie E. Gough**[1], **Jonny J. Blaker**[1,4]*

[1]Department of Materials and the Henry Royce Institute, The University of Manchester, Manchester, M13 9PL, United Kingdom

[2]Institute of Materials Research and Engineering (IMRE), Agency for Science Technology and Research (A*STAR), 138634, Singapore

[3]Department of Chemistry, National University of Singapore, 117543, Singapore

[4]Department of Biomaterials, Institute of Clinical Dentistry, University of Oslo, Oslo, 0317, Norway

*Corresponding author

Author contribution statement

AM fabricated the scaffolds and characterised the materials in terms of their physico-chemical and biological properties. Data analysis, manuscript and figure panels were compiled by AM. XL, JEG and JJB supervised the study. All authors contributed to experimental design, manuscript structuring, drafting and editing. An overview of the tasks carried out by the main author are provided below:

- Literature review
    - Carbon-based nanomaterials with a focus on graphene family materials

    - Nerve tissue engineering applications of graphene family nanomaterials
    - Role of electron/ion currents in conductivity and their effect on cellular behaviour
    - Role of GO and rGO in altering neuronal proliferation and differentiation
- Study design following advice from the supervisory team
    - Selection of materials and preparation techniques
    - Selection of cell line and experimental points
    - Characterisation methods
- Experimental work
    - Optimisation methods for the manufacturing of GO and rGO silk-based composites using electrospinning
    - Characterisation of the scaffolds in terms of fibre morphology, surface topography, chemical structure, conductivity and biological response
- Manuscript preparation
    - Writing initial draft
    - Revision following comments from the supervisory team

Overview

Electroconductive/active biomedical materials have gained interest in the last few years to promote the repair of electrically responsive cells and tissues. In particular, the use of carbon-based nanomaterials has attracted significant interest in the field of tissue engineering. The work described in this chapter provides a comprehensive comparative study on the effects of blending GO with SF into manufacturing electrospun composites, followed by optionally *in situ* post-reduction into electroconductive/active rGO/SF. It was hypothesised that the presence of GO within the silk matrix could enhance the biological properties of the scaffolds compared to neat silk, and that following GO reduction, the observed cellular responses could be further upregulated. The use of rGO over GO is a preferable choice to imbue the scaffolds with certain levels of conductivity. The produced scaffolds were physico-chemically characterised and biologically assessed with analogue neuronal cells.

Composite SF scaffolds with presence of GO or rGO up to a 10% wt. loading were successfully fabricated in a reproducible manner with no major influence among the different substrates, helping to decouple the effects of GO/rGO and the role of conductivity on cell response from other substrate traits. In line with the hypothesis, the biological response of the scaffolds was substantially improved – particularly by the presence of rGO over GO.

Abstract

This study systematically investigates the role of GO and reduced GO/silk-based composite micro/nano- fibrous scaffolds in regulating neuronal cell behaviour *in vitro*, given the limited comparative studies on the effects of graphene family materials on nerve regeneration. Fibrous scaffolds can mimic the architecture of the native ECM and are potential candidates for tissue engineering peripheral nerves. Silk/GO micro/nano- fibrous scaffolds were electrospun with GO loadings 1% to 10% wt., and optionally post-reduced *in situ* to explore a family of electrically conductive non-woven silk/rGO scaffolds. Conductivities up to 4×10^{-5} S cm^{-1} were recorded in the dry state, which increased up to 3×10^{-4} S cm^{-1} after hydration. Neuroma NG108-15 cells adhered and were viable on all substrates. Enhanced metabolic activity and proliferation were observed on the GO-containing scaffolds, and these cell responses were further promoted for electroactive silk/rGO. Neurite extensions up to 100 μm were achieved by day 5, with maximum outgrowth up to ~250 μm on some of the conductive substrates. These electroactive composite fibrous scaffolds exhibit potential to enhance the neuronal cell response and could be versatile supportive substrates for neural tissue engineering applications.

Keywords: Neuronal scaffold; silk fibroin; reduced graphene oxide; graphene oxide; electrospinning; neuronal cells

3.1 Introduction

Nerve tissue is electrically sensitive, and the inhibition of electrical signalling can impede normal tissue function. As electrical integrity is essential for this native tissue, one of the main strategies to enhance regeneration is through ES [336–338]. Consequently, extensive effort is invested in improving conduction to provide direct electrical activation to enhance cell and tissue function. A particularly interesting option to improve the outcome of nerve repair is the introduction of endogenous electrical regimes within the conduit lumen, where the physiological cues provided by endogenous electric fields at the wound site could help regulate cell behaviour and promote healing. Conductivity can be enhanced by facilitating ionic, protonic or electronic transport depending on the charged carrier [272–274]. Usually, the introduction of electroconductive moieties in tissue constructs is challenging due to aggregation, limited biocompatibility and poor dispersibility [339,340]. Several conjugated polymers based on polypyrrole (PPy), PANI and poly(3,4-ethylenedioxythiophene) (PEDOT) have been previously investigated to provide scaffolds for nerve regeneration with certain levels of conductivity [341]. In recent years, carbon-based materials (i.e. graphene family nanoplatelets and carbon nanotubes) have received great attention due to their high versatility and functionality [8].

Graphene is a strong candidate for developing scaffolds due to its electrical conductivity [342], mechanical strength [343], topographical features and high surface area [344]. GO is more readily dispersible thanks to oxygen-containing functional groups on its surface, and stands out for its easy processability, high affinity to specific biomolecules [345], and appropriate cell-interface interactions [346]. GO-based substrates can support adhesion, proliferation and differentiation of neurons [347–350] without the use of chemical inducers. Schwann cell secretion of neurotrophic factors has also been promoted on GO substrates [351], along with modulation of stem cell differentiation towards the neural lineage [297,352,353]. Graphene has demonstrated as well potential to improve neuronal cell responses, including cell attachment, proliferation and stem cell differentiation for neural tissue engineering applications [354,355]. In particular, graphene has been shown to promote neuro-specific gene expression, and neurite outgrowth and sprouting in several neuronal-like cells [356–358]. Differentiation of neuronal stem cells into neurons, rather than glia, has also been accelerated on graphene substrates [359]. Schwann cell behaviour has also been regulated on graphene-containing substrates by promoting migration, proliferation and myelination [360]. However, the underlying molecular mechanisms behind have remained largely unanswered. Only recently, a study showed that graphene could modulate the active and passive bioelectric properties of the cellular membrane [361].

Most research using graphene family materials are reported on traditional 2D coated surfaces, making them difficult to be developed into suitable 3D assemblies for tissue engineering. Therefore, despite the great potential of the various forms of graphene in neural applications, their use as implantable scaffolds is limited, decreasing their suitability for their clinical translation and applicability in more biological contexts. Instead, biohybrids manufactured from the combination of native polypeptides found in nature, along with graphene family materials, can offer a multifunctional platform in tissue engineering to develop suitable fibrous scaffolds. Of the many naturally occurring proteins, silks have been extensively investigated in nerve tissue repair and regeneration [362]. In particular, SF obtained from *Bombyx mori* silkworms is widely available as a raw material and easily processable. SF has demonstrated great potential due to its physicochemical, mechanical and biological properties: these include aqueous preparation, superior mechanical properties, suitable elasticity, adequate angiogenicity and controlled biodegradability [362,363]. Immobilizing graphene on silk via electrostatic adhesion is common, but thin coatings tend to lack the interfacial adhesion required in between the surfaces since graphene lacks polar groups to induce strong interactions [364]. A way around has been to coat silk fibres with GO instead and reduce it afterwards [365,366], with the interfacial strength arising from the polar groups of GO and the amide groups of silk. However, a thorough post-reduction of the GO coating can weaken the interfacial strength with silk and its conductive stability. More recently, graphene flakes were entrapped in between the silk fibres prior to fibre contraction induced by ethanol immersion [364], but the fibre morphology and underlying topography tend to be lost. Composite blends prior to fibre formation might be a better alternative.

This study explores composite micro/nano- fibrous scaffolds based on SF and GO or reduced GO (rGO). Decoupling the role of conductivity on cell behaviour is challenging, since manufacturing scaffolds with similar physico-mechanical properties but different levels of conductivity is difficult. Hybrid composites were fabricated here by dispersing GO into an SF solution at increasing controlled loadings (1%, 5% and 10% wt.) prior to electrospinning and *in situ* post-reduction to give electroactive SF/rGO. Micro/nanofibres with a multiscale structure similar to that of the native ECM have been widely investigated in nerve tissue engineering due to their suitability for neuronal cell growth. We hypothesise that the presence of (r)GO (i.e. GO or rGO) in the system positively influences the neuronal cell response, and that this can be further modulated by the electroactivity attributed to rGO. The biological performance of the scaffolds was assessed with analogue neuronal NG108-15 cells over their growth and differentiation phase. To the best of the author's knowledge, this is the first comparative study of silk-based composite micro/nano- fibrous scaffolds with GO and rGO for neural tissue engineering applications.

3.2 Materials and Methods

3.2.1 Preparation of silk fibroin

Extraction and purification of SF from *Bombyx mori* silkworm cocoons was carried out as previously described [367], with some modifications (**Scheme 3.1A**). Briefly, cocoons (Wildfibres, UK) were dewormed, sliced into small pieces, and degummed in a boiling aqueous solution of 0.02 M sodium carbonate (Na_2CO_3) (Sigma-Aldrich, UK) for 60 min. Degummed SF fibres were thoroughly washed in deionised water (DI water) and air-dried at room temperature (RT) overnight. The fibres were then dissolved in 7.9 M aqueous lithium bromide (LiBr) (Sigma-Aldrich, UK) to form a 16% w v^{-1} solution, under gentle continuous stirring at 60°C for 4 h. The resulting solution was centrifuged (10,000 ×g, 20 min) and dialyzed (10k MWCO SnakeSkin) (Thermo Fisher Scientific, UK) against 5L of DI water at 4°C for 2-3 days, with regular water changes. Presence of LiBr ions was tested with a simple silver nitrate test, with no precipitate observed after the first three changes of DI water. The concentration of SF post-dialysis was ~5-6% w v^{-1}. The RSF solution was centrifuged again, cast onto polystyrene dishes (Sigma-Aldrich, UK) and dried at 60°C for 2 h in a forced air-circulation oven (Memmert Universal, Germany). The resulting films were subsequently peeled off and kept in sealed vials as stock material.

3.2.2 Preparation of silk fibroin/graphene oxide solutions

GO flakes (2-DTech, UK) (with lateral dimension and number of layers quoted by the manufacturer as <4 μm lateral width and <2 layers) were used as filler. The GO powder was dispersed in ≥98% 1,1,1,3,3,3-hexafluoro-2-propanol (HFIP) (Sigma-Aldrich, UK) (**Scheme 3.1B1**) and sonicated at 80 Hz for 2 h using a temperature controlled (RT) ultrasonic bath (Elmasonic P60H, Germany).

Following sonication, the lateral width of the GO flakes was determined by field emission scanning electron microscopy (FESEM) (JEOL JSM6700F, SG). Briefly, silicon wafers were sonicated in acetone for 10 min for cleaning and left to dry at 60°C. A 10 μL drop of GO solution (at 0.0025 mg mL^{-1}) was then pipetted onto the centre of the wafer and left to dry overnight before imaging. The lateral width size of ~200 flakes was measured manually with Fiji 1.28 (NIH, USA). Measurements were performed in the horizontal direction through the centre of the flake.

SF films were then dissolved in the GO dispersion by mixing for up to 3 days at 250 rpm in an oil bath heated at 50°C. Solutions of 10% w v^{-1} SF/HFIP were obtained at increasing GO loading: control 0, 1, 5, and 10% wt.

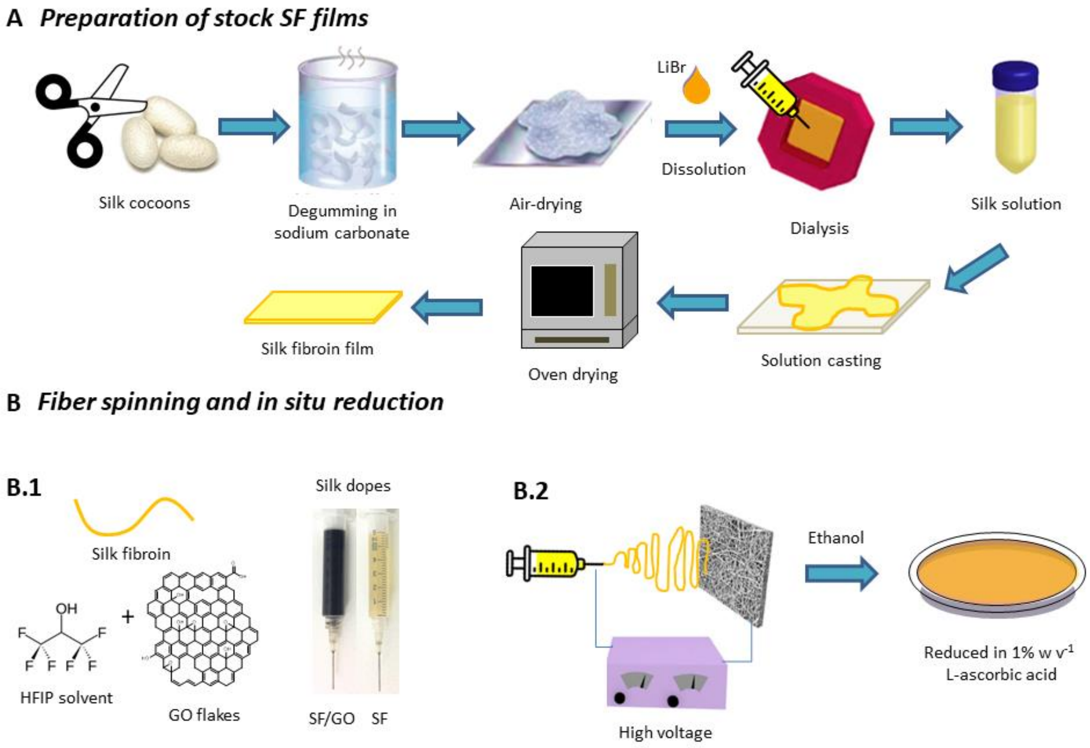

Scheme 3.1 (**A**) Schematic of the extraction and synthesis of SF. (**B**) Manufacturing of silk-based scaffolds: (**B1**) Preparation of silk-based dopes for spinning and (**B2**) schematic of the electrospinning of SF/GO solutions and *in situ* post-reduction into SF/rGO.

3.2.3 Fabrication of graphene oxide/silk fibroin composites and post-reduction treatment

Fibrous scaffolds of SF/GO blends were fabricated by electrospinning, giving SF/1G, SF/5G and SF/10G substrates. Briefly, the spinning solution was transferred into a disposable 6 mL Normject™ syringe (Thermo Fisher Scientific, SG) capped with a 19G blunt metallic needle (0.686 mm inner diameter) (Terumo, SG), fixed in a SP100iZ single-syringe infusion pump (World Precision Instruments, SG). A voltage of 15 kV was generated by a high-voltage DC power supply applied to the needle. A 15 cm × 15 cm static ground collector covered in aluminium foil was placed at a distance of 10 cm and the solution was dispensed at a constant rate of 0.8 mL h^{-1}. All experiments were performed at RT (~22°C) with relative humidity 25% controlled by a dehumidifier device (EuropAce, SG) inside a closed chamber.

The substrates were annealed by immersion in a bath of 80% v v^{-1} ethanol for 20 min to induce β-sheet conformational transition, thoroughly rinsed in DI water, and dried for 24 h sandwiched between filter paper (Whatman®) (Sigma-Aldrich, UK) to prevent curling or folding. The SF/GO scaffolds were post-reduced *in situ* (**Scheme 3.1B2**) by treating them with a 1% w v^{-1} solution of L-ascorbic acid (Sigma-Aldrich, UK) at 95°C for 1 h [326,366], giving SF/1R, SF/5R and SF/10R substrates. The scaffolds were subsequently washed thoroughly with DI water afterwards. Unmodified SF scaffolds were also treated under similar conditions to use as control.

3.2.4 Characterisation of the composites

3.2.4.1 Morphology and surface topography

Fibre morphology and surface topography of different batches of the scaffolds were examined via FESEM (JEOL JSM6700F, SG) at 5 kV with a working distance of ~8 mm. Fibre diameters were determined manually with Fiji software by measuring a minimum of 100 fibres.

3.2.4.2 Estimation of porosity and water sorption

Water sorption capacity of the scaffolds (n=3 per type) was investigated by weight differences between the hydrated and the dry state (Eq. 3.1). Briefly, samples (15 mm × 15 mm) were immersed in 10 mL of molecular biology grade water

(AccuGENE™) (Lonza, UK) and incubated at 37°C in a water bath overnight. Excess water was removed by sandwiching the samples in filter paper and weighting immediately afterwards with a high precision balance scale. Three measurements were taken per sample.

$$\text{Water sorption (\%)} = \frac{W_{wet} - W_{dried}}{W_{dried}} \times 100 \qquad \text{(Eq. 3.1)}$$

The overall percentage porosity of the scaffolds (n=5 per type) was determined through gravimetric analysis (Eq. 3.2) [368]. Briefly, the apparent density of the scaffolds in the dry state was calculated on the basis of mass (m), thickness (t) and area (A). Samples were punched into discs (12.7 mm in diameter) using a carbon steel hollow punch (Drapper, UK), and their thickness determined using a digital thickness gauge (Mitutoyo, Japan). The corresponding density of the composite was calculated on the basis of the mass fraction of its components, where the density of SF was taken as ~1.25 g cm^{-3} and that of graphene as ~1.8 g cm^{-3} [369,370].

$$\text{Porosity (\%)} = 1 - \frac{\frac{\mathrm{m}}{\mathrm{t} * \mathrm{A}}}{\rho_0} \times 100 \qquad \text{(Eq. 3.2)}$$

where

$$\frac{1}{\rho_0} = \frac{\chi\mathrm{A}}{\rho\mathrm{A}} + \frac{\chi\mathrm{B}}{\rho\mathrm{B}} \text{ and } \chi \text{ denotes the mass fraction of each component A} - \text{B}$$

The gravimetric estimate of the percentage porosity of the scaffolds was then used to model the pore size through statistical considerations derived by Eichhorn and Sampson [371], where the average equivalent pore diameter can be related to the fibre diameter and network porosity (Eq. 3.3):

$$\text{Pore size} = \frac{2 * \text{fibre diameter}}{\log\left(\frac{1}{\text{porosity}}\right)} \qquad \text{(Eq. 3.3)}$$

3.2.4.3 Chemical bond analysis

The conformational changes to the secondary structure of silk were evaluated within the spectrum of the amide I region ranging from 1700 to 1600 cm^{-1}, by means of Fourier self-deconvolution (FSD). The spectrum for each scaffold (n=2 per type) was taken with a Fourier transform infrared (FTIR) spectrometer (PerkinElmer 2000) equipped with a zinc selenide (ZnSe) crystal on attenuated total reflectance (ATR) mode. For each measurement, 32 scans were recorded with a resolution of 4 cm^{-1} and wavenumbers from 4000 to 600 cm^{-1}. Spectra within the amide I region were analysed using the peak analyser feature in Origin Pro 8.5.1 (Origin Lab). The peaks were assigned to different secondary structures (i.e. intermolecular/intramolecular β-sheet, random coil, α-helix, β-turn, and side chains) based on the second order derivative, and fitted using a Gaussian function [372–375].

3.2.4.4 Electroconductive properties

An automated electrical conductivity and resistivity system (A4P-200 MicroXACT, US) with a Jandel 4-point probe head (Tungsten Carbide tips, 40 µm tip radius and 1 mm tip spacing) (**Scheme 3.2**) was used to determine the conductivity [366,376,377] at different positions across the surface of the scaffolds (n=4 per type). Measurements were conducted at RT (~20°C) in the dry state, in the hydrated state, and in the dry state after one-day hydration. Precise positioning of the probe was controlled by two VXM stepper motors (Velmex Inc., SG), and supplied by a combined DC current source and digital voltmeter (Jandel RM3000). The MicroXACT LabView-based automated software was used to control the station. A relatively low input current was supplied through the two outermost tips of the probe to pass across the material. For hydrated scaffold testing, scaffolds were immersed in 10 mL PBS overnight, and excess removed using filter paper. For testing the samples in the dry state after one-day hydration, the scaffolds were immersed in 10 mL PBS over a 24 h period, washed with DI water and subsequently dried overnight at RT prior to testing.

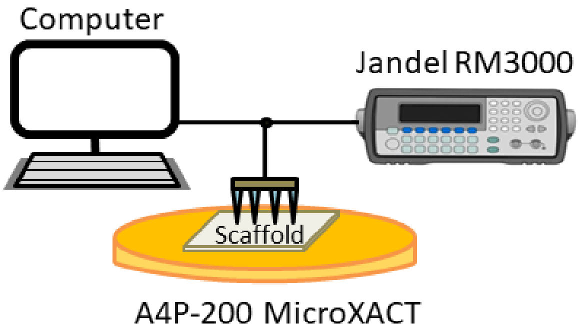

Scheme 3.2 Schematic of the experimental set-up of the four-point probe electrical station.

3.2.4.5 Raman spectroscopy

The presence of GO and rGO within the scaffolds (n=2 per type) was evaluated using a confocal LabRAM HR Evolution Raman microscope (HORIBA Scientific, SG), by acquiring the Raman spectra at different positions along the surface of the sample. Raman was acquired with a 785 nm wavelength laser beam, with a D1 optical density filter and a 200 μm confocal pinhole to prevent thermal damage to the sample. The laser was focused on the surface of the samples with a 50× long working distance objective (1.87 mW power). Raman measurements were taken with 300 mm^{-1} grating and spectral resolution of about 1 cm^{-1} in the range 600 to 3400 cm^{-1}. LabSpec software (HORIBA Scientific, SG) was used to control the Raman system and acquire the Raman spectra. Data acquisition times varied between 5 and 10 s depending on the Raman efficiency and background fluorescence of each individual sample. The laser beam position was calibrated by LabSpec. Due to the strong fluorescence background of some of the samples, the spectra signals were baseline corrected and normalised; background noise signal was removed in Origin with a Savitzky-Golay algorithm.

3.2.4.6 Profilometric surface analysis

Differences to the surface topography of the scaffolds (n=2 per type) were analysed at RT on a Countour GT-K1 3D optical profilometer (Veeco, USA) with light interferometer [378]. The device was calibrated prior to use with a golden sample. In order to ensure a near flat surface, scaffolds for testing were cut into 16 mm × 16 mm squares and positioned onto glass coverslips (12 mm × 12 mm, 0.13-0.16 mm thickness) (VWR, UK), with the excess length (~2 mm in each direction) wrapped around the edges. The scaffolds were fixed onto the coverslips with 80% v v^{-1} ethanol, and the surface of the scaffolds was firmly pressed. Annealed mounted scaffolds were treated with 70% v v^{-1} ethanol for 30 min and pre-conditioned in culture media overnight to reproduce the effects of the procedures used in cell culture. The scaffolds were then dehydrated in a series of ethanol dilutions (30, 50, 70-100% v v^{-1}) and dried at RT overnight prior to imaging. Samples were imaged in vertical scanning interferometry mode, with a ×50 interferometric objective (working distance of 3.4 mm) and a ×2 field of view multiplier tube. A total of 10 micrographs (66 µm × 87 µm analysed area for each image) were taken per sample at different fields of view, with an average of five measurements taken per image. Analysis of the surface roughness was carried out using Vision64 Map™ (Bruker, USA) software. The arithmetical mean surface height (Sa) and root mean square surface height (Sq) parameters of the 3D profile ordinates were analysed for each image taken, and the average values for each sample type determined.

3.2.4.7 Protein adsorption

The capacity of the scaffold (n=3 per type) to adsorb protein was evaluated using Engelbreth-Holm-Swarm murine laminin (Sigma-Aldrich, UK) and the NanoOrange® protein quantification kit (Thermo Fisher Scientific, UK), based on the amount of remaining protein in solution after adsorption. Scaffolds were incubated with 200 µL of 5 µg mL^{-1} laminin in sterile molecular biology grade water for 2 h at 37°C. Supernatants were collected after incubation. Samples of 200 µL were transferred to Eppendorf® tubes containing 200 µL of 1× NanoOrange reagent working solution, and then heated at 95°C for 10 min in a QBD2 Grant block heating system (Gem Scientific, UK) following the manufacturer's instructions. Samples were then cooled down at RT for 20 min prior to taking the reading. Protein concentration was calculated using a generated standard curve obtained from the protein solution of interest within the range of measured concentrations. All samples were conducted in triplicate. Scaffolds incubated in molecular biology grade water served as blanks, and DI water was used as negative control. Fluorescence intensity was read (ex./em. 485/590 nm) with a FLUOstar Optima microplate reader (BMG Labtech).

3.2.5 In vitro study

3.2.5.1 Cell culture of neuroma NG108-15 cells

In vitro cell culture experiments were conducted using a NG108-15 neuroblastoma × glioma rat/mouse hybrid neuronal-like cell line. Cells were subcultured in CellStar® tissue culture polystyrene (TCP) treated T25-75 flasks (Greiner Bio-One, UK). Cells were grown with high glucose (4.5 mg mL^{-1}) Dulbecco's modified Eagles medium (DMEM-HG) containing L-glutamine and without sodium pyruvate (Sigma-Aldrich, UK), 10% v v^{-1} foetal bovine serum (FBS) (Sigma-Aldrich, UK), 1% v v^{-1} 100× penicillin-streptomycin (Pen/Strep) solution (10,000 IU Pen and 10,000 µg mL^{-1} Strep) (Sigma-Aldrich, UK), and supplemented with a HAT 50× solution (Thermo Fisher Scientific, UK) to a final working concentration of 100 µM hypoxanthine, 0.4 µM aminopterin, and 16 µM thymidine. Cells were cultured in a humidified atmosphere incubator at 37°C (5% CO_2 and 95% air), with half of the medium changed every 2 days. Cells were used between passage P17-30 after they became 70-80% confluent.

For cell culture experiments, scaffolds (13 mm diameter) were clipped to CellCrown™ polycarbonate inserts (Scaffdex Oy, Finland) for 24-well plates (vol. 1 mL). Mounted annealed scaffolds were maintained in sterile molecular biology grade water for approximately 24 h prior to cell culture. The scaffolds were sterilised with 70% v v^{-1} ethanol for 30 min, followed by a 30 min wash in sterile PBS, transferred into sterile, low-binding 24-well plates (Corning, UK) and exposed to UV-light for 20 min (254 nm) inside a biosafety cabinet. Glass coverslips (12 mm diameter, 0.13-0.16 mm thickness) (VWR, UK) were used as positive controls. To improve cell adhesion, scaffolds were preconditioned overnight in supplemented medium to promote protein adsorption and facilitate cell attachment. Prior to cell seeding, scaffolds were air-dried inside a biosafety cabinet for 60 min to ensure that the cell suspension would not spread around. A cell seeding density of 10,000 cells per well within a ~50 µL droplet was used, and the scaffolds were left to adhere for ~2 h inside an incubator before adding fresh media. Half of the media was changed every 2 days.

3.2.5.2 Cell survival

Cellular viability of cells on the various scaffolds (n=2 per type) was evaluated at days 3, 5 and 7 using a LIVE/DEAD® viability/cytotoxicity fluorescence kit (Thermo Fisher Scientific, UK). The LIVE/DEAD working solution (2 µm calcein-AM and 4 µM EthD-1) was prepared by adding 10 µL of the 2 mM EthD-1 stock solution and 5 µL of the supplied 4 mM calcein-AM stock solution to 10 mL of sterile PBS. At each time point, culture medium was removed from the cell-laden scaffolds and gently rinsed twice in PBS prior to adding ~200 µL of the working solution ensuring that each sample was completely submerged. Samples were then incubated for 20 min in a cell culture incubator, washed twice with PBS and directly transferred onto glass microscopic slides (76×26 mm, 0.8-1 mm thickness, Fisher-Scientific, UK) prior to imaging. 3D imaging was carried out using a TCS SP8 confocal laser scanning microscope (Leica Microsystems Ltd., UK) at an ex./em. of 494/517 nm for live cells and 528/617 nm for non-viable cells. Z-stacked images were acquired with a 10× objective by scanning at least three different areas throughout the thickness of each scaffold at 5 µm per Z-step. Projection micrographs were then generated from each stack through maximum intensity algorithm. Cell quantification was carried out with Fiji software. Obtained projection micrographs were split into single channels, converted into gray scale and thresholded; touching cells were separated into individual objects by applying a watershed algorithm for automatic counting [379,380]. Data is expressed as the percentage of live cells versus non-viable/dead cells.

3.2.5.3 Metabolic activity and cellular proliferation

The metabolic activity of cells on the scaffolds (n=4 per type) was monitored on days 3, 5 and 7 using the alamarBlue™ reduction assay according to the manufacturer's instructions. At each time point, culture media was removed, the cell-laden scaffolds gently washed with sterile PBS and transferred to a new well. A 10× intermediate stock solution of Resazurin (Sigma-Aldrich, UK) was prepared at 0.125 mg mL^{-1} in PBS, and filter-sterilised using a 0.22 µm pore size hydrophilic polyethersulfone membrane (Merck Millipore, UK). About 1 mL of the Resazurin solution in cell culture medium at a 1:10 v v^{-1} ratio was added to each well, and the plate wrapped in aluminium foil and incubated for 4 h at 37°C. Triplicates of 100 μL of each sample were loaded into a black flat-bottom 96-well plate (Fisher Scientific, UK). Resazurin solution in culture medium of glass coverslip or scaffold without cells was used as blank; resazurin solution in culture medium was used as negative control. Fluorescence (ex./em. 544/590 nm) was measured with a FLUOstar Optima microplate reader (BMG Labtech, UK), and recorded as a function of the dsDNA content to give an indication of the metabolic activity relative to the number of cells in culture.

Cellular proliferation of the same samples at similar time points was then measured by the Quant-iT™ PicoGreen® dsDNA assay (Thermo Fisher Scientific, UK). Cell-laden scaffolds were gently washed twice with sterile PBS to remove any traces of Resazurin solution. About 500 μL of 1× lysis buffer (0.2% $v\ v^{-1}$ Triton X-100 in 1× TE buffer solution) was added to each sample, followed by 3 cycles of freezing at -86°C and thawing at RT to ensure complete cell lysis. Triplicates of 100 μL of each sample were then loaded into a black flat-bottom 96-well plate (Fisher Scientific, UK) and mixed with 100 μL of the working reagent at a 1:1 $v\ v^{-1}$ ratio following the manufacturer's instructions. Glass coverslip or scaffold without cells were used as blank. Molecular biology grade water was used as negative control. Fluorescence (ex./em. 485/520 nm) was measured with a FLUOstar Optima microplate reader (BMG Labtech), and compared with a generated lambda dsDNA standard curve obtained within the range of measured concentrations. Cell number was estimated based on the assumption that a single cell contains around 5 pg of DNA [381].

3.2.5.4 Neuronal differentiation

To induce neuronal differentiation, the cell culture medium was changed to a differentiation medium one day post-seeding, using serum-free medium. The culture was maintained for 5 days, with half of the medium removed and replaced with fresh medium every 2 days.

3.2.5.5 Immunocytochemistry (ICC)

Cell-laden scaffolds (n=2 per type) were harvested, gently washed twice with PBS and treated with 10% v v^{-1} neutral buffered formalin (NBF) (Sigma-Aldrich, UK) (equivalent to about 4% w v^{-1} paraformaldehyde) for 30 min at RT as a fixative solution. Samples were rinsed three times with PBS, permeabilised with 0.1% v v^{-1} Triton X-100 in PBS for 15 min and further rinsed three times with PBS. Samples were then blocked for non-specific binding with 1% w v^{-1} bovine serum albumin (BSA) in PBS for 30 min and rinsed three times with PBS.

To assess the differentiation of neuronal cell bodies, cell-laden samples were labelled with polyclonal rabbit anti-mouse/rat ß-tubulin III (Abcam, UK) as primary antibody, and preadsorbed polyclonal goat anti-rabbit IgG H&L Alexa Fluor® 488 (Abcam, UK) as secondary antibody. Samples were incubated at a 1:1000 v v^{-1} dilution in PBS for 2 h at RT, respectively; PBS was used to rinse in between steps. Cell nuclei were counterstained with 4’,6-diamidino-2-phenylindole dihydrochloride (DAPI) blue (1 mg mL^{-1}) (Sigma-Aldrich, UK) at a 1:1000 v v^{-1} dilution in molecular biology grade water for 2 min at RT. Samples were finally rinsed again with PBS three times. The volume of solution was ~200 µL per sample to ensure they were completely submerged.

Samples were mounted for imaging on Fisherbrand™ glass microscopic slides (76×26 mm, 0.8-1 mm thickness) (Fisher-Scientific, UK) using ProLong® Diamond Antifade Mountant (Thermo Fisher Scientific, UK); an appropriate sized glass coverslip (18×18 mm, 0.13-0.17 mm thickness) (VWR, UK) was then placed over the section of interest and cured at RT overnight following the manufacturer’s instructions. Samples were imaged using a TCS SP8 confocal laser scanning microscope (Leica Microsystems, UK) at an ex./em. of 340/488 nm for DAPI and 495/519 nm for Alexa Fluor® 488. Z-stacked images were acquired by scanning different areas throughout the thickness of the scaffold at 5 µm/Z-step. Images were visualised using Fiji software.

3.2.5.6 Neurite outgrowth

Neurite sprouting on each scaffold type was analysed from immunofluorescent micrographs. Only extended structures longer than 30 µm (measured from the middle of the cell body until the end of the projection) were considered as neuronal processes. A total of 10 neurites, across randomly selected fields of view, were measured per condition to determine neurite length. Quantification was carried out using Fiji software.

3.2.6 Data analysis

Statistical analysis was performed with GraphPad Prism 8 (San Diego, USA), and datasets checked for normality. Normally distributed data is presented as standard deviation (SD, error bars) of the mean values. For parametric data and multiple comparisons, significance was assessed by one-way ANOVA (one independent variable) or two-way ANOVA (two independent variables) with Tukey’s post hoc analysis test. Not normally distributed data was assessed by Kruskal-Wallis with Dunn’s post hoc analysis test. A value of $p<0.05$ was considered statistically significant.

3.3 Results and Discussion

Dissolution of SF is an important step in reprocessing it into fibres, but there are limited suitable solvents [382]. Here, we dispersed GO in HFIP, followed by sonication, SF addition and dissolution as described in the methodology. The distribution of the lateral width of GO flakes (**Figure 3.1A**) after 2 h sonication is shown in **Figure 3.1B**, with an average size of 167 (±54) nm. Longer sonication times can undermine the mechanical properties of GO, primarily attributed to a more aggressive fragmentation of the flakes resulting in an increased oxidation degree and the presence of more inter junctions and defects [383–385]. With this in mind, it was important to optimise a well-dispersed blended SF/GO solution, where the GO flakes could be effectively embedded within silk during electrospinning to form bead-free fibres.

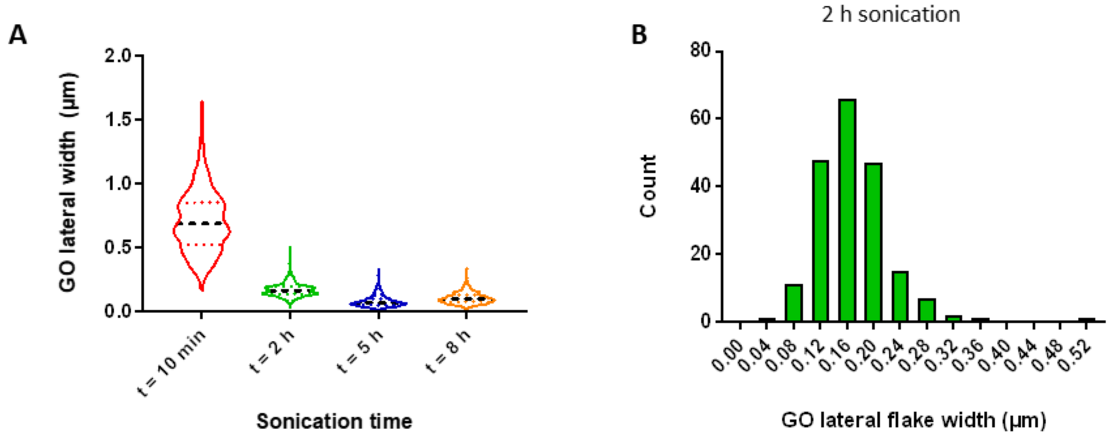

Figure 3.1 (A) Violin plot showing the frequency distribution (with the median and two quartiles) of the GO lateral width at increasing sonication time. (**B**) Histogram showing the distribution of the GO lateral width after 2 h sonication.

3.3.1 Fibrous morphology

The surface topographies and morphologies of the composite silk-based scaffolds are shown in **Figure 3.2**. Unmodified silk scaffolds appeared whitish in colour. Composite silk scaffolds were rendered increasing brown with increased GO loadings. After *in situ* post-reduction into SF/rGO, the samples turned into various shades of grey tending to black. Morphology of the fibres, as observed under FESEM, was smooth and consistent for every group tested, with an average fibre diameter of around 800 nm (**Figure 3.3A**). A decrease in the average fibre diameter due to larger fibre elongation during spinning has been reported with the incorporation of graphene and its derivatives [386,387]. While some differences could be observed compared with unmodified silk, fibres of similar diameter size were obtained with addition of GO up to 10% wt. – all blended solutions spun at similar conditions. Fibre diameter was not significantly affected by post-spinning annealing, but moderately increased ($p<0.01$) after post-reduction with ascorbic acid. In this respect, Huang et al. investigated the effects of different reducing agents on the properties of wet-spun GO fibres, and reported hydroiodic acid to result in lower fibre diameter, whereas hydrazine treatment caused larger diameters [388].

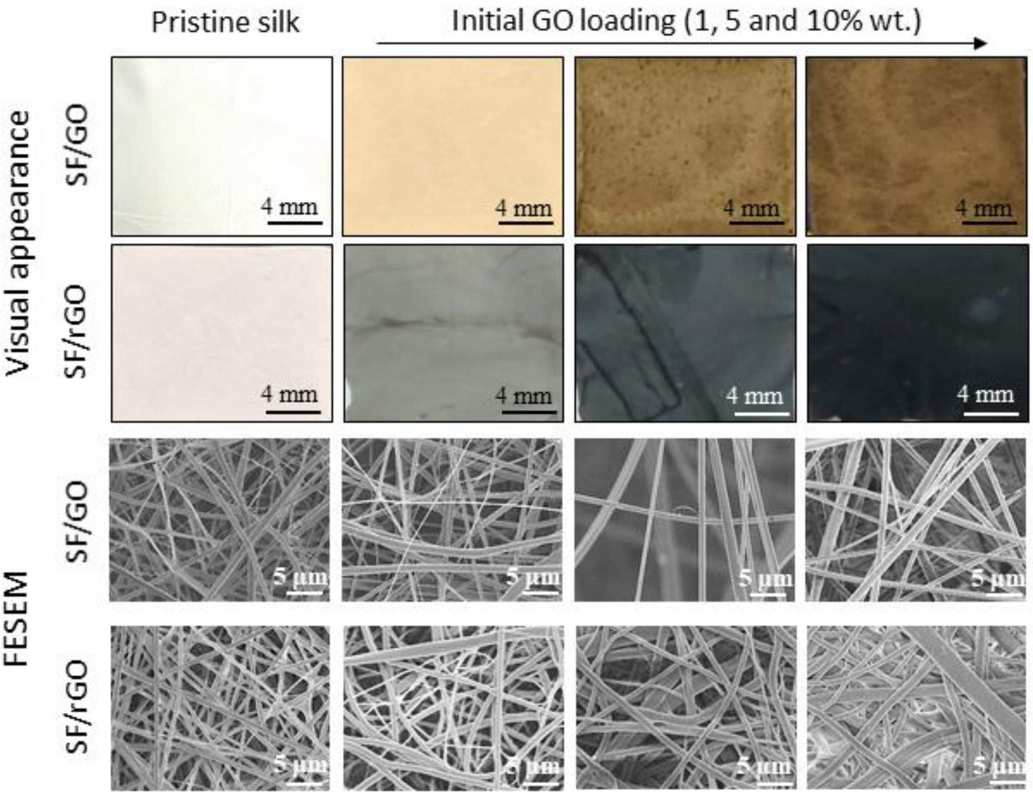

Figure 3.2 Effect of (r)GO content on the scaffold structure. Representative macroscopic views of the visual appearance of the scaffolds prior to and after post-reduction, and representative FESEM micrographs of the scaffolds; scale bars at 4 mm and 5 µm respectively.

3.3.2 Porosity and water sorption

Scaffolds manufactured by electrospinning usually consists of densely packed fibres with limited inter-fibre spacing and pore diameter [378]. However, a certain level of porosity is required in nerve conduits to allow infiltration of blood vessels and regulate nutrient uptake, oxygen diffusion and waste exchange [389]. Previously reported data has shown that the addition of carbon-based nanomaterials can lead to an increase in the pore diameter and overall scaffold porosity [390,391]. Following the determination of the percentage porosity, it was clear that the presence of (r)GO did not result in this case in major changes in the overall porosity (70-80%) or the estimated pore dimensions (~15 µm) (**Figure 3.3B-C**), and that these are a good compromise to provide a cell-friendly conduit lumen [389]. Indeed, scaffolds with excessive pore diameters may facilitate infiltration of non-neural cells along the conduit length and hinder neurite outgrowth [389]. In particular, pore diameters <30 µm in the conduit lumen are ideal to inhibit the invasion of fibroblasts and macrophagocytes for the regeneration of peripheral nerve [392].

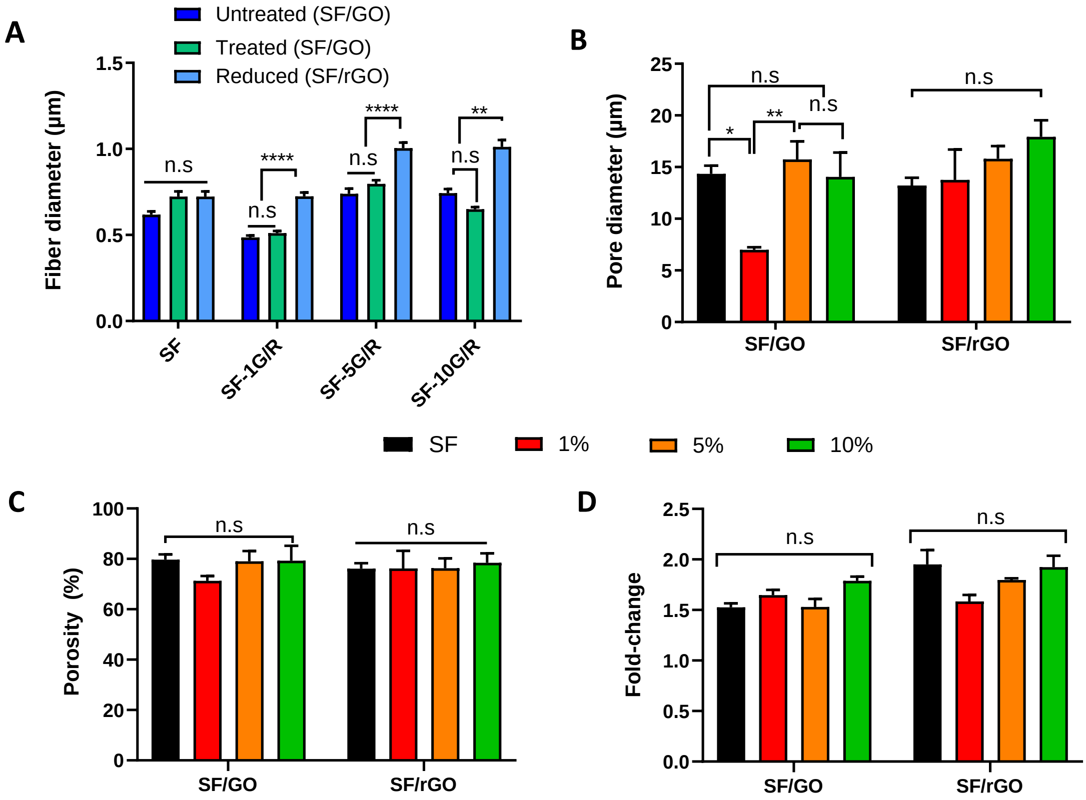

Figure 3.3 (**A**) Distribution of the fibre diameter size of the scaffolds before and after ethanol treatment (annealing) and with post-reduction (n=100 fibres). (**B**) Overall porosity of the scaffolds (n=5 per type) and (**C**) estimated average pore diameter. (**D**) Water sorption of the scaffolds (n=3 per type) after overnight incubation at physiological conditions. Differences between the experimental groups were analysed by two-way ANOVA with Tukey's test, or by Kruskal-Wallis with Dunn's test. n.s non-significant, * p<0.05, **p<0.01, ****p<0.0001.

Water sorption is an also an important feature that can influence the properties of the substrate prior to and after implantation. For instance, the void space might be reduced, increasing direct contact between the cells and the material [393]. Although SF presents a polymeric structure with hydrophobic regions, it has large sorption capacity to hold moisture thanks to its alternating hydrophilic regions [394]. Enhanced hydrophilicity can lead to increased cell attachment [395]. While the hydrophilicity/hydrophobicity of graphene and its derivatives has remained under constant debate over the last few years, it has been recently demonstrated that when graphene is placed in a water-like environment, it presents hydrophilic properties close to those of pure water [396]. Here, all substrates showed great water sorption capability; while some changes were observed with the presence of (r)GO in the fibres, these differences were non-significant (**Figure 3.3D**).

3.3.3 Molecular structure of silk and the effect of graphene derivatives

The addition of (r)GO into the silk system has previously been reported to lead to changes in the amount of β-sheet structures after ethanol treatment [372,397,398]. The chemical structure of SF was analysed by FTIR-ATR (**Figure 3.4A**). There were no obvious differences in the spectra, which indicates no generation of new groups. Since the (r)GO content is low compared with that of SF, and some of their characteristic peaks are very close, it is difficult to analyse the (r)GO-SF interactions from the FTIR spectra. Therefore, the proportion of secondary structures within the amide I region was quantified by means of deconvolution (**Figure 3.4B**). As expected, the amount of β-sheet structures increased after ethanol treatment due to increased crystallisation resulting from the transition of α-helix into β-sheet [399]. Indeed, it has been suggested that the mobility of the polypeptide chains is likely to be reduced as ethanol strips off the water shell around fibroin, resulting in an increased rate of β-sheet formation [400]. A similar proportion of the various secondary structures were quantified on the substrates at the different GO loadings (**Figure 3.4B**), with a slight reduction in the β-sheet content (p-value non-significant) at increased GO inclusion. These results tend to agree with those by Zhang et al. [397], who suggested that GO addition was not favourable for the transition of random coil or α-helix to β-sheets during post-treatment. A similar proportion of the secondary structures were quantified for the various samples after *in situ* post-reduction into SF/rGO (**Figure 3.4B**), with no significant differences with regards to the crystalline β-sheet content similar to the work of Zulan et al. [365]. Overall, similar silk-based scaffolds with no major changes in the molecular structure of silk were manufactured regardless of the addition of (r)GO. This is indeed important to help decoupling the influence of GO and rGO in subsequent cell-based assays.

Further studies were carried out to understand the compositional distribution of the fibres, where the presence of GO and rGO was confirmed by Raman spectroscopy (**Figure 3.4C**). The Raman spectra of the GO-containing scaffolds displayed two prominent peaks at around 1330 cm^{-1} and at 1595 cm^{-1}, ascribed to the D and G bands respectively. The G band is characteristic of sp2-hybridized C–C bonds in a two-dimensional hexagonal lattice, while the D band corresponds to the defects and disorder in the planar carbon network [401]. For the case of the rGO-containing scaffolds, the D band slightly retracted towards 1315 cm^{-1}, while the G band did not reveal any changes. A characteristic band attributed to β-sheets [366] could be observed at around 1670 cm^{-1} for unmodified silk, and the absence of graphene in these fibres was demonstrated by the lack of the characteristic spectral bands. The D/G intensity ratio can also be used as an indicator of the defects in the graphene structure. In this study, the intensity ratio of the samples (**Figure 3.4D**) was found to increase with the filler content, which can be correlated to increased carbonaceous presence in the composites [366]. The intensity ratio decreased for rGO-containing samples, which could be attributed to a decreased amount of oxygenated groups or structural defects after the reduction process [402,403].

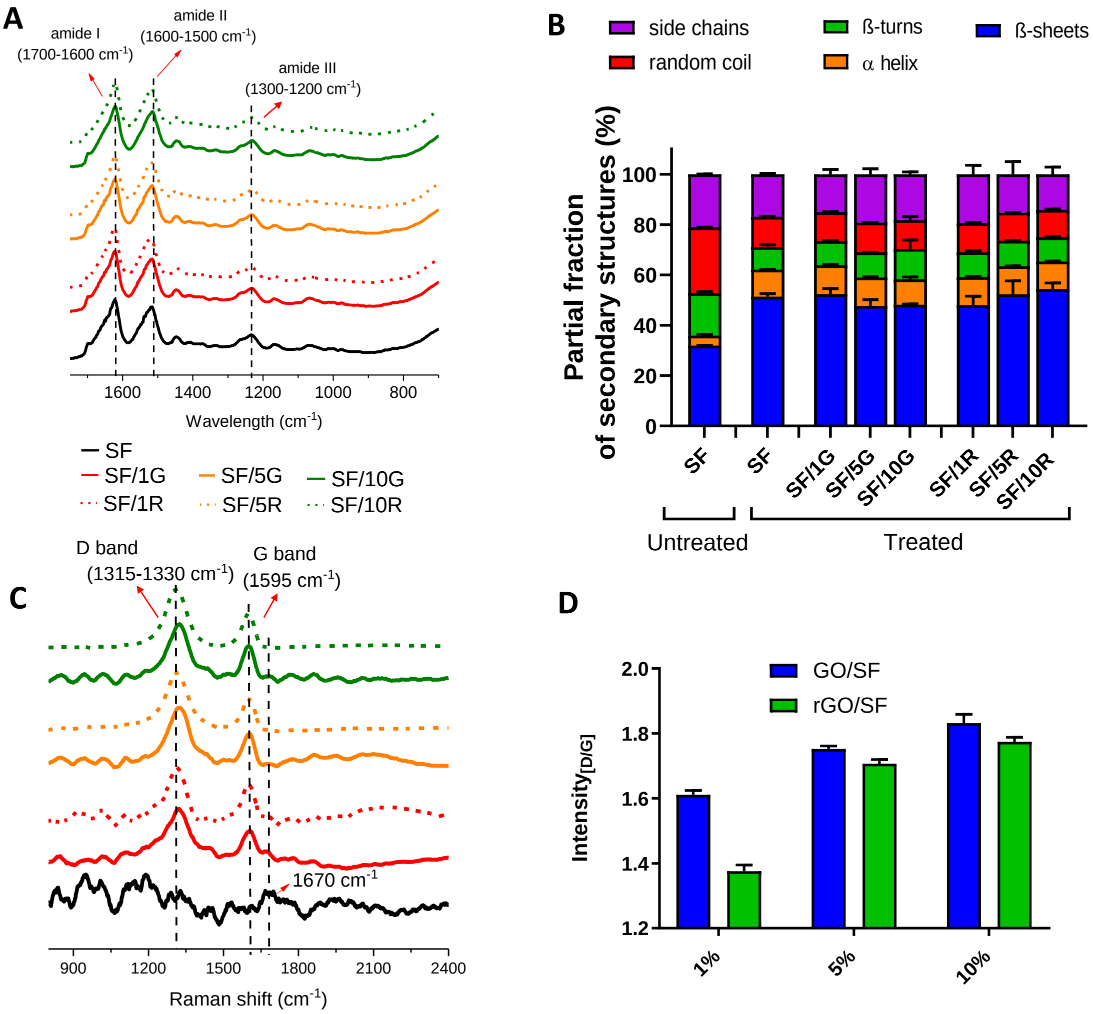

Figure 3.4 Effect of the presence of (r)GO on the chemical structure of silk. (**A**) Representative FTIR spectrum of the various scaffolds showing the typical fingerprint of silk. (**B**) Quantitative analysis of the secondary structure composition of silk, before and after treatment, within the amide I region (1700-1600 cm^{-1}). (**C**) Representative Raman spectra of the scaffolds. (**D**) Intensity ratio of the D and G spectral bands.

3.3.4 Conductive properties

Electrical conductance is dependent upon various factors, such as hydration degree, solvent or doping agent presence [376]. In this study, rGO flakes act as high aspect ratio electroconductive fillers in biohybrid composite electrospun silk-based scaffolds. Well-dispersed flakes within the fibres can contribute to the formation of conductive networks, generating self-assembling conductive pathways by forming conduction anchor nodes throughout. These conductive pathways facilitate and enhance electronic transport, along with protonic (e.g. molecules of bound water and amino acid side groups of proteins [404]) and ionic (e.g. electrolytes from the medium; the conductivity of cells is ionic in nature) currents throughout the substrate. Cell-cell communication in electrically sensitive tissues can be enhanced this way. For instance, it has been shown that hydrogels synthesised in combination with MWNTs [390] or PEDOT–PSS [405] can act as internal enhanced electrical systems to promote the cell response. In both studies, cell-cell communication between cardiomyocytes was facilitated by enhancing the overall substrate's conduction and inducing cell elongation and unidirectional cell alignment with improved coupling and beating.

Conductivity of SF/GO (**Figure 3.5A**) and electroactive SF/rGO scaffolds (**Figure 3.5B**) was estimated with a 4-point probe station. As expected, low conductivities were recorded on SF/GO scaffolds. Some differences were observed following addition of GO, though, in agreement with a previous study on protein-based hydrogels with GO incorporation [406]. Reduced GO offers higher electrical conductivity in comparison to GO for applications where tuning electrical properties is the main target. The presence of rGO increased the overall conductivity up to ~ 4×10^{-5} S cm^{-1} in the dry state, and peaked at ~ 3×10^{-4} S cm^{-1} in the hydrated state. This was a synergic effect provided by both the substrate (electronic and protonic conductivity) and the electrolytes of the medium (ionic conductivity), and differs from the trend previously reported by Martins et al. where the conductivity of a carbon nanofibre/chitosan scaffold was dominated by the aqueous media and decreased upon hydration [304]. However, even in those cases where the ionic conductivity provided by the aqueous environment could dominate over substrates of lower inherent conductivity [304], local changes in conductivity attributed to the electroconductive/active moiety may directly affect the properties of cells by altering their resistance or capacitance. Hydrated protein-based materials [274,334,407–409], in this case SF [410], can also be considered as proton conductors. Water-mediated proton hopping takes place due to peptide and peptenol flip-flopping [410], and is known as the *Grotthuss mechanism* [274]. The electroactive SF/rGO scaffolds maintained their original conductivity in the dry state after one-day hydration.

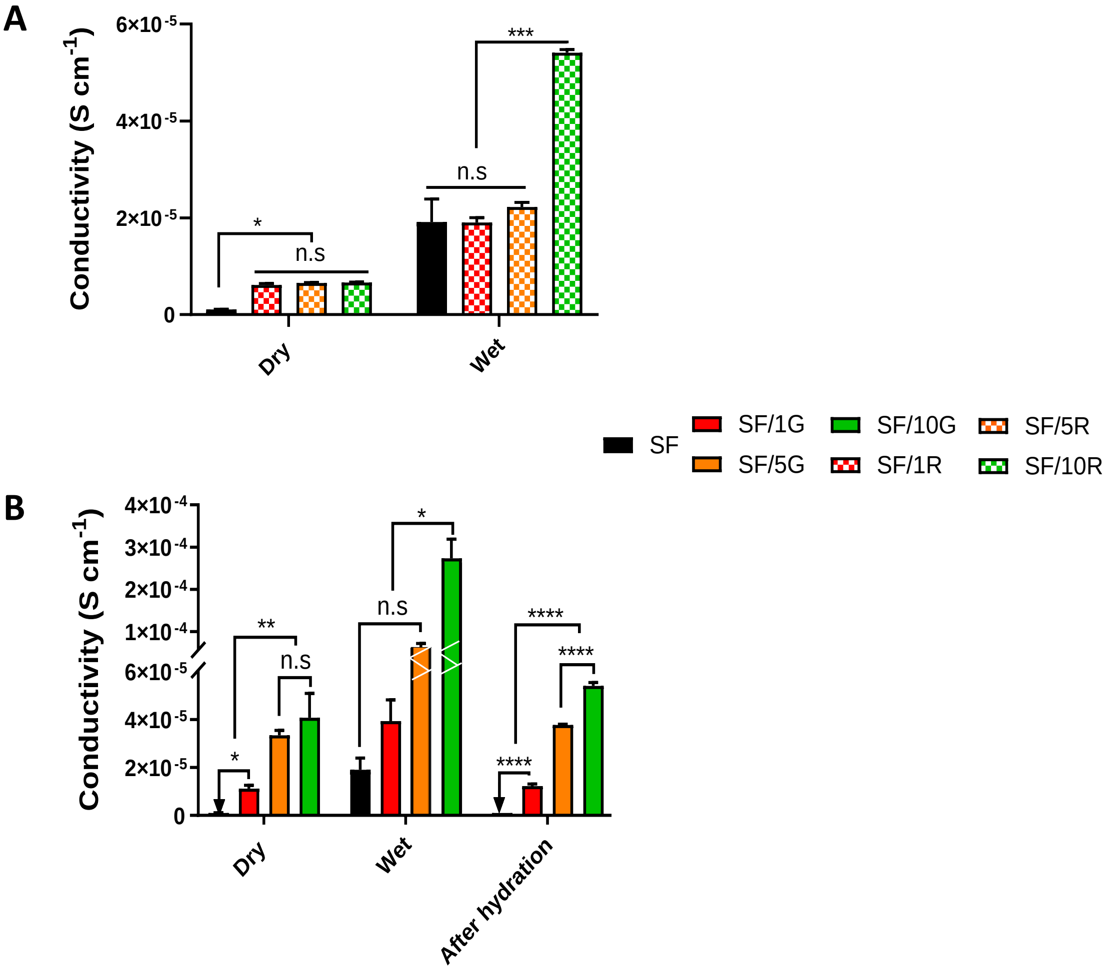

Figure 3.5 (A) Estimated conductivity of SF/GO scaffolds. Quantitative analysis of the conductivity properties of the scaffolds (n=4 per type) in the dry state and in the wet state. **(B)** Estimated conductivity of electroactive SF/rGO scaffolds. Quantitative analysis of the conductivity properties of the scaffolds (n=4 per type) in the dry state, in the hydrated state and in the dry state after one-day hydration. Differences between the experimental groups were analysed by two-way ANOVA with Tukey's test. n.s non-significant, *p<0.05, **p<0.01, ***p<0.001, ****p<0.0001. Zigzag in white indicates discontinued bar chart portion.

On the other hand, rGO offers limited conductivity due to the presence of defects on the carbon backbone and the small flake size achieved during processing. Furthermore, high conductivity is subjected to achieving percolation threshold and a successful dispersion of the flakes within the polymer matrix. Although the conductivity exhibited here for most SF/rGO samples (dry/hydrated states) may fall short [411], it has been reported that a range 1×10^{-6} to 8×10^{-5} S cm^{-1} is sufficient for conducting electrical regimes *in vivo* [412,413]. The conductivities exhibited here in the dry/hydrated state fall within such range and exceed it, and could even be further tuned to match or even surpass native tissues' conductivity by incorporating pristine graphene.

3.3.5 Neuronal cell viability, metabolic activity and proliferation

Neuronal-like cells were seeded onto all sample groups and their viability, metabolic activity and proliferation profiles were evaluated. A viability assay was used to assess the potential cytotoxicity of the different scaffolds, as well as evaluate attachment and survival of NG108-15 cells. Representative confocal micrographs and semi-quantitative analysis of viable and non-viable cells are shown in **Figure 3.6 and Figure 3.7**. In all substrates, few dead cells were observed (**Figure 3.6**), with the great majority of cells being alive (**Figure 3.7A-C)**. The percentage of viable cells after 7 days of culture was >95% for all scaffolds (**Figure 3.7C**). No major differences in the ratio of viable cells were observed among the different substrates and the controls, demonstrating that the presence of GO or rGO in the scaffold up to 10% wt. does not induce any major cytotoxic effects *in vitro*. During the growth phase, cells were observed to present round shapes with limited processes along their surface and grew clustered together in colonies. This is typical of NG108-15 cells and may have been further promoted by the randomly distribution of the fibres.

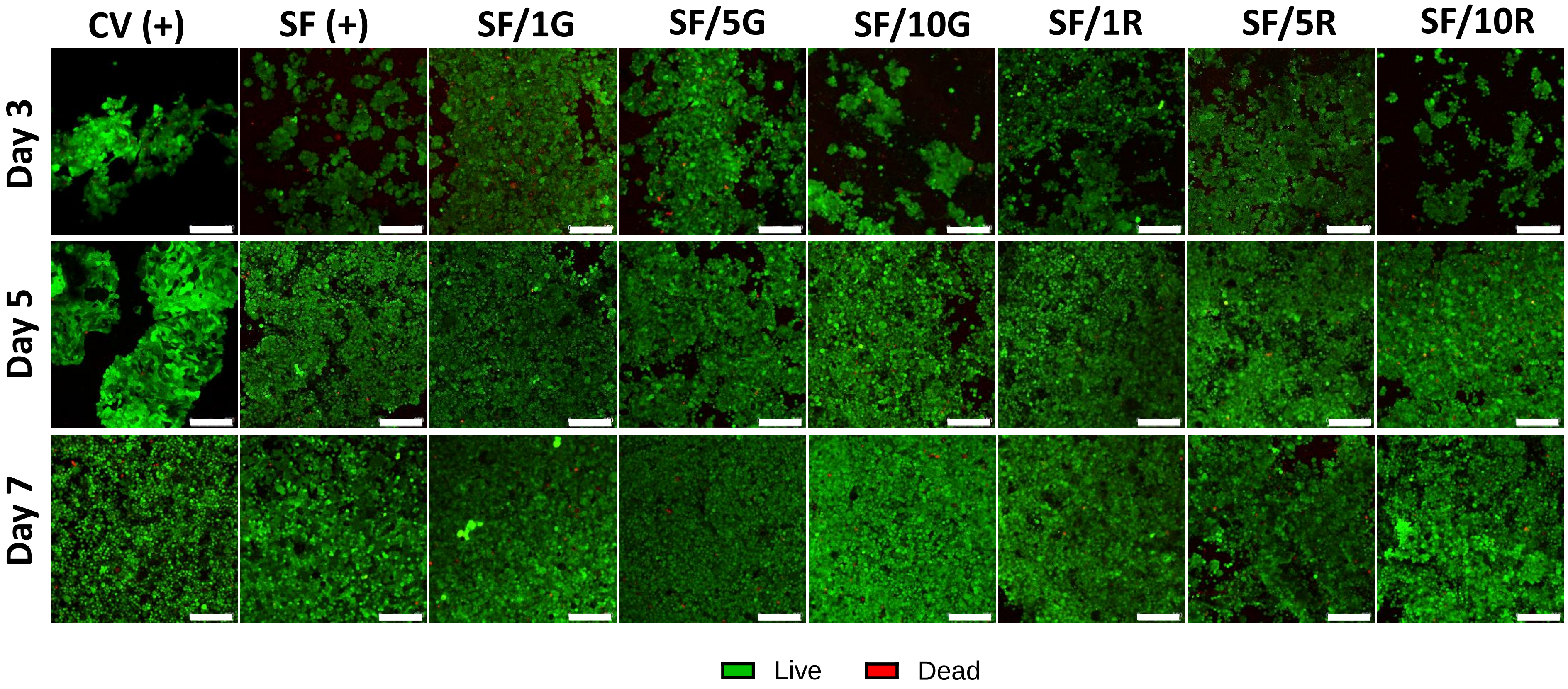

Figure 3.6 Cellular viability of NG108-15 cells on SF/GO and SF/rGO composite scaffolds over 7 days of culture. Representative confocal micrographs of cells labelled with calcein AM (green) and ethidium homodimer-1 (red) as markers of cell viability; scale bars at 250 µm. Coverslip (CV) and silk fibroin (SF) were used as controls.

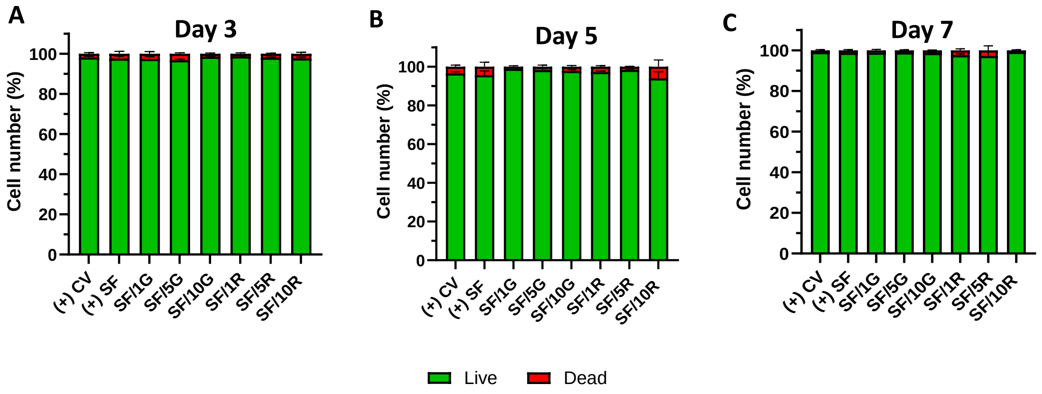

Figure 3.7 Cellular viability of NG108-15 cells on SF/GO and SF/rGO composite scaffolds over 7 days of culture. **(A-C)** Semi-quantitative analysis of the percentage of viable and non-viable cells over 7 days in culture (n=2 scaffolds per type. Coverslip (CV) and silk fibroin (SF) were used as controls.

The metabolic activity of NG108-15 cells is displayed in **Figure 3.8A**, shown as a function of the dsDNA concentration in **Figure 3.8B**. The latter provides an indication of the metabolic activity of the culture relative to the number of cells present on it. Cells exhibited greater metabolic activity on substrates containing GO and rGO compared to unmodified silk, tending to increase with filler content. By day 5, cells grown on electroactive SF/rGO samples were metabolically more active than those grown on SF/GO, while by day 7 the trend was opposite (**Figure 3.8B**), which might suggest cell confluency. The metabolic activity results were well supported in terms of cellular proliferation on the various substrates over time (**Figure 3.8C-D**), with the SF/rGO scaffolds accelerating cellular proliferation to the greatest extent by day 7 compared with SF/GO. These differences in cellular behaviour could be directly attributed to the presence of electroactive rGO as opposed to GO. The great proliferation response observed on glass coverslip at day 7 might be explained by the rigid and flat 2D surface, which is typically used for standard cell expansion and proliferation.

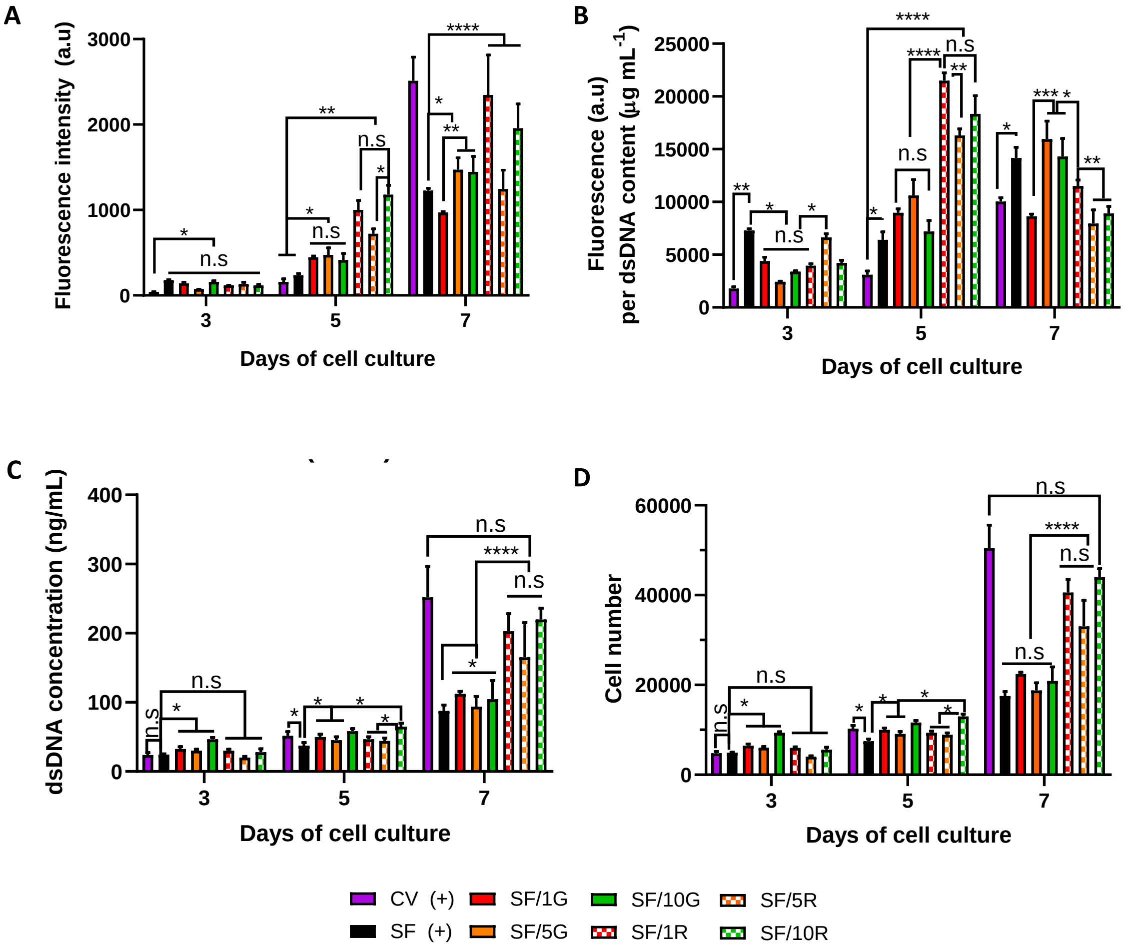

Figure 3.8 Cellular metabolic activity and proliferation of NG108-15 cells on SF/GO and SF/rGO composite scaffolds over 7 days of culture. (**A**) Metabolic activity (n=4 scaffolds per type). (**B**) Metabolic activity relative to dsDNA content (n=4 scaffolds per type). (**C**) Total dsDNA content (n=4 scaffolds per type). (**D**) Cellular proliferation; estimated number of cells (n=4 scaffolds per type). Differences between the experimental groups were analysed with two-way ANOVA with Tukey's test. n.s non-significant, *p<0.05, **p<0.01, ****p<0.0001. Coverslip (CV) and silk fibroin (SF) were used as controls.

Nevertheless, surface roughness and protein adsorption can also affect cell-material interactions [414], leading to changes in cellular adhesion, proliferation and biosynthesis of ECM components. Addition of (r)GO into the silk system led to a significant increase (p<0.001) in surface roughness for all samples tested (**Figure 3.9A-B**) compared to unmodified silk. Similarly, previous reports have shown increased surface roughness at increased graphene [415], carbon nanofibre [416] and carbon nanotube [417] content within various composites. Such changes may lead to regionally organised micro/nano- topographies that can contribute to micro/nano-structure-induced cellular interactions [417]. Non-significant differences in surface roughness were observed between the GO and rGO counterparts prior to and after post-reduction. The ability of the scaffolds to adsorb protein was also quantified (**Figure 3.9C**). Protein adsorption tended to increase especially at increased (r)GO loading compared with unmodified silk. This is in agreement with other studies [416,418] that have correlated an increase in protein adsorption with an increase in surface roughness. However, regardless of the GO and rGO counterparts presenting similar surface roughness, lower amounts of laminin were adsorbed on the rGO-containing samples. These results are in line with previous findings that have demonstrated that GO shows greater adsorption of proteins on its surface compared with rGO [419–421]. Therefore, while some studies have suggested that surface roughness and protein adsorption can be more vital traits over the electronic configuration of the scaffold [273], the tendency of electroactive SF/rGO to outperform SF/GO substrates in terms of the cellular response (**Figure 3.8**) could be attributed here to the endogenous electrical regimes induced by rGO.

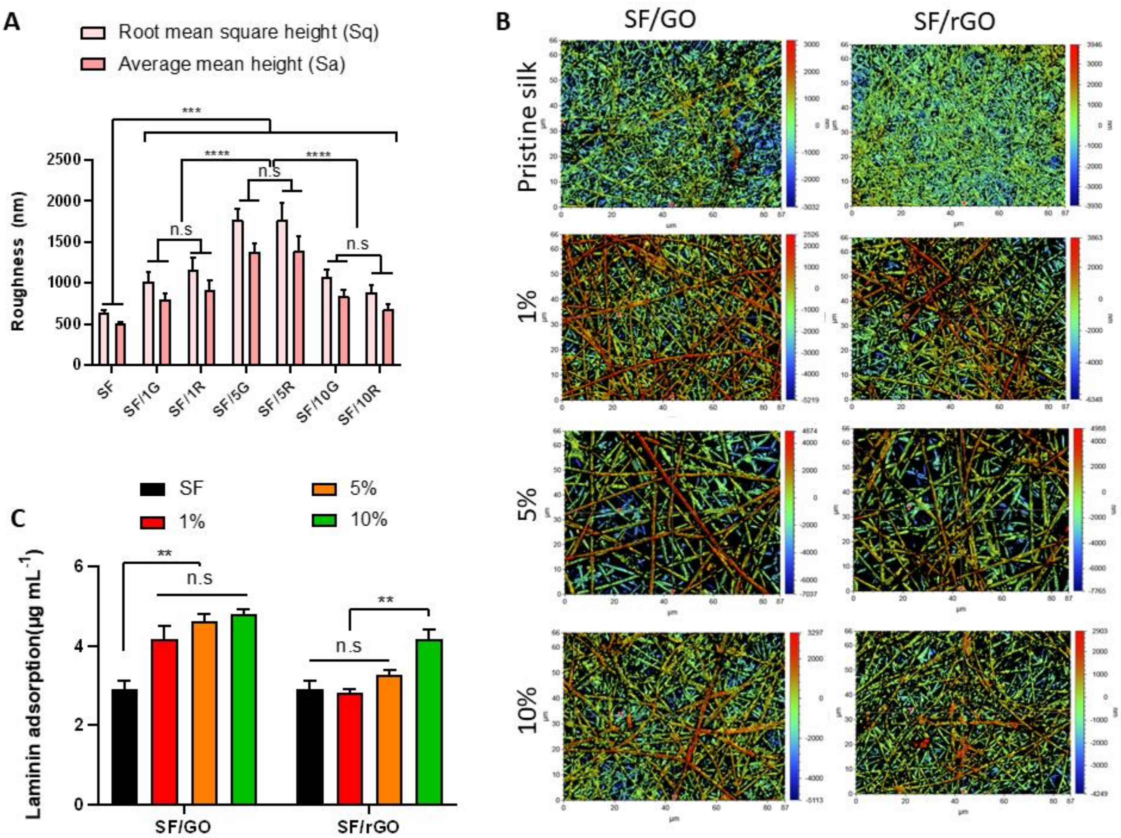

Figure 3.9 Surface roughness and protein adsorption capacity of the composite scaffolds. (**A**) Quantitative analysis of the surface roughness parameters (Sq – root mean square height, and Sa – average mean height) of the scaffolds (n=2 per type). (**B**) Representative optical profilometry micrographs of the surface roughness of SF/GO and SF/rGO composite scaffolds. (**C**) Quantitative analysis of laminin adsorption on the scaffolds (n=3 per type) after 2 h incubation. Differences between the experimental groups were analysed by two-way ANOVA with Tukey's test. n.s non-significant, $^{**}p<0.01$, $^{***}p<0.001$, $^{****}p<0.0001$

3.6 Neuronal outgrowth

Neurite outgrowth, axonal elongation and the formation of neuronal circuits are essential for the nerve tissue repair and regeneration process. Neurite outgrowth can be guided by physical cues in the substrate, but also directed by electrical regimes. Inspired by the cell metabolic activity and proliferation results, NG108-15 neuronal-like cells were grown on the various scaffolds in serum-deprived conditions and immunolabelled with β-tubulin III as a marker for neurite outgrowth and differentiation (**Figure 3.10**).

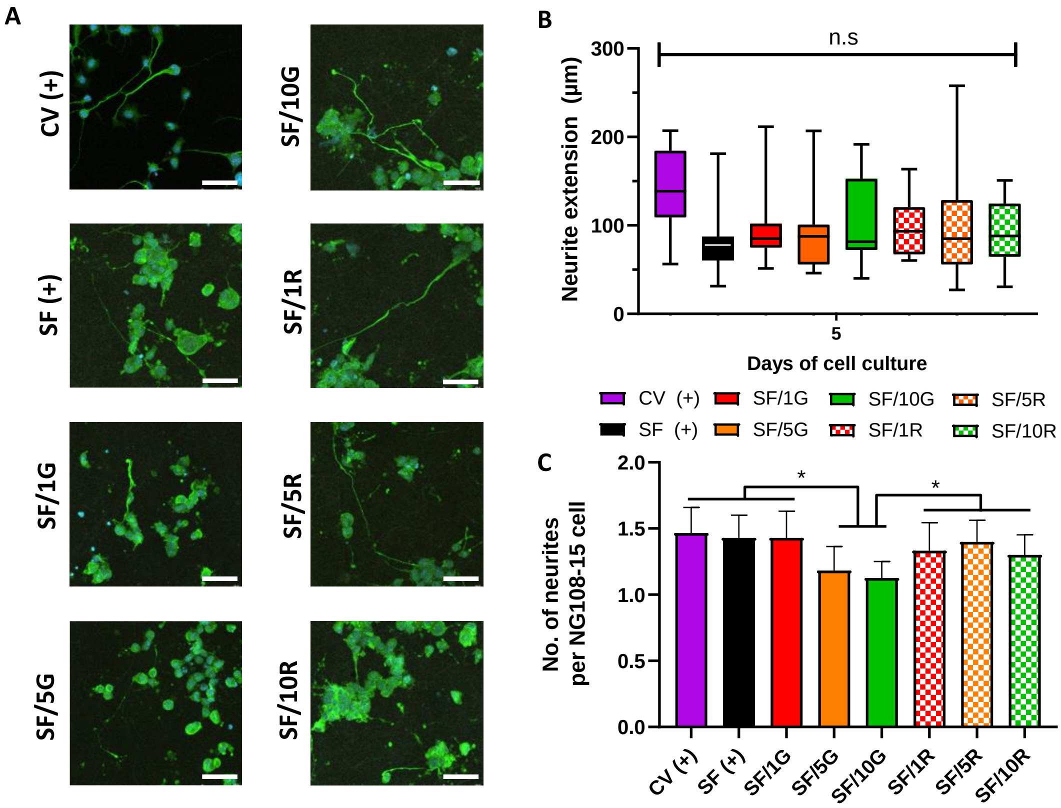

Figure 3.10 Neuronal differentiation of NG1081-15 cells on SF/GO and SF/rGO composite scaffolds after 5 days of culture. **(A)** Representative confocal micrographs of differentiated cells immunolabelled with β-tubulin III (green) and cell nuclei counterstained with DAPI (blue); scale bar at 75 µm. **(B)** Box-and-whisker plot showing neurite extension distribution on each scaffold. **(C)** Semi-quantitative analysis of the average number of neurites per neuronal cell body for each scaffold. Differences between the experimental groups were analysed with one-way ANOVA with Tukey's test. n.s non-significant, $*p<0.05$. Coverslip (CV) and silk fibroin (SF) were used as controls.

β-tubulin III is a marker expressed in neuronal cell bodies, dendrites, axons, and axonal terminations. Cell-laden samples in serum-supplemented medium served as negative controls of differentiation (**Figure 3.11**), with cells growing very clustered together without neurite extension.

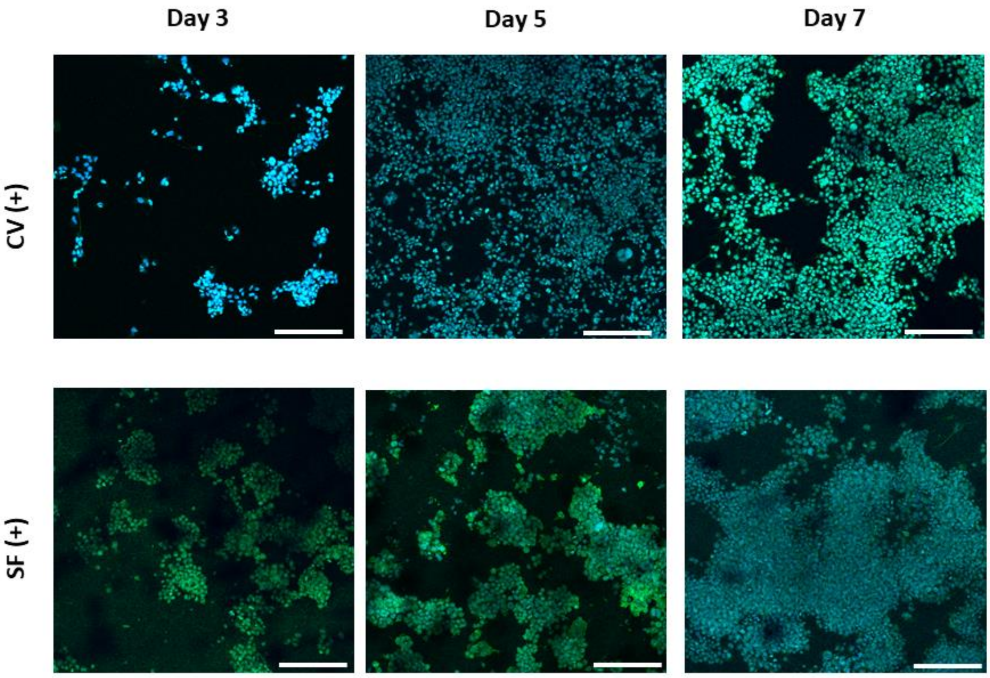

Figure 3.11 Representative confocal micrographs of undifferentiated NG108-15 cells over 7 days of culture on glass coverslip (CV) and silk fibroin (SF) scaffolds. Cells were immunolabelled with β-tubulin III (green) and cell nuclei counterstained with DAPI (blue); scale bars at 250 μm.

Representative micrographs of the various cell-laden substrates after induced differentiation are shown in **Figure 3.10A**. Neurite outgrowth on all substrates could be clearly observed after immunolabelling. Neurite length was quantified for each scaffold type (**Figure 3.10B**), with no significant differences in terms of neurite extension among sample groups. Further analysis revealed maximum neurite extensions of 207, 181, 212, 207, 192, 164, 258 and 151 μm for coverslip, SF, SF/1G, SF/5G, SF/10G, SF/1R, SF/5R and SF/10R, respectively. The average number of neurites expressed per NG108-15 neuronal cell body was estimated at ~1.4 (**Figure 3.10C**), in line with what has been previously reported using the same NG108-15 cell line on other scaffolds [422,423]. The average number of neurites per neuronal cell body decreased at increased GO content, while no differences were observed among the rGO/silk composites.

3.4 Conclusion

Delineating the role of electrical conductivity in cell behaviour is challenging, since it is difficult to manufacture scaffolds with similar physico-mechanical properties but different levels of conductivity, completely decoupling combined effects. Here, SF composite fibrous scaffolds were manufactured by incorporating GO at loading concentrations up to 10% wt., optionally followed by *in situ* post-reduction into electroactive SF/rGO. Presence of GO or rGO did not substantially influence the substrates in terms of the fibre size distribution, porosity, water sorption or protein secondary structure in silk. In contrast, surface roughness and protein adsorption capacity tended to increase with increasing filler content. Reduction treatment into SF/rGO greatly enhanced the electrical conductivity of the scaffolds, which was further promoted after hydration. Analogue neuronal NG108-15 cells were able to adhere and survive on all samples. Cellular proliferation was enhanced with the presence of GO compared with SF, notably outperformed after reduction into electroactive SF/rGO. No significant differences in neurite extension were observed, though. While it is difficult to pinpoint the parameter responsible for the differing cell responses observed between the GO and rGO counterparts, the inherent electrical regimes conferred by rGO seem to be an important trait over differences in surface roughness or protein adsorption, and further investigation should be warranted. Future studies can look at screening these substrates with other neuronal and Schwann cells, or in co-culture conditions. In addition, promotion of neurite outgrowth could be further investigated in combination with aligned fibrous substrates and direct ES.

Chapter 4

Modulation of neuronal cell affinity on PEDOT–PSS non-woven silk scaffolds for neural tissue engineering

Note: A version of this chapter has been published as Magaz *et al*. “Modulation of neuronal cell affinity on PEDOT–PSS non-woven silk scaffolds for neural tissue engineering”. *ACS Biomaterials Science & Engineering.* 2020;6(12):6906–16

Adrián Magaz[1,2]**, Ben F. Spencer**[1]**, John G. Hardy**[3,4]**, Xu Li**[2,5], **Julie E. Gough**[1], **Jonny J. Blaker**[1,6]*

[1]Department of Materials and the Henry Royce Institute, The University of Manchester, Manchester, M13 9PL, United Kingdom

[2]Institute of Materials Research and Engineering (IMRE), Agency for Science Technology and Research (A*STAR), 138634, Singapore

[3]Department of Chemistry, Lancaster University, Lancaster, LA1 4YB, United Kingdom

[4]Materials Science Institute, Lancaster University, Lancaster, LA1 4YB, United Kingdom

[5]Department of Chemistry, National University of Singapore, 117543, Singapore

[6]Department of Biomaterials, Institute of Clinical Dentistry, University of Oslo, Oslo, 0317, Norway

*Corresponding author

Author contribution statement

AM fabricated the scaffolds and characterised the materials in terms of their physico-chemical and biological properties. BFS acquired HAXPES data. Data analysis, manuscript and figure panels were compiled by AM. JGH, XL, JEG and JJB supervised the study. All authors contributed to experimental design, manuscript structuring, drafting and editing. An overview of the tasks carried out by the main author are provided below:

- Literature review
    - Conjugated polymers with a focus on PEDOT–PSS
    - Surface functionalisation techniques
    - Tuning conductive properties with a polar solvent
    - Role of conductivity in altering cellular response
- Study design following advice from the supervisory team
    - Selection of materials and preparation techniques
    - Selection of cell line and experimental points
    - Characterisation methods
- Experimental work
    - Optimisation methods for the manufacturing of highly conductive PEDOT–PSS hybrids based on functionalisation of silk-based scaffolds produced by electrospinning
    - Characterisation of the scaffolds in terms of fibre morphology, surface topography, element composition, chemical structure, conductivity and biological response
- Manuscript preparation
    - Writing initial draft
    - Revision following comments from the supervisory team

Overview

While there exist different strategies to imbue materials with certain conductivity, it is challenging to manufacture scaffolds that exhibit high conductance and good biological response. The use of carbon-based fillers in composites is limited to achieving dispersion for the formation of conductive networks, and rGO in particular tends to exhibit low conductivity. This chapter describes a second approach to imbue electrical conductivity to electrospun SF scaffolds by surface functionalisation with PEDOT–PSS and DMSO-treated PEDOT–PSS. It was hypothesised that conjugation with PEDOT–PSS on the surface would lead to higher conductive values, which could be tuned in terms of the coating concentration and further boosted by DMSO treatment. The produced scaffolds were physico-chemically characterised and biologically assessed with analogue neuronal-like cells.

The assembled PEDOT–PSS silk scaffolds showed higher conductance at increased coating concentration with no major changes in surface roughness but increased protein adsorption. Treating PEDOT–PSS with DMSO greatly boosted the conductivity of the scaffolds and partially promoted their biological response in comparison to PEDOT–PSS. Whether it is due to differences in conductivity or other secondary effects, or more likely a synergic cascade of different events, the overall biological response of the scaffolds was enhanced compared with unmodified silk.

Abstract

PNI is a common consequence of trauma with low regenerative potential. Electroconductive scaffolds can provide appropriate cell growth microenvironments and synergistic cell guidance cues for nerve tissue engineering. In the present study, electrically conductive scaffolds were prepared by conjugating PEDOT–PSS or DMSO-treated PEDOT–PSS on electrospun silk scaffolds. Conductance could be tuned by the coating concentration and was further boosted by DMSO treatment. Analogue NG108-15 neuronal cells were cultured on the scaffolds to evaluate neuronal cell growth, proliferation and differentiation. Cellular viability was maintained on all scaffold groups, while showing comparatively better metabolic activity and proliferation than unmodified silk. DMSO-treated PEDOT–PSS functionalised scaffolds partially outperformed their PEDOT–PSS counterparts. Differentiation assessments suggested that these PEDOT–PSS assembled silk scaffolds could support neurite sprouting, indicating that they show promise to be used as a future platform to restore electrochemical coupling at the site of injury and preserve normal nerve function.

Keywords: PEDOT–PSS; silk fibroin; electrospinning; neuronal scaffold

4.1 Introduction

Electroconductive scaffolds have shown great promise in engineering electrically sensitive tissues such as muscle (e.g. cardiac, skeletal, smooth) and nerve [273], which are highly dependent on electrochemical signalling between or within cells [424]. Materials that are intended to interact with tissues should be engineered to stimulate the wound healing response. In particular, neural tissue exhibits low regenerative potential. Since electrical integrity is essential for the repair and regeneration process of the nervous system, different avenues to improve conduction of biomaterials and enhance tissue function have been explored over the years, as recently reviewed [273,425].

Conjugated polymers such as PPy, PANI and PEDOT are attractive candidates in tissue engineering due to their versatility in many biomedical applications and highly electrically conductive nature [426,427]. PEDOT is the most studied polythiophene derivative due to its higher electrical conductivity and chemical stability [428]. Unlike other conductive polymers, PEDOT doped with polystyrene sulfonate is easily dispersed in aqueous solution, it is amenable to solution processing and retains a significant amount of its conductive properties in physiological conditions [429,430]. Accordingly, the use of PEDOT–PSS is a promising candidate for developing conductive scaffolds [377,405,431] with the ability to support cell adhesion, and facilitate cell growth and differentiation. PEDOT–PSS transduces charge by both ion and electron/hole exchange [432]. Its conductance can be further optimised by treatment with polar solvents such as DMSO, a process by which the anionic PSS shells are partially washed away leading to a shift in the structure of disentangled PEDOT–PSS with more efficient orbital overlap and interchain packing for charge transport [433]. The use of pure conjugated polymers tends to be limited, though, due to their poor processability, non-degradability, brittle behaviour and tendency to crack attributed to the tight coil-like conformation in the polymer chain backbone [434]. Therefore, they are usually incorporated via blending or coating with another polymer.

An important cue in tissue engineering is the recapitulation of the fibrillary topography of native tissues, where many of the major components of the ECM exist as fibres that mediate cellular responses such as attachment, migration, growth, proliferation and differentiation [435,436]. Myriad micro-/nano-fabrication technologies for engineering fibrous scaffolds for tissue engineering applications have been developed over the years [437]. Electrospinning remains the most common technique to manufacture micro-/nano-fibrous structures at the multiscale with high surface area to volume ratio and defined spatial density both in 2D and 3D [438].

SF is readily available from silkworm cocoons (e.g. *Bombyx mori*), and has been demonstrated to support the growth of a wide range of cell types *in vitro* and tissue ingrowth *in vivo* [11,311,362]. The relatively ease of its processing, along with the versatility of the physico-chemical and mechanical properties of silk, has made it one of the most commonly used naturally-occurring proteins for biomedical applications [11,95]. Previous studies have reported the testing and manufacture of electroconductive/active scaffolds based on silks and the incorporation of carbon-based nanomaterials or metallic nanoparticles, as reviewed in [8]. Functionalisation with conjugated polymers could be a more direct approach to achieve excellent electrical conductivity for enhanced cellular signalling response. The combination of PEDOT and silk has been primarily explored in the area of microelectronics [125,318,439–443], with some reports studying their biological response in biosensor devices [444,445]. Even less attention has been paid to hybrid scaffolds made of PEDOT and silk for regenerative medicine applications [446].

In this study, fibrous scaffolds based on SF were fabricated by electrospinning and rendered conductive by functionalisation with PEDOT–PSS or DMSO-treated PEDOT–PSS. NG108-15 neuronal cells were seeded to assess the biological response of these substrates. The contribution of PEDOT could enhance the neuronal cell response in terms of adhesion, proliferation and neurite outgrowth.

4.2 Experimental section

4.2.1 Preparation of regenerated silk fibroin

Extraction and purification of SF from *Bombyx mori* was carried out following a previously described protocol [367] based on a degumming process to remove sericin and lithium bromide dissolution of the degummed fibres, followed by dialysis against water for 3 days. The resulting regenerated SF solution was cast onto polystyrene dishes (Sigma-Aldrich, UK) and dried in a forced air-circulation oven (Memmert Universal, Germany). SF films were peeled off and kept as stock material for further use.

4.2.2 Fabrication of electrospun silk scaffolds

Regenerated SF films were dissolved in HFIP (Sigma-Aldrich, UK) at 10% w v^{-1} and subsequently electrospun into fibres. Scaffolds were spun using a single needle, targeted towards a static collector using a custom-built electrospinning set-up with the following parameters: continuous flow rate, 0.8 mL h^{-1}; tip-to-collector distance, 10 cm; applied voltage, 15 kV; relative humidity, 25%; needle gauge, 19 G. As-spun scaffolds were annealed by immersion in a bath of 80% v v^{-1} ethanol to induce β-sheet conformational transition, dried overnight between filter paper to prevent folding, and stored in a desiccator for further use.

4.2.3 Surface functionalisation of silk scaffolds with PEDOT–PSS and DMSO-treated PEDOT–PSS

Electrospun SF scaffolds were functionalised with PEDOT–PSS or DMSO-treated PEDOT–PSS (**Scheme 4.1A-B**), wherein the PEDOT and PSS interact primarily through electrostatic interactions yielding highly durable conductance on degummed silk-based materials [441].

For this purpose, PEDOT–PSS particles should be negatively charged in an aqueous solution that is sufficiently acidic for the silk fibres to be positively charged, based on the silk fibroin's isoelectric point [447,448]. PEDOT–PSS aqueous dispersions were prepared by dilution into different concentrations (0.5, 1, 3, 9, 13 mg mL^{-1}), from a commercial solution (pH = 2, supplied at a 1.3% wt. dispersion in water) (Sigma-Aldrich, UK). SF scaffolds (13 mm diameter, ~100 μm thickness) were submerged (1 mL per scaffold) and sonicated in a water bath at RT for 1 h in the prepared PEDOT–PSS solutions. Scaffolds were then thoroughly rinsed in deionised (DI) water to remove excess PEDOT–PSS and air-dried for 2 h at RT. This process was repeated twice. Based on the PEDOT–PSS solution concentration (ranging from 0.5 to 13 mg mL^{-1}) the functionalised scaffolds were named SF-0.5P (0.5), SF-1P (1), SF-3P (3), SF-9P (9) and SF-13P (13). Separately, DMSO-treated PEDOT–PSS solutions were prepared by mixing 95% v v^{-1} of PEDOT–PSS with 5% v v^{-1} DMSO (Sigma-Aldrich, UK), vortexed and allowed to settle overnight. Adjustment to pH 2 followed, and a similar process as described above was carried out to give SF-0.5PD, SF-1PD, SF-3PD, SF-9PD and SF-13PD scaffolds. The PEDOT–PSS and DMSO-treated PEDOT–PSS uptake mass on the produced scaffolds (13 mm diameter, n=3 per scaffold type) was estimated based on weight differences before and after functionalisation.

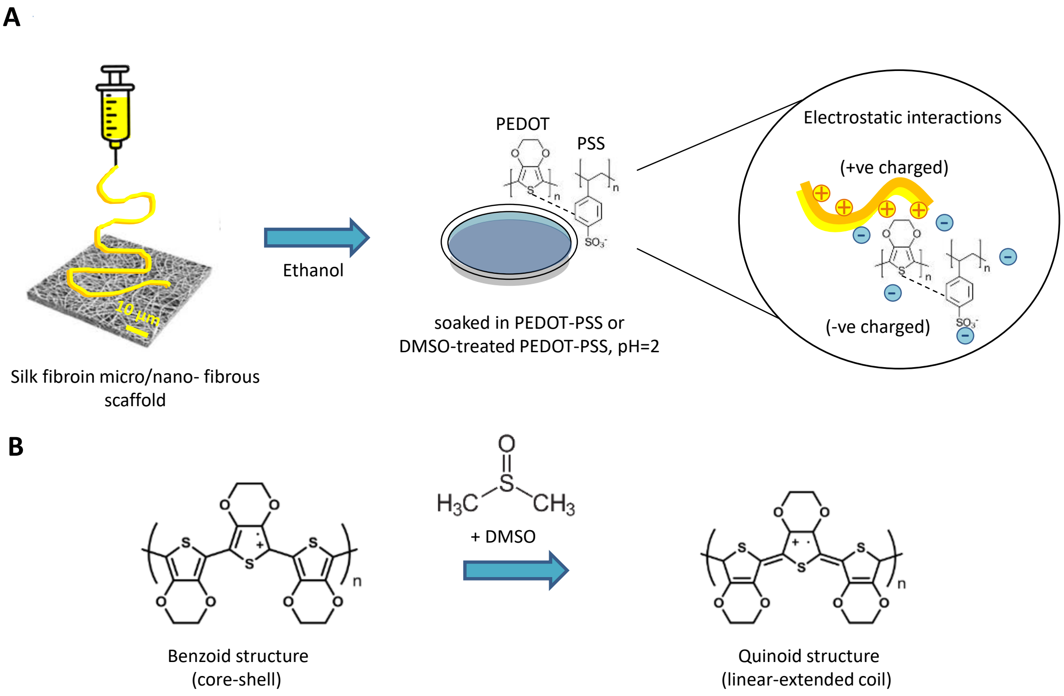

Scheme 4.1 (**A**) Schematic of electrospun SF scaffolds followed by conjugation with PEDOT–PSS or DMSO-treated PEDOT–PSS. (**B**) Schematic of the conformational change of the PEDOT–PSS structure after treatment with DMSO, from core-shell (i.e. benzoid) towards linear-extended coil (i.e. quinoid).

4.2.4 Zeta potential and particle size measurements

The zeta potential and particle size of PEDOT–PSS and DMSO-treated PEDOT–PSS were determined using a Zeta Sizer Nano dynamic light scattering (DLS) instrument (Malvern Panalytical, SG). Aliquots (n=3 per type) of freshly prepared dispersions (0.2 mg mL^{-1}) were pipetted into disposable folded capillary cells (DTS1070) (Malvern Panalytical, SG) and used for measurements in a volume of 750 µL. A refractive index of 1.334 was used for PEDOT–PSS, according to the manufacturer. Three measurements, with 10-100 runs each, were taken per sample at 25° C with an equilibration time of 30 s. Zetasizer software (Malvern Panalytical, SG) was used for data analysis.

4.2.5 Characterisation of the scaffolds

4.2.5.1 Morphology and surface topography

FESEM images from different batches of samples were taken using a JEOL JSM6700F at an accelerating voltage of 5 kV and ~ 8 mm working distance. Fibre diameter size distribution was analysed with Fiji 1.28 (NIH, USA); a minimum of 100 individual fibres per sample were analysed.

4.2.5.2 Hard X-ray photoelectron spectroscopy

The surface and bulk-like compositions of the functionalised scaffolds were quantitatively analysed with a high-throughput lab-based hard X-ray photoelectron spectroscope (HAXPES, Scienta Omicron) equipped with a Ga Kα X-ray source (9.25 keV; Excillum). For measurements, scaffolds were mounted on Omicron flag-style sample plates using double-sided adhesive copper tape. The survey spectra were measured using an EW4000 electron energy analyser with 500 eV pass energy and ~2 eV energy resolution. Core level spectra of elements of interest were measured with 200 eV pass energy and ~0.8 eV energy resolution [449]. Atomic concentrations were calculated based on sensitivity factors for the core levels, as listed in [450]. The sampling depth for HAXPES was calculated using the TPP-2M formula to be ~54 nm, and surface sensitive XPS using a standard Al Kα X-ray source (1.486 keV) was also performed with a sampling depth of ~11 nm; the operating pressure was 6×10^{-10} mbar. Quantitative analysis of spectra was carried out with CasaXPS (v. 2.3.23) processing software in the range of 160–175 eV (S 2p, XPS, ~11 nm) and 2460–2485 eV (S 1s, HAXPES, ~54 nm) (**Figure 4.1**). The PSS and PEDOT peaks were fitted using Voigt-approximation Gaussian-Lorenztian peaks and the PSS to PEDOT ratios were subsequently calculated. PSS and PEDOT are easily identified in the spectra since PSS is chemically shifted by 4 eV to higher binding energy than PEDOT for the S 2p core level measured with XPS, and 5 eV for the S 1s core level measured with HAXPES [451].

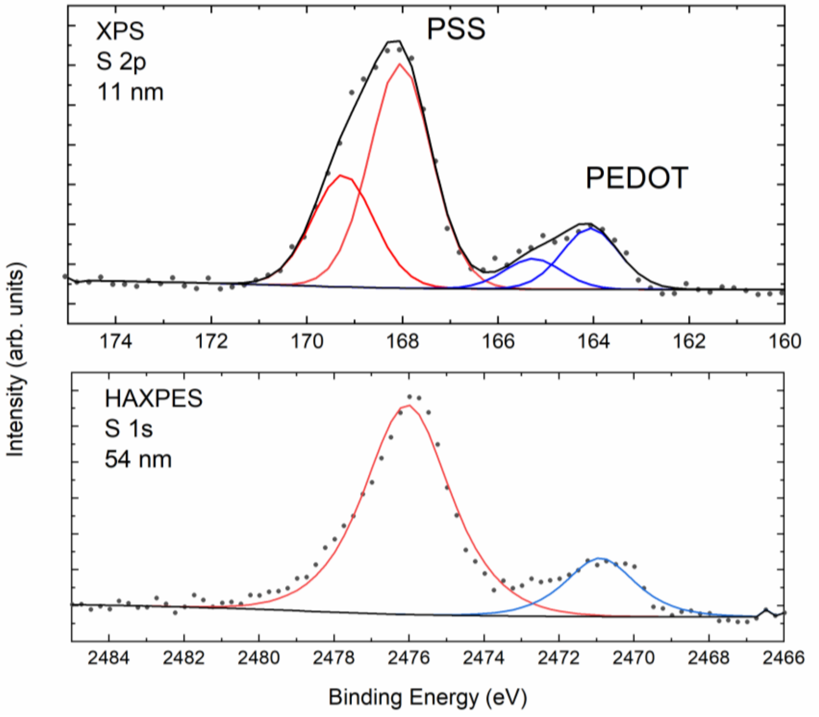

Figure 4.1 Representative HAXPES spectra of the functionalised scaffolds (e.g. SF-0.5P) at two different sampling depths (S 2p ~11 nm, S 1s ~54 nm) showing the characteristic PSS and PEDOT peaks, along with curve fitting.

4.2.5.3 Protein adsorption

The ability of the scaffolds (n=3 per type) to adsorb protein was evaluated with BSA (Sigma-Aldrich, UK), quantified with a Pierce™ bicinchoninic acid (BCA) protein assay kit (Thermo Fisher Scientific, UK) based on the amount of remaining BSA in solution after adsorption. Samples were incubated at 37°C overnight in 1 mL of 500 µg mL^{-1} BSA in DI water. Absorbance was measured at 562 nm using a microplate reader (Infinite M200) (Tecan Life Sciences, SG). The amount of protein was calculated using a standard curve obtained from BSA within the range of measured concentrations. All samples were conducted in triplicate. Scaffolds incubated in DI water served as blanks, and DI water was used as negative control.

4.2.5.4 Surface roughness

Surface morphology was assessed using a Countour GT-K1 3D optical profilometer (Veeco, USA). Briefly, scaffolds (n=2 per type) were placed on glass coverslips and fixed with ethanol to ensure a near flat surface. They were then pre-conditioned in supplemented culture media overnight and dehydrated in a series of ethanol solutions prior to imaging. Samples were imaged in vertical scanning interferometry mode. A total of 10 micrographs (66 µm × 87 µm) were taken per sample at different fields of view, with an average of five measurements per image. Analysis of the surface roughness (arithmetical mean surface height (Sa) and root mean square surface height (Sq)) based on 3D profile ordinates was performed with the Vision64 Map™ (Bruker, USA) software.

4.2.5.5 Electroconductive properties

An automated 4-point probe electrical conductivity and resistivity station (A4P-200 MicroXACT) connected to a combined DC current source and digital voltmeter (Jandel RM3000) was used for the experiments [366,376,377]. The conductivity was estimated in four different locations on each scaffold (n=4 per type), in the dry state and in the hydrated state after overnight incubation in phosphate buffered saline (PBS). Excess water was removed using blotting paper.

4.2.5.6 Chemical structure

Chemical bond analysis of the functionalised scaffolds was conducted using FTIR spectroscopy. PEDOT–PSS and DMSO-treated PEDOT–PSS solutions were cast on a petri dish, let air-dry overnight and peeled off as films for comparison. FTIR spectra were taken with a PerkinElmer 2000 spectrometer equipped with a zinc selenide (ZnSe) crystal in ATR mode, in the range 4000-600 cm^{-1} and resolution 4 cm^{-1}, with 32 scans taken per measurement.

4.2.6 In vitro study

4.2.6.1 NG108-15 cell culture

Analogue NG108-15 neuronal cells were grown in NG108-15 growth medium as previously described [452] and used between passage P17-30.

For cell culture experiments, functionalised scaffolds (13 mm diameter) were positioned onto CellCrown™ polycarbonate inserts (Scaffdex Oy, Finland) for 24-well plates. Scaffolds were maintained in molecular biology grade water (AccuGENE™) (Lonza, UK) for 24 h, air-dried and sterilised under UV light (254 nm) radiation (30 min on each side, top and bottom) in a class II biosafety cabinet. Glass coverslips (CV)

(12 mm diameter, 0.13-0.16 mm thickness) (VWR, UK) served as positive controls. Scaffolds were preconditioned in supplemented media and seeded at a density of 20,000 cells per well with minimum media to ensure maximum cell attachment (~2 h) before being topped up to 1 mL. The culture was maintained for 7 days, with half of the medium changed every other day.

4.2.6.2 Cell viability, metabolic activity and proliferation

Cellular viability was measured at specific time intervals on cells on the scaffolds (n=2 per type) with a LIVE/DEAD® viability/cytotoxicity fluorescence kit (Thermo Fisher Scientific, UK) following the manufacturer's instructions. Samples were 3D imaged using a TCS SP8 confocal laser scanning microscope (Leica Microsystems, UK). Data is expressed as the percentage of live cells versus non-viable/dead cells, analysed from several fields of view.

The metabolic activity of cells on the scaffolds (n=3 per type) was monitored with the alamarBlue™ reduction assay based on resazurin sodium salt (Sigma-Aldrich, UK). Metabolic activity is expressed relative to dsDNA concentration – quantified using a Quant-iT™ PicoGreen® dsDNA assay kit (Thermo Fisher Scientific, UK) following the manufacturer's instructions. Cellular proliferation is expressed in terms of cell number, estimated based on a single cell's DNA content [381].

4.2.6.3 Neurite outgrowth

To induce terminal differentiation, cells were grown in serum-free culture media. The culture was maintained for 5 days, with half of the media removed and replaced with fresh media every other day. After 5 days of culture, cell-laden scaffolds (n=2 per type) were harvested, fixed, permeabilised and blocked against non-specific binding. Differentiated cells on the scaffolds were stained with polyclonal rabbit anti-mouse/rat ß-tubulin III (Abcam, UK) conjugated to Alexa Fluor® 488 (Abcam, UK) (1:1000 v v^{-1} dilution). Cell nuclei were counterstained with DAPI (Sigma-Aldrich, UK). Samples were mounted and 3D imaged with a TCS SP8 confocal laser scanning microscope (Leica Microsystems, UK).

For analysis of cell differentiation, neurite length was determined on a cell-by-cell basis on each scaffold type from immunofluorescent micrographs using Fiji software. Only cell processes longer than 30 µm were considered for analysis. Neurites were sampled from randomly selected fields of view; a total of 15 neurites per condition were measured to determine neurite length.

4.2.7 Data analysis

Statistical analysis was performed with GraphPad Prism 8 (San Diego, USA), and datasets checked for normality. Normally distributed data is presented as SD (error bars) of the mean values. For parametric data and multiple comparisons, significance was assessed by one-way ANOVA (one independent variable) or two-way ANOVA (two independent variables) using Tukey’s post hoc analysis test. For comparing parametric data between two groups, two-tailed unpaired Student's t-test was used. Not normally distributed data was assessed by Kruskal-Wallis with Dunn’s post hoc analysis test. A value of $p<0.05$ was considered statistically significant.

4.3 Results and Discussion

This work aimed to develop an electroconductive silk-based scaffold which can enhance maturation and physiological properties of engineered nerve tissues. For this purpose, the (bio)functionality of SF was harnessed together with the inherent highly electroconductive property of PEDOT–PSS, which was further boosted by DMSO treatment. Treatment of PEDOT–PSS with DMSO resulted in an increase in particle size (**Figure 4.2A**) based on DLS analysis,[405] with no significant change in surface charge (**Figure 4.2B**). It has been reported that the geometry of PEDOT–PSS changes from coil-structure towards a more linear-extended morphology after DMSO treatment [453]. While the DLS technique assumes a spherical model acceptable for PEDOT–PSS, it can still provide a reasonable estimate of the order of magnitude in the case of DMSO-treated PEDOT–PSS.

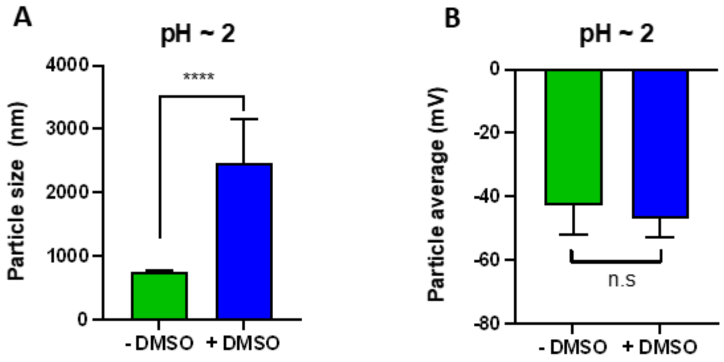

Figure 4.2 Characterisation of PEDOT–PSS and DMSO-treated PEDOT–PSS: (**A**) particle size (n=3 per dispersion type) and (**B**) zeta potential (n=3 per dispersion type). Differences between the experimental groups were analysed by a two-tailed unpaired Student's t test. n.s. non-significant, ****p<0.0001.

Native neural tissue is comprised of several structural fibrillary proteins ranging from several nanometres to micrometres in diameter [454]. Consequently, the fabrication of biomimetic fibrous structures plays a key role in the properties of tissue engineered scaffolds. Visual appearance and fibre morphology of the scaffolds are shown in **Figure 4.3A-B**. Compared to neat silk, which is whitish in appearance, scaffolds became increasingly darker blue upon functionalisation, qualitatively indicating that the coverage amount on the scaffolds increased gradually with increasing amounts of PEDOT–PSS or DMSO-treated PEDOT–PSS. Likewise, increased mass uptake of PEDOT–PSS or DMSO-treated PEDOT–PSS on the scaffolds was observed at increasing coating concentration (**Table 4.1**). This was further confirmed by FESEM analysis. FESEM micrographs revealed PEDOT particles attached on the surface of the fibres to different extents based on the coating concentration, with some inter-fibre pores partially occluded. Analysis of the fibre diameter size distribution (**Figure 4.4**) demonstrated some differences after functionalisation compared to neat silk. The average fibre diameter size remained ~0.5 μm for all samples.

Table 4.1 Estimated mass uptake of PEDOT–PSS and DMSO-treated PEDOT–PSS on the scaffolds after functionalisation

	Scaffold type	**Mass uptake (mg)**
PEDOT-PSS	SF-0.5P	0.54 (±0.12)
	SF-1P	0.63 (±0.17)
	SF-3P	0.84 (±0.16)
	SF-9P	1.00 (±0.03)
	SF-13P	1.20 (±0.08)
DMSO-treated PEDOT-PSS	SF-0.5PD	0.18 (±0.03)
	SF-1PD	0.46 (±0.07)
	SF-3PD	0.50 (±0.3)
	SF-9PD	0.80 (±0.14)
	SF-13PD	0.97 (±0.30)

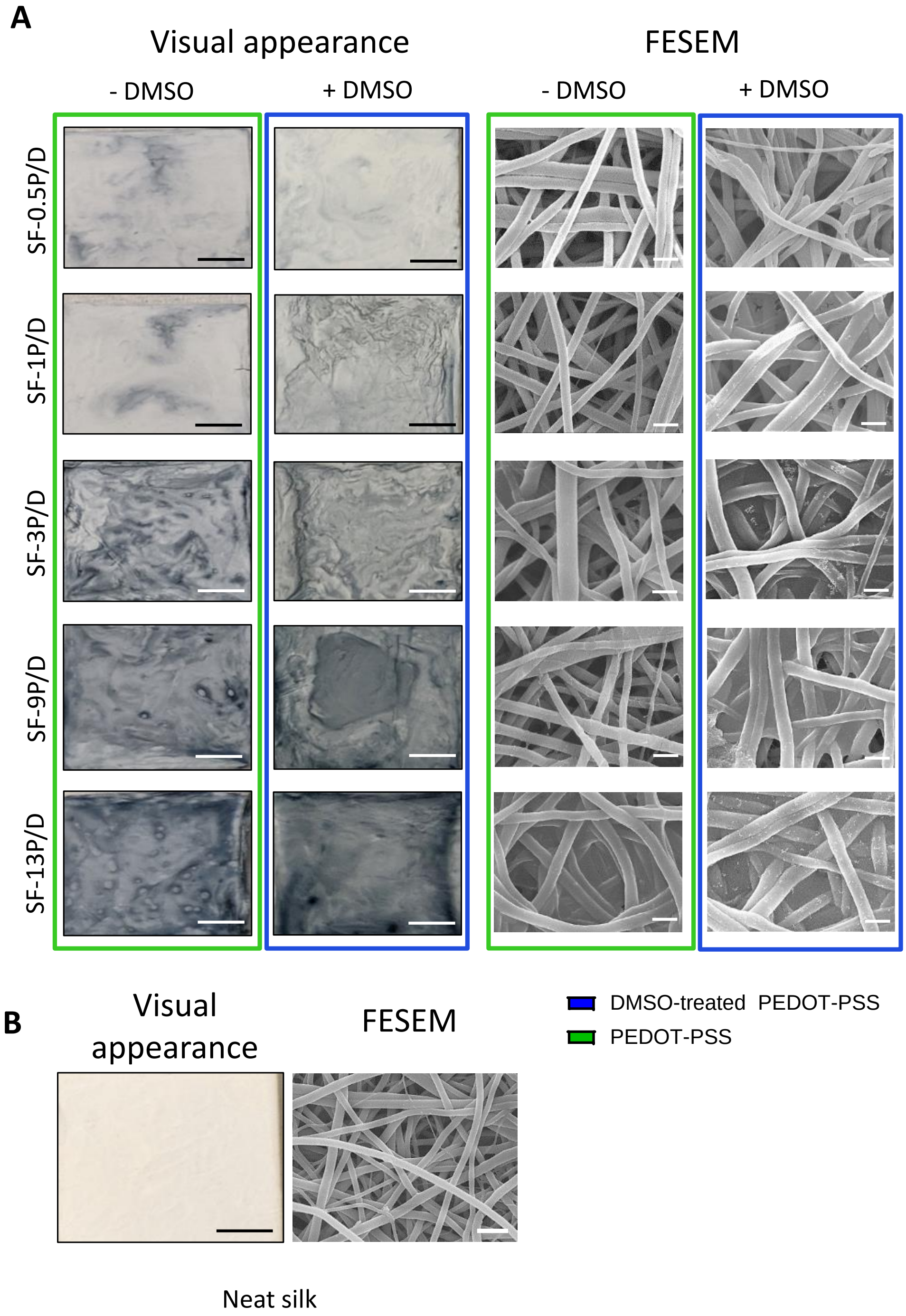

Figure 4.3 Effect of PEDOT–PSS and DMSO-treated PEDOT–PSS conjugation on scaffold microstructures. (**A**) Representative visual appearance and FESEM micrographs of the different scaffolds after functionalization at increasing concentration; scale bars at 3 mm and 900 nm, respectively. (**B**) Representative visual appearance and FESEM micrograph of neat silk; scale bars at 3 mm and 2 μm, respectively.

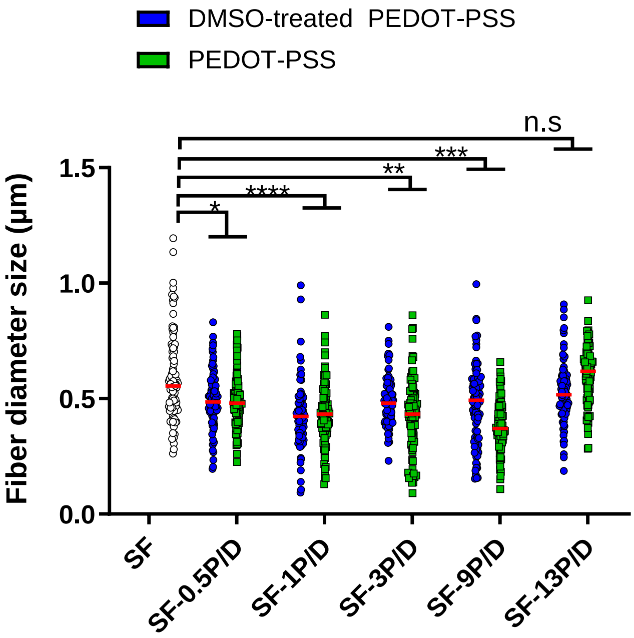

Figure 4.4 Fibre diameter size distributions of the various scaffolds. Differences between the experimental groups were analysed by Kruskal-Wallis with Dunn's test. n.s non-significant, *p<0.05, **p<0.01, ***p<0.001, ****p<0.0001.

The relative percentage of sulfur (S), representing PEDOT and PSS, is shown in **Figure 4.5A** in a concentrated-dependent manner at increasing coating concentration after functionalisation. As expected, higher relative S percentage is observed at the surface rather than at the bulk-like of the scaffolds. A decrease in the relative ratio of PSS to PEDOT both at the surface and bulk-like of the scaffolds was also observed (**Figure 4.5B)** after DMSO-treated PEDOT–PSS functionalisation. This is likely to be due to the accepted conclusion that DMSO treatment of PEDOT–PSS removes excess of anionic PSS chains, in line with previous studies on films [455,456]. We show this is also true for the fibrous functionalised scaffolds investigated here.

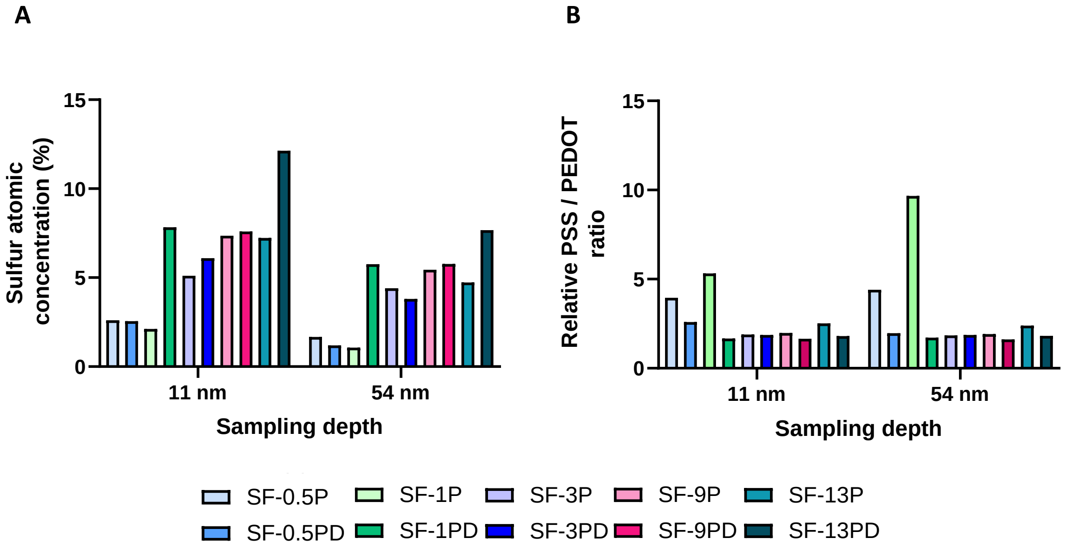

Figure 4.5 HAXPES of PEDOT–PSS and DMSO-treated PEDOT–PSS functionalised scaffolds at the surface (S 2p ~11 nm) and bulk-like (S 1s ~54 nm). (**A**) Percentage of sulfur. (**B**) PSS to PEDOT ratio.

The ability of the scaffolds to adsorb and retain BSA, as a model protein, was investigated to assess the functionalised scaffolds. Cell-material interactions can be affected by surface chemistry and the physical features of the substrate onto which cells adhere [457]. For instance, differences in surface roughness have been shown to modulate cell adhesion, proliferation and differentiation of a variety of different cell types through surface adsorption of proteins [458,459]. The amount of BSA retained on the scaffolds is shown in **Figure 4.6A**. Greater amounts of protein were adsorbed on the functionalised scaffolds, further boosted at increased PEDOT content. Surface roughness (average mean height, Sa) increased after PEDOT functionalisation compared with unmodified silk, with no major changes observed among the various functionalised scaffolds (**Figure 4.6B, Figure 4.7**). Therefore, the greater protein adsorption observed here at increased PEDOT content could have primarily been influenced by alterations in local electrostatic interactions [460,461] and by electrical charges [307] attributed to the endogenous electrical regimes of the conjugated polymer. Indeed, BSA is negatively charged under physiological conditions since its isoelectric point is around 4.7 [462]. If anionic PSS is partially washed away during PEDOT–PSS treatment with DMSO [433], the scaffold's surface will be less negatively charged which will clearly have an effect on the adsorption of proteins and other biomolecules on their surfaces (**Figure 4.6A**).

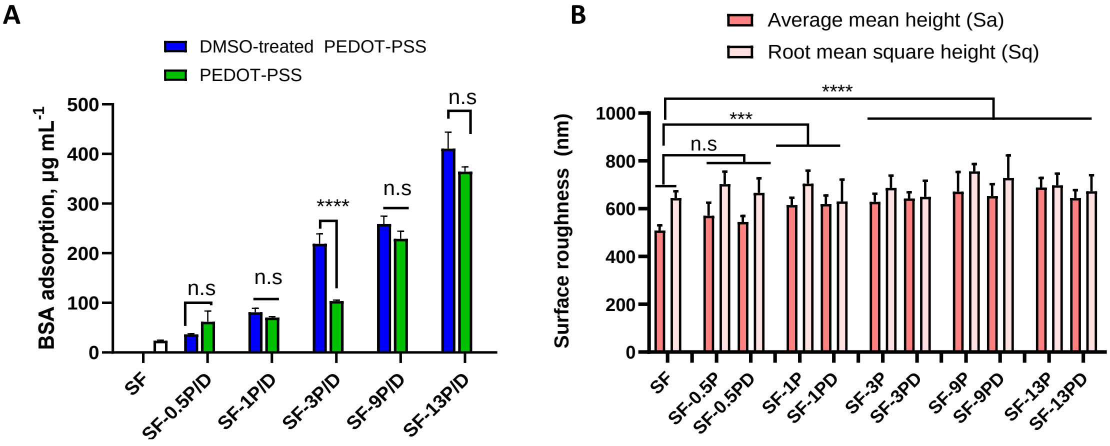

Figure 4.6 Effect of PEDOT–PSS and DMSO-treated PEDOT–PSS on protein adsorption and surface roughness. (**A**) Quantification of BSA adsorption on the various scaffolds (n=3 per type). Differences between the experimental groups were analysed by two-way ANOVA with Tukey's post hoc test. n.s. non-significant, ****p<0.0001. (**B**) Quantitative analysis of surface roughness of the scaffold (n=2 per type). Differences between the experimental groups (average mean height, Sa) were analysed by two-way ANOVA with Tukey's post hoc test compared with neat silk. n.s. non-significant, ***p<0.001, ****p<0.0001.

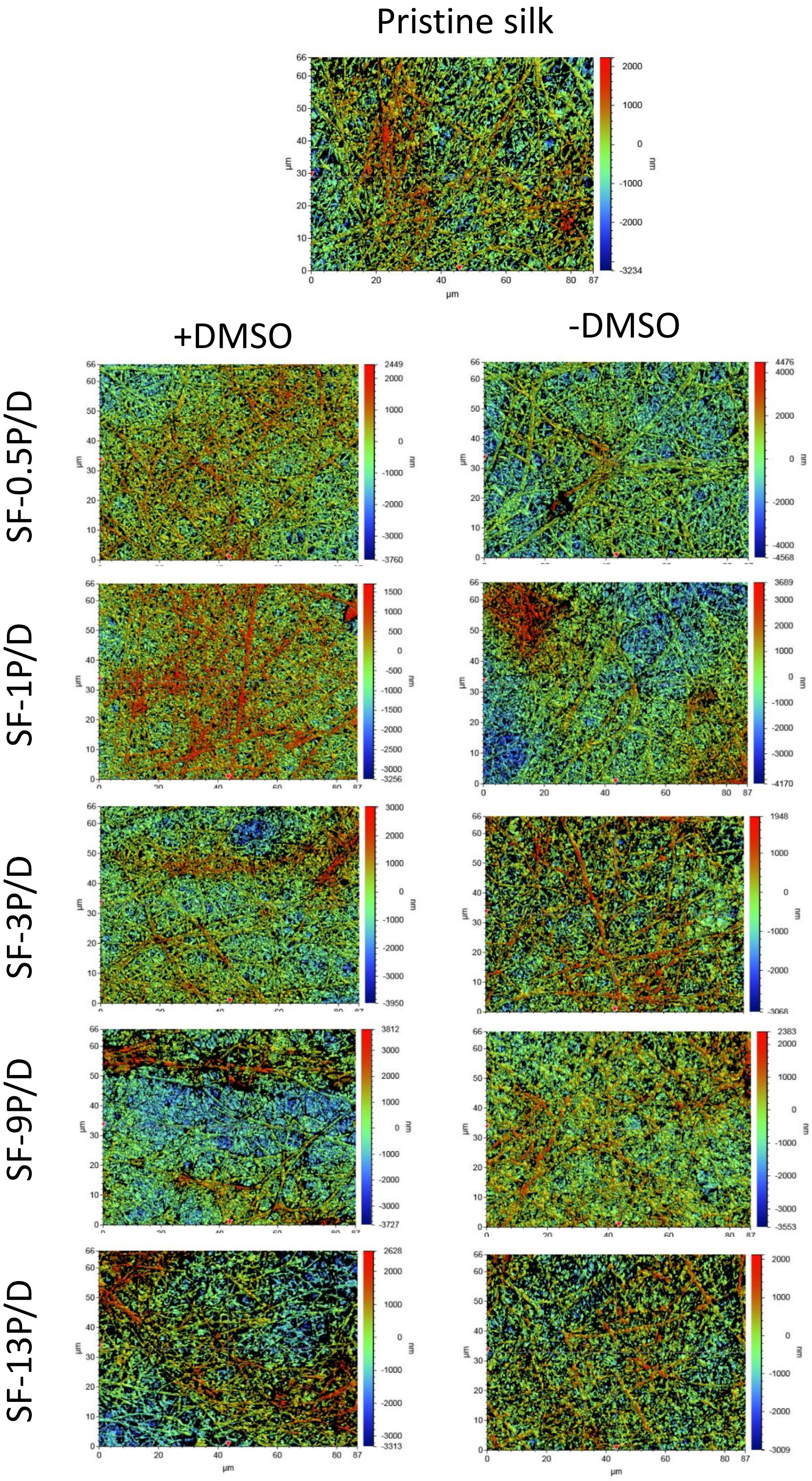

Figure 4.7 Representative optical profilometry micrographs of the surface roughness of PEDOT–PSS and DMSO-treated PEDOT–PSS functionalised silk scaffolds.

Electrical conductivity of the scaffolds was estimated via 4-point probe testing (**Figure 4.8**, **Table 4.2**). Neat silk can be considered as a low proton/ion conductor [410]; here the scaffolds became highly conductive with the incorporation of PEDOT–PSS. Conductance could be tuned in the dry state in the range $\times 10^{-5}$ to 10^{-1} S cm^{-1} by varying the coating concentration used for functionalisation (**Figure 4.8A**). Treatment of PEDOT–PSS with DMSO resulted in a substantial enhancement of the conductivity of the scaffolds compared with their PEDOT–PSS counterparts. Indeed, several methods have been investigated to boost PEDOT–PSS conductivity [453,463,464]. Solvent treatment with DMSO is widely used amongst other polar solvents such as methanol, dimethylformamide, tetrahydrofuran or ethylene glycol [463]. It has been postulated that the PSS chains are partially washed away during solvent treatment [464], with the structure of PEDOT changing from benzoid (i.e. coil conformation) to quinoid (i.e. linear-extended coil conformation) (**Scheme 4.1B**) [453]. Disentangled PEDOT–PSS leads to alterations in orbital overlap and more efficient interchain packing, inducing the formation of π-stack lamellas and creating a better pathway for charge transport, thereby boosting conductivity [433]. Conductivity of the scaffolds was also characterised in a wet state after hydration overnight (**Figure 4.8B**). Some sample groups led to a small decrease compared with their dry-state counterparts (**Table 4.2**). In this regard, some authors have observed an increase in conductivity when scaffolds have been saturated in culture media or other aqueous environments [376], in contrast to others who have observed a substantial decrease [273,304]. This demonstrates the difficulty to decouple the electronic contribution of conductive moieties with respect to the ionic contribution of buffered electrolytes.

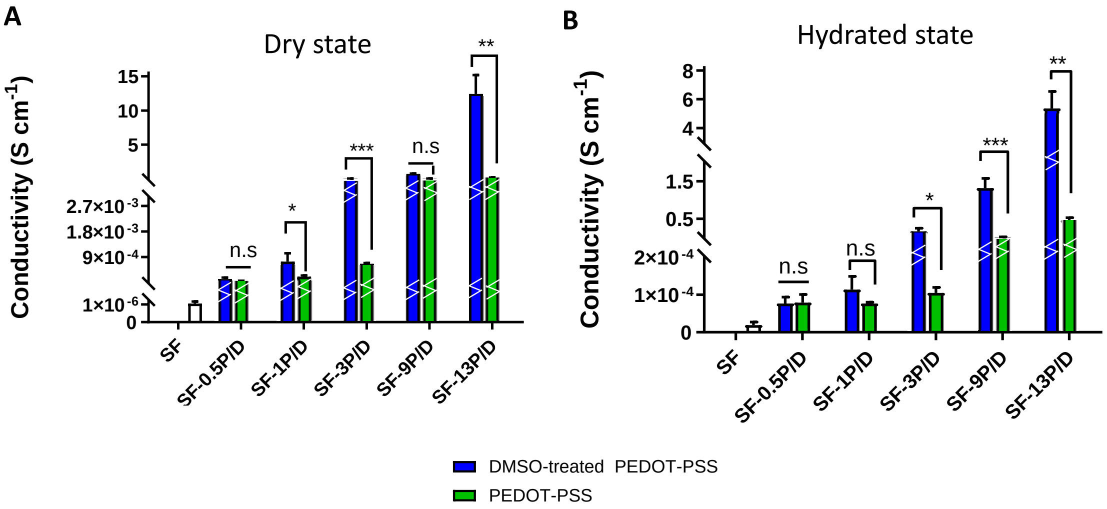

Figure 4.8 Effect of PEDOT–PSS and DMSO-treated PEDOT–PSS on conductivity. (**A-B**) Estimated electroconductivity of the scaffolds (n=4 per type) in the dry and hydrated states. Differences between the experimental groups were analysed by two-way ANOVA with Tukey's post hoc test. n.s. non-significant, *p<0.05, **p<0.01, ***p<0.001, ****p<0.0001. Zigzag in white indicates discontinued bar chart portion.

Table 4.2 Estimated electrical conductivity of the scaffolds (n=4 per type) after functionalisation with PEDOT–PSS and DMSO-treated PEDOT–PSS, in the dry state and in the hydrated state.

	Scaffold type	**Dry state (S cm^{-1})**	**Hydrated state (S cm^{-1})**
	SF	1×10^{-6} ($\pm$ 1×10^{-7})	1.8×10^{-5} ($\pm$ 8.0×10^{-6})
PEDOT-PSS	SF-0.5P	6×10^{-5} ($\pm$ 6×10^{-6})	7.8×10^{-5} ($\pm$ 2.0×10^{-6})
	SF-1P	2×10^{-4} ($\pm$ 5×10^{-5})	7.6×10^{-5} ($\pm$ 4.0×10^{-6})
	SF-3P	7×10^{-4} ($\pm$ 2×10^{-5})	1×10^{-4} ($\pm$ 1×10^{-5})
	SF-9P	0.30 (± 0.01)	0.010 (± 0.002)
	SF-13P	0.20 (± 0.01)	0.50 (± 0.06)
DMSO-treated PEDOT-PSS	SF-0.5PD	1×10^{-4} ($\pm$ 5×10^{-5})	7.5×10^{-5} ($\pm$ 2.0×10^{-6})
	SF-1PD	7×10^{-4} ($\pm$ 3×10^{-4})	1×10^{-4} ($\pm$ 3×10^{-5})
	SF-3PD	0.040 (± 0.007)	0.20 (± 0.08)
	SF-9PD	0.70 (± 0.05)	1.3 (± 0.3)
	SF-13PD	12.1 (± 2.7)	5.4 (± 1.2)

FTIR-ATR was performed (**Figure 4.9A**) to explore the change of the surface chemical groups on the scaffolds. The typical fingerprint regions of silk were observed in the spectrum of the neat sample, with peaks corresponding to the amide I (1700-1600 cm^{-1}), II (1600-1500 cm^{-1}) and III (1300-1200 cm^{-1}) bands [465]. The bands corresponding to the amide I and II regions slightly shifted after coating with PEDOT–PSS or DMSO-treated PEDOT–PSS. These changes suggest that PEDOT-PSS interacts (e.g. electrostatic interactions and hydrogen bond interactions) with the silk (notable as sulfate anions [like those displayed on PSS] are kosmotropic anions that encourage “salting out” of protein chains from solution). The characteristic vibration frequencies corresponding to β-sheets were present in all functionalised scaffolds, indicating the retention of the secondary structure of silk after the chemical modification process with PEDOT-PSS. The intensity of the silk peaks gradually decreased with increasing concentration of PEDOT–PSS on the scaffolds. The peak corresponding to the amide III region (1300-1200 cm^{-1}) was not fully observed in the spectra at high coating concentrations. Some distinguishing peaks previously reported typical of PEDOT–PSS [318] could be observed in the spectra: peaks at around 1005 (SO_3 symmetric stretching vibrations) [466], 976 and 835 cm^{-1} (C–S–C deformation vibration). The double peaks observed at around 2920 and 2850 cm^{-1} correspond to C–H stretching vibrations [467]. FTIR-ATR spectra of PEDOT–PSS and DMSO-treated PEDOT–PSS are shown in **Figure 4.9B**.

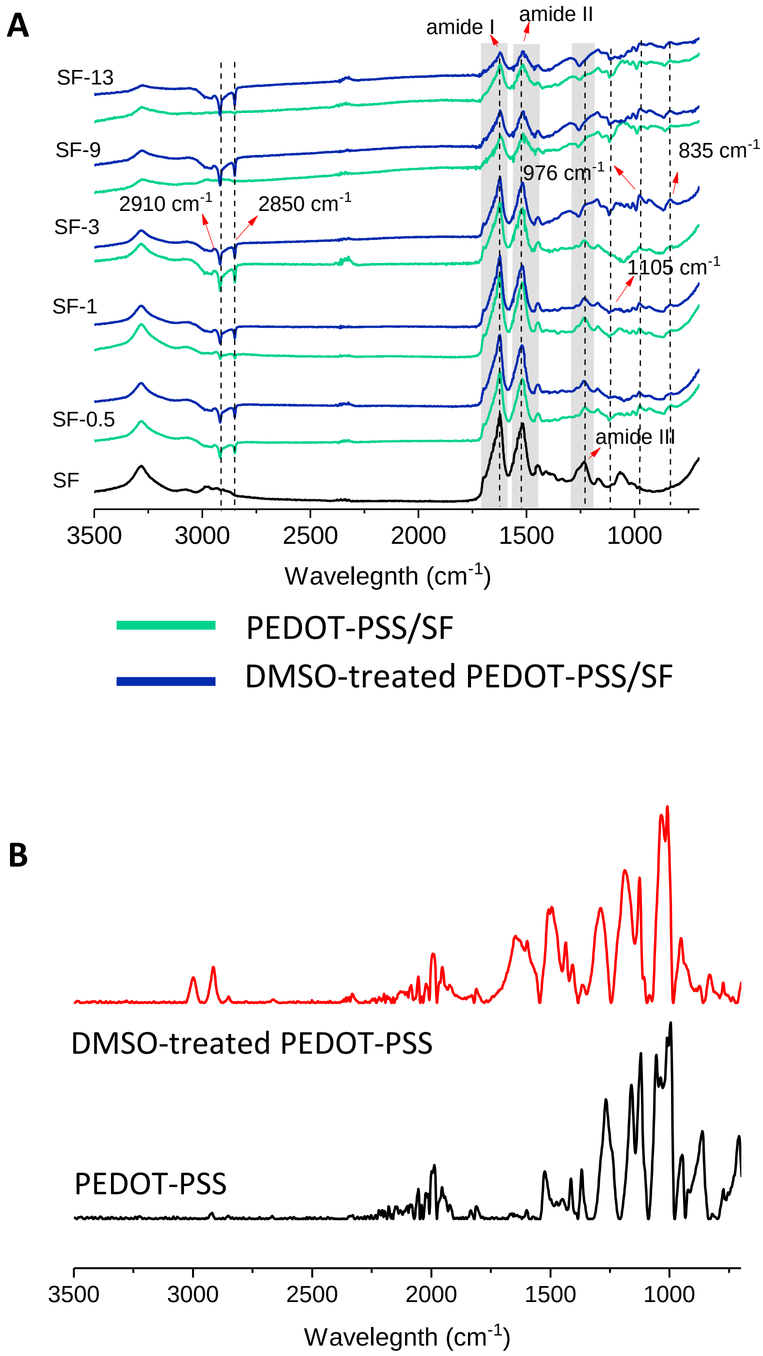

Figure 4.9 (**A**) Representative FTIR spectrum of the scaffolds after functionalisation with PEDOT–PSS and DMSO-treated PEDOT–PSS, showing the typical fingerprint of SF along with some characteristic peaks attributed to PEDOT–PSS. (**B**) Representative FTIR-ATR spectrum of PEDOT–PSS and DMSO-treated PEDOT–PSS.

Here we demonstrate that systematic variations in the formulation of PEDOT–PSS result in silk-based scaffolds with highly tuneable electroconductivity. These scaffolds may support the electrical pathways of nerve tissue by aiding in the propagation of electrical signals among neurons. Nerve tissues are electrically sensitive, and neurons rely on electrical stimuli for maintaining tissue homeostasis and function. Electroconductive scaffolds hold great potential for nerve tissue engineering since they can promote the propagation of electrical impulses. The ability of the functionalised scaffolds (PEDOT–PSS and DMSO-treated PEDOT–PSS; coating concentrations at 0.5 mg mL^{-1} – low, 3 mg mL^{-1} – medium, and 13 mg mL^{-1} – high) to support neuronal cell growth and differentiation was evaluated with NG108-15 neuronal-like cells.

Presence of low to high contents of PEDOT–PSS or DMSO-treated PEDOT–PSS on the scaffolds did not have major cytotoxic effects over the cell culture period compared with glass coverslip or unmodified silk (**Figure 4.10, Figure 4.11**). Representative confocal micrographs of viable and non-viable cells laden on the various scaffolds are shown in **Figure 4.10**, indicating increased cell coverage in a time-dependent manner. After 7 days of culture, cells on the scaffolds remained highly viable for every group tested (**Figure 4.11**).

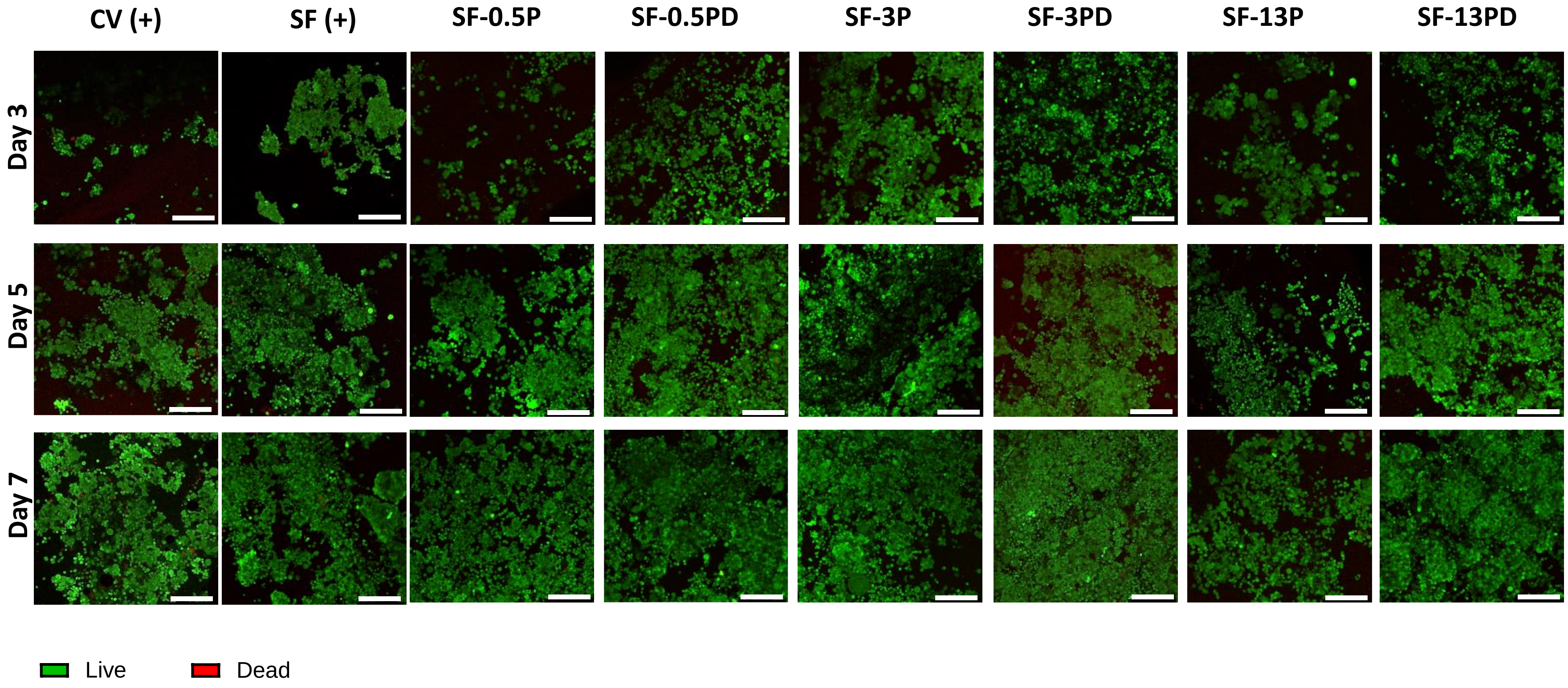

Figure 4.10 Cellular viability of NG108-15 cells on PEDOT–PSS and DMSO-treated PEDOT–PSS functionalised scaffolds (low, medium, and high coating concentration). Representative confocal micrographs showing cellular viability over 7 days of culture: viable cells are labelled with calcein AM (green) and dead cells are labelled with ethidium homodimer-1 (red); scale bar at 250 μm. Coverslip (CV) and silk fibroin (SF) were used as controls.

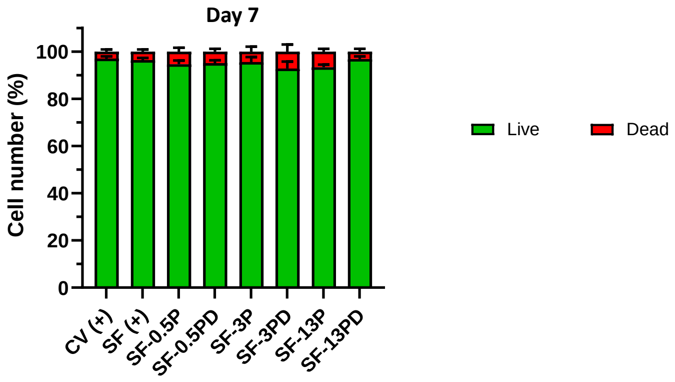

Figure 4.11 Semi-quantitative analysis of the percentage of viable and non-viable cells after 7 days on PEDOT–PSS and DMSO-treated PEDOT–PSS functionalised scaffolds (n=2 per type). Coverslip (CV) and silk fibroin (SF) were used as controls.

The metabolic activity of NG108-15 cells seeded on the scaffolds **(Figure 4.12A)** is shown as a function of the dsDNA concentration in **Figure 4.12B**, giving an indication of the metabolic activity of the culture relative to the number of cells present on it. Cells remained metabolically active on all scaffold groups, with their profile increasing steadily over time. Cells were metabolically more active on the functionalised scaffolds compared with unmodified silk. No significant differences in terms of metabolic activity were observed between the DMSO-treated PEDOT–PSS and PEDOT–PSS counterparts; by day 7 cells were metabolically more active on scaffolds functionalised at higher coating concentration (**Figure 4.12B**). Cellular proliferation, on the other hand, exhibited a different trend (**Figure 4.12C-D**), demonstrating greater cellular response on the functionalised scaffolds at the DMSO-treated PEDOT–PSS interface as opposed to PEDOT–PSS. Scaffolds functionalised with the high coating concentration exhibited lower proliferation after 7 days of culture. This indicates that while low to medium contents of PEDOT could be beneficial to NG108-15 cells, too much coating may hinder their proliferation.

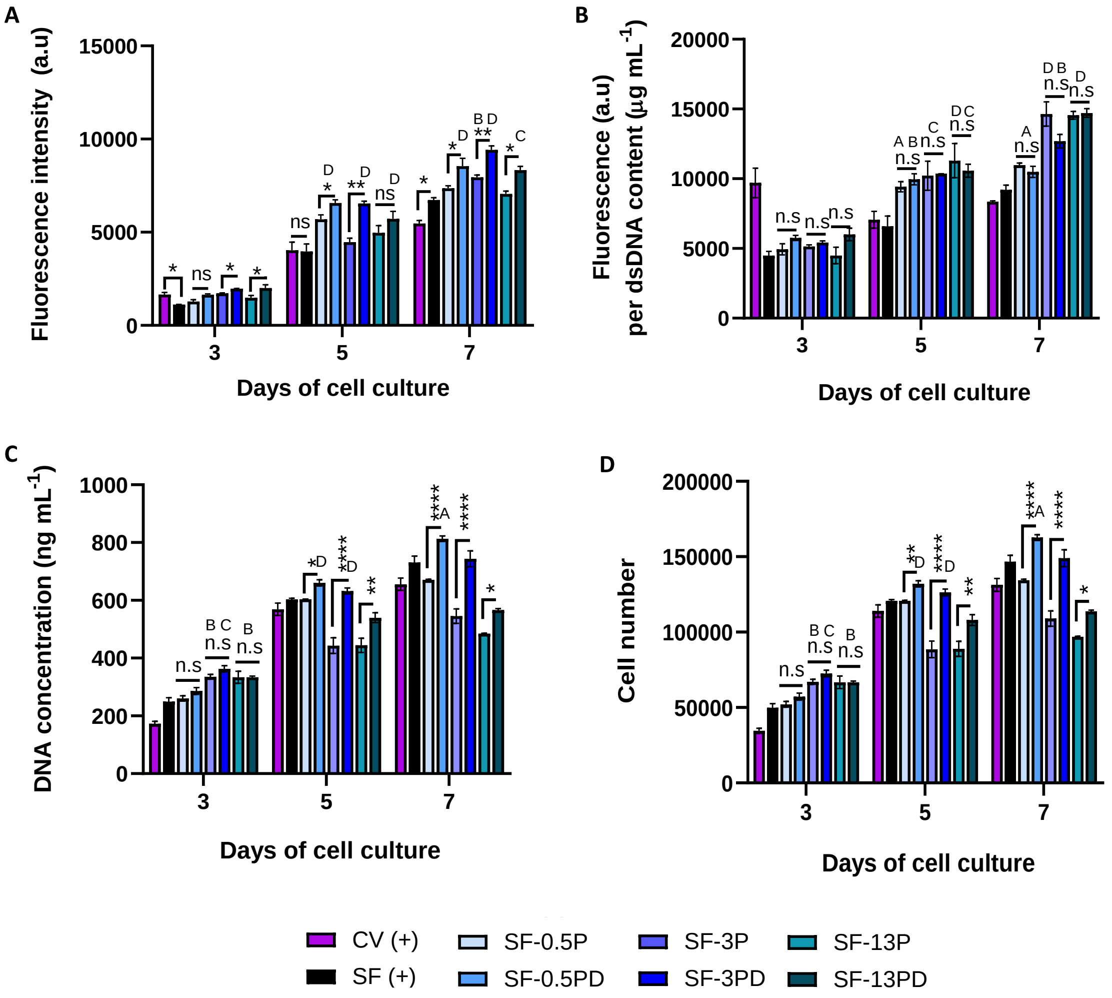

Figure 4.12 Cellular metabolic activity and proliferation of NG108-15 cells on PEDOT–PSS and DMSO-treated PEDOT–PSS functionalised scaffolds (low, medium, and high coating concentration) over 7 days of culture. (**A**) Metabolic activity (n=3 scaffolds per type). (**B**) Metabolic activity relative to dsDNA content (n=3 scaffolds per type). (**C**) Total dsDNA content (n=3 scaffolds per type). (**D**) Cellular proliferation; estimated number of cells (n=3 scaffolds per type). Differences between the experimental groups were analysed by two-way ANOVA with Tukey's post hoc test. n.s. non-significant, *p<0.05, **p<0.01, ****p<0.0001; (with respect to SF: $^{A}p<0.05$; $^{B}p<0.01$; $^{C}p<0.001$; $^{D}p<0.0001$). Coverslip (CV) and silk fibroin (SF) were used as controls.

The outgrowth of neurites and axonal elongation is under complex control and is essential for building functional neural circuits during regeneration, vital for the function of neuronal cells. Differentiation of NG108-15 cells on the scaffolds was morphologically assessed after 5 days of culture with a marker for ß-tubulin III (**Figure 4.13A**). Differentiation potential was semi-quantitatively measured in terms of neurite length (**Figure 4.13B**). Neuronal cells exhibited neurites on all scaffold groups; while some differences were observed among the different samples in terms of neurite extension distribution, only the SF-3PD scaffold showed significantly ($p<0.05$) greater average neurite extension compared with unmodified silk.

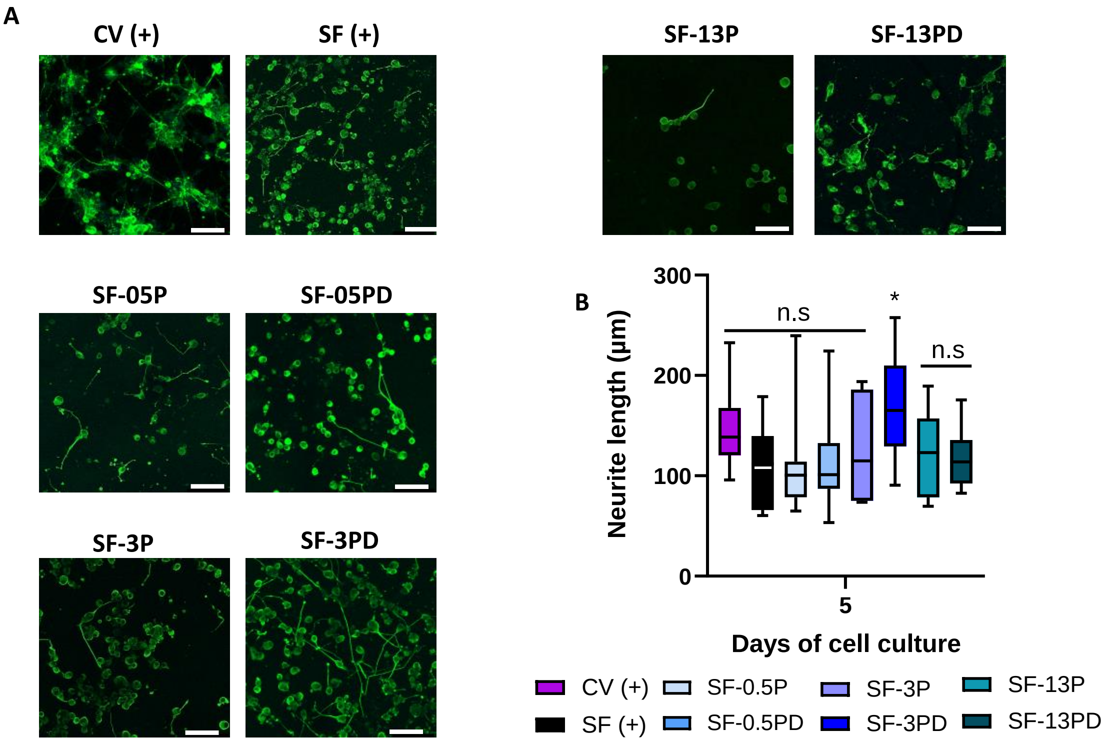

Figure 4.13 (**A**) Representative confocal micrographs showing differentiated NG108-15 cells on PEDOT–PSS and DMSO-treated PEDOT–PSS functionalised scaffolds (low, medium, and high coating concentration) after 5 days of culture, immunolabelled with ß-tubulin III (green) as a marker of neuronal differentiation and cell nuclei counterstained with DAPI (blue); scale bar at 100 µm. (**B**) Box-and-whisker plot showing neurite extension distribution on each scaffold. Differences between the experimental groups (with respect to SF) were analysed by one-way ANOVA with Tukey's post hoc test; n.s non-significant; *$p<0.05$. Coverslip (CV) and silk fibroin (SF) were used as controls.

The increased cellular responses observed after functionalisation may be explained by the presence of PEDOT. Conjugated polymers can interact with and release ions into solution [377]. This in turn may affect ion flux and ECM potential fluctuations, endowing the scaffold with enhanced biological activity mediated by cell-surface interactions [468]. Furthermore, the inherent electrical conductivity of the substrates and greater protein adsorption observed at increased coating concentration may have played key roles in modulating the cellular response. Previous studies have reported better neuronal PC12 and neuronal stem cell adhesion and proliferation on freeze-dried chitosan/gelatin scaffolds after PEDOT incorporation, along with enhanced differentiation [377,431]. In a subsequent study, cell adhesion efficiency of PC12 neurons and gene expression levels linked to synapse growth were also improved at increased hyaluronic acid-PEDOT content on similarly developed chitosan/gelatin scaffolds [469]. As previously reviewed [273], some authors have attributed these improvements to the electrostatic interactions between the electroconductive moieties and the negatively charged cell membrane [308], or to changes in the local electrostatic charge of the scaffold [307]. While the incorporation of an electroconductive enhancer during scaffold synthesis may contribute to increased surface roughness (known to affect protein adsorption and eventual changes in the cellular response such as cell adhesion), differences here were no significant among the different functionalised samples. Therefore, changes in the biological response of the scaffolds may be attributed to the synergic contribution of the endogenous electrical regimen conferred by the presence of PEDOT–PSS and further enhanced by DMSO-treated PEDOT–PSS, enhanced protein adsorption of the substrates, and the more negatively charged (e.g. PEDOT–PSS) or less negatively charged surface (e.g. DMSO-treated PEDOT–PSS) at the cell-material interface. Indeed, the cell membrane is negatively charged and a possible explanation for the decrease in proliferation observed on the PEDOT–PSS counterparts, as opposed to functionalisation with DMSO-treated PEDOT–PSS, is the presence of more anionic PSS chains [430], as confirmed by HAXPES (**Figure 4.5**). The lower cellular proliferation observed for the high coating concentration may have been due to reduced inter-fibre porosity (**Figure 4.3A**), which could have affected initial cell attachment. The presence of DMSO, even in very low concentrations, is known to inhibit neuronal cell activity [470–472]. The fact that the cellular response was not impaired on the DMSO-treated PEDOT–PSS functionalised scaffolds, but rather enhanced over their PEDOT–PSS counterparts, confirms that it is unlikely that there is any presence of DMSO remaining and leaking out into the culture after the preparation steps for cell culture.

Nevertheless, how intracellular cell signalling pathways are specifically modulated to control neuronal cell activity remains to be explored. Integrins and other proteins of the native ECM may redistribute and cluster in response to the conductive polymer, initiating signalling transduction cascades that alter cell behaviour [473]. On the other hand, intracellular ion levels such as Ca^{2+} seem to play an important role in regulating neuronal cell behaviour [474–476]. In that respect, it has been postulated that conductive substrates may increase intracellular ion levels in neuronal cells [361,431]. Therefore, the contribution of a highly conductive substrate may have activated specific voltage-ion gated channels of the neuronal cells, leading to the differing cell responses observed. Whether it is conductivity or a cascade of secondary effects, or more likely a synergy of them all, the study presented here represents an important step forward in the benefits of using conductive substrates for regenerating electrically sensitive tissues, and increases our knowledge about the biological response of electrically excitable cells on PEDOT–PSS assembled silk interfaces. The conductivity of native tissue has been reported $\geq 10^{-4}$ S cm^{-1} [411], and therefore the SF-3PD scaffold could be a suitable candidate to be further explored for nerve tissue engineering applications.

4.4 Conclusions

Electroconductive fibrous scaffolds were produced by electrospinning, synthesised from naturally occurring SF protein and functionalised with PEDOT–PSS or DMSO-treated PEDOT–PSS. These functionalised assembled silk-based scaffolds provided an electroconductive environment with enhanced morphological and electrical properties, readily tuneable by varying the concentration of PEDOT–PSS and further boosted by DMSO treatment. No significant differences in surface roughness were observed among the different counterparts, but protein adsorption capacity substantially increased in a concentrated-dependent way. The ability of these electroconductive silk scaffolds to modulate growth and differentiation of NG108-15 cells was evaluated *in vitro*. Cells remained viable in all scaffolds tested. Metabolic activity was enhanced at increased coating concentration compared with unmodified silk, but no differences were observed between DMSO-treated PEDOT–PSS and PEDOT–PSS counterparts. DMSO-treated PEDOT–PSS functionalisation led to enhanced cellular proliferation compared with PEDOT–PSS. Among all functionalised scaffolds, only the SF-3PD group showed statistically greater neurite outgrowth compared with unmodified silk. Overall, these electroconductive scaffolds show promise to potentially be used as platforms for peripheral nerve regeneration, and further investigation should be warranted. The electrical conductivity of these scaffolds in its relation to external ES could be explored in the future to further promote neurite outgrowth.

Blank page

Chapter 5

Neuronal cell growth and differentiation on biosynthetic reflectin functionalized silk fibrous scaffolds

Adrián Magaz[1,2], **Emmanuel Wolde-Michael**[3], **Derren J. Heyes**[3], **Eriko Takano**[3], **Nigel S. Scrutton**[3], **Xu Li**[2,4], **Julie E. Gough**[1], **Jonny J. Blaker**[1,5]*

[1]Department of Materials and the Henry Royce Institute, The University of Manchester, Manchester, M13 9PL, United Kingdom

[2]Institute of Materials Research and Engineering (IMRE), Agency for Science Technology and Research (A*STAR), 138634, Singapore

[3]EPSRC/BBSRC Future Biomanufacturing Research Hub, Manchester Institute of Biotechnology, Manchester Synthetic Biology Research Centre SYNBIOCHEM, Department of Chemistry, The University of Manchester, Manchester, M1 7DN, United Kingdom

[4]Department of Chemistry, National University of Singapore, 117543, Singapore

[5]Department of Biomaterials, Institute of Clinical Dentistry, University of Oslo, Oslo, 0317, Norway

*Corresponding author

Author contribution statement

EWM synthesised and characterised the reflectin isoforms with help from DJH. AM fabricated the scaffolds, functionalized them, and characterized the substrates in terms of their physico-chemical and biological properties. Data analysis, manuscript and figure panels were compiled by AM. ET, NSS, XL, JEG and JJB supervised the study. All authors contributed to experimental design, manuscript structuring, drafting and editing. An overview of the tasks carried out by the main author are provided below:

- Literature review
    - Reflectin as an active material
    - Proton conductors in nature
    - Recombinant technologies for the production of biological materials
    - Effects of motif frequency and tandem repeat sequence
    - Peptide functionalisation techniques
- Study design following advice from the supervisory team
    - Selection of materials and preparation techniques
    - Selection of cell line and experimental points
    - Characterisation methods
- Experimental work
    - Optimisation methods for the immobilisation of biosynthetic reflectin isoforms on electrospun silk-based scaffolds
    - Characterisation of the scaffolds in terms of fibre morphology, chemical structure, conductivity and biological response
- Manuscript preparation
    - Writing initial draft
    - Revision following comments from the supervisory team

Overview

Reflectins are naturally occurring proteins central to cephalopods' neuronal development. Reflectins exhibit intrinsic conductive properties and have recently been reported among the highest proton conductors in nature. The human body uses ion and proton currents to conduct electricity, and so it is important to explore other means of improving conduction to promote the nerve tissue repair and regeneration process. It was hypothesised that SF scaffolds produced by electrospinning could be functionalised with recombinant reflectin to exhibit enhanced conductance and promote the biological response. Reflectin derivatives with different motif frequency were recombinantly synthesised and functionalised onto silk by physical adsorption or chemisorption. The produced scaffolds were physico-chemically characterised and biologically assessed with neuronal-like cells.

In line with the hypothesis, recombinant reflectin-immobilized silk scaffolds enhanced proton/ion conduction at increased reflectin motif frequency. Chemisorption was a much more efficient route to bind reflectin, which provided a supportive microenvironment with bioactive molecule incorporation for enhanced neuronal proliferation and neurite outgrowth support.

Abstract

Reflectins are proteins central to cephalopod structural colouration, and have been widely investigated for their self-assembling and optical properties as camouflage features. More recently, reflectins have been found to play a key role in cephalopods' neuronal development, and they have been reported among the highest proton conductors in nature. The nervous tissue is electrically sensitive, and the human body uses ion and proton currents to conduct electricity. Furthermore, many of the major components of the native ECM exist as fibres that mediate cell behaviour. In the present study, micro/nano- fibrous silk substrates were decorated through physical or chemical adsorption of recombinant reflectin A2 isoforms of different motif frequency, and they were investigated as a potential platform for neural tissue engineering. Chemisorption with native reflectin enhanced proton/ion conduction to the greatest extent among the different isoforms, promoted enhanced metabolic activity and proliferation, and supported differentiation of analogue neuronal NG108-15 cells.

Keywords: Reflectin; silk fibroin; electrospinning; nerve tissue engineering

5.1 Introduction

Reflectins are a unique family of self-assembling proteins native to cephalopods (e.g. squid, octopus, and cuttlefish), first detected in the Hawaiian bobtail squid *Euprymna scolopes* [477]. These proteins play a crucial role in cephalopod structural colouration to closely mimic their surroundings as an adaptive camouflage feature [478]. This ability stems from a mechanism by which a neurotransmitter, acetylcholine (Ach), sets in motion a cascade of events resulting in the phosphorylation of reflectin, reducing their net charge and triggering reversible hierarchical assembly into a more condensed structure, leading to a change in colouration [479–482]. For this reason, reflectins have been traditionally explored for their optical properties [232,477,481–483]. Reflectins have an unusual amino acid composition rich in tyrosine, methionine, arginine and tryptophan. They usually exist in a block-copolymeric structure consisting of positively charged polyelectrolyte linker regions interspersed with highly conserved polyampholyte repeating motifs $(M/F\text{-}D\text{-}X_5)(M\text{-}D\text{-}X_5)_n(M\text{-}D\text{-}X_{3\text{-}4})$ [484] (**Scheme 5.1**). The polyelectrolytic linkers are particularly rich in aromatic and arginine residues, almost entirely devoid of negatively charged residues. The repeating motifs exist in two forms, one highly conserved at the N-terminal (RMn), and another distributed throughout the rest of the protein (RM). These repeating motifs are particularly rich in aromatic and methionine residues, the frequency of which are thought to drive reflectin's properties among different isoforms [477], and the precise relationship between charge neutralisation and reflectin assembly size enable tight photonic tuning [485].

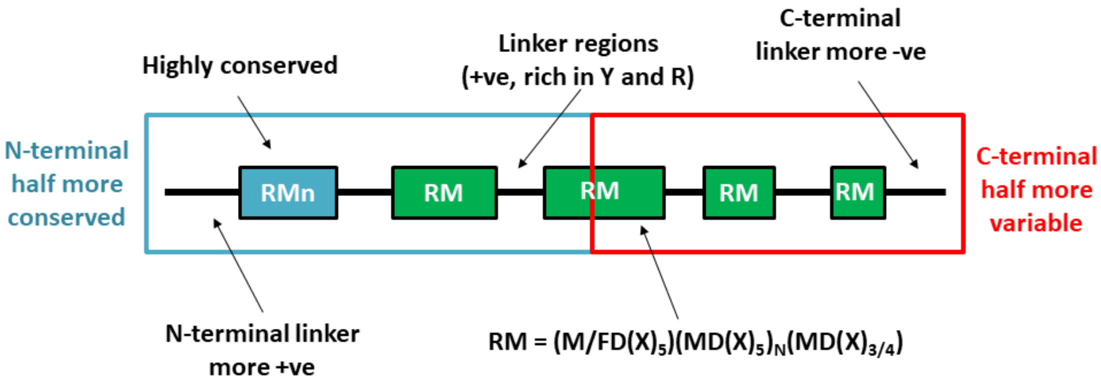

Scheme 5.1 Schematic illustration of the general structure of reflectin: N-terminal region (blue) with highly conserved repeating reflectin motif, reflectin motif distributed throughout the rest of the protein (green), C-terminal region (red). M, methionine; F, phenylalanine; D, aspartic acid; Y, tyrosine; R, arginine; X, variable amino acid

Recently, reflectins have been implicated in some of the major steps of cephalopods' neuronal development, specifically when brain maturation and growth occurs [233,486]. Furthermore, a number of anatomical and functional similarities have been found between the nervous systems of cephalopods and vertebrates [487,488]. These findings have led to investigating reflectin for tissue engineering applications of the nervous system [234,235]. In this regard, bulk films of reflectin have been demonstrated to be effective substrates for the adhesion, proliferation, and differentiation *in vitro* of relatively difficult-to-culture human and murine neural stem/progenitor cells [234,235]. The nerve tissue is electrically sensitive, and electrical regimes play a crucial role in the repair and regeneration process. While many research groups have explored the use of electroconductive/active materials, where electrons and ions are the main charge carriers, the human body uses ion and proton currents to conduct electricity [273]. Reflectin proteins exhibit intrinsic conductivity [489] and stand out among the highest proton conductors reported in nature [334,409,490,491], with values of $\sim 2\times10^{-4}$ S cm^{-1} at body temperature and reaching up to $\sim 3\times10^{-3}$ S cm^{-1} at much higher temperatures [334]. Consequently, reflectins have an untapped potential to be used as active materials for neural tissue engineering.

Mimicking the fibrillary topography of the native tissue is also important to mediate cellular responses such as attachment, migration, growth, proliferation and differentiation [435,436]. To this regard, fibrous meshes of both synthetic and natural polymers have been tested as lumen modifications of NGCs as a way to recapitulate more components of the biological milieu and guide tissue regeneration. Specifically, polypeptides are preferred over other materials due to their similarity with the ECM of the native tissue, and in many cases, the presence of cell-binding motifs. The fibrous proteins of silk represent a unique and important class of structural proteins found in nature with a wide range of mechanical and functional properties that could be emulated for biomaterials applications. For instance, the manipulation of the genetic sequence of silk through synthetic biology tools [492,493] has provided insights into their protein expression and assembly, with tailorable control of their properties. Silks have been extensively used in nerve tissue engineering [8,362], and are strong candidates due to their unique combination of strength, elasticity, toughness, and slow degradation [363].

Herein, we explore the potential use of recombinant reflectin A2 (*Doryteuthis opalescens*) and its derivatives to functionalise *Bombyx mori* silk scaffolds as a potential platform for neural tissue engineering. Two different routes for functionalisation were explored: physical adsorption and chemisorption. A study of the effects of reflectin functionalisation on proton/ion conduction, along with its preliminary impact on growth and differentiation of NG108-15 neuronal-like cells, was carried out.

5.2 Materials and Methods

5.2.1 Preparation of scaffolds

5.2.1.1 Isolation of silk fibroin and synthesis of regenerated silk

Extraction and purification of SF from *Bombyx mori* silkworm cocoons was carried out as previously described [367], with some modifications. Briefly, cocoons (Wildfibres, UK) were dewormed and degummed in boiling 0.02 M sodium carbonate (Sigma-Aldrich, UK) for 60 min, and the resulting SF was thoroughly washed in DI water and air-dried. The degummed fibres were dissolved (16% w v^{-1}) in 7.9 M lithium bromide (Sigma-Aldrich, UK) at 60°C for 4 h, and the solution centrifuged and dialyzed against DI water over the course of 3 days with regular water changes. The resulting regenerated SF solution was film-cast and stored as stock material.

5.2.1.2 Electrospinning of silk fibroin

A 10% w v^{-1} silk solution in HFIP (Sigma-Aldrich, UK) was synthesised, and fibrous scaffolds were produced by electrospinning, collected onto an electrically ground static collector using the following spinning parameters: flow rate, 0.8 mL h^{-1}; tip-to-collector distance, 10 cm; applied voltage, 15 kV; relative humidity, 25%; needle gauge, 19 G. The scaffolds were annealed by immersion in ethanol, washed thoroughly with DI water, dried between filter paper to prevent curling, and stored in a desiccator until further use.

5.2.1.3 Synthesis, expression and purification of recombinant reflectin

An *E. coli* codon optimised gene coding for wild-type reflectin-like protein A2 from *Doryteuthis opalescens* (NCBI GenBank® KF661516.1) was synthesised and cloned (Life Technologies Inc.) into a bacterial plasmid expression vector (**Scheme 5.2A**). The gene sequence of reflectin A2 is shown in **Scheme 5.2B**. Isoforms with different motif frequency (**Scheme 5.2C**) were designed by truncation: A2(M1), A2(M2), A2(M3) and A2(n), where MX denotes the number of repeat motifs with n = native.

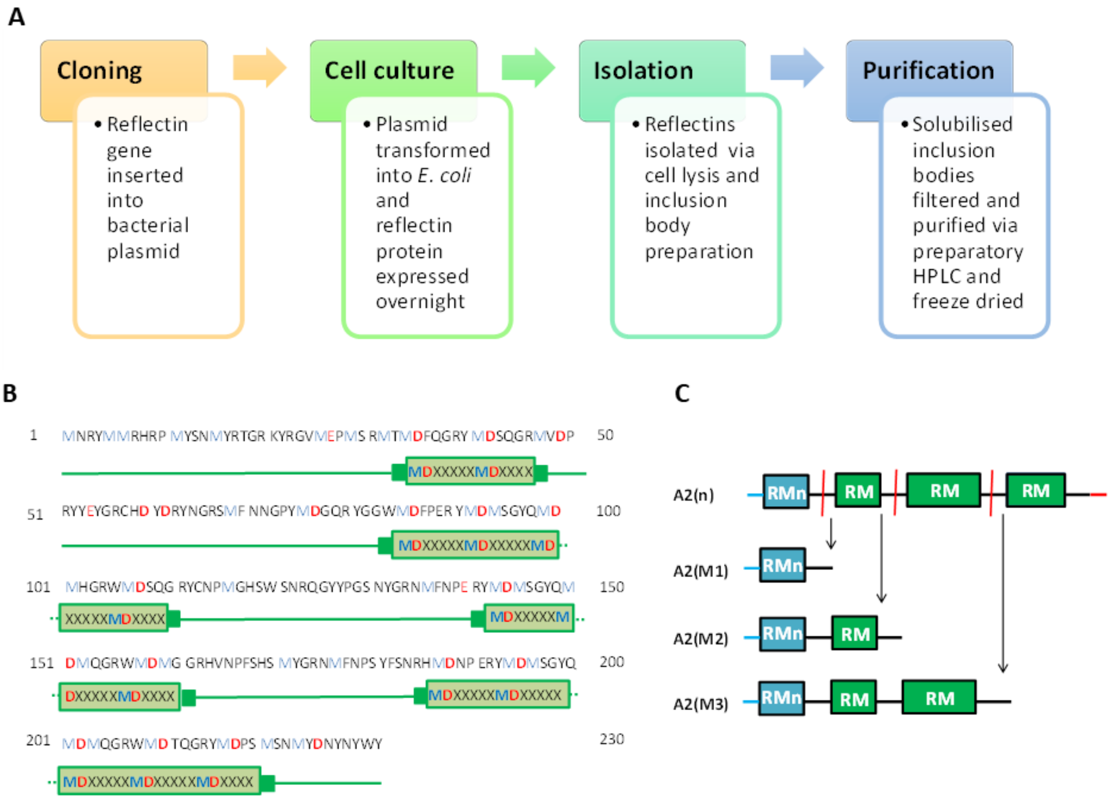

Scheme 5.2 Schematic of the synthesis of recombinant reflectin A2 isoforms. (**A**) Vector cloning, cell transformation, expression and purification of recombinant reflectin. (**B**) Primary sequence and subdomains of reflectin-like A2 protein. The primary sequence of reflectin A2 from *Doryteuthis opalescens* contains four repeating subdomains with the (M/F-D-X_5)(M-D-X_5)$_n$(M-D-$X_{3\text{-}4}$) sequence motif. The subdomains are depicted in green; aspartic and glutamic amino acid residues, along with linker regions are highlighted in red; methionine and phenylalanine residues are highlighted in blue. (**C**) Truncation protocol; native reflectin A2 truncation sites (red); subsequent cloned vectors contain progressively fewer RMs.

A general protocol [334] was used for the expression and purification of wild-type A2 recombinant reflectin, with some modifications as previously described [482]. In brief, pET-M11 (+) expression vectors containing the genes encoding the protein of interest were transformed into BL21(DE3) *E. coli* cells. The proteins were expressed at 37°C using Overnight Express™ Instant Terrific Broth (TB) medium (Sigma-Aldrich, UK) supplemented with 30 μg mL^{-1} kanamycin or 50 μg mL^{-1} ampicillin (Sigma-Aldrich, UK). The proteins were completely insoluble when expressed at 37°C and thus they were sequestered in inclusion bodies which were solubilised in denaturing buffer (6 M guanidine hydrochloride; pH = 8). The samples were filtered, clarified by centrifugation and purified using high-performance liquid chromatography with a gradient that evolved from 95% buffer A : 5% buffer B to 5% buffer A : 95% buffer B (buffer A – 99.9% H_2O and 0.1% trifluoroacetic acid (TFA); buffer B – 99.9% acetonitrile, 0.1% TFA). The pure reflectin was then pooled, flash-frozen in liquid nitrogen, and lyophilised. Protein expression and purity were analysed by sodium dodecyl sulfate polyacrylamide gel electrophoresis (SDS-PAGE) using 4–12% Bis–Tris precast gels (Bio-Rad, USA) for optimal separation over a broad range of molecular weights. Protein content and yield were determined in triplicate using a Nanodrop 2000 (Thermo Fisher Scientific, UK) on the basis of the extinction coefficient and molecular weight for each protein according to the ExPASy ProtParam tool.

5.2.1.4 Surface functionalisation of silk with reflectin

Freeze-dried reflectin isoforms were dissolved in molecular biology grade water (AccuGENE™) (Lonza, UK) at a concentration of 100 μg mL^{-1}, and the annealed SF scaffolds were functionalized by means of physical or chemical adsorption (**Scheme 5.3**) to obtain reflectin A2 immobilized silk scaffolds: SF-A2(M1), SF-A2(M2), SF-A2(M3) and SF-A2(n).

Physical adsorption of reflectin was achieved by incubating the scaffolds with the various reflectin isoform solutions at 37°C overnight. The scaffolds were thoroughly rinsed in DI water and air-dried for further analysis.

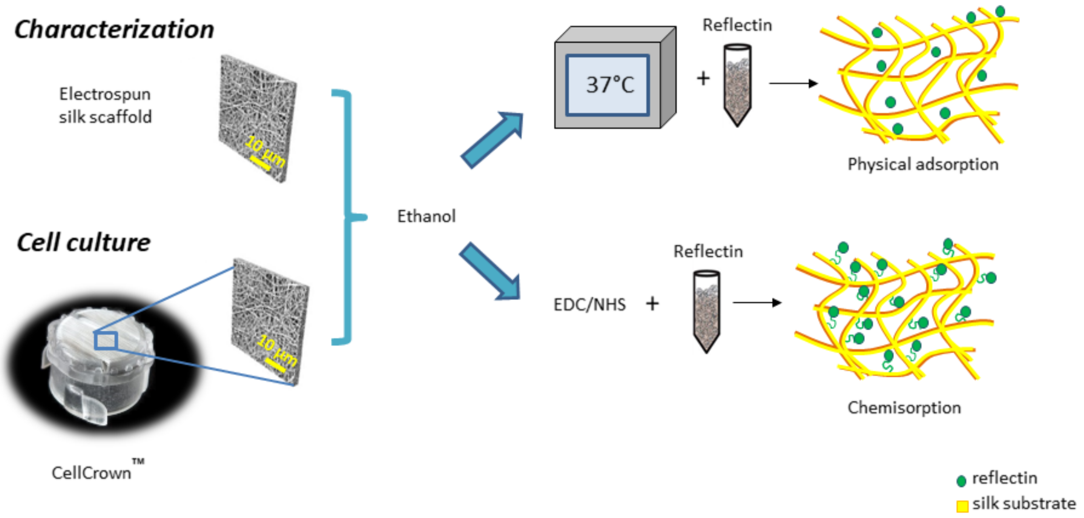

Scheme 5.3 Schematic of the functionalisation of silk with recombinant reflectin by means of physical adsorption or chemisorption.

Surface covalent functionalisation of SF with recombinant reflectin was carried out using a previously described protocol for covalent peptide binding [494–498]. Briefly, silk scaffolds were first soaked in PBS for 30 min. Immersion for 15 min at RT then followed in an activation buffer consisting of 0.5 mg mL^{-1} of 1-ethyl-3-(dimethylaminopropyl) carbodiimide hydrochloride (EDC) (Sigma-Aldrich, UK) and 0.7 mg mL^{-1} of N-hydroxysuccinimide (NHS) (Sigma-Aldrich, UK) in DI water to create amine-reactive NHS-esters from carboxylic groups in SF [498]. The activated NHS-esters were then reacted with the reflectin isoform solutions at RT for 2 h. After reaction, excess protein solution was removed and the scaffolds were thoroughly rinsed in DI water and air-dried.

5.2.2 Characterisation of the scaffolds

5.2.2.1 Morphology and surface topography

The top surface of the scaffolds was visualised with a JEOL JSM6700F FESEM at an accelerating voltage of 5 kV and working distance of 8 mm. The fibre diameter distribution was analysed with Fiji 1.28 software (NIH, USA) by measuring a minimum of 100 fibres.

5.2.2.2 Reflectin immobilisation

The efficiency of reflectin immobilisation on the scaffolds (n=3 per type) was indirectly monitored with a Pierce™ BCA protein assay kit (Thermo Fisher Scientific, UK) based on the amount of reflectin remaining in solution after adsorption. An aliquot (~25µL) of solution was incubated with 200 µL of the BCA working reagent for 2 h at 37°C following the manufacturer's instructions. The absorbance was measured with a microplate reader (Infinite M200) (Tecan Life Sciences, SG) at an ex. 562 nm, and normalised to the standard isoform solution used for functionalisation. Scaffolds in DI water served as blank and DI water was used as negative control. All samples were conducted in triplicate.

5.2.2.3 Chemical structure

Changes to the surface chemical groups on the scaffolds were explored by FTIR spectroscopy, using a PerkinElmer 2000 equipped with a zinc selenide (ZnSe) crystal on ATR mode. For each measurement, 32 scans were recorded with a resolution of 4 cm^{-1} and wavenumbers from 4000 to 600 cm^{-1}. Conformational changes to the protein secondary structure were explored by means of FSD within the amide I region ranging from 1700 to 1600 cm^{-1}, as described previously [372–374].

5.2.2.4 Conductivity of the scaffolds

Conductivity of the scaffolds (n=4 per type) was estimated in DC mode across four different locations on each scaffold using an A4P-200 MicroXACT automated electrical conductivity and resistivity system [360,376,377]. A Jandel 4-point probe head (Tungsten Carbide tips, 40 µm tip radius and 1 mm tip spacing) connected to a combined current source and digital voltmeter (Jandel RM3000) was used for the experiments. Samples were incubated in PBS overnight, with excess removed using blotting paper prior to testing. Samples were evaluated at RT ~20°C and in a controlled chamber at 37°C.

5.2.3 *In vitro* study

5.2.3.1 NG108-15 cell culture and seeding

NG108-15 neuronal-like cells, taken from stock, were used between passage P17-30, grown and maintained in NG108-15 growth medium [452] as per the supplier's instructions.

For cell culture experiments, as-spun silk scaffolds were positioned onto CellCrown™ polycarbonate inserts (Scaffdex Oy, Finland) for 24-well (vol. 1 mL) plates (**Scheme 5.3**), ethanol treated and functionalised with reflectin via chemisorption. The scaffolds were air-dried and sterilised under UV light (254 nm) radiation (30 min on each side, top and bottom) in a class II biosafety cabinet. Glass coverslips (CV) (12 mm diameter, 0.13-0.16 mm thickness) (VWR, UK) were used as positive controls. The scaffolds were seeded at 10,000 cells per well. The volume of seeding medium was minimised to ensure maximum contact of the cells with the scaffolds; once adhered (~2 h), the well was flooded with excess media. Half of the medium was changed every 2 days.

For experimental differentiation, growth culture media was changed to serum-deprived media one-day post-seeding. The culture was maintained for 5 days, with half of the medium removed and replaced with fresh medium every 2 days.

5.2.3.2 Cell viability and cell spreading

Viability of cells on the scaffolds (n=2 per type) was assessed with a LIVE/DEAD® viability/cytotoxicity fluorescence kit (Thermo Fisher Scientific, UK) following the manufacturer's instructions. Viable cells were labelled with calcein AM and non-viable/dead cells were labelled with ethidium homodimer. Following incubation, samples were examined under a TCS SP8 confocal laser scanning microscope (Leica Microsystems, UK) and 3D imaged. Cell number is expressed as the percentage of live cells versus non-viable cells. Surface area covered by cells was estimated using Fiji software across different fields of view.

5.2.3.3 Metabolic activity and proliferation

The metabolic activity and proliferation profiles of cells on the scaffolds (n=4 per type) were monitored over 7 days with the alamarBlue™ reduction assay based on resazurin (Sigma-Aldrich, UK) and the Quant-iT™ PicoGreen® dsDNA assay (Thermo Fisher Scientific, UK), respectively, following the manufacturers' instructions. The metabolic activity is recorded relative to the number of cells, which were estimated based on a single cell's DNA content [381].

5.2.3.4 Immunolabelling of NG108-15 neuronal cells

Cell-laden scaffolds (n=2 per type) were harvested, fixed, permeabilised and blocked against non-specific binding. Polyclonal rabbit anti-mouse/rat ß-tubulin III (Abcam, UK) was used as primary antibody (1:1000 v v^{-1}, 2 h), and polyclonal goat anti-rabbit Alexa Fluor® 488 (Abcam, UK) as secondary antibody (1:1000 v v^{-1}, 2 h); cell nuclei were counterstained with DAPI (1:1000 v v^{-1}, 2 min) (Sigma-Aldrich, UK). All staining was performed at RT. Cell-laden samples were mounted with ProLong® Diamond Antifade (Thermo Fisher Scientific, UK) and imaged using a TCS SP8 confocal laser scanning microscope (Leica Microsystems, UK).

5.2.3.5 Neurite outgrowth assessment

Differentiated cells were assessed in terms of neurite outgrowth, analysed from immunofluorescent micrographs using the Fiji software. Only extensions longer than 30 µm were considered as neurites. A total of 15 neurites per condition were measured to determine neurite length.

5.2.4 Data analysis

Statistical analysis was performed with GraphPad Prism 8 (San Diego, USA), and checked for normality. Normally distributed data is presented as SD (error bars) of the mean values. For parametric data and multiple comparisons, significance was assessed by two-way ANOVA (two independent variables) using Tukey's post hoc analysis test. Not normally distributed data was assessed by Kruskal-Wallis with Dunn's post hoc analysis test. A value of $p<0.05$ was considered statistically significant.

5.3 Results and Discussion

5.3.1 Synthesis and expression of recombinant reflectin

Reflectins are highly repetitive structural proteins (85 to 98% similarity) with varying molecular weight [478]. Reflectins are differently distributed within the cephalopod's tissue [492]; the main two types of reflectin are A1 and A2. Reflectins consist of one to six highly conserved repeating subdomains of a highly repeating sequence [499]. Recent sequencing of reflectins has shown that this highly conserved repeating sequence [484] is of the form $(M/F\text{-}D\text{-}X_5)(M\text{-}D\text{-}X_5)_n(M\text{-}D\text{-}X_{3\text{-}4})$ (where M, methionine; F, phenylalanine; D, aspartic acid; Y, tyrosine; R, arginine; X, variable amino acid) (**Scheme 5.1B)** [477]. Despite this general common motif, variations in composition, molecular weight and length of segments are common, having a direct impact on their properties [500,501]. For instance, reflectin A2 has lower number of subdomains, and thus lower molecular weight, lower histidine content and lower net charge compared with reflectin A1.

In this study, we designed different isoforms (i.e. A2(M1), A2(M2) and A2(M3)) of reflectin-like A2 protein from *Doryteuthis opalescens* based on truncation of the wild-type protein. SDS-PAGE gels of the recombinant proteins with one, two, three and four repeat motifs are shown in **Figure 5.1A-B**, where A2(M1) (one repeat motif, ~10.5 kDa), A2(M2) (two repeat motifs, ~17.6 kDa), A2(M3) (three repeat motifs, ~ 22.8 kDa) and A2(n) (four repeat motifs, ~28.4 kDa) following purification.

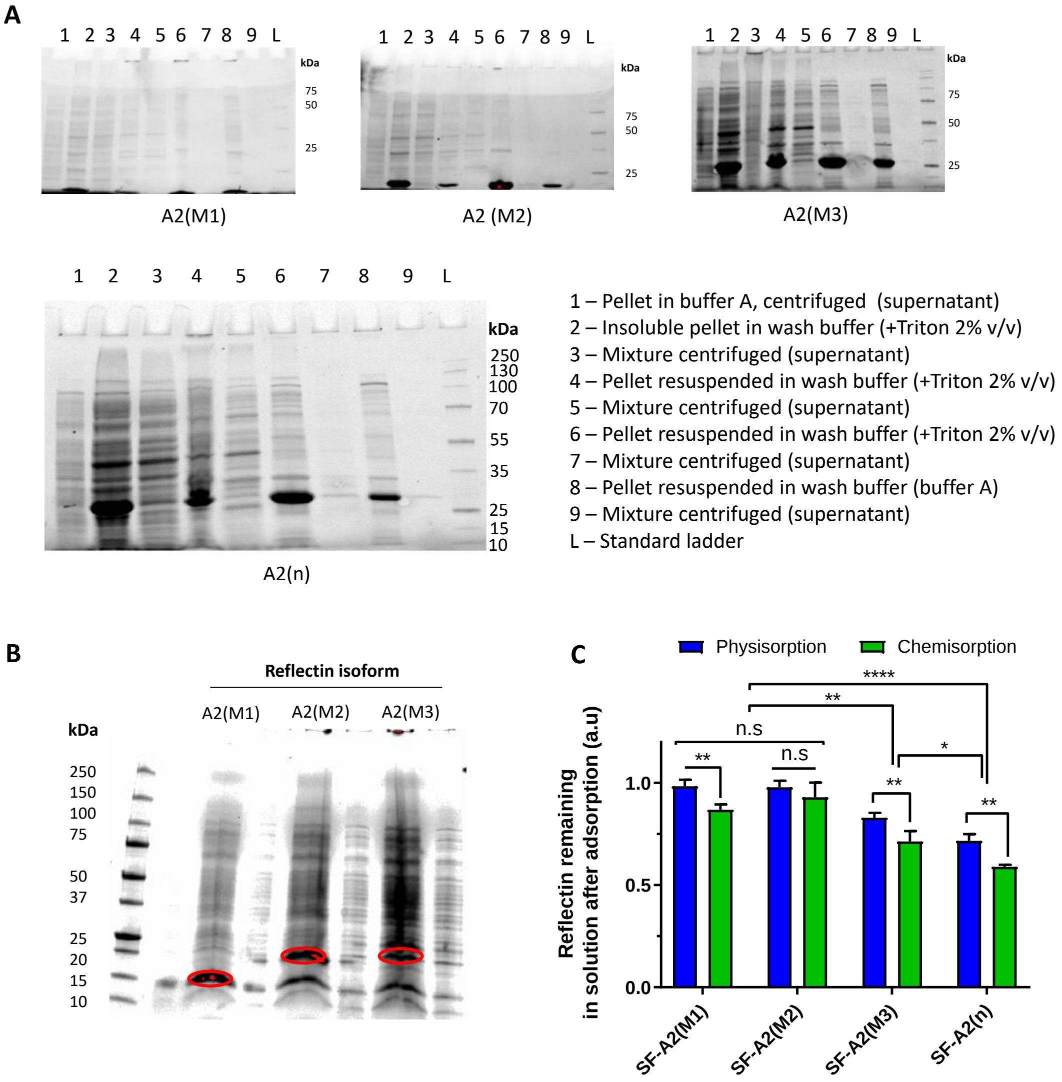

Figure 5.1 (**A**) Molecular weight showing stability of the cell lysates of the various reflectin A2 isoforms (*Doryteuthis opalescens*) under different conditions, as demonstrated by SDS-PAGE. (**B**) Molecular weight of the three truncated reflectin A2 isoforms as demonstrated by SDS-PAGE. (**C**) Reflectin remaining in solution after adsorption onto the scaffolds (n=3 per type), normalised to the corresponding standard isoform solution used for functionalisation. Differences between the experimental groups were analysed by two-way ANOVA with Tukey's post hoc test. *$p<0.05$, **$p<0.01$, ****$p<0.0001$.

5.3.2 Immobilisation of reflectin on silk scaffolds

Different approaches have been investigated over the years to introduce bioactive elements to silk materials. Common methods include blending silk with proteins found in the ECM of native tissues [502], or using genetic engineering to fuse two or more protein motifs together – such as in the case of silk-elastin [228,503].

Another route is through chemical modification, by covalently attaching different peptide sequences [494,504].

Here, electrospun SF scaffolds were decorated with reflectin isoforms through physical adsorption or chemisorption. Covalent modification of silk was carried out following the standard method of Kaplan et al. [498]. Some degree of crosslinking is to be expected. However, this is dependent on the paradigm of the crosslinking, mainly governed by the reaction time and concentration of the EDC/NHS buffer [497,505,506]. Furthermore, SF here is in the form of fibres rather than dissolved in solution. Some authors have reported the use of trinitrobenzene sulfonic acid for quantification of primary free amine groups and crosslinking degree in silk [506], but this assay is highly flammable and toxic. Immobilisation of reflectin onto the scaffolds was indirectly monitored by measuring the presence of reflectin remaining in solution after adsorption, normalised to the corresponding standard isoform solution used for functionalisation [507]. Results showed a great amount of reflectin remaining in solution for those scaffolds coated with reflectin isoforms of low tandem repeat motif number (i.e. A2(M1) and A2(M2)), meaning that very little amount of these isoforms was actually adsorbed on the scaffolds (**Figure 5.1C).** In contrast, a substantial lower amount of reflectin was found in solution after adsorption for the A2(M3) ($p<0.01$) and A2(n) ($p<0.0001$) isoforms in comparison, indicating much better adsorption onto the scaffolds. Overall, less amount of reflectin remaining in solution after adsorption tended to be detected for chemisorption in comparison with the physical adsorption route ($p<0.01$). This suggests that covalent functionalisation through reactive amide linkages was a more effective route to adsorb the reflectin isoforms onto the scaffolds. Indeed, protein physisorption is mainly governed by molecular interactions such as electrostatic, hydrophobic, van der Waals, or hydrogen bonding between the protein and the scaffold. Non-covalent bonds are weaker compared with covalent bonding, especially in aqueous environments [508]. Therefore, desorption of loosely attached peptides (i.e. physisorption) is inevitable after rinsing or long soaking periods.

5.3.3 Surface morphology and fibre structure

The surface morphology of the scaffolds, in terms of fibre diameter distribution and structure after functionalisation, was observed via FESEM (**Figure 5.2A-B**).

Micrographs of the surface-functionalised scaffolds showed a homogenous fibrous-like morphology for all sample groups, with no major differences in terms of the average fibre diameter compared with neat silk (**Figure 5.2C**). Furthermore, neither the integrity of the scaffolds nor the micro-structure of the fibres was affected by the functionalisation process.

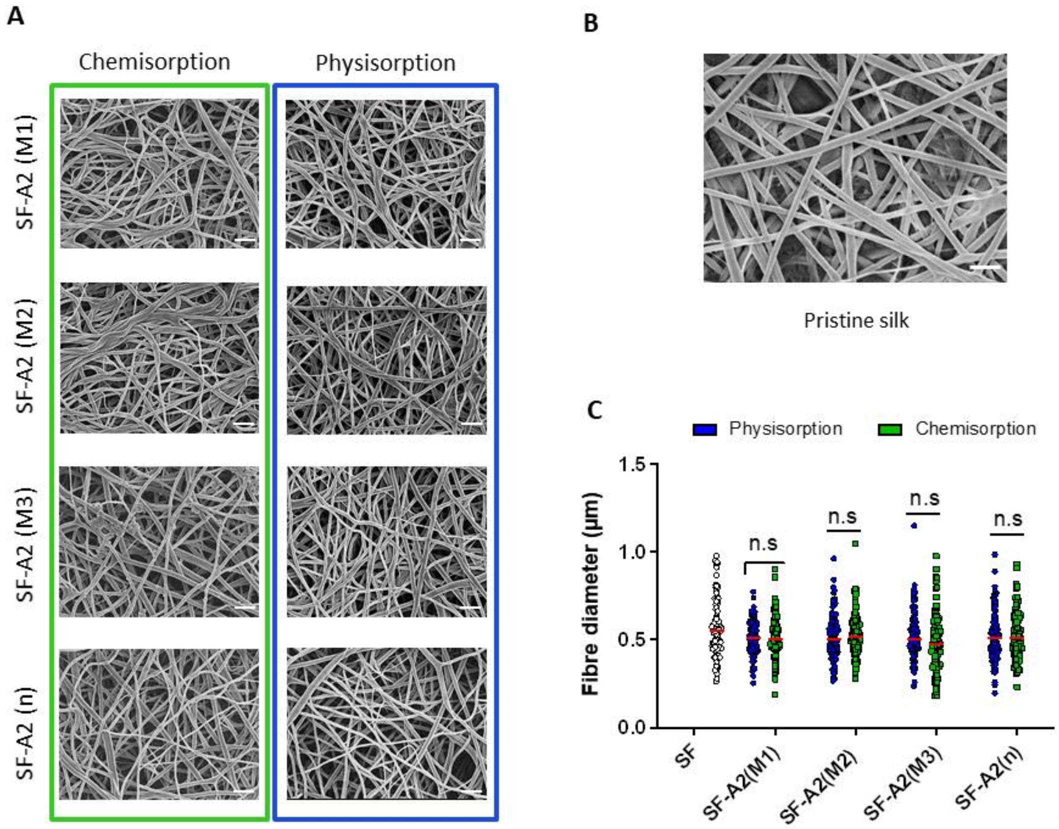

Figure 5.2 Effect of surface functionalisation with reflectin on the scaffold microstructure. (**A-B**) Representative FESEM micrographs of the surface topography of the scaffolds after functionalisation by physical adsorption or chemisorption; scale bars at 3 μm. (**C**) Distribution of the fibre diameter size among the various scaffolds. Differences between the experimental groups were analysed by Kruskal-Wallis with Dunn’s test. n.s non-significant.

5.3.4 FTIR characterisation

The surface chemical groups on the scaffolds were explored by FTIR-ATR (**Figure 5.3A**). The amide A band, corresponding to N−H stretching vibrations, was found at 3200-3400 cm^{-1}. Compared with neat silk, a conspicuous increase in absorption for the amide B band (asymmetrical stretch of CH_2) positions of reflectins from reflectin functionalised silk scaffolds was found at 2920–2940 cm^{-1}. As-produced scaffolds also showed amide peaks characteristic of the co-existence of random helical and β-sheet conformation (e.g. 1631, 1517 cm^{-1}). The characteristic vibration frequencies of β-sheets were observed for all functionalised scaffolds, indicating the retention of the β-sheet secondary structure, and hence, stability under cell culture conditions. The amide I region ($C{=}O$ stretching) in the range 1700-1600 cm^{-1} is particularly very sensitive and useful for predicting the conformation of proteins from the spectrum [509]. Conformational changes to the secondary protein structure were assessed by deconvoluting the amide I band of the FTIR spectra [372,374], and the estimated secondary structural contents are presented in **Figure 5.3B.** Zero interference of reflectin incorporation in the proportion of β-sheet structures (non-significant differences) in the scaffolds was observed when the protein was physically adsorbed. Some differences ($p<0.001$) were observed when reflectin was chemisorbed, which could be attributed in part to the effect of EDC/NHS [510] as no differences among the isoforms were observed.

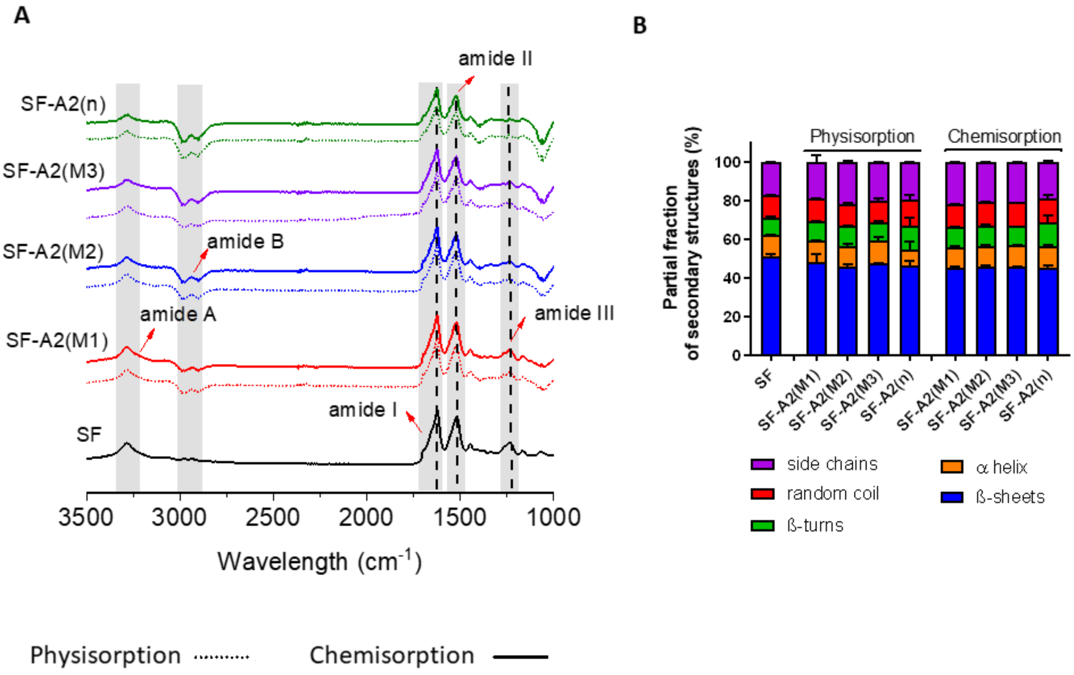

Figure 5.3 Effect of reflectin functionalisation on the chemical structure. (**A**) Representative FTIR spectrum of the various scaffolds. (**B**) Quantitative analysis of the secondary structure of the scaffolds (n=2 per type) functionalised with various reflectin A2 isoforms, either by physical adsorption or chemisorption.

5.3.5 Conductive properties

Conductivity of the scaffolds in the hydrated state was found to scale up with the number of repeat motifs of reflectin A2 used for functionalisation (**Figure 5.4**). This is as expected after protein truncation, since the electrical properties of reflectins are dependent on the relative arrangement and abundance of their charged amino acids [489]. Furthermore, very little amount of reflectin with one and two motifs (i.e. A2(M1) and A2(M2)) was detected on the scaffolds after adsorption (**Figure 5.1C**). Indeed, the conductivity of silk scaffolds coated with these two isoforms showed non-significant differences with respect to SF alone. In contrast, silk scaffolds decorated with reflectin A2(n) (i.e. full sequence) exhibited a maximum at ~3×10^{-4} S cm^{-1}, significantly greater compared with neat silk used as control.

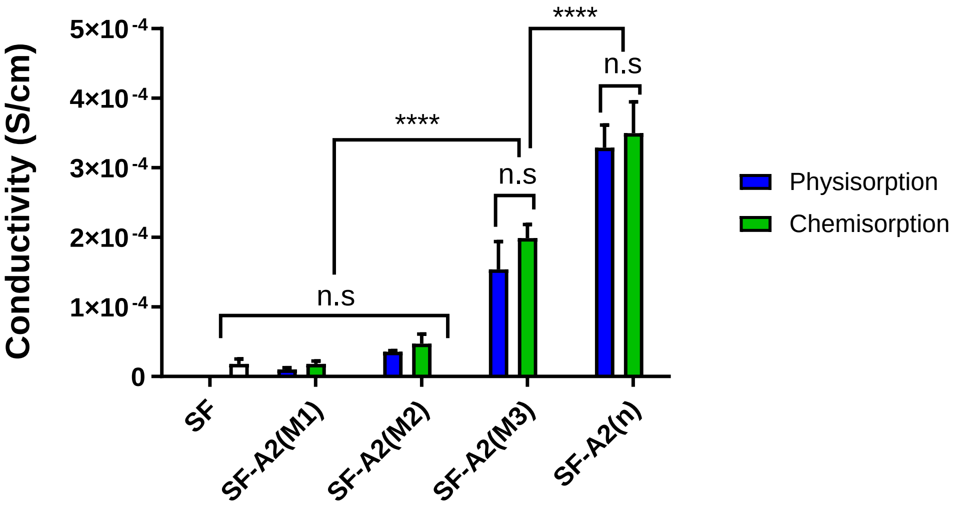

Figure 5.4 Quantitative analysis of the estimated conductivity of the scaffolds (n=4 per type) functionalised with various reflectin A2 isoforms, either by physical adsorption or chemisorption. Differences between the experimental groups were analysed by two-way ANOVA with Tukey's post hoc test. n.s non-significant, ****$p<0.0001$.

Protein based materials, such as silk fibroin, can be considered as proton/ion conductors [274,334,407–409], with reflectin being among the highest ones found in nature. Results shown here confirm the contributing factor of the reflectin isoform to increase conduction, where the relative arrangement and abundance of the charged amino acids of reflectins serves proton donation and facilitate Grotthuss-type proton transport [489,511]. Conductivity of bulk films of reflectin A1 (*Doryteuthis pealeii*) had been reported at ~2×10^{-4} S cm^{-1} at body temperature [334], one order of magnitude lower than the value reported here on silk scaffolds coated with reflectin A2(n) (*Doryteuthis opalescens*). The distinct species used among the studies, with a different relative arrangement and abundance of their charged amino acids, along with the protonic/ionic nature of SF itself, could contribute to the contrasting findings. Furthermore, materials water content (hydration state) influences the electrical properties of reflectins [334] and the hydration degree/humidity of the sample was not controlled during measurements. Therefore, the use of more advanced techniques could provide better estimates.

5.3.6 Cellular response

Based on the reflectin adsorption efficiency of the isoforms and the properties of the functionalized scaffolds, covalently immobilized reflectin A2(n) silk (i.e. SF-A2n) was chosen as the best biologically active candidate to evaluate the neuronal cell response.

A fluorescent cell viability assay was carried out after 5 days of culture (**Figure 5.5A**). NG108-15 cells on the scaffolds were highly viable (**Figure 5.5B**), with very few dead cells and no predominant differences compared with glass coverslip controls. Cell coverage was estimated across several fields of view (**Figure 5.5C**), suggesting that cell distribution was enhanced on the functionalised silk scaffold.

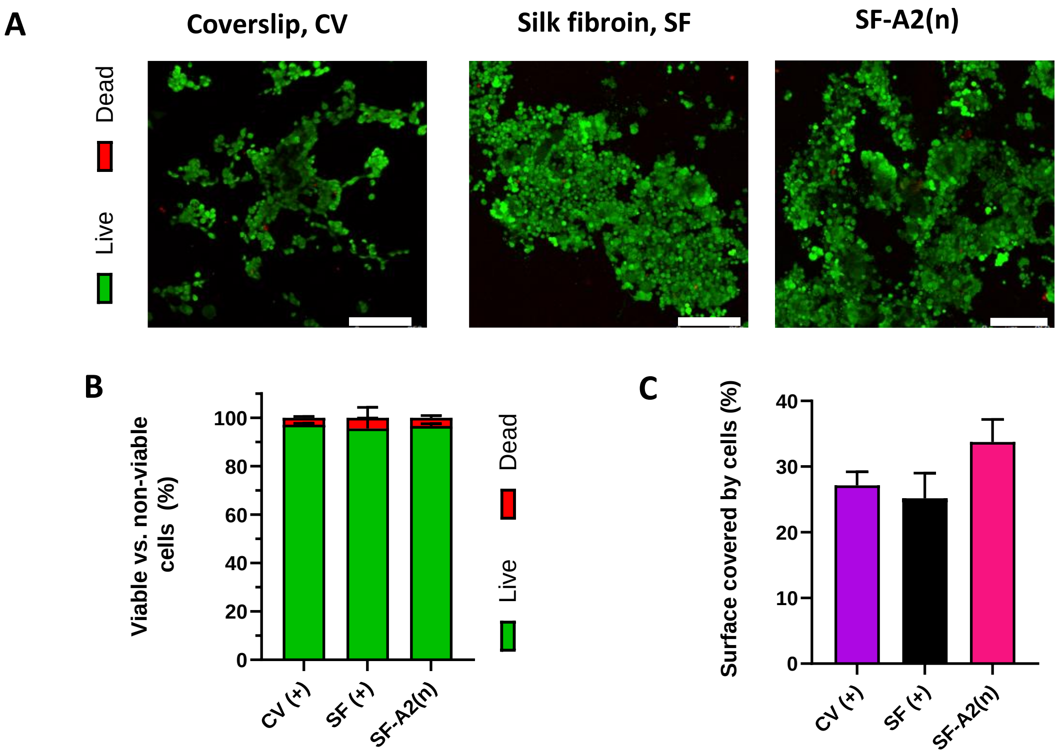

Figure 5.5 Cellular viability of NG108-15 cells on reflectin A2(n) functionalised SF scaffolds. **(A)** Representative confocal micrographs at day 5 showing cell viability: viable cells are labelled with calcein AM (green) and dead cells are labelled with ethidium homodimer-1 (red); scale bar at 250 µm. (**B**) Semi-quantitative analysis of the percentage of viable and non-viable cells (n=2 scaffolds per type) after 5 days of culture. **(C)** Estimated surface covered by cells after 5 days of culture (n=2 scaffolds per type). Coverslip (CV) and silk fibroin (SF) were used as controls.

The metabolic activity (**Figure 5.6A-B**) and proliferation (**Figure 5.6C-D**) profiles were next evaluated over 7 days, increasing steadily over time. The presence of reflectin on the scaffold had a positive impact towards both the metabolic activity (**Figure 5.6A**) and proliferation (**Figure 5.6C**) of cells in the culture, with significantly greater cell activity compared with neat silk alone. Metabolic activity of NG108-15 cells seeded on the scaffolds is shown in **Figure 5.6B** as a function of the dsDNA concentration, giving an indication of the metabolic activity of the culture relative to the number of cells present on it. As reported by the estimated number of cells in culture (**Figure 5.6D**), cellular proliferation was greatly enhanced since the early stage of the cell culture after functionalisation with reflectin.

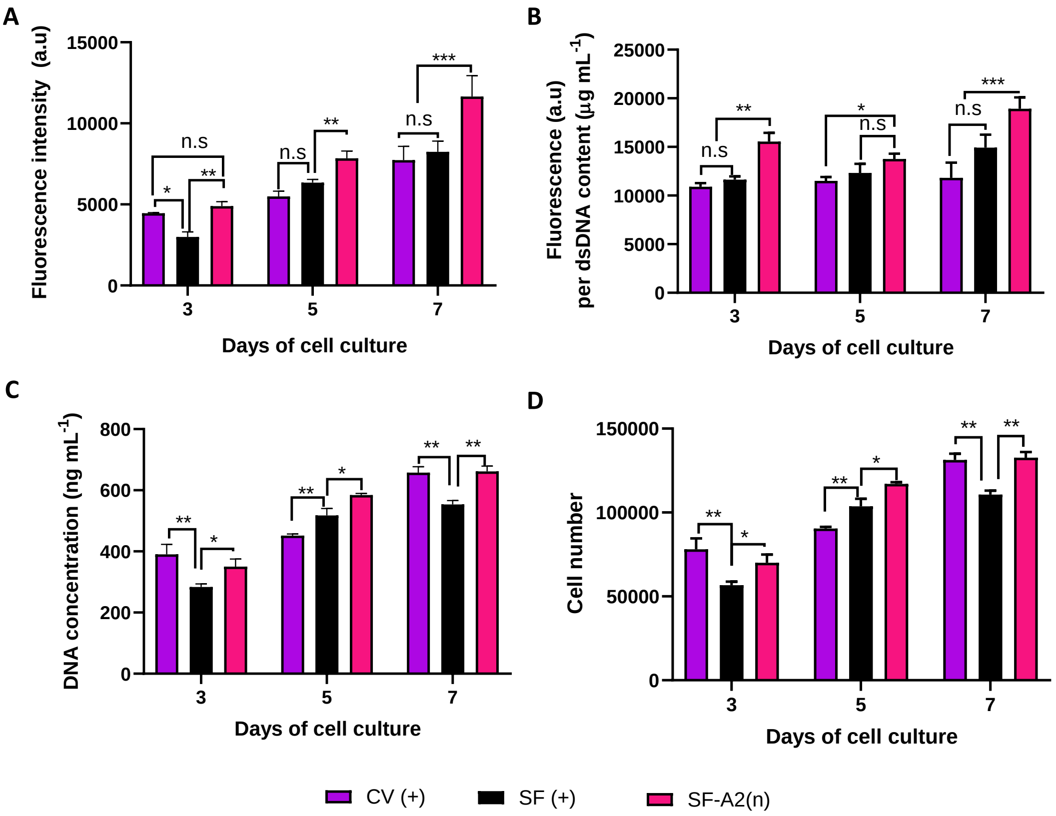

Figure 5.6 Cellular metabolic activity and proliferation of NG108-15 cells on reflectin A2(n) functionalised SF scaffolds over 7 days of culture. **(A)** Metabolic activity (n=4 scaffolds per type). (**B**) Metabolic activity relative to dsDNA content (n=4 scaffolds per type). **(C)** Total dsDNA content (n=4 scaffolds per type). (**D**) Cellular proliferation; estimated cell number (n=4 scaffolds per type). Differences between the experimental groups were analysed by one-way ANOVA with Tukey's test. n.s non-significant. *p<0.05, **p<0.01, ***p<0.0001. Coverslip (CV) and silk fibroin (SF) were used as controls.

The differentiation response of NG108-15 cells on the scaffolds was further evaluated in serum-deprived medium conditions. Neurite outgrowth occurs during the development of the nervous system but also during regeneration. Neurite formation is under complex control and is essential for the function of nerve cells. Neurite length is physically impaired at higher cell densities, preventing accurate interpretation; therefore, the experiments were terminated at day 5 (**Figure 5.7A**). No significant differences were observed in terms of neurite length across the three sample groups (**Figure 5.7B**), with maximum extension measured on the reflectin-immobilized silk scaffold compared with SF alone.

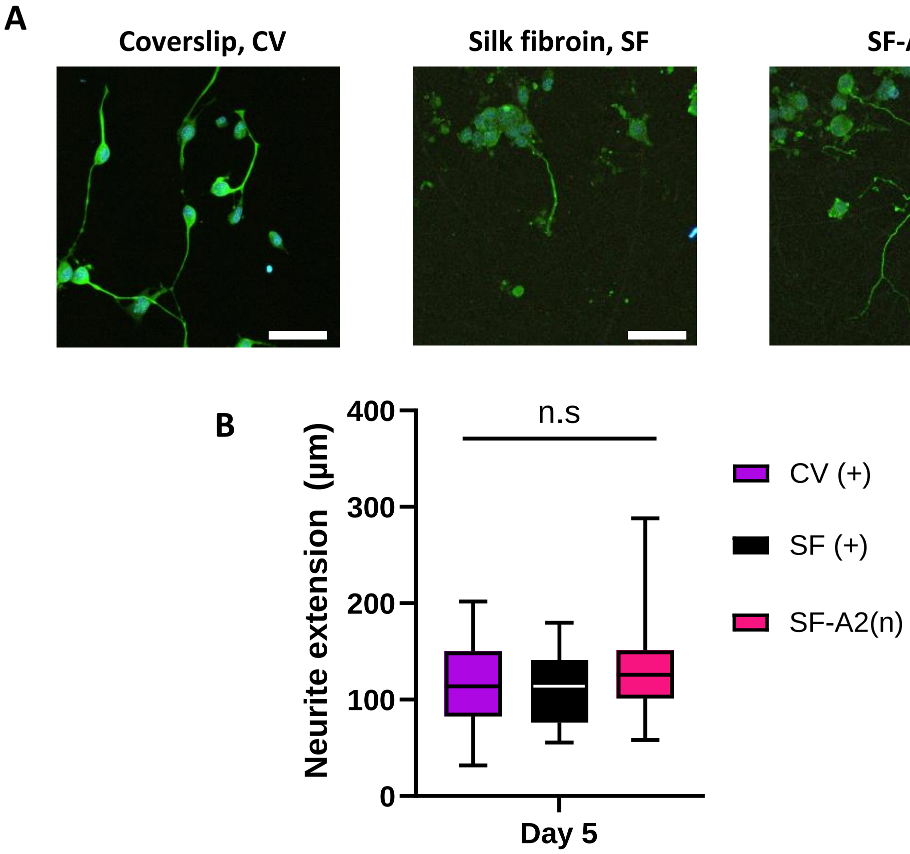

Figure 5.7 (A-B) Neuronal differentiation of NG108-15 cells after 5 days of culture in serum-deprived conditions. **(A)** Representative confocal micrographs of differentiated cells immunolabelled with β-tubulin III (green) as a marker of neurite outgrowth, and cell nuclei counterstained with DAPI (blue); scale bar at 75 μm. **(B)** Box-and-whisker plot showing neurite extension distribution on each scaffold. Differences between the experimental groups were analysed by one-way ANOVA with Tukey's test. n.s non-significant. *p<0.05, **p<0.01, ***p<0.0001. Coverslip (CV) and silk fibroin (SF) were used as controls.

Proteins such as fibronectin, laminin or short peptide derivatives [512–514], along with glycosaminoglycans of the native ECM [515,516], are involved in proliferation, neural plasticity and regeneration of the nervous system. Accordingly, they have traditionally been used to stimulate processes such as neuronal adhesion, migration and neurite formation, in combination with synthetic and natural polymer-based scaffolds [517–521]. However, if combined into single blends, most of these biologicals tend to remain hidden in the bulk and unavailable for cell-substrate interactions [520]. The Gorodetsky lab had evaluated the effects of reflectin A1 (*Doryteuthis pealeii*) films on progenitor neuronal cells [234,235], finding that their proliferation and differentiation potential were greatly enhanced in comparison to the use of laminin and fibronectin. Following this, we used reflectin A2 (*Doryteuthis opalescens*) as a coating on electrospun SF scaffolds, focusing it on the surfaces that could be in contact with cells and endowing the fibres with enhanced metabolic and proliferation responses (**Figure 5.6**). A synergic contribution of several factors could be responsible for the differing cellular responses observed. It has been previously reported that the biological activity of a scaffold can be influenced by electrostatic interactions between the substrate and the negatively charged cell membrane [273,308], or by changes in the local electrostatic charge of the scaffold [307] that can contribute to the adsorption of serum proteins from the medium. Indeed, neuronal cell adhesion and growth on reflectin films appear to occur via electrostatic means and be protein-sequence dependent [235], with reflectins containing a large number of charged amino acid residues in comparison to other protein-based materials such as laminin or fibronectin. On the other hand, previous studies have shown that intracellular levels of Ca^{2+}, K^+ and Na^+ appear to affect neuronal cell responses [474–476,522,523]. In this regard, it has been postulated that conductive substrates may lead to increased intracellular ion levels in neuronal cells [431], and so, the bioelectric interface attributed to reflectin may have played a role in initiating key signal transduction cascades altering the cell response. However, no significant differences in terms of neurite length were observed in this study, and further investigation is required (e.g. by looking at molecular mechanisms and specific intracellular cell signalling pathways involved in controlling neuronal cell activity).

While this study represents a proof-of-concept to the use of reflectin as a coating on micro/nano- fibrous scaffolds for *in vitro* cell culture, it is not one without limitations, and grafting multiple combinations or quantities of different ECM components (e.g. gradients) may further potentiate the scaffold’s function (e.g. neurite outgrowth). Scale-up remains an issue for electrospinning technologies and recombinant protein production, and it is currently being addressed. New developments in recent years have seen more efficient methods for the industrial production of micro/nano- fibres at significantly higher rates [524], such as solution blow spinning [367,525], along with the scale-up of microbial fermentation processes for recombinant protein production to meet the requirements of the pharmaceutical industry [526,527].

5.4 Conclusion

We present here a neural tissue engineered platform based on SF scaffolds decorated with recombinant reflectin A2 isoforms from *Doryteuthis opalescens.* Chemisorption with native reflectin A2 provided a supportive microenvironment with bioactive molecule incorporation to promote growth and differentiation of NG108-15 neuronal-like cells. Relatively scarce protein-based protonic materials found in nature have exhibited excellent conductive properties and can support cellular attachment and proliferation. This, therefore, is another step towards cephalopod-inspired, protein-based materials capable of controlling cellular activity. These findings hold particular significance from the perspective of bioelectronics, where reflectin may serve as an active material. The human body uses ion and proton currents to conduct electricity, and reflectins' favourable intrinsic conductive properties open up opportunities in a wide range of electrically sensitive tissues.

Chapter 6

Conclusions and future perspectives

6.1 Conclusions

The use of electrical regimes in neural tissue engineering appears as a promising alternative to tackle nerve-related defects and injuries, although challenges persist on the way towards their clinical practice. In this thesis, electroconductive/active micro/nano- fibrous silk-based scaffolds were explored. Three different strategies for imbuing conductive properties were assessed towards improving nerve regeneration, with the scaffolds tested *in vitro* with neuroma analogue neuronal NG108-15 cells.

- In **Chapter 3**, GO was blended at controlled loadings with SF and successfully electrospun into a family of composites. *In situ* post-reduction into electroactive SF/rGO led to increased conductance upon the filler's content, although limited in range. Neuronal cell growth and proliferation were supported in all scaffolds, but SF/rGO outperformed unmodified silk and SF/GO composites. Neurite outgrowth was observed in all scaffold groups, but no significant differences in length were reported. Decoupling the role of conductivity in cell behaviour from other substrate's traits or effects (e.g. surface roughness, protein adsorption) is difficult, but results of this study suggest that the endogenous electrical regime attributed to rGO over GO might be an important trait.

- Using carbon-based nanomaterials as electroconductive moieties is subjected to achieving percolation threshold and formation of a conductive network. The use of rGO as a filler in composites resulted in limited conductivity. A wider range in conductance, matching and surpassing native mammalian tissues', was achieved in **Chapter 4** by functionalizing SF scaffolds with PEDOT–PSS.

Conductivity was easily tuned upon the coating concentration and further boosted by DMSO treatment, resulting in enhanced protein adsorption and no major changes in surface roughness. Neuronal cell growth and proliferation were well supported, with DMSO-treated PEDOT–PSS functionalised scaffolds partially outperforming PEDOT–PSS counterparts. Scaffolds coated with 3 mg mL^{-1} of DMSO-treated PEDOT–PSS were found as the most suitable candidate, with significantly greater neurite length compared with unmodified silk. Whether due to local changes in conductivity or a synergy of secondary effects such as protein adsorption or a less negatively charged cell-material interface, the overall biological response of these electroconductive scaffolds tended to be enhanced compared with unmodified silk.

- Electrons and ions are the main charged carriers in carbon-based materials and intrinsically conducting polymers. However, the human body uses ion/proton currents to conduct electricity. Functionalisation of silk with different recombinantly synthesised isoforms of intrinsic conductive reflectin, reported among the highest proton/ion conductors in nature, was explored in **Chapter 5**. Chemisorption resulted in a more successful route than physical adsorption to decorate silk with reflectin A2, and conduction was found to be directly proportional to the isoform motif frequency. A significant improvement over the metabolic activity and neuronal proliferation responses was observed on SF scaffolds functionalised with the native isoform with respect to unmodified silk. However, no significant differences in terms of neurite extension were observed compared with unmodified silk.

In summary, the work presented here shows that electroconductive/active silk scaffolds can lead to enhanced metabolic activity and proliferation of NG1080-15 neuronal-like cells, compared with unmodified silk scaffolds. However, no major differences in terms of neurite length were observed. Whether endogenous electrical regimes (i.e. passive stimulation) on their own are enough to control the neuronal cellular response, or how intracellular cell signalling pathways are specifically modulated, remain unanswered.

6.2 Future work

The potential of this field of research is limitless and can be continued in various ways. Future work can be performed around three major themes: optimisation of the scaffolds, signalling pathways involved in cell response to changes in conductivity, and translation to the clinic. Some future lines of investigation are detailed below.

With respect to nerve repair, future challenges are to create a conductive 3D conduit peripheral nerve model with mature and relevant ultrastructure based on a combination of the electroconductive/active microenvironments explored here:

- The use of benign solvents (e.g. aqueous systems) should be investigated as a way to overcome the restrictions of toxic and harsh solvents typically used in electrospinning. Furthermore, higher throughput manufacturing techniques, such as solution blow spinning, could be assessed towards the rapid fabrication of scalable fibrous substrates (refer to **Appendix A** "*Porous, aligned and biomimetic fibres of regenerated silk fibroin produced by solution blow spinning*"). In this respect, more relevant fibrous structures (e.g. aligned fibres and porous fibres) could be assessed towards directing neurite outgrowth and Schwann cell alignment.
- Cell-laden 2D spun scaffolds could be rolled into 3D conduit structures using a cell sheet rolling system towards the production of NGCs. On the other hand, conduit scaffolds could be engineered by directly spinning onto a deposition rod-like mandrel. In addition, a gradual angular alignment approach based on stacking several layers of spun scaffolds together could be investigated on the lining of the conduit to provide the model with appropriate mechanical properties.
- Despite the current efforts to use 2D spun scaffolds, there remain challenges to truly mimic a natural microenvironment that resembles the native ECM. Spun scaffolds can be combined into more complex structures by incorporating hydrogels to provide truly 3D hydrophilic structures that can support cell viability, proliferation, differentiation and matrix production.

- The stability of the scaffolds, degradation properties and their overall shelf-life should be investigated. Furthermore, the electroconductive stability of the scaffolds should be explored over the long term (e.g. over different periods of incubation) – for which cyclic voltammetry or electrochemical impedance spectroscopy techniques are best suited – as way forward to assess transmission of the bioelectrical signals required by cells and tissues.

- While NG108-15 cells are versatile and very practical, the results obtained with a single cell line are not conclusive. Experiments using primary cells would result in more accurate estimations of neuronal regeneration as they more closely mimic the nerve tissue microenvironment. Therefore, these materials should be screened further, for example by using co-cultures with primary cells (DRG neuronal cells, primary Schwann cells) or other cell lines (PC12 neuroma cells, SH-SY5Y cells, RN22 Schwannoma cells). Another interesting line of research is to assess the effects of these electroconductive/active scaffolds on (neural) stem cells, and investigate whether their adhesion, proliferation and differentiation towards neuronal cells could be significantly upregulated.

- Signalling proteins and intracellular ion levels play a critical role in cell-to-cell communication. While the overall effects of these conductive scaffolds have been studied on the neuronal cell response, the molecular mechanisms regulating these responses remain largely unknown. In-depth protein, gene expression and intracellular ion analysis would provide a deeper understanding on the interactions between the cells and these electroconductive microenvironments.

- Neurite outgrowth assessment should be further explored with a larger neurite population, and measuring neurite extension by means of deep-learning algorithms could reduce bias. Other than looking into fibre alignment, neurite outgrowth could be further promoted by exploring the use of exogenous electrical regimes (i.e. direct ES) applied to cell-laden scaffolds. Furthermore, as a way forward to explore the electrical responsiveness of some of these constructs, macromolecular therapeutics (e.g. growth factors, genes or small interface RNA molecules) of interest in nerve repair could be loaded into the scaffolds and their delivery controlled in a pulsatile fashion upon the on/off application of an electrical stimulus (refer to **Appendix B** "*Electroresponsive silk-based biohybrid composites for electrochemically controlled growth factor delivery*").

- The use of gradient concentrations of growth factors or combinations of ECM molecules could be investigated towards directing neuronal cell responses. For instance, different gradient patterns could be created by digital light photolithography on the scaffold substrates.
- Inflammation and scarring are commonly associated with nerve repair. An interesting avenue of research is to explore the local delivery of anti-inflammatory cytokines (e.g. interleukin 10) and anti-scarring molecules (e.g. mannose-6-phosphate) that could help improve functional repair.
- Spun fibrous scaffolds in tissue engineering commonly use alcohol submersion or UV radiation methods for sterilisation purposes, like in the case of the current *in vitro* studies. However, these methods are only acceptable for laboratory-based research since they do not fully eradicate microorganism contaminants and are not approved by regulatory bodies for implantation in humans. The impact of approved medically grade sterilisation techniques (e.g. ethylene oxide, gamma radiation) on the properties of the developed scaffolds should be investigated regarding medical device development intended for human implantation.
- Short and long-term *in vivo* experiments in animal models (e.g. rodents, rabbits, dogs) would need to be carried out to truly assess the biological and functional response of the developed scaffolds to bridge short nerve gap injuries. Short-term studies can focus on the inflammatory response towards the constructs, while long-term studies can provide information about the functionality of the scaffolds (e.g. regeneration efficiency) and degradation relative to new tissue formation. In particular, quantitative studies of vital nerve regeneration parameters could be assessed and compared with respect to autografting outcomes.

Other than for nerve repair, *in vitro* 3D models based on these electroconductive/active microenvironments could be used to study disease conditions of interest, in accordance with the principles of 3Rs (e.g. replacement, refinement and reduction) regarding animal use in experiments.

References

1. Gaudin, R.; Knipfer, C.; Henningsen, A.; Smeets, R.; Heiland, M.; Hadlock, T. Approaches to Peripheral Nerve Repair: Generations of Biomaterial Conduits Yielding to Replacing Autologous Nerve Grafts in Craniomaxillofacial Surgery. *BioMed Res. Int.* **2016**, *2016*, 3856262, doi:10.1155/2016/3856262.
2. Kehoe, S.; Zhang, X.F.; Boyd, D. FDA Approved Guidance Conduits and Wraps for Peripheral Nerve Injury: A Review of Materials and Efficacy. *Injury* **2012**, *43*, 553–572, doi:10.1016/j.injury.2010.12.030.
3. Jiang, B.; Zhang, P.; Jiang, B. Advances in Small Gap Sleeve Bridging Peripheral Nerve Injury. *Artif. Cells. Blood Substit. Immobil. Biotechnol.* **2010**, *38*, 1–4, doi:10.3109/10731190903495652.
4. Schmidt, C.E.; Leach, J.B. Neural Tissue Engineering: Strategies for Repair and Regeneration. *Annu. Rev. Biomed. Eng.* **2003**, *5*, 293–347, doi:10.1146/annurev.bioeng.5.011303.120731.
5. Babu, P.; Behl, A.; Chakravarty, B.; Bhandari, P.; Bhatti, T.; Maurya, S. Entubulation Techniques in Peripheral Nerve Repair. *Indian J. Neurotrauma* **2008**, *5*, 15–20, doi:10.1016/S0973-0508(08)80023-8.
6. Huang, W.; Begum, R.; Barber, T.; Ibba, V.; Tee, N.C.H.; Hussain, M.; Arastoo, M.; Yang, Q.; Robson, L.G.; Lesage, S.; et al. Regenerative Potential of Silk Conduits in Repair of Peripheral Nerve Injury in Adult Rats. *Biomaterials* **2012**, *33*, 59–71, doi:10.1016/j.biomaterials.2011.09.030.
7. de Ruiter, G.C.W.; Malessy, M.J.A.; Yaszemski, M.J.; Windebank, A.J.; Spinner, R.J. Designing Ideal Conduits for Peripheral Nerve Repair. *Neurosurg. Focus* **2009**, *26*, E5, doi:10.3171/FOC.2009.26.2.E5.
8. Magaz, A.; Faroni, A.; Gough, J.E.; Reid, A.J.; Li, X.; Blaker, J.J. Bioactive Silk-Based Nerve Guidance Conduits for Augmenting Peripheral Nerve Repair. *Adv. Healthc. Mater.* **2018**, *7*, 1800308, doi:10.1002/adhm.201800308.
9. Chen, C.; Bai, X.; Ding, Y.; Lee, I.-S. Electrical Stimulation as a Novel Tool for Regulating Cell Behavior in Tissue Engineering. *Biomater. Res.* **2019**, *23*, 25, doi:10.1186/s40824-019-0176-8.
10. Wang, Y.; Kim, H.-J.; Vunjak-Novakovic, G.; Kaplan, D.L. Stem Cell-Based Tissue Engineering with Silk Biomaterials. *Biomaterials* **2006**, *27*, 6064–6082, doi:10.1016/j.biomaterials.2006.07.008.
11. Altman, G.H.; Diaz, F.; Jakuba, C.; Calabro, T.; Horan, R.L.; Chen, J.; Lu, H.; Richmond, J.; Kaplan, D.L. Silk-Based Biomaterials. *Biomaterials* **2003**, *24*, 401–416, doi:10.1016/s0142-9612(02)00353-8.
12. Jonsson, S.; Wiberg, R.; McGrath, A.M.; Novikov, L.N.; Wiberg, M.; Novikova, L.N.; Kingham, P.J. Effect of Delayed Peripheral Nerve Repair on Nerve Regeneration, Schwann Cell Function and Target Muscle Recovery. *PloS One* **2013**, *8*, e56484, doi:10.1371/journal.pone.0056484.
13. Bruyns, C.N.P.; Jaquet, J.-B.; Schreuders, T.A.R.; Kalmijn, S.; Kuypers, P.D.L.; Hovius, S.E.R. Predictors for Return to Work in Patients with Median and Ulnar Nerve Injuries. *J. Hand Surg.* **2003**, *28*, 28–34, doi:10.1053/jhsu.2003.50026.

14. McAllister, R.M.; Gilbert, S.E.; Calder, J.S.; Smith, P.J. The Epidemiology and Management of Upper Limb Peripheral Nerve Injuries in Modern Practice. *J. Hand Surg. Edinb. Scotl.* **1996**, *21*, 4–13, doi:10.1016/s0266-7681(96)80004-0.
15. Rosberg, H.E.; Carlsson, K.S.; HöjgÅrd, S.; Lindgren, B.; Lundborg, G.; Dahlin, L.B. Injury to the Human Median and Ulnar Nerves in the Forearm – Analysis of Costs for Treatment and Rehabilitation of 69 Patients in Southern Sweden. *J. Hand Surg. Br. Eur. Vol.* **2005**, *30*, 35–39, doi:10.1016/j.jhsb.2004.09.003.
16. Grinsell, D.; Keating, C.P. Peripheral Nerve Reconstruction after Injury: A Review of Clinical and Experimental Therapies. *BioMed Res. Int.* **2014**, *2014*, doi:10.1155/2014/698256.
17. Mohanna, P.-N.; Young, R.C.; Wiberg, M.; Terenghi, G. A Composite Poly-Hydroxybutyrate–Glial Growth Factor Conduit for Long Nerve Gap Repairs. *J. Anat.* **2003**, *203*, 553–565, doi:10.1046/j.1469-7580.2003.00243.x.
18. Bekelis, K.; Missios, S.; Spinner, R.J. Falls and Peripheral Nerve Injuries: An Age-Dependent Relationship. *J. Neurosurg.* **2015**, *123*, 1223–1229, doi:10.3171/2014.11.JNS142111.
19. Noble, J.; Munro, C.A.; Prasad, V.S.; Midha, R. Analysis of Upper and Lower Extremity Peripheral Nerve Injuries in a Population of Patients with Multiple Injuries. *J. Trauma* **1998**, *45*, 116–122, doi:10.1097/00005373-199807000-00025.
20. Terzis, J.K.; Sun, D.D.; Thanos, P.K. Historical and Basic Science Review: Past, Present, and Future of Nerve Repair. *J. Reconstr. Microsurg.* **1997**, *13*, 215–225, doi:10.1055/s-2007-1006407.
21. Pfister, B.J.; Gordon, T.; Loverde, J.R.; Kochar, A.S.; Mackinnon, S.E.; Cullen, D.K. Biomedical Engineering Strategies for Peripheral Nerve Repair: Surgical Applications, State of the Art, and Future Challenges. *Crit. Rev. Biomed. Eng.* **2011**, *39*, 81–124, doi:10.1615/critrevbiomedeng.v39.i2.20.
22. Yap, C.B.; Hirota, T. Sciatic Nerve Motor Conduction Velocity Study. *J. Neurol. Neurosurg. Psychiatry* **1967**, *30*, 233–239, doi:10.1136/jnnp.30.3.233.
23. Gustafson, K.J.; Grinberg, Y.; Joseph, S.; Triolo, R.J. Human Distal Sciatic Nerve Fascicular Anatomy: Implications for Ankle Control Using Nerve-Cuff Electrodes. *J. Rehabil. Res. Dev.* **2012**, *49*, 309–321, doi:10.1682/jrrd.2010.10.0201.
24. Schröder, J.M.; Bohl, J.; von Bardeleben, U. Changes of the Ratio between Myelin Thickness and Axon Diameter in Human Developing Sural, Femoral, Ulnar, Facial, and Trochlear Nerves. *Acta Neuropathol. (Berl.)* **1988**, *76*, 471–483, doi:10.1007/bf00686386.
25. Topp, K.S.; Boyd, B.S. Structure and Biomechanics of Peripheral Nerves: Nerve Responses to Physical Stresses and Implications for Physical Therapist Practice. *Phys. Ther.* **2006**, *86*, 92–109, doi:10.1093/ptj/86.1.92.
26. Griffin, J.W.; Hogan, M.V.; Chhabra, A.B.; Deal, D.N. Peripheral Nerve Repair and Reconstruction. *J. Bone Joint Surg. Am.* **2013**, *95*, 2144–2151, doi:10.2106/jbjs.l.00704.
27. Snaidero, N.; Simons, M. Myelination at a Glance. *J. Cell Sci.* **2014**, *127*, 2999–3004, doi:10.1242/jcs.151043.
28. Sharpee, T.O. Towards Functional Classification of Neuronal Types. *Neuron* **2014**, *83*, 1329–1334, doi:10.1016/j.neuron.2014.08.040.
29. Fields, R.D.; Stevens-Graham, B. New Insights into Neuron-Glia Communication. *Science* **2002**, *298*, 556–562, doi:10.1126/science.298.5593.556.

30. Armstrong, S.J.; Wiberg, M.; Terenghi, G.; Kingham, P.J. ECM Molecules Mediate Both Schwann Cell Proliferation and Activation to Enhance Neurite Outgrowth. *Tissue Eng.* **2007**, *13*, 2863–2870, doi:10.1089/ten.2007.0055.

31. Koopmans, G.; Hasse, B.; Sinis, N. Chapter 19: The Role of Collagen in Peripheral Nerve Repair. *Int. Rev. Neurobiol.* **2009**, *87*, 363–379, doi:10.1016/S0074-7742(09)87019-0.

32. Gao, X.; Wang, Y.; Chen, J.; Peng, J. The Role of Peripheral Nerve ECM Components in the Tissue Engineering Nerve Construction. *Rev. Neurosci.* **2013**, *24*, 443–453, doi:10.1515/revneuro-2013-0022.

33. Chernousov, M.A.; Yu, W.-M.; Chen, Z.-L.; Carey, D.J.; Strickland, S. Regulation of Schwann Cell Function by the Extracellular Matrix. *Glia* **2008**, *56*, 1498–1507, doi:10.1002/glia.20740.

34. Palm, S.L.; Furcht, L.T. Production of Laminin and Fibronectin by Schwannoma Cells: Cell-Protein Interactions in Vitro and Protein Localization in Peripheral Nerve in Vivo. *J. Cell Biol.* **1983**, *96*, 1218–1226, doi:10.1083/jcb.96.5.1218.

35. Guan, W.; Puthenveedu, M.A.; Condic, M.L. Sensory Neuron Subtypes Have Unique Substratum Preference and Receptor Expression before Target Innervation. *J. Neurosci. Off. J. Soc. Neurosci.* **2003**, *23*, 1781–1791, doi:10.1523/jneurosci.23-05-01781.2003.

36. Plantman, S.; Patarroyo, M.; Fried, K.; Domogatskaya, A.; Tryggvason, K.; Hammarberg, H.; Cullheim, S. Integrin-Laminin Interactions Controlling Neurite Outgrowth from Adult DRG Neurons in Vitro. *Mol. Cell. Neurosci.* **2008**, *39*, 50–62, doi:10.1016/j.mcn.2008.05.015.

37. Deister, C.; Aljabari, S.; Schmidt, C.E. Effects of Collagen 1, Fibronectin, Laminin and Hyaluronic Acid Concentration in Multi-Component Gels on Neurite Extension. *J. Biomater. Sci. Polym. Ed.* **2007**, *18*, 983–997, doi:10.1163/156856207781494377.

38. Labrador, R.O.; Butí, M.; Navarro, X. Influence of Collagen and Laminin Gels Concentration on Nerve Regeneration after Resection and Tube Repair. *Exp. Neurol.* **1998**, *149*, 243–252, doi:10.1006/exnr.1997.6650.

39. Baron-Van Evercooren, A.; Kleinman, H.K.; Seppä, H.E.; Rentier, B.; Dubois-Dalcq, M. Fibronectin Promotes Rat Schwann Cell Growth and Motility. *J. Cell Biol.* **1982**, *93*, 211–216, doi:10.1083/jcb.93.1.211.

40. Lee, H.K.; Seo, I.A.; Suh, D.J.; Park, H.T. Nidogen Plays a Role in the Regenerative Axon Growth of Adult Sensory Neurons through Schwann Cells. *J. Korean Med. Sci.* **2009**, *24*, 654–659, doi:10.3346/jkms.2009.24.4.654.

41. Zuo, J.; Neubauer, D.; Graham, J.; Krekoski, C.A.; Ferguson, T.A.; Muir, D. Regeneration of Axons after Nerve Transection Repair Is Enhanced by Degradation of Chondroitin Sulfate Proteoglycan. *Exp. Neurol.* **2002**, *176*, 221–228, doi:10.1006/exnr.2002.7922.

42. Burnett, M.G.; Zager, E.L. Pathophysiology of Peripheral Nerve Injury: A Brief Review. *Neurosurg. Focus* **2004**, *16*, E1, doi:10.3171/foc.2004.16.5.2.

43. Jessen, K.R.; Mirsky, R. The Repair Schwann Cell and Its Function in Regenerating Nerves. *J. Physiol.* **2016**, *594*, 3521–3531, doi:10.1113/JP270874.

44. Keynes, R.; Cook, G.M. Axon Guidance Molecules. *Cell* **1995**, *83*, 161–169, doi:10.1016/0092-8674(95)90157-4.

45. Fawcett, J.W.; Keynes, R.J. Peripheral Nerve Regeneration. *Annu. Rev. Neurosci.* **1990**, *13*, 43–60, doi:10.1146/annurev.ne.13.030190.000355.

46. Chen, Z.-L.; Yu, W.-M.; Strickland, S. Peripheral Regeneration. *Annu. Rev. Neurosci.* **2007**, *30*, 209–233, doi:10.1146/annurev.neuro.30.051606.094337.

47. Fontana, X.; Hristova, M.; Da Costa, C.; Patodia, S.; Thei, L.; Makwana, M.; Spencer-Dene, B.; Latouche, M.; Mirsky, R.; Jessen, K.R.; et al. C-Jun in Schwann Cells Promotes Axonal Regeneration and Motoneuron Survival via Paracrine Signaling. *J. Cell Biol.* **2012**, *198*, 127–141, doi:10.1083/jcb.201205025.
48. Martini, R.; Fischer, S.; López-Vales, R.; David, S. Interactions between Schwann Cells and Macrophages in Injury and Inherited Demyelinating Disease. *Glia* **2008**, *56*, 1566–1577, doi:10.1002/glia.20766.
49. Barrette, B.; Hébert, M.-A.; Filali, M.; Lafortune, K.; Vallières, N.; Gowing, G.; Julien, J.-P.; Lacroix, S. Requirement of Myeloid Cells for Axon Regeneration. *J. Neurosci. Off. J. Soc. Neurosci.* **2008**, *28*, 9363–9376, doi:10.1523/jneurosci.1447-08.2008.
50. Rotshenker, S. Wallerian Degeneration: The Innate-Immune Response to Traumatic Nerve Injury. *J. Neuroinflammation* **2011**, *8*, 109, doi:10.1186/1742-2094-8-109.
51. Terenghi, G. Peripheral Nerve Injury and Regeneration. *Histol. Histopathol.* **1995**, *10*, 709–718.
52. Faroni, A. Expression of GABA Receptors in Stem Cell Derived Schwann Cells and Their Role in the Peripheral Nervous System, The University of Manchester, 2012.
53. Sedaghati, T.; Jell, G.; Seifalian, A.M. Chapter 57 - nerve regeneration and bioengineering. In *Regenerative Medicine Applications in Organ Transplantation*; Lerut, J., Soker, S., Stratta, R.J., Eds.; Academic Press: Boston, 2014; pp. 799–810 ISBN 978-0-12-398523-1.
54. Tupper, J.W.; Crick, J.C.; Matteck, L.R. Fascicular Nerve Repairs. A Comparative Study of Epineurial and Fascicular (Perineurial) Techniques. *Orthop. Clin. North Am.* **1988**, *19*, 57–69.
55. Orgel, M.G. Epineurial versus Perineurial Repair of Peripheral Nerves. *Clin. Plast. Surg.* **1984**, *11*, 101–104.
56. Piskin, A.; Altunkaynak, B.Z.; Çıtlak, A.; Sezgin, H.; Yazıcı, O.; Kaplan, S. Immediate versus Delayed Primary Nerve Repair in the Rabbit Sciatic Nerve. *Neural Regen. Res.* **2013**, *8*, 3410–3415, doi:10.3969/j.issn.1673-5374.2013.36.006.
57. Mackinnon, S.E.; Hudson, A.R. Clinical Application of Peripheral Nerve Transplantation. *Plast. Reconstr. Surg.* **1992**, *90*, 695–699, doi:10.1097/00006534-199210000-00024.
58. Schlosshauer, B.; Dreesmann, L.; Schaller, H.-E.; Sinis, N. Synthetic Nerve Guide Implants in Humans: A Comprehensive Survey. *Neurosurgery* **2006**, *59*, 740–747, doi:10.1227/01.neu.0000235197.36789.42.
59. Nichols, C.M.; Brenner, M.J.; Fox, I.K.; Tung, T.H.; Hunter, D.A.; Rickman, S.R.; Mackinnon, S.E. Effects of Motor versus Sensory Nerve Grafts on Peripheral Nerve Regeneration. *Exp. Neurol.* **2004**, *190*, 347–355, doi:10.1016/j.expneurol.2004.08.003.
60. Weber, R.A.; Breidenbach, W.C.; Brown, R.E.; Jabaley, M.E.; Mass, D.P. A Randomized Prospective Study of Polyglycolic Acid Conduits for Digital Nerve Reconstruction in Humans. *Plast. Reconstr. Surg.* **2000**, *106*, 1036–1048, doi:10.1097/00006534-200010000-00013.
61. Kim, J.; Dellon, A.L. Reconstruction of a Painful Post-Traumatic Medial Plantar Neuroma with a Bioabsorbable Nerve Conduit: A Case Report. *J. Foot Ankle Surg. Off. Publ. Am. Coll. Foot Ankle Surg.* **2001**, *40*, 318–323, doi:10.1016/s1067-2516(01)80069-7.
62. Navissano, M.; Malan, F.; Carnino, R.; Battiston, B. Neurotube for Facial Nerve Repair. *Microsurgery* **2005**, *25*, 268–271, doi:10.1002/micr.20128.

63. Ducic, I.; Maloney, C.T.; Dellon, A.L. Reconstruction of the Spinal Accessory Nerve with Autograft or Neurotube? Two Case Reports. *J. Reconstr. Microsurg.* **2005**, *21*, 29–34, doi:10.1055/s-2005-862777.

64. Battiston, B.; Geuna, S.; Ferrero, M.; Tos, P. Nerve Repair by Means of Tubulization: Literature Review and Personal Clinical Experience Comparing Biological and Synthetic Conduits for Sensory Nerve Repair. *Microsurgery* **2005**, *25*, 258–267, doi:10.1002/micr.20127.

65. Dellon, A.L.; Maloney, C.T. Salvage of Sensation in a Hallux-to-Thumb Transfer by Nerve Tube Reconstruction. *J. Hand Surg.* **2006**, *31*, 1495–1498, doi:10.1016/j.jhsa.2006.07.003.

66. Donoghoe, N.; Rosson, G.D.; Dellon, A.L. Reconstruction of the Human Median Nerve in the Forearm with the Neurotube. *Microsurgery* **2007**, *27*, 595–600, doi:10.1002/micr.20408.

67. Hung, V.; Dellon, A.L. Reconstruction of a 4-Cm Human Median Nerve Gap by Including an Autogenous Nerve Slice in a Bioabsorbable Nerve Conduit: Case Report. *J. Hand Surg.* **2008**, *33*, 313–315, doi:10.1016/j.jhsa.2007.12.008.

68. Rosson, G.D.; Williams, E.H.; Dellon, A.L. Motor Nerve Regeneration across a Conduit. *Microsurgery* **2009**, *29*, 107–114, doi:10.1002/micr.20580.

69. Meek, M.F.; Jansen, K. Two Years after in Vivo Implantation of Poly(DL-Lactide-Epsilon-Caprolactone) Nerve Guides: Has the Material Finally Resorbed? *J. Biomed. Mater. Res. A* **2009**, *89*, 734–738, doi:10.1002/jbm.a.32024.

70. Bertleff, M.J.O.E.; Meek, M.F.; Nicolai, J.-P.A. A Prospective Clinical Evaluation of Biodegradable Neurolac Nerve Guides for Sensory Nerve Repair in the Hand. *J. Hand Surg.* **2005**, *30*, 513–518, doi:10.1016/j.jhsa.2004.12.009.

71. Meek, M.F.; Nicolai, J.-P.A.; Robinson, P.H. Secondary Digital Nerve Repair in the Foot with Resorbable p(DLLA-Epsilon-CL) Nerve Conduits. *J. Reconstr. Microsurg.* **2006**, *22*, 149–151, doi:10.1055/s-2006-939959.

72. Chiriac, S.; Facca, S.; Diaconu, M.; Gouzou, S.; Liverneaux, P. Experience of Using the Bioresorbable Copolyester Poly(DL-Lactide-ε-Caprolactone) Nerve Conduit Guide Neurolac^{TM} for Nerve Repair in Peripheral Nerve Defects: Report on a Series of 28 Lesions. *J. Hand Surg. Eur. Vol.* **2012**, *37*, 342–349, doi:10.1177/1753193411422685.

73. Taras, J.S.; Jacoby, S.M. Repair of Lacerated Peripheral Nerves with Nerve Conduits. *Tech. Hand Up. Extrem. Surg.* **2008**, *12*, 100–106, doi:10.1097/bth.0b013e31815e6334.

74. Ashley, W.W.; Weatherly, T.; Park, T.S. Collagen Nerve Guides for Surgical Repair of Brachial Plexus Birth Injury. *J. Neurosurg.* **2006**, *105*, 452–456, doi:10.3171/ped.2006.105.6.452.

75. Farole, A.; Jamal, B.T. A Bioabsorbable Collagen Nerve Cuff (NeuraGen) for Repair of Lingual and Inferior Alveolar Nerve Injuries: A Case Series. *J. Oral Maxillofac. Surg.* **2008**, *66*, 2058–2062, doi:10.1016/j.joms.2008.06.017.

76. Bushnell, B.D.; McWilliams, A.D.; Whitener, G.B.; Messer, T.M. Early Clinical Experience with Collagen Nerve Tubes in Digital Nerve Repair. *J. Hand Surg.* **2008**, *33*, 1081–1087, doi:10.1016/j.jhsa.2008.03.015.

77. Mosahebi, A.; Simon, M.; Wiberg, M.; Terenghi, G. A Novel Use of Alginate Gydrogel as Schwann Cell Matrix. *Tissue Eng.* **2001**, *7*, 525–534, doi:10.1089/107632701753213156.

78. Gunn, S.; Cosetti, M.; Roland, J.T. Processed Allograft: Novel Use in Facial Nerve Repair after Resection of a Rare Racial Nerve Paraganglioma. *The Laryngoscope* **2010**, *120 Suppl 4*, S206, doi:10.1002/lary.21674.
79. Karabekmez, F.E.; Duymaz, A.; Moran, S.L. Early Clinical Outcomes with the Use of Decellularized Nerve Allograft for Repair of Sensory Defects within the Hand. *Hand N. Y. N* **2009**, *4*, 245–249, doi:10.1007/s11552-009-9195-6.
80. Whitlock, E.L.; Tuffaha, S.H.; Luciano, J.P.; Yan, Y.; Hunter, D.A.; Magill, C.K.; Moore, A.M.; Tong, A.Y.; Mackinnon, S.E.; Borschel, G.H. Processed Allografts and Type I Collagen Conduits for Repair of Peripheral Nerve Gaps. *Muscle Nerve* **2009**, *39*, 787–799, doi:10.1002/mus.21220.
81. Mano, J.F.; Sousa, R.A.; Boesel, L.F.; Neves, N.M.; Reis, R.L. Bioinert, Biodegradable and Injectable Polymeric Matrix Composites for Hard Tissue Replacement: State of the Art and Recent Developments. *Compos. Sci. Technol.* **2004**, *64*, 789–817, doi:10.1016/j.compscitech.2003.09.001.
82. Emans, P.J.; Rhijn, L.W. van; Welting, T.J.M.; Cremers, A.; Wijnands, N.; Spaapen, F.; Voncken, J.W.; Shastri, V.P. Autologous Engineering of Cartilage. *Proc. Natl. Acad. Sci.* **2010**, *107*, 3418–3423, doi:10.1073/pnas.0907774107.
83. Stevens, M.M.; Marini, R.P.; Schaefer, D.; Aronson, J.; Langer, R.; Shastri, V.P. In Vivo Engineering of Organs: The Bone Bioreactor. *Proc. Natl. Acad. Sci. U. S. A.* **2005**, *102*, 11450–11455, doi:10.1073/pnas.0504705102.
84. Hart, A.; Terenghi, G.; Wiberg, M. Tissue engineering for peripheral nerve regeneration. In *Tissue Engineering*; Springer, Berlin, Heidelberg, 2011; pp. 245–262 ISBN 978-3-642-02823-6.
85. Ciardelli, G.; Chiono, V. Materials for Peripheral Nerve Regeneration. *Macromol. Biosci.* **2006**, *6*, 13–26, doi:10.1002/mabi.200500151.
86. Arslantunali, D.; Dursun, T.; Yucel, D.; Hasirci, N.; Hasirci, V. Peripheral Nerve Conduits: Technology Update. *Med. Devices Auckl. NZ* **2014**, *7*, 405–424, doi:10.2147/mder.S59124.
87. Ai, J.; Kiasat-Dolatabadi, A.; Ebrahimi-Barough, S.; Ai, A.; Lotfibakhshaiesh, N.; Norouzi-Javidan, A.; Saberi, H.; Arjmand, B.; Aghayan, H.R. Polymeric Scaffolds in Neural Tissue Engineering: A Review. *Arch. Neurosci.* **2014**, *1*, 15–20, doi:10.5812/archneurosci.9144.
88. Siemionow, M.; Bozkurt, M.; Zor, F. Regeneration and Repair of Peripheral Nerves with Different Biomaterials: Review. *Microsurgery* **2010**, *30*, 574–588, doi:10.1002/micr.20799.
89. Sedaghati, T.; Yang, S.Y.; Mosahebi, A.; Alavijeh, M.S.; Seifalian, A.M. Nerve Regeneration with Aid of Nanotechnology and Cellular Engineering. *Biotechnol. Appl. Biochem.* **2011**, *58*, 288–300, doi:10.1002/bab.51.
90. Sarker, M.D.; Naghieh, S.; McInnes, A.D.; Schreyer, D.J.; Chen, X. Regeneration of Peripheral Nerves by Nerve Guidance Conduits: Influence of Design, Biopolymers, Cells, Growth Factors, and Physical Stimuli. *Prog. Neurobiol.* **2018**, *171*, 125–150, doi:10.1016/j.pneurobio.2018.07.002.
91. Meek, M.F.; Coert, J.H. US Food and Drug Administration/Conformit Europe-Approved Absorbable Nerve Conduits for Clinical Repair of Peripheral and Cranial Nerves. *Ann. Plast. Surg.* **2008**, *60*, 110–116, doi:10.1097/sap.0b013e31804d441c.
92. Yang, Y.; Chen, X.; Ding, F.; Zhang, P.; Liu, J.; Gu, X. Biocompatibility Evaluation of Silk Fibroin with Peripheral Nerve Tissues and Cells in Vitro. *Biomaterials* **2007**, *28*, 1643–1652, doi:10.1016/j.biomaterials.2006.12.004.

93. Yang, Y.; Ding, F.; Wu, J.; Hu, W.; Liu, W.; Liu, J.; Gu, X. Development and Evaluation of Silk Fibroin-Based Nerve Grafts Used for Peripheral Nerve Regeneration. *Biomaterials* **2007**, *28*, 5526–5535, doi:10.1016/j.biomaterials.2007.09.001.

94. Guinea, G.V.; Elices, M.; Pérez-Rigueiro, J.; Plaza, G.R. 9 - Structure and properties of spider and silkworm silk for tissue scaffolds. In *Silk Biomaterials for Tissue Engineering and Regenerative Medicine*; Kundu, S.C., Ed.; Woodhead Publishing, 2014; pp. 239–274 ISBN 978-0-85709-699-9.

95. Das, S.; Bora, U.; Borthakur, B.B. 2 - Applications of silk biomaterials in tissue engineering and regenerative medicine. In *Silk Biomaterials for Tissue Engineering and Regenerative Medicine*; Kundu, S.C., Ed.; Woodhead Publishing, 2014; pp. 41–77 ISBN 978-0-85709-699-9.

96. Adams, I.W.; Bell, M.S.; Driver, R.M.; Fry, W.G. A Comparative Trial of Polyglycolic Acid and Silk as Suture Materials for Accidental Wounds. *Lancet Lond. Engl.* **1977**, *2*, 1216–1217, doi:10.1016/s0140-6736(77)90450-0.

97. Lawrence, B.D.; Wharram, S.; Kluge, J.A.; Leisk, G.G.; Omenetto, F.G.; Rosenblatt, M.I.; Kaplan, D.L. Effect of Hydration on Silk Film Material Properties. *Macromol. Biosci.* **2010**, *10*, 393–403, doi:10.1002/mabi.200900294.

98. Minoura, N.; Tsukada, M.; Nagura, M. Fine Structure and Oxygen Permeability of Silk Fibroin Membrane Treated with Methanol. *Polymer* **1990**, *31*, 265–269, doi:10.1016/0032-3861(90)90117-H.

99. Tang, X.; Ding, F.; Yang, Y.; Hu, N.; Wu, H.; Gu, X. Evaluation on in Vitro Biocompatibility of Silk Fibroin-Based Biomaterials with Primarily Cultured Hippocampal Neurons. *J. Biomed. Mater. Res. A* **2009**, *91A*, 166–174, doi:10.1002/jbm.a.32212.

100. Naghashzargar, E.; Farè, S.; Catto, V.; Bertoldi, S.; Semnani, D.; Karbasi, S.; Tanzi, M.C. Nano/Micro Hybrid Scaffold of PCL or P3HB Nanofibers Combined with Silk Fibroin for Tendon and Ligament Tissue Engineering. *J. Appl. Biomater. Funct. Mater.* **2015**, *13*, 156–168, doi:10.5301/jabfm.5000216.

101. Wang, Y.; Rudym, D.D.; Walsh, A.; Abrahamsen, L.; Kim, H.-J.; Kim, H.S.; Kirker-Head, C.; Kaplan, D.L. In Vivo Degradation of Three-Dimensional Silk Fibroin Scaffolds. *Biomaterials* **2008**, *29*, 3415–3428, doi:10.1016/j.biomaterials.2008.05.002.

102. Fan, H.; Liu, H.; Toh, S.L.; Goh, J.C.H. Anterior Cruciate Ligament Regeneration Using Mesenchymal Stem Cells and Silk Scaffold in Large Animal Model. *Biomaterials* **2009**, *30*, 4967–4977, doi:10.1016/j.biomaterials.2009.05.048.

103. Zhou, J.; Cao, C.; Ma, X.; Hu, L.; Chen, L.; Wang, C. In Vitro and in Vivo Degradation Behavior of Aqueous-Derived Electrospun Silk Fibroin Scaffolds. *Polym. Degrad. Stab.* **2010**, *95*, 1679–1685, doi:10.1016/j.polymdegradstab.2010.05.025.

104. Muthumanickkam, A.; Subramanian, S.; Goweri, M.; Beaula, W.S.; Ganesh, V. Comparative Study on Eri Silk and Mulberry Silk Fibroin Scaffolds for Biomedical Applications. *Iran. Polym. J.* **2013**, *22*, 143–154, doi:10.1007/s13726-012-0113-3.

105. Patra, C.; Talukdar, S.; Novoyatleva, T.; Velagala, S.R.; Mühlfeld, C.; Kundu, B.; Kundu, S.C.; Engel, F.B. Silk Protein Fibroin from Antheraea Mylitta for Cardiac Tissue Engineering. *Biomaterials* **2012**, *33*, 2673–2680, doi:10.1016/j.biomaterials.2011.12.036.

106. Yang, M.; Tanaka, C.; Yamauchi, K.; Ohgo, K.; Kurokawa, M.; Asakura, T. Silklike Materials Constructed from Sequences of Bombyx Mori Silk Fibroin, Fibronectin, and Elastin. *J. Biomed. Mater. Res. A* **2008**, *84*, 353–363, doi:10.1002/jbm.a.31348.

107. Wei, G.-J.; Yao, M.; Wang, Y.-S.; Zhou, C.-W.; Wan, D.-Y.; Lei, P.-Z.; Wen, J.; Lei, H.-W.; Dong, D.-M. Promotion of Peripheral Nerve Regeneration of a Peptide Compound Hydrogel Scaffold. *Int. J. Nanomedicine* **2013**, *8*, 3217–3225, doi:10.2147/ijn.S43681.

108. Xu, M.; Lewis, R.V. Structure of a Protein Superfiber: Spider Dragline Silk. *Proc. Natl. Acad. Sci. U. S. A.* **1990**, *87*, 7120–7124, doi:10.1073/pnas.87.18.7120.

109. Takei, F.; Kikuchi, Y.; Kikuchi, A.; Mizuno, S.; Shimura, K. Further Evidence for Importance of the Subunit Combination of Silk Fibroin in Its Efficient Secretion from the Posterior Silk Gland Cells. *J. Cell Biol.* **1987**, *105*, 175–180, doi:10.1083/jcb.105.1.175.

110. Tanaka, K.; Kajiyama, N.; Ishikura, K.; Waga, S.; Kikuchi, A.; Ohtomo, K.; Takagi, T.; Mizuno, S. Determination of the Site of Disulfide Linkage between Heavy and Light Chains of Silk Fibroin Produced by Bombyx Mori. *Biochim. Biophys. Acta BBA - Protein Struct. Mol. Enzymol.* **1999**, *1432*, 92–103, doi:10.1016/S0167-4838(99)00088-6.

111. Asakura, T.; Yao, J.; Yamane, T.; Umemura, K.; Ulrich, A.S. Heterogeneous Structure of Silk Fibers from Bombyx Mori Resolved by 13C Solid-State NMR Spectroscopy. *J. Am. Chem. Soc.* **2002**, *124*, 8794–8795, doi:10.1021/ja020244e.

112. Gosline, J.M.; Denny, M.W.; DeMont, M.E. Spider Silk as Rubber. *Nature* **1984**, *309*, 551–552, doi:10.1038/309551a0.

113. Hu, A.J.; Zuo, B.Q.; Zhang, F.; Lan, Q.; Zhang, H.X. In Vitro Evaluation of the Growth and Migration of Schwann Cells on Electrospun Silk Fibroin Nanofibers. *Adv. Mater. Res.* **2011**, *175–176*, 220–223, doi:10.4028/www.scientific.net/amr.175-176.220.

114. Allmeling, C.; Jokuszies, A.; Reimers, K.; Kall, S.; Vogt, P.M. Use of Spider Silk Fibres as an Innovative Material in a Biocompatible Artificial Nerve Conduit. *J. Cell. Mol. Med.* **2006**, *10*, 770–777, doi:10.1111/j.1582-4934.2006.tb00436.x.

115. Yu, Q.; Xu, S.; Zhang, H.; Gu, L.; Xu, Y.; Ko, F. Structure–Property Relationship of Regenerated Spider Silk Protein Nano/Microfibrous Scaffold Fabricated by Electrospinning. *J. Biomed. Mater. Res. A* **2014**, *102*, 3828–3837, doi:10.1002/jbm.a.35051.

116. Kuhbier, J.W.; Allmeling, C.; Reimers, K.; Hillmer, A.; Kasper, C.; Menger, B.; Brandes, G.; Guggenheim, M.; Vogt, P.M. Interactions between Spider Silk and Cells--NIH/3T3 Fibroblasts Seeded on Miniature Weaving Frames. *PloS One* **2010**, *5*, 12032, doi:10.1371/journal.pone.0012032.

117. Radtke, C.; Allmeling, C.; Waldmann, K.-H.; Reimers, K.; Thies, K.; Schenk, H.C.; Hillmer, A.; Guggenheim, M.; Brandes, G.; Vogt, P.M. Spider Silk Constructs Enhance Axonal Regeneration and Remyelination in Long Nerve Defects in Sheep. *PloS One* **2011**, *6*, e16990, doi:10.1371/journal.pone.0016990.

118. Allmeling, C.; Jokuszies, A.; Reimers, K.; Kall, S.; Choi, C.Y.; Brandes, G.; Kasper, C.; Scheper, T.; Guggenheim, M.; Vogt, P.M. Spider Silk Fibres in Artificial Nerve Constructs Promote Peripheral Nerve Regeneration. *Cell Prolif.* **2008**, *41*, 408–420, doi:10.1111/j.1365-2184.2008.00534.x.

119. Zhang, H.; Wang, K.; Xing, Y.; Yu, Q. Lysine-Doped Polypyrrole/Spider Silk Protein/Poly(l-Lactic) Acid Containing Nerve Growth Factor Composite Fibers for Neural Application. *Mater. Sci. Eng. C* **2015**, *56*, 564–573, doi:10.1016/j.msec.2015.06.024.

120. Kornfeld, T.; Vogt, P.M.; Bucan, V.; Peck, C.-T.; Reimers, K.; Radtke, C. Characterization and Schwann Cell Seeding of up to 15.0 Cm Long Spider Silk Nerve Conduits for Reconstruction of Peripheral Nerve Defects. *J. Funct. Biomater.* **2016**, *7*, 30, doi:10.3390/jfb7040030.

121. Yanagisawa, S.; Zhu, Z.; Kobayashi, I.; Uchino, K.; Tamada, Y.; Tamura, T.; Asakura, T. Improving Cell-Adhesive Properties of Recombinant Bombyx Mori Silk by Incorporation of Collagen or Fibronectin Derived Peptides Produced by Transgenic Silkworms. *Biomacromolecules* **2007**, *8*, 3487–3492, doi:10.1021/bm700646f.

122. Teulé, F.; Cooper, A.R.; Furin, W.A.; Bittencourt, D.; Rech, E.L.; Brooks, A.; Lewis, R.V. A Protocol for the Production of Recombinant Spider Silk-like Proteins for Artificial Fiber Spinning. *Nat. Protoc.* **2009**, *4*, 341–355, doi:10.1038/nprot.2008.250.

123. Lewicka, M.; Hermanson, O.; Rising, A.U. Recombinant Spider Silk Matrices for Neural Stem Cell Cultures. *Biomaterials* **2012**, *33*, 7712–7717, doi:10.1016/j.biomaterials.2012.07.021.

124. Xia, X.-X.; Qian, Z.-G.; Ki, C.S.; Park, Y.H.; Kaplan, D.L.; Lee, S.Y. Native-Sized Recombinant Spider Silk Protein Produced in Metabolically Engineered Escherichia Coli Results in a Strong Fiber. *Proc. Natl. Acad. Sci. U. S. A.* **2010**, *107*, 14059–14063, doi:10.1073/pnas.1003366107.

125. Müller, C.; Jansson, R.; Elfwing, A.; Askarieh, G.; Karlsson, R.; Hamedi, M.; Rising, A.; Johansson, J.; Inganäs, O.; Hedhammar, M. Functionalisation of Recombinant Spider Silk with Conjugated Polyelectrolytes. *J. Mater. Chem.* **2011**, *21*, 2909–2915, doi:10.1039/c0jm03270k.

126. Rammensee, S.; Huemmerich, D.; Hermanson, K.D.; Scheibel, T.; Bausch, A.R. Rheological Characterization of Hydrogels Formed by Recombinantly Produced Spider Silk. *Appl. Phys. A* **2005**, *82*, 261, doi:10.1007/s00339-005-3431-x.

127. Tokareva, O.; Michalczechen-Lacerda, V.A.; Rech, E.L.; Kaplan, D.L. Recombinant DNA Production of Spider Silk Proteins. *Microb. Biotechnol.* **2013**, *6*, 651–663, doi:10.1111/1751-7915.12081.

128. Heidebrecht, A.; Eisoldt, L.; Diehl, J.; Schmidt, A.; Geffers, M.; Lang, G.; Scheibel, T. Biomimetic Fibers Made of Recombinant Spidroins with the Same Toughness as Natural Spider Silk. *Adv. Mater.* **2015**, *27*, 2189–2194, doi:10.1002/adma.201404234.

129. Mello, C.M.; Soares, J.W.; Arcidiacono, S.; Butler, M.M. Acid Extraction and Purification of Recombinant Spider Silk Proteins. *Biomacromolecules* **2004**, *5*, 1849–1852, doi:10.1021/bm049815g.

130. Hinman, M.B.; Jones, J.A.; Lewis, R.V. Synthetic Spider Silk: A Modular Fiber. *Trends Biotechnol.* **2000**, *18*, 374–379, doi:10.1016/S0167-7799(00)01481-5.

131. Jansson, R.; Lau, C.H.; Ishida, T.; Ramström, M.; Sandgren, M.; Hedhammar, M. Functionalized Silk Assembled from a Recombinant Spider Silk Fusion Protein (Z-4RepCT) Produced in the Methylotrophic Yeast Pichia Pastoris. *Biotechnol. J.* **2016**, *11*, 687–699, doi:10.1002/biot.201500412.

132. Aigner, T.B.; DeSimone, E.; Scheibel, T. Biomedical Applications of Recombinant Silk-Based Materials. *Adv. Mater. 30*, 1704636, doi:10.1002/adma.201704636.

133. Rising, A.; Widhe, M.; Johansson, J.; Hedhammar, M. Spider Silk Proteins: Recent Advances in Recombinant Production, Structure–Function Relationships and Biomedical Applications. *Cell. Mol. Life Sci.* **2011**, *68*, 169–184, doi:10.1007/s00018-010-0462-z.

134. Widhe, M.; Bysell, H.; Nystedt, S.; Schenning, I.; Malmsten, M.; Johansson, J.; Rising, A.; Hedhammar, M. Recombinant Spider Silk as Matrices for Cell Culture. *Biomaterials* **2010**, *31*, 9575–9585, doi:10.1016/j.biomaterials.2010.08.061.

135. Johansson, U.; Al-Khalili, L.; Chotteau, V.; Hedhammar, M. Functionalized Recombinant Spider Silk as Support for Muscle Engineering. *Front. Bioeng. Biotechnol.*, doi:10.3389/conf.fbioe.2016.01.02238.

136. Shalaly, N.D.; Ria, M.; Johansson, U.; Åvall, K.; Berggren, P.-O.; Hedhammar, M. Silk Matrices Promote Formation of Insulin-Secreting Islet-like Clusters. *Biomaterials* **2016**, *90*, 50–61, doi:10.1016/j.biomaterials.2016.03.006.

137. Johansson, U.; Ria, M.; Åvall, K.; Dekki Shalaly, N.; Zaitsev, S.V.; Berggren, P.-O.; Hedhammar, M. Pancreatic Islet Survival and Engraftment Is Promoted by Culture on Functionalized Spider Silk Matrices. *PloS One* **2015**, *10*, 130169, doi:10.1371/journal.pone.0130169.

138. Fredriksson, C.; Hedhammar, M.; Feinstein, R.; Nordling, K.; Kratz, G.; Johansson, J.; Huss, F.; Rising, A. Tissue Response to Subcutaneously Implanted Recombinant Spider Silk: An in Vivo Study. *Materials* **2009**, *2*, 1908–1922, doi:10.3390/ma2041908.

139. Widhe, M.; Johansson, J.; Hedhammar, M.; Rising, A. Current Progress and Limitations of Spider Silk for Biomedical Applications. *Biopolymers* **2012**, *97*, 468–478, doi:10.1002/bip.21715.

140. Scheibel, T. Spider Silks: Recombinant Synthesis, Assembly, Spinning, and Engineering of Synthetic Proteins. *Microb. Cell Factories* **2004**, *3*, 14, doi:10.1186/1475-2859-3-14.

141. An, B.; Tang-Schomer, M.; Huang, W.; He, J.; Jones, J.; Lewis, R.V.; Kaplan, D.L. Physical and Biological Regulation of Neuron Regenerative Growth and Network Formation on Recombinant Dragline Silks. *Biomaterials* **2015**, *48*, 137–146, doi:10.1016/j.biomaterials.2015.01.044.

142. Widhe, M.; Johansson, U.; Hillerdahl, C.-O.; Hedhammar, M. Recombinant Spider Silk with Cell Binding Motifs for Specific Adherence of Cells. *Biomaterials* **2013**, *34*, 8223–8234, doi:10.1016/j.biomaterials.2013.07.058.

143. Moisenovich, M.M.; Pustovalova, O.L.; Yu Arhipova, A.; Vasiljeva, T.V.; Sokolova, O.S.; Bogush, V.G.; Debabov, V.G.; Sevastianov, V.I.; Kirpichnikov, M.P.; Agapov, I.I. In Vitro and in Vivo Biocompatibility Studies of a Recombinant Analogue of Spidroin 1 Scaffolds. *J. Biomed. Mater. Res. A* **2011**, *96A*, 125–131, doi:10.1002/jbm.a.32968.

144. Murphy, A.R.; Romero, I.S. 8 - Biochemical and biophysical properties of native Bombyx mori silk for tissue engineering applications. In *Silk Biomaterials for Tissue Engineering and Regenerative Medicine*; Kundu, S.C., Ed.; Woodhead Publishing, 2014; pp. 219–238 ISBN 978-0-85709-699-9.

145. Koeppel, A.; Holland, C. Progress and Trends in Artificial Silk Spinning: A Systematic Review. *ACS Biomater. Sci. Eng.* **2017**, *3*, 226–237, doi:10.1021/acsbiomaterials.6b00669.

146. Dai, T.; Tanaka, M.; Huang, Y.-Y.; Hamblin, M.R. Chitosan Preparations for Wounds and Burns: Antimicrobial and Wound-Healing Effects. *Expert Rev. Anti Infect. Ther.* **2011**, *9*, 857–879, doi:10.1586/eri.11.59.

147. Wei, Y.; Gong, K.; Zheng, Z.; Wang, A.; Ao, Q.; Gong, Y.; Zhang, X. Chitosan/Silk Fibroin-Based Tissue-Engineered Graft Seeded with Adipose-Derived Stem Cells Enhances Nerve Regeneration in a Rat Model. *J. Mater. Sci. Mater. Med.* **2011**, *22*, 1947–1964, doi:10.1007/s10856-011-4370-z.

148. Gu, Y.; Zhu, J.; Xue, C.; Li, Z.; Ding, F.; Yang, Y.; Gu, X. Chitosan/Silk Fibroin-Based, Schwann Cell-Derived Extracellular Matrix-Modified Scaffolds for Bridging Rat Sciatic Nerve Gaps. *Biomaterials* **2014**, *35*, 2253–2263, doi:10.1016/j.biomaterials.2013.11.087.

149. Xu, Y.; Zhang, Z.; Chen, X.; Li, R.; Li, D.; Feng, S. A Silk Fibroin/Collagen Nerve Scaffold Seeded with a Co-Culture of Schwann Cells and Adipose-Derived Stem Cells

for Sciatic Nerve Regeneration. *PloS One* **2016**, *11*, 147184, doi:10.1371/journal.pone.0147184.

150. Bax, D.V.; Rodgers, U.R.; Bilek, M.M.M.; Weiss, A.S. Cell Adhesion to Tropoelastin Is Mediated via the C-Terminal GRKRK Motif and Integrin AVβ3. *J. Biol. Chem.* **2009**, *284*, 28616–28623, doi:10.1074/jbc.M109.017525.

151. White, J.D.; Wang, S.; Weiss, A.S.; Kaplan, D.L. Silk–Tropoelastin Protein Films for Nerve Guidance. *Acta Biomater.* **2015**, *14*, 1–10, doi:10.1016/j.actbio.2014.11.045.

152. Wang, Y.; Gu, X.; Kong, Y.; Feng, Q.; Yang, Y. Electrospun and Woven Silk Fibroin/Poly(Lactic-Co- Glycolic Acid) Nerve Guidance Conduits for Repairing Peripheral Nerve Injury. *Neural Regen. Res.* **2015**, *10*, 1635, doi:10.4103/1673-5374.167763.

153. Li, S.; Wu, H.; Hu, X.-D.; Tu, C.-Q.; Pei, F.-X.; Wang, G.-L.; Lin, W.; Fan, H.-S. Preparation of Electrospun PLGA-Silk Fibroin Nanofibers-Based Nerve Conduits and Evaluation in Vivo. *Artif. Cells. Blood Substit. Immobil. Biotechnol.* **2012**, *40*, 171–178, doi:10.3109/10731199.2011.637927.

154. Wang, C.-Y.; Zhang, K.-H.; Fan, C.-Y.; Mo, X.-M.; Ruan, H.-J.; Li, F.-F. Aligned Natural–Synthetic Polyblend Nanofibers for Peripheral Nerve Regeneration. *Acta Biomater.* **2011**, *7*, 634–643, doi:10.1016/j.actbio.2010.09.011.

155. Li, G.; Kong, Y.; Zhao, Y.; Zhao, Y.; Zhang, L.; Yang, Y. Fabrication and Characterization of Polyacrylamide/Silk Fibroin Hydrogels for Peripheral Nerve Regeneration. *J. Biomater. Sci. Polym. Ed.* **2015**, *26*, 899–916, doi:10.1080/09205063.2015.1066109.

156. Wu, H.; Zhang, J.; Luo, Y.; Wan, Y.; Sun, S. Mechanical Properties and Permeability of Porous Chitosan–Poly(p-Dioxanone)/Silk Fibroin Conduits Used for Peripheral Nerve Repair. *J. Mech. Behav. Biomed. Mater.* **2015**, *50*, 192–205, doi:10.1016/j.jmbbm.2015.06.016.

157. Teixeira, A.I.; Abrams, G.A.; Bertics, P.J.; Murphy, C.J.; Nealey, P.F. Epithelial Contact Guidance on Well-Defined Micro- and Nanostructured Substrates. *J. Cell Sci.* **2003**, *116*, 1881–1892, doi:10.1242/jcs.00383.

158. Flemming, R.G.; Murphy, C.J.; Abrams, G.A.; Goodman, S.L.; Nealey, P.F. Effects of Synthetic Micro- and Nano-Structured Surfaces on Cell Behavior. *Biomaterials* **1999**, *20*, 573–588, doi:10.1016/s0142-9612(98)00209-9.

159. Tsimbouri, P.; Gadegaard, N.; Burgess, K.; White, K.; Reynolds, P.; Herzyk, P.; Oreffo, R.; Dalby, M.J. Nanotopographical Effects on Mesenchymal Stem Cell Morphology and Phenotype. *J. Cell. Biochem.* **2014**, *115*, 380–390, doi:10.1002/jcb.24673.

160. Spivey, E.C.; Khaing, Z.Z.; Shear, J.B.; Schmidt, C.E. The Fundamental Role of Subcellular Topography in Peripheral Nerve Repair Therapies. *Biomaterials* **2012**, *33*, 4264–4276, doi:10.1016/j.biomaterials.2012.02.043.

161. Sun, M.; McGowan, M.; Kingham, P.J.; Terenghi, G.; Downes, S. Novel Thin-Walled Nerve Conduit with Microgrooved Surface Patterns for Enhanced Peripheral Nerve Repair. *J. Mater. Sci. Mater. Med.* **2010**, *21*, 2765–2774, doi:10.1007/s10856-010-4120-7.

162. Mobasseri, A.; Faroni, A.; Minogue, B.M.; Downes, S.; Terenghi, G.; Reid, A.J. Polymer Scaffolds with Preferential Parallel Grooves Enhance Nerve Regeneration. *Tissue Eng. Part A* **2015**, *21*, 1152–1162, doi:10.1089/ten.tea.2014.0266.

163. Zhang, K.; Jinglei, W.; Huang, C.; Mo, X. Fabrication of Silk Fibroin/P(LLA-CL) Aligned Nanofibrous Scaffolds for Nerve Tissue Engineering. *Macromol. Mater. Eng.* **2013**, *298*, 565–574, doi:10.1002/mame.201200038.

164. Mahairaki, V.; Lim, S.H.; Christopherson, G.T.; Xu, L.; Nasonkin, I.; Yu, C.; Mao, H.-Q.; Koliatsos, V.E. Nanofiber Matrices Promote the Neuronal Differentiation of Human Embryonic Stem Cell-Derived Neural Precursors in Vitro. *Tissue Eng. Part A* **2011**, *17*, 855–863, doi:10.1089/ten.tea.2010.0377.

165. Zheng, J.; Kontoveros, D.; Lin, F.; Hua, G.; Reneker, D.H.; Becker, M.L.; Willits, R.K. Enhanced Schwann Cell Attachment and Alignment Using One-Pot "Dual Click" GRGDS and YIGSR Derivatized Nanofibers. *Biomacromolecules* **2015**, *16*, 357–363, doi:10.1021/bm501552t.

166. Xie, J.; MacEwan, M.R.; Li, X.; Sakiyama-Elbert, S.E.; Xia, Y. Neurite Outgrowth on Nanofiber Scaffolds with Different Orders, Structures, and Surface Properties. *ACS Nano* **2009**, *3*, 1151–1159, doi:10.1021/nn900070z.

167. Gnavi, S.; Fornasari, B.E.; Tonda-Turo, C.; Laurano, R.; Zanetti, M.; Ciardelli, G.; Geuna, S. The Effect of Electrospun Gelatin Fibers Alignment on Schwann Cell and Axon Behavior and Organization in the Perspective of Artificial Nerve Design. *Int. J. Mol. Sci.* **2015**, *16*, 12925–12942, doi:10.3390/ijms160612925.

168. Gupta, D.; Venugopal, J.; Prabhakaran, M.P.; Dev, V.R.G.; Low, S.; Choon, A.T.; Ramakrishna, S. Aligned and Random Nanofibrous Substrate for the in Vitro Culture of Schwann Cells for Neural Tissue Engineering. *Acta Biomater.* **2009**, *5*, 2560–2569, doi:10.1016/j.actbio.2009.01.039.

169. Christopherson, G.T.; Song, H.; Mao, H.-Q. The Influence of Fiber Diameter of Electrospun Substrates on Neural Stem Cell Differentiation and Proliferation. *Biomaterials* **2009**, *30*, 556–564, doi:10.1016/j.biomaterials.2008.10.004.

170. Chen, Y.S.; Hsieh, C.L.; Tsai, C.C.; Chen, T.H.; Cheng, W.C.; Hu, C.L.; Yao, C.H. Peripheral Nerve Regeneration Using Silicone Rubber Chambers Filled with Collagen, Laminin and Fibronectin. *Biomaterials* **2000**, *21*, 1541–1547.

171. Yang, Y.; Ding, F.; Wu, J.; Chen, X.; Liu, J.; Gu, X. Development and biocompatibility evaluation of silk fibroin-based nerve grafts for peripheral nerve regeneration. In *7th Asian-Pacific Conference on Medical and Biological Engineering*; Peng, Y., Weng, X., Eds.; IFMBE Proceedings; Springer Berlin Heidelberg, 2008; pp. 4–8 ISBN 978-3-540-79038-9.

172. Ghaznavi, A.M.; Kokai, L.E.; Lovett, M.L.; Kaplan, D.L.; Marra, K.G. Silk Fibroin Conduits: A Cellular and Functional Assessment of Peripheral Nerve Repair. *Ann. Plast. Surg.* **2011**, *66*, 273–279, doi:10.1097/sap.0b013e3181e6cff7.

173. Tang, X.; Xue, C.; Wang, Y.; Ding, F.; Yang, Y.; Gu, X. Bridging Peripheral Nerve Defects with a Tissue Engineered Nerve Graft Composed of an in Vitro Cultured Nerve Equivalent and a Silk Fibroin-Based Scaffold. *Biomaterials* **2012**, *33*, 3860–3867, doi:10.1016/j.biomaterials.2012.02.008.

174. Yao, L.; de Ruiter, G.C.W.; Wang, H.; Knight, A.M.; Spinner, R.J.; Yaszemski, M.J.; Windebank, A.J.; Pandit, A. Controlling Dispersion of Axonal Regeneration Using a Multichannel Collagen Nerve Conduit. *Biomaterials* **2010**, *31*, 5789–5797, doi:10.1016/j.biomaterials.2010.03.081.

175. Dinis, T.M.; Elia, R.; Vidal, G.; Dermigny, Q.; Denoeud, C.; Kaplan, D.L.; Egles, C.; Marin, F. 3D Multi-Channel Bi-Functionalized Silk Electrospun Conduits for Peripheral Nerve Regeneration. *J. Mech. Behav. Biomed. Mater.* **2015**, *41*, 43–55, doi:10.1016/j.jmbbm.2014.09.029.

176. Zhang, Q.; Zhao, Y.; Yan, S.; Yang, Y.; Zhao, H.; Li, M.; Lu, S.; Kaplan, D.L. Preparation of Uniaxial Multichannel Silk Fibroin Scaffolds for Guiding Primary Neurons. *Acta Biomater.* **2012**, *8*, 2628–2638, doi:10.1016/j.actbio.2012.03.033.

177. Hu, A.; Zuo, B.; Zhang, F.; Zhang, H.; Lan, Q. Evaluation of Electronspun Silk Fibroin-Based Transplants Used for Facial Nerve Repair. *Otol. Neurotol.* **2013**, *34*, 311–318, doi:10.1097/mao.0b013e31827b4bd4.

178. Lundborg, G.; Kanje, M. Bioartificial Nerve Grafts. A Prototype. *Scand. J. Plast. Reconstr. Surg. Hand Surg.* **1996**, *30*, 105–110, doi:10.3109/02844319609056391.

179. Lundborg, G.; Dahlin, L.; Dohi, D.; Kanje, M.; Terada, N. A New Type of “Bioartificial” Nerve Graft for Bridging Extended Defects in Nerves. *J. Hand Surg. Edinb. Scotl.* **1997**, *22*, 299–303.

180. Wang, X.; Hu, W.; Cao, Y.; Yao, J.; Wu, J.; Gu, X. Dog Sciatic Nerve Regeneration across a 30-Mm Defect Bridged by a Chitosan/PGA Artificial Nerve Graft. *Brain J. Neurol.* **2005**, *128*, 1897–1910, doi:10.1093/brain/awh517.

181. Yang, Y.; Yuan, X.; Ding, F.; Yao, D.; Gu, Y.; Liu, J.; Gu, X. Repair of Rat Sciatic Nerve Gap by a Silk Fibroin-Based Scaffold Added with Bone Marrow Mesenchymal Stem Cells. *Tissue Eng. Part A* **2011**, *17*, 2231–2244, doi:10.1089/ten.tea.2010.0633.

182. Lovett, M.; Cannizzaro, C.; Vunjak-Novakovic, G.; Kaplan, D.L. Gel Spinning of Silk Tubes for Tissue Engineering. *Biomaterials* **2008**, *29*, 4650–4657, doi:10.1016/j.biomaterials.2008.08.025.

183. Uebersax, L.; Mattotti, M.; Papaloïzos, M.; Merkle, H.P.; Gander, B.; Meinel, L. Silk Fibroin Matrices for the Controlled Release of Nerve Growth Factor (NGF). *Biomaterials* **2007**, *28*, 4449–4460, doi:10.1016/j.biomaterials.2007.06.034.

184. Mottaghitalab, F.; Farokhi, M.; Zaminy, A.; Kokabi, M.; Soleimani, M.; Mirahmadi, F.; Shokrgozar, M.A.; Sadeghizadeh, M. A Biosynthetic Nerve Guide Conduit Based on Silk/SWNT/Fibronectin Nanocomposite for Peripheral Nerve Regeneration. *PloS One* **2013**, *8*, 74417, doi:10.1371/journal.pone.0074417.

185. Rao, J.; Cheng, Y.; Liu, Y.; Ye, Z.; Zhan, B.; Quan, D.; Xu, Y. A Multi-Walled Silk Fibroin/Silk Sericin Nerve Conduit Coated with Poly(Lactic-Co-Glycolic Acid) Sheath for Peripheral Nerve Regeneration. *Mater. Sci. Eng. C* **2017**, *73*, 319–332, doi:10.1016/j.msec.2016.12.085.

186. McWhorter, F.Y.; Davis, C.T.; Liu, W.F. Physical and Mechanical Regulation of Macrophage Phenotype and Function. *Cell. Mol. Life Sci. CMLS* **2015**, *72*, 1303–1316, doi:10.1007/s00018-014-1796-8.

187. Reeves, A.R.D.; Spiller, K.L.; Freytes, D.O.; Vunjak-Novakovic, G.; Kaplan, D.L. Controlled Release of Cytokines Using Silk-Biomaterials for Macrophage Polarization. *Biomaterials* **2015**, *73*, 272–283, doi:10.1016/j.biomaterials.2015.09.027.

188. Naskar, D.; Nayak, S.; Dey, T.; Kundu, S.C. Non-Mulberry Silk Fibroin Influence Osteogenesis and Osteoblast-Macrophage Cross Talk on Titanium Based Surface. *Sci. Rep.* **2014**, *4*, 4745, doi:10.1038/srep04745.

189. Cui, X.; Wen, J.; Zhao, X.; Chen, X.; Shao, Z.; Jiang, J.J. A Pilot Study of Macrophage Responses to Silk Fibroin Particles. *J. Biomed. Mater. Res. A* **2013**, *101*, 1511–1517, doi:10.1002/jbm.a.34444.

190. Mokarram, N.; Merchant, A.; Mukhatyar, V.; Patel, G.; Bellamkonda, R.V. Effect of Modulating Macrophage Phenotype on Peripheral Nerve Repair. *Biomaterials* **2012**, *33*, 8793–8801, doi:10.1016/j.biomaterials.2012.08.050.

191. Galeotti, F.; Andicsova, A.; Yunus, S.; Botta, C. Precise Surface Patterning of Silk Fibroin Films by Breath Figures. *Soft Matter* **2012**, *8*, 4815–4821, doi:10.1039/c2sm25089f.

192. Mitropoulos, A.N.; Marelli, B.; Ghezzi, C.E.; Applegate, M.B.; Partlow, B.P.; Kaplan, D.L.; Omenetto, F.G. Transparent, Nanostructured Silk Fibroin Hydrogels with

Tunable Mechanical Properties. *ACS Biomater. Sci. Eng.* **2015**, *1*, 964–970, doi:10.1021/acsbiomaterials.5b00215.

193. Dionigi, C.; Posati, T.; Benfenati, V.; Sagnella, A.; Pistone, A.; Bonetti, S.; Ruani, G.; Dinelli, F.; Padeletti, G.; Zamboni, R.; et al. A Nanostructured Conductive Bio-Composite of Silk Fibroin–Single Walled Carbon Nanotubes. *J. Mater. Chem. B* **2014**, *2*, 1424–1431, doi:10.1039/C3TB21172J.

194. Wieringa, P.; Tonazzini, I.; Micera, S.; Cecchini, M. Nanotopography Induced Contact Guidance of the F11 Cell Line during Neuronal Differentiation: A Neuronal Model Cell Line for Tissue Scaffold Development. *Nanotechnology* **2012**, *23*, 275102, doi:10.1088/0957-4484/23/27/275102.

195. Béduer, A.; Vieu, C.; Arnauduc, F.; Sol, J.-C.; Loubinoux, I.; Vaysse, L. Engineering of Adult Human Neural Stem Cells Differentiation through Surface Micropatterning. *Biomaterials* **2012**, *33*, 504–514, doi:10.1016/j.biomaterials.2011.09.073.

196. Lizarraga-Valderrama, L.R.; Taylor, C.S.; Claeyssens, F.; Haycock, J.W.; Knowles, J.C.; Roy, I. Unidirectional Neuronal Cell Growth and Differentiation on Aligned Polyhydroxyalkanoate Blend Microfibres with Varying Diameters. *J. Tissue Eng. Regen. Med.* **2019**, *13*, 1581–1594, doi:https://doi.org/10.1002/term.2911.

197. Wieringa, P.A.; Gonçalves de Pinho, A.R.; Micera, S.; van Wezel, R.J.A.; Moroni, L. Biomimetic Architectures for Peripheral Nerve Repair: A Review of Biofabrication Strategies. *Adv. Healthc. Mater.* **2018**, *7*, 1701164, doi:10.1002/adhm.201701164.

198. You, R.; Zhang, Q.; Li, X.; Yan, S.; Luo, Z.; Qu, J.; Li, M. Multichannel Bioactive Silk Nanofiber Conduits Direct and Enhance Axonal Regeneration after Spinal Cord Injury. *ACS Biomater. Sci. Eng.* **2020**, *6*, 4677–4686, doi:10.1021/acsbiomaterials.0c00698.

199. Park, S.Y.; Ki, C.S.; Park, Y.H.; Lee, K.G.; Kang, S.W.; Kweon, H.Y.; Kim, H.J. Functional Recovery Guided by an Electrospun Silk Fibroin Conduit after Sciatic Nerve Injury in Rats. *J. Tissue Eng. Regen. Med.* **2015**, *9*, 66–76, doi:10.1002/term.1615.

200. Wang, Y.; Kong, Y.; Zhao, Y.; Feng, Q.; Wu, Y.; Tang, X.; Gu, X.; Yang, Y. Electrospun, Reinforcing Network-Containing, Silk Fibroin-Based Nerve Guidance Conduits for Peripheral Nerve Repair. *J. Biomater. Tissue Eng.* **2016**, *6*, 53–60, doi:10.1166/jbt.2016.1417.

201. Jeffries, E.M.; Wang, Y. Biomimetic Micropatterned Multi-channel Nerve Guides by Templated Electrospinning. *Biotechnol. Bioeng.* **2012**, *109*, 1571–1582, doi:10.1002/bit.24412.

202. Townsend-Nicholson, A.; Jayasinghe, S.N. Cell Electrospinning: A Unique Biotechnique for Encapsulating Living Organisms for Generating Active Biological Microthreads/Scaffolds. *Biomacromolecules* **2006**, *7*, 3364–3369, doi:10.1021/bm060649h.

203. Jayasinghe, S.N. Cell Electrospinning: A Novel Tool for Functionalising Fibres, Scaffolds and Membranes with Living Cells and Other Advanced Materials for Regenerative Biology and Medicine. *Analyst* **2013**, *138*, 2215–2223, doi:10.1039/c3an36599a.

204. Arumuganathar, S.; Irvine, S.; McEwan, J.R.; Jayasinghe, S.N. A Novel Direct Aerodynamically Assisted Threading Methodology for Generating Biologically Viable Microthreads Encapsulating Living Primary Cells. *J. Appl. Polym. Sci.* **2008**, *107*, 1215–1225, doi:10.1002/app.27190.

205. Griessinger, E.; Jayasinghe, S.N.; Bonnet, D. Aerodynamically Assisted Bio-Jetting of Hematopoietic Stem Cells. *The Analyst* **2012**, *137*, 1329–1333, doi:10.1039/c2an16027g.

206. Joly, P.; Chavda, N.; Eddaoudi, A.; Jayasinghe, S.N. Bio-Electrospraying and Aerodynamically Assisted Bio-Jetting Whole Human Blood: Interrogating Cell Surface Marker Integrity. *Biomicrofluidics* **2010**, *4*, 011101, doi:10.1063/1.3294083.

207. Geach, T.J.; Mongkoldhumrongkul, N.; Zimmerman, L.B.; Jayasinghe, S.N. Bio-Electrospraying Living Xenopus Tropicalis Embryos: Investigating the Structural, Functional and Biological Integrity of a Model Organism. *Analyst* **2009**, *134*, 743–747, doi:10.1039/b817827e.

208. Cheng, J.; Park, D.; Jun, Y.; Lee, J.; Hyun, J.; Lee, S.-H. Biomimetic Spinning of Silk Fibers and in Situ Cell Encapsulation. *Lab. Chip* **2016**, *16*, 2654–2661, doi:10.1039/c6lc00488a.

209. Cheng, J.; Jun, Y.; Qin, J.; Lee, S.-H. Electrospinning versus Microfluidic Spinning of Functional Fibers for Biomedical Applications. *Biomaterials* **2017**, *114*, 121–143, doi:10.1016/j.biomaterials.2016.10.040.

210. Ştefãnescu, O.; Enescu, D.M.; Lascăr, I. Schwann Cell Cultures: Recent Advances and Novel Approaches to the Reconstruction of Peripheral Nerve Defects. *Rom. J. Morphol. Embryol.* **2012**, *53*, 467–471.

211. Strauch, B.; Rodriguez, D.M.; Diaz, J.; Yu, H.L.; Kaplan, G.; Weinstein, D.E. Autologous Schwann Cells Drive Regeneration through a 6-Cm Autogenous Venous Nerve Conduit. *J. Reconstr. Microsurg.* **2001**, *17*, 589–595, doi:10.1055/s-2001-18812.

212. Hess, J.R.; Brenner, M.J.; Fox, I.K.; Nichols, C.M.; Myckatyn, T.M.; Hunter, D.A.; Rickman, S.R.; Mackinnon, S.E. Use of Cold-Preserved Allografts Seeded with Autologous Schwann Cells in the Treatment of a Long-Gap Peripheral Nerve Injury. *Plast. Reconstr. Surg.* **2007**, *119*, 246–259, doi:10.1097/01.prs.0000245341.71666.97.

213. Tohill, M.; Terenghi, G. Stem-Cell Plasticity and Therapy for Injuries of the Peripheral Nervous System. *Biotechnol. Appl. Biochem.* **2004**, *40,* 17–24, doi:10.1042/ba20030173.

214. Mahay, D.; Terenghi, G.; Shawcross, S.G. Schwann Cell Mediated Trophic Effects by Differentiated Mesenchymal Stem Cells. *Exp. Cell Res.* **2008**, *314*, 2692–2701, doi:10.1016/j.yexcr.2008.05.013.

215. Xu, Y.; Liu, L.; Li, Y.; Zhou, C.; Xiong, F.; Liu, Z.; Gu, R.; Hou, X.; Zhang, C. Myelin-Forming Ability of Schwann Cell-like Cells Induced from Rat Adipose-Derived Stem Cells in Vitro. *Brain Res.* **2008**, *1239*, 49–55, doi:10.1016/j.brainres.2008.08.088.

216. Mortimer, A.E.; Faroni, A.; Kilic, M.A.; Reid, A.J. Maintenance of a Schwann-like Phenotype in Differentiated Adipose-Derived Stem Cells Requires the Synergistic Action of Multiple Growth Factors. *Stem Cells Int.* **2017**, *2017*, 1479137, doi:10.1155/2017/1479137.

217. Schuh, C.M.A.P.; Monforte, X.; Hackethal, J.; Redl, H.; Teuschl, A.H. Covalent Binding of Placental Derived Proteins to Silk Fibroin Improves Schwann Cell Adhesion and Proliferation. *J. Mater. Sci. Mater. Med.* **2016**, *27*, 188, doi:10.1007/s10856-016-5783-5.

218. Musson, D.S.; Naot, D.; Chhana, A.; Matthews, B.G.; McIntosh, J.D.; Lin, S.T.C.; Choi, A.J.; Callon, K.E.; Dunbar, P.R.; Lesage, S.; et al. In Vitro Evaluation of a Novel Non-Mulberry Silk Scaffold for Use in Tendon Regeneration. *Tissue Eng. Part A* **2015**, *21*, 1539–1551, doi:10.1089/ten.tea.2014.0128.

219. Sun, W.; Incitti, T.; Migliaresi, C.; Quattrone, A.; Casarosa, S.; Motta, A. Viability and Neuronal Differentiation of Neural Stem Cells Encapsulated in Silk Fibroin Hydrogel Functionalized with an IKVAV Peptide. *J. Tissue Eng. Regen. Med.* **2015**, *11*, 1532–1541, doi:10.1002/term.2053.

220. Madduri, S.; Papaloïzos, M.; Gander, B. Trophically and Topographically Functionalized Silk Fibroin Nerve Conduits for Guided Peripheral Nerve Regeneration. *Biomaterials* **2010**, *31*, 2323–2334, doi:10.1016/j.biomaterials.2009.11.073.

221. Lin, Y.-C.; Ramadan, M.; Hronik-Tupaj, M.; Kaplan, D.L.; Philips, B.J.; Sivak, W.; Rubin, J.P.; Marra, K.G. Spatially Controlled Delivery of Neurotrophic Factors in Silk Fibroin–Based Nerve Conduits for Peripheral Nerve Repair. *Ann. Plast. Surg.* **2011**, *67*, 147–155, doi:10.1097/sap.0b013e3182240346.

222. Tian, L.; Prabhakaran, M.P.; Hu, J.; Chen, M.; Besenbacher, F.; Ramakrishna, S. Coaxial Electrospun Poly(Lactic Acid)/Silk Fibroin Nanofibers Incorporated with Nerve Growth Factor Support the Differentiation of Neuronal Stem Cells. *RSC Adv.* **2015**, *5*, 49838–49848, doi:10.1039/c5ra05773f.

223. Yu, W.-M.; Yu, H.; Chen, Z.-L.; Strickland, S. Disruption of Laminin in the Peripheral Nervous System Impedes Nonmyelinating Schwann Cell Development and Impairs Nociceptive Sensory Function. *Glia* **2009**, *57*, 850–859, doi:10.1002/glia.20811.

224. Gardiner, N.J. Integrins and the Extracellular Matrix: Key Mediators of Development and Regeneration of the Sensory Nervous System. *Dev. Neurobiol.* **2011**, *71*, 1054–1072, doi:10.1002/dneu.20950.

225. Romano, N.H.; Madl, C.M.; Heilshorn, S.C. Matrix RGD Ligand Density and L1CAM-Mediated Schwann Cell Interactions Synergistically Enhance Neurite Outgrowth. *Acta Biomater.* **2015**, *11*, 48–57, doi:10.1016/j.actbio.2014.10.008.

226. Widhe, M.; Shalaly, N.D.; Hedhammar, M. A Fibronectin Mimetic Motif Improves Integrin Mediated Cell Biding to Recombinant Spider Silk Matrices. *Biomaterials* **2016**, *74*, 256–266, doi:10.1016/j.biomaterials.2015.10.013.

227. Tassler, P.L.; Dellon, A.L.; Canoun, C. Identification of Elastic Fibres in the Peripheral Nerve. *J. Hand Surg. Edinb. Scotl.* **1994**, *19*, 48–54, doi:10.1016/0266-7681(94)90049-3.

228. Xia, X.-X.; Xu, Q.; Hu, X.; Qin, G.; Kaplan, D.L. Tunable Self-Assembly of Genetically Engineered Silk–Elastin-like Protein Polymers. *Biomacromolecules* **2011**, *12*, 3844–3850, doi:10.1021/bm201165h.

229. Wang, Q.; Xia, X.; Huang, W.; Lin, Y.; Xu, Q.; Kaplan, D.L. High Throughput Screening of Dynamic Silk-Elastin-like Protein Biomaterials. *Adv. Funct. Mater.* **2014**, *24*, 4303–4310, doi:10.1002/adfm.201304106.

230. Huang, W.; Rollett, A.; Kaplan, D.L. Silk-Elastin-like Protein Biomaterials for the Controlled Delivery of Therapeutics. *Expert Opin. Drug Deliv.* **2015**, *12*, 779–791, doi:10.1517/17425247.2015.989830.

231. Ghezzi, C.E.; Rnjak-Kovacina, J.; Weiss, A.S.; Kaplan, D.L. Multifunctional Silk-Tropoelastin Biomaterial Systems. *Isr. J. Chem.* **2013**, *53*, 777–786, doi:10.1002/ijch.201300082.

232. Kramer, R.M.; Crookes-Goodson, W.J.; Naik, R.R. The Self-Organizing Properties of Squid Reflectin Protein. *Nat. Mater.* **2007**, *6*, 533–538, doi:10.1038/nmat1930.

233. Bassaglia, Y.; Bekel, T.; Da Silva, C.; Poulain, J.; Andouche, A.; Navet, S.; Bonnaud, L. ESTs Library from Embryonic Stages Reveals Tubulin and Reflectin Diversity in Sepia Officinalis (Mollusca — Cephalopoda). *Gene* **2012**, *498*, 203–211, doi:10.1016/j.gene.2012.01.100.

234. Phan, L.; Kautz, R.; Arulmoli, J.; Kim, I.H.; Le, D.T.T.; Shenk, M.A.; Pathak, M.M.; Flanagan, L.A.; Tombola, F.; Gorodetsky, A.A. Reflectin as a Material for Neural Stem Cell Growth. *ACS Appl. Mater. Interfaces* **2016**, *8*, 278–284, doi:10.1021/acsami.5b08717.

235. Kautz, R.; Phan, L.; Arulmoli, J.; Chatterjee, A.; Kerr, J.P.; Naeim, M.; Long, J.; Allevato, A.; Leal-Cruz, J.E.; Le, L.; et al. Growth and Spatial Control of Murine Neural Stem Cells on Reflectin Films. *ACS Biomater. Sci. Eng.* **2020**, *6*, 1311–1320, doi:10.1021/acsbiomaterials.9b00824.

236. Hersel, U.; Dahmen, C.; Kessler, H. RGD Modified Polymers: Biomaterials for Stimulated Cell Adhesion and Beyond. *Biomaterials* **2003**, *24*, 4385–4415, doi:10.1016/S0142-9612(03)00343-0.

237. Yang, Y.J.; Kwon, Y.; Choi, B.-H.; Jung, D.; Seo, J.H.; Lee, K.H.; Cha, H.J. Multifunctional Adhesive Silk Fibroin with Blending of RGD-Bioconjugated Mussel Adhesive Protein. *Biomacromolecules* **2014**, *15*, 1390–1398, doi:10.1021/bm500001n.

238. Zhang, N.; He, L.; Wu, W. Self-Assembling Peptide Nanofibrous Hydrogel as a Promising Strategy in Nerve Repair after Traumatic Injury in the Nervous System. *Neural Regen. Res.* **2016**, *11*, 717–718, doi:10.4103/1673-5374.182687.

239. Itoh, S.; Takakuda, K.; Samejima, H.; Ohta, T.; Shinomiya, K.; Ichinose, S. Synthetic Collagen Fibers Coated with a Synthetic Peptide Containing the YIGSR Sequence of Laminin to Promote Peripheral Nerve Regeneration in Vivo. *J. Mater. Sci. Mater. Med.* **1999**, *10*, 129–134, doi:10.1023/a:1008977221827.

240. Xiao, W.; Hu, X.Y.; Zeng, W.; Huang, J.H.; Zhang, Y.G.; Luo, Z.J. Rapid Sciatic Nerve Regeneration of Rats by a Surface Modified Collagen-Chitosan Scaffold. *Injury* **2013**, *44*, 941–946, doi:10.1016/j.injury.2013.03.029.

241. Venugopal, J.; Low, S.; Choon, A.T.; Ramakrishna, S. Interaction of Cells and Nanofiber Scaffolds in Tissue Engineering. *J. Biomed. Mater. Res. B Appl. Biomater.* **2008**, *84*, 34–48, doi:10.1002/jbm.b.30841.

242. Gordon, T. The Role of Neurotrophic Factors in Nerve Regeneration. *Neurosurg. Focus* **2009**, *26*, E3, doi:10.3171/foc.2009.26.2.E3.

243. Liu, Q.; Huang, J.; Shao, H.; Song, L.; Zhang, Y. Dual-Factor Loaded Functional Silk Fibroin Scaffolds for Peripheral Nerve Regeneration with the Aid of Neovascularization. *RSC Adv.* **2016**, *6*, 7683–7691, doi:10.1039/c5ra22054h.

244. Catrina, S.; Gander, B.; Madduri, S. Nerve Conduit Scaffolds for Discrete Delivery of Two Neurotrophic Factors. *Eur. J. Pharm. Biopharm.* **2013**, *85*, 139–142, doi:10.1016/j.ejpb.2013.03.030.

245. Kapur, T.A.; Shoichet, M.S. Immobilized Concentration Gradients of Nerve Growth Factor Guide Neurite Outgrowth. *J. Biomed. Mater. Res. A* **2004**, *68*, 235–243, doi:10.1002/jbm.a.10168.

246. Adams, D.N.; Kao, E.Y.-C.; Hypolite, C.L.; Distefano, M.D.; Hu, W.-S.; Letourneau, P.C. Growth Cones Turn and Migrate up an Immobilized Gradient of the Laminin IKVAV Peptide. *J. Neurobiol.* **2005**, *62*, 134–147, doi:10.1002/neu.20075.

247. Moore, K.; MacSween, M.; Shoichet, M. Immobilized Concentration Gradients of Neurotrophic Factors Guide Neurite Outgrowth of Primary Neurons in Macroporous Scaffolds. *Tissue Eng.* **2006**, *12*, 267–278, doi:10.1089/ten.2006.12.267.

248. Wheeler, B.C.; Corey, J.M.; Brewer, G.J.; Branch, D.W. Microcontact Printing for Precise Control of Nerve Cell Growth in Culture. *J. Biomech. Eng.* **1999**, *121*, 73–78, doi:10.1115/1.2798045.

249. Kam, L.; Shain, W.; Turner, J.N.; Bizios, R. Axonal Outgrowth of Hippocampal Neurons on Micro-Scale Networks of Polylysine-Conjugated Laminin. *Biomaterials* **2001**, *22*, 1049–1054, doi:10.1016/S0142-9612(00)00352-5.

250. Oliva, A.A.; James, C.D.; Kingman, C.E.; Craighead, H.G.; Banker, G.A. Patterning Axonal Guidance Molecules Using a Novel Strategy for Microcontact Printing. *Neurochem. Res.* **2003**, *28*, 1639–1648, doi:10.1023/A:1026052820129.

251. Kokai, L.E.; Ghaznavi, A.M.; Marra, K.G. Incorporation of Double-Walled Microspheres into Polymer Nerve Guides for the Sustained Delivery of Glial Cell Line-Derived Neurotrophic Factor. *Biomaterials* **2010**, *31*, 2313–2322, doi:10.1016/j.biomaterials.2009.11.075.

252. Johnson, B.N.; Lancaster, K.Z.; Zhen, G.; He, J.; Gupta, M.K.; Kong, Y.L.; Engel, E.A.; Krick, K.D.; Ju, A.; Meng, F.; et al. 3D Printed Anatomical Nerve Regeneration Pathways. *Adv. Funct. Mater.* **2015**, *25*, 6205–6217, doi:10.1002/adfm.201501760.

253. Roy, J.; Kennedy, T.E.; Costantino, S. Engineered Cell Culture Substrates for Axon Guidance Studies: Moving beyond Proof of Concept. *Lab Chip* **2013**, *13*, 498–508, doi:10.1039/c2lc41002h.

254. Leng, T.; Wu, P.; Mehenti, N.Z.; Bent, S.F.; Marmor, M.F.; Blumenkranz, M.S.; Fishman, H.A. Directed Retinal Nerve Cell Growth for Use in a Retinal Prosthesis Interface. *Invest. Ophthalmol. Vis. Sci.* **2004**, *45*, 4132–4137, doi:10.1167/iovs.03-1335.

255. Dinis, T.M.; Elia, R.; Vidal, G.; Auffret, A.; Kaplan, D.L.; Egles, C. Method to Form a Fiber/Growth Factor Dual-Gradient along Electrospun Silk for Nerve Regeneration. *ACS Appl. Mater. Interfaces* **2014**, *6*, 16817–16826, doi:10.1021/am504159j.

256. Lee, K.; Silva, E.A.; Mooney, D.J. Growth Factor Delivery-Based Tissue Engineering: General Approaches and a Review of Recent Developments. *J. R. Soc. Interface* **2011**, *8*, 153–170, doi:10.1098/rsif.2010.0223.

257. Tung, T.H. Clinical Strategies to Enhance Nerve Regeneration. *Neural Regen. Res.* **2015**, *10*, 22–24, doi:10.4103/1673-5374.150641.

258. Kloth, L.C. Electrical Stimulation for Wound Healing: A Review of Evidence from in Vitro Studies, Animal Experiments, and Clinical Trials. *Int. J. Low. Extrem. Wounds* **2005**, *4*, 23–44, doi:10.1177/1534734605275733.

259. Wang, E.; Zhao, M. Regulation of Tissue Repair and Regeneration by Electric Fields. *Chin. J. Traumatol. Zhonghua Chuang Shang Za Zhi* **2010**, *13*, 55–61.

260. Willand, M.P.; Nguyen, M.-A.; Borschel, G.H.; Gordon, T. Electrical Stimulation to Promote Peripheral Nerve Regeneration. *Neurorehabil. Neural Repair* **2015**, *30*, 490–6, doi:10.1177/1545968315604399.

261. Kerns, J.M.; Fakhouri, A.J.; Weinrib, H.P.; Freeman, J.A. Electrical Stimulation of Nerve Regeneration in the Rat: The Early Effects Evaluated by a Vibrating Probe and Electron Microscopy. *Neuroscience* **1991**, *40*, 93–107, doi:10.1016/0306-4522(91)90177-p.

262. Wood, M.D.; Willits, R.K. Applied Electric Field Enhances DRG Neurite Growth: Influence of Stimulation Media, Surface Coating and Growth Supplements. *J. Neural Eng.* **2009**, *6*, 046003, doi:10.1088/1741-2560/6/4/046003.

263. Geremia, N.M.; Gordon, T.; Brushart, T.M.; Al-Majed, A.A.; Verge, V.M.K. Electrical Stimulation Promotes Sensory Neuron Regeneration and Growth-Associated Gene Expression. *Exp. Neurol.* **2007**, *205*, 347–359, doi:10.1016/j.expneurol.2007.01.040.

264. Freeman, J.A.; Manis, P.B.; Snipes, G.J.; Mayes, B.N.; Samson, P.C.; Wikswo, J.P.; Freeman, D.B. Steady Growth Cone Currents Revealed by a Novel Circularly Vibrating Probe: A Possible Mechanism Underlying Neurite Growth. *J. Neurosci. Res.* **1985**, *13*, 257–283, doi:10.1002/jnr.490130118.

265. Kimura, K.; Yanagida, Y.; Haruyama, T.; Kobatake, E.; Aizawa, M. Gene Expression in the Electrically Stimulated Differentiation of PC12 Cells. *J. Biotechnol.* **1998**, *63*, 55–65.

266. Patel, N.; Poo, M.M. Orientation of Neurite Growth by Extracellular Electric Fields. *J. Neurosci. Off. J. Soc. Neurosci.* **1982**, *2*, 483–496, doi:10.1523/jneurosci.02-04-00483.1982.
267. Sisken, B.F.; Kanje, M.; Lundborg, G.; Herbst, E.; Kurtz, W. Stimulation of Rat Sciatic Nerve Regeneration with Pulsed Electromagnetic Fields. *Brain Res.* **1989**, *485*, 309–316, doi:10.1016/0006-8993(89)90575-1.
268. Sun, S.; Titushkin, I.; Cho, M. Regulation of Mesenchymal Stem Cell Adhesion and Orientation in 3D Collagen Scaffold by Electrical Stimulus. *Bioelectrochemistry Amst. Neth.* **2006**, *69*, 133–141, doi:10.1016/j.bioelechem.2005.11.007.
269. Al-Majed, A.A.; Brushart, T.M.; Gordon, T. Electrical Stimulation Accelerates and Increases Expression of BDNF and TrkB MRNA in Regenerating Rat Femoral Motoneurons. *Eur. J. Neurosci.* **2000**, *12*, 4381–4390.
270. Al-Majed, A.A.; Tam, S.L.; Gordon, T. Electrical Stimulation Accelerates and Enhances Expression of Regeneration-Associated Genes in Regenerating Rat Femoral Motoneurons. *Cell. Mol. Neurobiol.* **2004**, *24*, 379–402, doi:10.1023/b:cemn.0000022770.66463.f7.
271. Strittmatter, S.M.; Vartanian, T.; Fishman, M.C. GAP-43 as a Plasticity Protein in Neuronal Form and Repair. *J. Neurobiol.* **1992**, *23*, 507–520, doi:10.1002/neu.480230506.
272. Palza, H.; Zapata, P.A.; Angulo-Pineda, C. Electroactive Smart Polymers for Biomedical Applications. *Materials* **2019**, *12*, 277, doi:10.3390/ma12020277.
273. Burnstine-Townley, A.; Eshel, Y.; Amdursky, N. Conductive Scaffolds for Cardiac and Neuronal Tissue Engineering: Governing Factors and Mechanisms. *Adv. Funct. Mater.* **2020**, *30*, 1901369, doi:10.1002/adfm.201901369.
274. Amdursky, N.; Wang, X.; Meredith, P.; Bradley, D.D.C.; Stevens, M.M. Long-range Proton Conduction across Free-standing Serum Albumin Mats. *Adv. Mater. Deerfield Beach Fla* **2016**, *28*, 2692–2698, doi:10.1002/adma.201505337.
275. Lu, M.-C.; Ho, C.-Y.; Hsu, S.-F.; Lee, H.-C.; Lin, J.-H.; Yao, C.-H.; Chen, Y.-S. Effects of Electrical Stimulation at Different Frequencies on Regeneration of Transected Peripheral Nerve. *Neurorehabil. Neural Repair* **2008**, *22*, 367–373, doi:10.1177/1545968307313507.
276. Lu, M.-C.; Tsai, C.-C.; Chen, S.-C.; Tsai, F.-J.; Yao, C.-H.; Chen, Y.-S. Use of Electrical Stimulation at Different Current Levels to Promote Recovery after Peripheral Nerve Injury in Rats. *J. Trauma* **2009**, *67*, 1066–1072, doi:10.1097/TA.0b013e318182351a.
277. Kunkel-Bagden, E.; Dai, H.N.; Bregman, B.S. Methods to Assess the Development and Recovery of Locomotor Function after Spinal Cord Injury in Rats. *Exp. Neurol.* **1993**, *119*, 153–164, doi:10.1006/exnr.1993.1017.
278. Yeh, C.-C.; Lin, Y.-C.; Tsai, F.-J.; Huang, C.-Y.; Yao, C.-H.; Chen, Y.-S. Timing of Applying Electrical Stimulation Is an Important Factor Deciding the Success Rate and Maturity of Regenerating Rat Sciatic Nerves. *Neurorehabil. Neural Repair* **2010**, *24*, 730–735, doi:10.1177/1545968310376758.
279. Xie, J.; MacEwan, M.R.; Willerth, S.M.; Li, X.; Moran, D.W.; Sakiyama-Elbert, S.E.; Xia, Y. Conductive Core–Sheath Nanofibers and Their Potential Application in Neural Tissue Engineering. *Adv. Funct. Mater.* **2009**, *19*, 2312–2318, doi:10.1002/adfm.200801904.
280. Schmidt, C.E.; Shastri, V.R.; Vacanti, J.P.; Langer, R. Stimulation of Neurite Outgrowth Using an Electrically Conducting Polymer. *Proc. Natl. Acad. Sci. U. S. A.* **1997**, *94*, 8948–8953, doi:10.1073/pnas.94.17.8948.

281. Zhang, Z.; Rouabhia, M.; Wang, Z.; Roberge, C.; Shi, G.; Roche, P.; Li, J.; Dao, L.H. Electrically Conductive Biodegradable Polymer Composite for Nerve Regeneration: Electricity-Stimulated Neurite Outgrowth and Axon Regeneration. *Artif. Organs* **2007**, *31*, 13–22, doi:10.1111/j.1525-1594.2007.00335.x.

282. Cullen, D.K.; R Patel, A.; Doorish, J.F.; Smith, D.H.; Pfister, B.J. Developing a Tissue-Engineered Neural-Electrical Relay Using Encapsulated Neuronal Constructs on Conducting Polymer Fibers. *J. Neural Eng.* **2008**, *5*, 374–384, doi:10.1088/1741-2560/5/4/002.

283. Richardson-Burns, S.M.; Hendricks, J.L.; Foster, B.; Povlich, L.K.; Kim, D.-H.; Martin, D.C. Polymerization of the Conducting Polymer Poly(3,4-Ethylenedioxythiophene) (PEDOT) around Living Neural Cells. *Biomaterials* **2007**, *28*, 1539–1552, doi:10.1016/j.biomaterials.2006.11.026.

284. Bolin, M.H.; Svennersten, K.; Wang, X.; Chronakis, I.S.; Richter-Dahlfors, A.; Jager, E.W.H.; Berggren, M. Nano-Fiber Scaffold Electrodes Based on PEDOT for Cell Stimulation. *Sens. Actuators B Chem.* **2009**, *142*, 451–456, doi:10.1016/j.snb.2009.04.062.

285. Shin, J.-Y.; Kong, S.-Y.; Yoon, H.J.; Ann, J.; Lee, J.; Kim, H.-J. An Aminopropyl Carbazole Derivative Induces Neurogenesis by Increasing Final Cell Division in Neural Stem Cells. *Biomol. Ther.* **2015**, *23*, 313–319, doi:10.4062/biomolther.2015.016.

286. Lee, Y.-S.; Collins, G.; Arinzeh, T.L. Neurite Extension of Primary Neurons on Electrospun Piezoelectric Scaffolds. *Acta Biomater.* **2011**, *7*, 3877–3886, doi:10.1016/j.actbio.2011.07.013.

287. Young, T.-H.; Chang, H.-H.; Lin, D.-J.; Cheng, L.-P. Surface Modification of Microporous PVDF Membranes for Neuron Culture. *J. Membr. Sci.* **2010**, *350*, 32–41, doi:10.1016/j.memsci.2009.12.009.

288. Young, T.-H.; Lu, J.-N.; Lin, D.-J.; Chang, C.-L.; Chang, H.-H.; Cheng, L.-P. Immobilization of L-Lysine on Dense and Porous Poly(Vinylidene Fluoride) Surfaces for Neuron Culture. *Desalination* **2008**, *234*, 134–143, doi:10.1016/j.desal.2007.09.079.

289. Valentini, R.F.; Vargo, T.G.; Gardella, J.A.; Aebischer, P. Electrically Charged Polymeric Substrates Enhance Nerve Fibre Outgrowth in Vitro. *Biomaterials* **1992**, *13*, 183–190.

290. Valentini, R.F.; Vargo, T.G.; Gardella, J.A.; Aebischer, P. Patterned Neuronal Attachment and Outgrowth on Surface Modified, Electrically Charged Fluoropolymer Substrates. *J. Biomater. Sci. Polym. Ed.* **1993**, *5*, 13–36, doi:10.1163/156856294x00626.

291. Aebischer, P.; Valentini, R.F.; Dario, P.; Domenici, C.; Galletti, P.M. Piezoelectric Guidance Channels Enhance Regeneration in the Mouse Sciatic Nerve after Axotomy. *Brain Res.* **1987**, *436*, 165–168, doi:10.1016/0006-8993(87)91570-8.

292. Fine, E.G.; Valentini, R.F.; Bellamkonda, R.; Aebischer, P. Improved Nerve Regeneration through Piezoelectric Vinylidenefluoride-Trifluoroethylene Copolymer Guidance Channels. *Biomaterials* **1991**, *12*, 775–780, doi:10.1016/0142-9612(91)90029-a.

293. Delaviz, H.; Faghihi, A.; Azizzadeh Delshad, A.; Bahadori, M. hadi; Mohamadi, J.; Roozbehi, A. Repair of Peripheral Nerve Defects Using a Polyvinylidene Fluoride Channel Containing Nerve Growth Factor and Collagen Gel in Adult Rats. *Cell J. Yakhteh* **2011**, *13*, 137–142.

294. Park, S.Y.; Park, J.; Sim, S.H.; Sung, M.G.; Kim, K.S.; Hong, B.H.; Hong, S. Enhanced Differentiation of Human Neural Stem Cells into Neurons on Graphene. *Adv. Mater. Deerfield Beach Fla* **2011**, *23*, H263-267, doi:10.1002/adma.201101503.

295. Lorenzoni, M.; Brandi, F.; Dante, S.; Giugni, A.; Torre, B. Simple and Effective Graphene Laser Processing for Neuron Patterning Application. *Sci. Rep.* **2013**, *3*, doi:10.1038/srep01954.

296. Tang, M.; Song, Q.; Li, N.; Jiang, Z.; Huang, R.; Cheng, G. Enhancement of Electrical Signaling in Neural Networks on Graphene Films. *Biomaterials* **2013**, *34*, 6402–6411, doi:10.1016/j.biomaterials.2013.05.024.

297. Yang, D.; Li, T.; Xu, M.; Gao, F.; Yang, J.; Yang, Z.; Le, W. Graphene Oxide Promotes the Differentiation of Mouse Embryonic Stem Cells to Dopamine Neurons. *Nanomed.* **2014**, *9*, 2445–2455, doi:10.2217/nnm.13.197.

298. Lovat, V.; Pantarotto, D.; Lagostena, L.; Cacciari, B.; Grandolfo, M.; Righi, M.; Spalluto, G.; Prato, M.; Ballerini, L. Carbon Nanotube Substrates Boost Neuronal Electrical Signaling. *Nano Lett.* **2005**, *5*, 1107–1110, doi:10.1021/nl050637m.

299. Hu, H.; Ni, Y.; Montana, V.; Haddon, R.C.; Parpura, V. Chemically Functionalized Carbon Nanotubes as Substrates for Neuronal Growth. *Nano Lett.* **2004**, *4*, 507–511, doi:10.1021/nl035193d.

300. Hu, H.; Ni, Y.; Mandal, S.K.; Montana, V.; Zhao, B.; Haddon, R.C.; Parpura, V. Polyethyleneimine Functionalized Single-Walled Carbon Nanotubes as a Substrate for Neuronal Growth. *J. Phys. Chem. B* **2005**, *109*, 4285–4289, doi:10.1021/jp0441137.

301. Mattson, M.P.; Haddon, R.C.; Rao, A.M. Molecular Functionalization of Carbon Nanotubes and Use as Substrates for Neuronal Growth. *J. Mol. Neurosci.* *14*, 175–182, doi:10.1385/jmn:14:3:175.

302. Li, L.; Yu, M.; Ma, P.X.; Guo, B. Electroactive Degradable Copolymers Enhancing Osteogenic Differentiation from Bone Marrow Derived Mesenchymal Stem Cells. *J. Mater. Chem. B* **2016**, *4*, 471–481, doi:10.1039/c5tb01899d.

303. You, J.-O.; Rafat, M.; Ye, G.J.C.; Auguste, D.T. Nanoengineering the Heart: Conductive Scaffolds Enhance Connexin 43 Expression. *Nano Lett.* **2011**, *11*, 3643–3648, doi:10.1021/nl201514a.

304. Martins, A.M.; Eng, G.; Caridade, S.G.; Mano, J.F.; Reis, R.L.; Vunjak-Novakovic, G. Electrically Conductive Chitosan/Carbon Scaffolds for Cardiac Tissue Engineering. *Biomacromolecules* **2014**, *15*, 635–643, doi:10.1021/bm401679q.

305. Baheiraei, N.; Yeganeh, H.; Ai, J.; Gharibi, R.; Ebrahimi-Barough, S.; Azami, M.; Vahdat, S.; Baharvand, H. Preparation of a Porous Conductive Scaffold from Aniline Pentamer-Modified Polyurethane/PCL Blend for Cardiac Tissue Engineering. *J. Biomed. Mater. Res. A* **2015**, *103*, 3179–3187, doi:10.1002/jbm.a.35447.

306. Kai, D.; Prabhakaran, M.P.; Jin, G.; Ramakrishna, S. Polypyrrole-Contained Electrospun Conductive Nanofibrous Membranes for Cardiac Tissue Engineering. *J. Biomed. Mater. Res. A* **2011**, *99A*, 376–385, doi:10.1002/jbm.a.33200.

307. Kotwal, A.; Schmidt, C.E. Electrical Stimulation Alters Protein Adsorption and Nerve Cell Interactions with Electrically Conducting Biomaterials. *Biomaterials* **2001**, *22*, 1055–1064, doi:10.1016/S0142-9612(00)00344-6.

308. Mihardja, S.S.; Sievers, R.E.; Lee, R.J. The Effect of Polypyrrole on Arteriogenesis in an Acute Rat Infarct Model. *Biomaterials* **2008**, *29*, 4205–4210, doi:10.1016/j.biomaterials.2008.07.021.

309. Li, M.; Guo, Y.; Wei, Y.; MacDiarmid, A.G.; Lelkes, P.I. Electrospinning Polyaniline-Contained Gelatin Nanofibers for Tissue Engineering Applications. *Biomaterials* **2006**, *27*, 2705–2715, doi:10.1016/j.biomaterials.2005.11.037.

310. Repair, Protection and Regeneration of Peripheral Nerve Injury. *Neural Regen. Res.* **2015**, *10*, 1777–1798, doi:10.4103/1673-5374.170301.

311. Das, S.; Sharma, M.; Saharia, D.; Sarma, K.K.; Sarma, M.G.; Borthakur, B.B.; Bora, U. In Vivo Studies of Silk Based Gold Nano-Composite Conduits for Functional Peripheral Nerve Regeneration. *Biomaterials* **2015**, *62*, 66–75, doi:10.1016/j.biomaterials.2015.04.047.

312. Altizer, A.M.; Moriarty, L.J.; Bell, S.M.; Schreiner, C.M.; Scott, W.J.; Borgens, R.B. Endogenous Electric Current Is Associated with Normal Development of the Vertebrate Limb. *Dev. Dyn. Off. Publ. Am. Assoc. Anat.* **2001**, *221*, 391–401, doi:10.1002/dvdy.1158.

313. Adali, T.; Kavalci, E.; Kurt, I. Electrically Conductive Silk Fibroin/Glycerine/Polypyroll Biofilms for Biomedical Applications. *J. Biotechnol.* **2014**, *185*, S36, doi:10.1016/j.jbiotec.2014.07.121.

314. Aznar-Cervantes, S.; Roca, M.I.; Martinez, J.G.; Meseguer-Olmo, L.; Cenis, J.L.; Moraleda, J.M.; Otero, T.F. Fabrication of Conductive Electrospun Silk Fibroin Scaffolds by Coating with Polypyrrole for Biomedical Applications. *Bioelectrochemistry* **2012**, *85*, 36–43, doi:10.1016/j.bioelechem.2011.11.008.

315. Romero, I.S.; Schurr, M.L.; Lally, J.V.; Kotlik, M.Z.; Murphy, A.R. Enhancing the Interface in Silk–Polypyrrole Composites through Chemical Modification of Silk Fibroin. *ACS Appl. Mater. Interfaces* **2013**, *5*, 553–564, doi:10.1021/am301844c.

316. Fengel, C.V.; Bradshaw, N.P.; Severt, S.Y.; Murphy, A.R.; Leger, J.M. Biocompatible Silk-Conducting Polymer Composite Trilayer Actuators. *Smart Mater. Struct.* **2017**, *26*, 055004, doi:10.1088/1361-665X/aa65c4.

317. Hardy, J.G.; Khaing, Z.Z.; Xin, S.; Tien, L.W.; Ghezzi, C.E.; Mouser, D.J.; Sukhavasi, R.C.; Preda, R.C.; Gil, E.S.; Kaplan, D.L.; et al. Into the Groove: Instructive Silk-Polypyrrole Films with Topographical Guidance Cues Direct DRG Neurite Outgrowth. *J. Biomater. Sci. Polym. Ed.* **2015**, *26*, 1327–1342, doi:10.1080/09205063.2015.1090181.

318. Xia, Y.; Lu, Y. Fabrication and Properties of Conductive Conjugated Polymers/Silk Fibroin Composite Fibers. *Compos. Sci. Technol.* **2008**, *68*, 1471–1479, doi:10.1016/j.compscitech.2007.10.044.

319. Zhang, J.; Qiu, K.; Sun, B.; Fang, J.; Zhang, K.; EI-Hamshary, H.; Al-Deyab, S.S.; Mo, X. The Aligned Core–Sheath Nanofibers with Electrical Conductivity for Neural Tissue Engineering. *J. Mater. Chem. B* **2014**, *2*, 7945–7954, doi:10.1039/c4tb01185f.

320. Wang, L.; Wu, Y.; Guo, B.; Ma, P.X. Nanofiber Yarn/Hydrogel Core–Shell Scaffolds Mimicking Native Skeletal Muscle Tissue for Guiding 3D Myoblast Alignment, Elongation, and Differentiation. *ACS Nano* **2015**, *9*, 9167–9179, doi:10.1021/acsnano.5b03644.

321. Zhang, M.; Guo, B. Electroactive 3D Scaffolds Based on Silk Fibroin and Water-Borne Polyaniline for Skeletal Muscle Tissue Engineering. *Macromol. Biosci.* **2017**, *17*, 1700147, doi:10.1002/mabi.201700147.

322. Das, S.; Sharma, M.; Saharia, D.; Sarma, K.K.; Muir, E.M.; Bora, U. Electrospun Silk-Polyaniline Conduits for Functional Nerve Regeneration in Rat Sciatic Nerve Injury Model. *Biomed. Mater.* **2017**, *12*, 045025, doi:10.1088/1748-605x/aa7802.

323. Hardy, J.G.; Geissler, S.A.; Aguilar, D.; Villancio-Wolter, M.K.; Mouser, D.J.; Sukhavasi, R.C.; Cornelison, R.C.; Tien, L.W.; Preda, R.C.; Hayden, R.S.; et al. Instructive Conductive 3d Silk Foam-Based Bone Tissue Scaffolds Enable Electrical Stimulation of Stem Cells for Enhanced Osteogenic Differentiation. *Macromol. Biosci.* **2015**, *15*, 1490–1496, doi:10.1002/mabi.201500171.

324. Aznar-Cervantes, S.; Martínez, J.G.; Bernabeu-Esclapez, A.; Lozano-Pérez, A.A.; Meseguer-Olmo, L.; Otero, T.F.; Cenis, J.L. Fabrication of Electrospun Silk Fibroin Scaffolds Coated with Graphene Oxide and Reduced Graphene for Applications in Biomedicine. *Bioelectrochemistry* **2016**, *108*, 36–45, doi:10.1016/j.bioelechem.2015.12.003.

325. Yang, Y.; Ding, X.; Zou, T.; Peng, G.; Liu, H.; Fan, Y. Preparation and Characterization of Electrospun Graphene/Silk Fibroin Conductive Fibrous Scaffolds. *RSC Adv.* **2017**, *7*, 7954–7963, doi:10.1039/c6ra26807b.

326. Aznar-Cervantes, S.; Pagán, A.; Martínez, J.G.; Bernabeu-Esclapez, A.; Otero, T.F.; Meseguer-Olmo, L.; Paredes, J.I.; Cenis, J.L. Electrospun Silk Fibroin Scaffolds Coated with Reduced Graphene Promote Neurite Outgrowth of PC-12 Cells under Electrical Stimulation. *Mater. Sci. Eng. C* **2017**, *79*, 315–325, doi:10.1016/j.msec.2017.05.055.

327. Hu, X.; Li, J.; Bai, Y. Fabrication of High Strength Graphene/Regenerated Silk Fibroin Composite Fibers by Wet Spinning. *Mater. Lett.* **2017**, *194*, 224–226, doi:10.1016/j.matlet.2017.02.057.

328. Piri, N.; Mottaghitalab, V.; Arbab, S. Conductive Regenerated Silk Fibroin Composite Fiber Containing MWNTs. *E-Polym.* **2013**, *13*, 67–81, doi:10.1515/epoly.2013.13.1.67.

329. Zuo, L.; Zhang, F.; Gao, B.; Zuo, B. Fabrication of Electrical Conductivity and Reinforced Electrospun Silk Nanofibers with MWNTs. *Fibres Text. East. Eur.* **2017**, *25*, 123, doi:10.5604/12303666.1237223.

330. Ling, S.; Qin, Z.; Li, C.; Huang, W.; Kaplan, D.L.; Buehler, M.J. Polymorphic Regenerated Silk Fibers Assembled through Bioinspired Spinning. *Nat. Commun.* **2017**, *8*, 1387, doi:10.1038/s41467-017-00613-5.

331. Cohen-Karni, T.; Jeong, K.J.; Tsui, J.H.; Reznor, G.; Mustata, M.; Wanunu, M.; Graham, A.; Marks, C.; Bell, D.C.; Langer, R.; et al. Nanocomposite Gold-Silk Nanofibers. *Nano Lett.* **2012**, *12*, 5403–5406, doi:10.1021/nl302810c.

332. Yu, D.; Kang, G.; Tian, W.; Lin, L.; Wang, W. Preparation of Conductive Silk Fabric with Antibacterial Properties by Electroless Silver Plating. *Appl. Surf. Sci.* **2015**, *357, Part A*, 1157–1162, doi:10.1016/j.apsusc.2015.09.074.

333. Sun, B.; Wu, T.; Wang, J.; Li, D.; Wang, J.; Gao, Q.; Bhutto, M.A.; El-Hamshary, H.; Al-Deyab, S.S.; Mo, X. Polypyrrole-Coated Poly(L-Lactic Acid-Co-ε-Caprolactone)/Silk Fibroin Nanofibrous Membranes Promoting Neural Cell Proliferation and Differentiation with Electrical Stimulation. *J. Mater. Chem. B* **2016**, *4*, 6670–6679, doi:10.1039/c6tb01710j.

334. Ordinario, D.D.; Phan, L.; Walkup, W.G.; Jocson, J.-M.; Karshalev, E.; Hüsken, N.; Gorodetsky, A.A. Bulk Protonic Conductivity in a Cephalopod Structural Protein. *Nat. Chem.* **2014**, *6*, 596–602, doi:10.1038/nchem.1960.

335. Manchineella, S.; Thrivikraman, G.; Khanum, K.K.; Ramamurthy, P.C.; Basu, B.; Govindaraju, T. Pigmented Silk Nanofibrous Composite for Skeletal Muscle Tissue Engineering. *Adv. Healthc. Mater.* **2016**, *5*, 1222–1232, doi:10.1002/adhm.201501066.

336. Haastert-Talini, K.; Grothe, C. Electrical Stimulation for Promoting Peripheral Nerve Regeneration. *Int. Rev. Neurobiol.* **2013**, *109*, 111–124, doi:10.1016/B978-0-12-420045-6.00005-5.

337. Gordon, T.; English, A.W. Strategies to Promote Peripheral Nerve Regeneration: Electrical Stimulation and/or Exercise. *Eur. J. Neurosci.* **2016**, *43*, 336–350, doi:10.1111/ejn.13005.

338. Gordon, T.; Sulaiman, O.A.R.; Ladak, A. Chapter 24: Electrical Stimulation for Improving Nerve Regeneration: Where Do We Stand? *Int. Rev. Neurobiol.* **2009**, *87*, 433–444, doi:10.1016/S0074-7742(09)87024-4.

339. Hatakeyama, K.; Awaya, K.; Koinuma, M.; Shimizu, Y.; Hakuta, Y.; Matsumoto, Y. Production of Water-Dispersible Reduced Graphene Oxide without Stabilizers Using Liquid-Phase Photoreduction. *Soft Matter* **2017**, *13*, 8353–8356, doi:10.1039/c7sm01386h.

340. Kaur, G.; Adhikari, R.; Cass, P.; Bown, M.; Gunatillake, P. Electrically Conductive Polymers and Composites for Biomedical Applications. *RSC Adv.* **2015**, *5*, 37553–37567, doi:10.1039/c5ra01851j.

341. Song, S.; George, P.M. Conductive Polymer Scaffolds to Improve Neural Recovery. *Neural Regen. Res.* **2017**, *12*, 1976–1978, doi:10.4103/1673-5374.221151.

342. Castro Neto, A.H.; Guinea, F.; Peres, N.M.R.; Novoselov, K.S.; Geim, A.K. The Electronic Properties of Graphene. *Rev. Mod. Phys.* **2009**, *81*, 109–162, doi:10.1103/RevModPhys.81.109.

343. Lee, C.; Wei, X.; Kysar, J.W.; Hone, J. Measurement of the Elastic Properties and Intrinsic Strength of Monolayer Graphene. *Science* **2008**, *321*, 385–388, doi:10.1126/science.1157996.

344. Stoller, M.D.; Park, S.; Zhu, Y.; An, J.; Ruoff, R.S. Graphene-Based Ultracapacitors. *Nano Lett.* **2008**, *8*, 3498–3502, doi:10.1021/nl802558y.

345. Lee, J.; Kim, J.; Kim, S.; Min, D.-H. Biosensors Based on Graphene Oxide and Its Biomedical Application. *Adv. Drug Deliv. Rev.* **2016**, *105*, 275–287, doi:10.1016/j.addr.2016.06.001.

346. Singh, D.P.; Herrera, C.E.; Singh, B.; Singh, S.; Singh, R.K.; Kumar, R. Graphene Oxide: An Efficient Material and Recent Approach for Biotechnological and Biomedical Applications. *Mater. Sci. Eng. C* **2018**, *86*, 173–197, doi:10.1016/j.msec.2018.01.004.

347. Lv, M.; Zhang, Y.; Liang, L.; Wei, M.; Hu, W.; Li, X.; Huang, Q. Effect of Graphene Oxide on Undifferentiated and Retinoic Acid-Differentiated SH-SY5Y Cells Line. *Nanoscale* **2012**, *4*, 3861–3866, doi:10.1039/c2nr30407d.

348. Tasnim, N.; Kumar, A.; Joddar, B. Attenuation of the in Vitro Neurotoxicity of 316L SS by Graphene Oxide Surface Coating. *Mater. Sci. Eng. C* **2017**, *73*, 788–797, doi:10.1016/j.msec.2016.12.123.

349. Oh, H.-G.; Nam, H.-G.; Kim, D.-H.; Kim, M.-H.; Jhee, K.-H.; Song, K.S. Neuroblastoma Cells Grown on Fluorine or Oxygen Treated Graphene Sheets. *Mater. Lett.* **2014**, *131*, 328–331, doi:10.1016/j.matlet.2014.06.013.

350. Serrano, M.C.; Patiño, J.; García-Rama, C.; Ferrer, M.L.; Fierro, J.L.G.; Tamayo, A.; Collazos-Castro, J.E.; Monte, F. del; Gutiérrez, M.C. 3D Free-Standing Porous Scaffolds Made of Graphene Oxide as Substrates for Neural Cell Growth. *J. Mater. Chem. B* **2014**, *2*, 5698–5706, doi:10.1039/c4tb00652f.

351. Wang, J.; Zheng, W.; Chen, L.; Zhu, T.; Shen, W.; Fan, C.; Wang, H.; Mo, X. Enhancement of Schwann Cells Function Using Graphene-Oxide-Modified Nanofiber Scaffolds for Peripheral Nerve Regeneration. *ACS Biomater. Sci. Eng.* **2019**, *5*, 2444–2456, doi:10.1021/acsbiomaterials.8b01564.

352. Yang, K.; Lee, J.; Lee, J.S.; Kim, D.; Chang, G.-E.; Seo, J.; Cheong, E.; Lee, T.; Cho, S.-W. Graphene Oxide Hierarchical Patterns for the Derivation of Electrophysiologically Functional Neuron-like Cells from Human Neural Stem Cells. *ACS Appl. Mater. Interfaces* **2016**, *8*, 17763–17774, doi:10.1021/acsami.6b01804.

353. Portone, A.; Moffa, M.; Gardin, C.; Ferroni, L.; Tatullo, M.; Fabbri, F.; Persano, L.; Piattelli, A.; Zavan, B.; Pisignano, D. Lineage-Specific Commitment of Stem Cells with Organic and Graphene Oxide–Functionalized Nanofibers. *Adv. Funct. Mater.* **2019**, *29*, 1806694, doi:10.1002/adfm.201806694.

354. Ma, Q.; Yang, L.; Jiang, Z.; Song, Q.; Xiao, M.; Zhang, D.; Ma, X.; Wen, T.; Cheng, G. Three-Dimensional Stiff Graphene Scaffold on Neural Stem Cells Behavior. *ACS Appl. Mater. Interfaces* **2016**, *8*, 34227–34233, doi:10.1021/acsami.6b12305.

355. Guo, W.; Wang, S.; Yu, X.; Qiu, J.; Li, J.; Tang, W.; Li, Z.; Mou, X.; Liu, H.; Wang, Z. Construction of a 3D RGO–Collagen Hybrid Scaffold for Enhancement of the Neural Differentiation of Mesenchymal Stem Cells. *Nanoscale* **2016**, *8*, 1897–1904, doi:10.1039/c5nr06602f.

356. Lee, J.S.; Lipatov, A.; Ha, L.; Shekhirev, M.; Andalib, M.N.; Sinitskii, A.; Lim, J.Y. Graphene Substrate for Inducing Neurite Outgrowth. *Biochem. Biophys. Res. Commun.* **2015**, *460*, 267–273, doi:10.1016/j.bbrc.2015.03.023.

357. Hong, S.W.; Lee, J.H.; Kang, S.H.; Hwang, E.Y.; Hwang, Y.-S.; Lee, M.H.; Han, D.-W.; Park, J.-C. Enhanced Neural Cell Adhesion and Neurite Outgrowth on Graphene-Based Biomimetic Substrates. *BioMed Res. Int.* **2014**, *2014*, 212149, doi:10.1155/2014/212149.

358. Tu, Q.; Pang, L.; Wang, L.; Zhang, Y.; Zhang, R.; Wang, J. Biomimetic Choline-like Graphene Oxide Composites for Neurite Sprouting and Outgrowth. *ACS Appl. Mater. Interfaces* **2013**, *5*, 13188–13197, doi:10.1021/am4042004.

359. Akhavan, O.; Ghaderi, E. The Use of Graphene in the Self-Organized Differentiation of Human Neural Stem Cells into Neurons under Pulsed Laser Stimulation. *J. Mater. Chem. B* **2014**, *2*, 5602–5611, doi:10.1039/c4tb00668b.

360. Wang, J.; Cheng, Y.; Chen, L.; Zhu, T.; Ye, K.; Jia, C.; Wang, H.; Zhu, M.; Fan, C.; Mo, X. In Vitro and in Vivo Studies of Electroactive Reduced Graphene Oxide-Modified Nanofiber Scaffolds for Peripheral Nerve Regeneration. *Acta Biomater.* **2019**, *84*, 98–113, doi:10.1016/j.actbio.2018.11.032.

361. Guo, R.; Zhang, S.; Xiao, M.; Qian, F.; He, Z.; Li, D.; Zhang, X.; Li, H.; Yang, X.; Wang, M.; et al. Accelerating Bioelectric Functional Development of Neural Stem Cells by Graphene Coupling: Implications for Neural Interfacing with Conductive Materials. *Biomaterials* **2016**, *106*, 193–204, doi:10.1016/j.biomaterials.2016.08.019.

362. Alessandrino, A.; Fregnan, F.; Biagiotti, M.; Muratori, L.; Bassani, G.A.; Ronchi, G.; Vincoli, V.; Pierimarchi, P.; Geuna, S.; Freddi, G. SilkBridge^{TM}: A Novel Biomimetic and Biocompatible Silk-Based Nerve Conduit. *Biomater. Sci.* **2019**, *7*, 4112–4130, doi:10.1039/c9bm00783k.

363. Gholipourmalekabadi, M.; Samadikuchaksaraei, A.; Seifalian, A.M.; Urbanska, A.M.; Ghanbarian, H.; Hardy, J.G.; Omrani, M.D.; Mozafari, M.; Reis, R.L.; Kundu, S.C. Silk Fibroin/Amniotic Membrane 3D Bi-Layered Artificial Skin. *Biomed. Mater.* **2018**, *13*, 035003, doi:10.1088/1748-605x/aa999b.

364. Zhang, C.; Fan, S.; Shao, H.; Hu, X.; Zhu, B.; Zhang, Y. Graphene Trapped Silk Scaffolds Integrate High Conductivity and Stability. *Carbon* **2019**, *148*, 16–27, doi:10.1016/j.carbon.2019.03.042.

365. Zulan, L.; Zhi, L.; Lan, C.; Sihao, C.; Dayang, W.; Fangyin, D. Reduced Graphene Oxide Coated Silk Fabrics with Conductive Property for Wearable Electronic Textiles Application. *Adv. Electron. Mater.* **2019**, *5*, 1800648, doi:10.1002/aelm.201800648.

366. Zhao, G.; Qing, H.; Huang, G.; Genin, G.M.; Lu, T.J.; Luo, Z.; Xu, F.; Zhang, X. Reduced Graphene Oxide Functionalized Nanofibrous Silk Fibroin Matrices for Engineering Excitable Tissues. *NPG Asia Mater.* **2018**, *10*, 982, doi:10.1038/s41427-018-0092-8.

367. Magaz, A.; Roberts, A.D.; Faraji, S.; Nascimento, T.R.L.; Medeiros, E.S.; Zhang, W.; Greenhalgh, R.D.; Mautner, A.; Li, X.; Blaker, J.J. Porous, Aligned, and Biomimetic Fibers of Regenerated Silk Fibroin Produced by Solution Blow Spinning. *Biomacromolecules* **2018**, *19*, 4542–4553, doi:10.1021/acs.biomac.8b01233.

368. Hodge, J.; Quint, C. The Improvement of Cell Infiltration in an Electrospun Scaffold with Multiple Synthetic Biodegradable Polymers Using Sacrificial PEO Microparticles. *J. Biomed. Mater. Res. A* **2019**, *107*, 1954–1964, doi:10.1002/jbm.a.36706.

369. Francolini, I.; Perugini, E.; Silvestro, I.; Lopreiato, M.; Scotto d'Abusco, A.; Valentini, F.; Placidi, E.; Arciprete, F.; Martinelli, A.; Piozzi, A. Graphene Oxide Oxygen Content Affects Physical and Biological Properties of Scaffolds Based on Chitosan/Graphene Oxide Conjugates. *Materials* **2019**, *12*, 1142, doi:10.3390/ma12071142.

370. Guo, C.; Li, C.; Vu, H.V.; Hanna, P.; Lechtig, A.; Qiu, Y.; Mu, X.; Ling, S.; Nazarian, A.; Lin, S.J.; et al. Thermoplastic Moulding of Regenerated Silk. *Nat. Mater.* **2020**, *19*, 102–108, doi:10.1038/s41563-019-0560-8.

371. Eichhorn, S.J.; Sampson, W.W. Relationships between Specific Surface Area and Pore Size in Electrospun Polymer Fibre Networks. *J. R. Soc. Interface* **2010**, *7*, 641–649, doi:10.1098/rsif.2009.0374.

372. Balu, R.; Reeder, S.; Knott, R.; Mata, J.; de Campo, L.; Dutta, N.K.; Choudhury, N.R. Tough Photocrosslinked Silk Fibroin/Graphene Oxide Nanocomposite Hydrogels. *Langmuir* **2018**, *34*, 9238–9251, doi:10.1021/acs.langmuir.8b01141.

373. Peng, Z.; Yang, X.; Liu, C.; Dong, Z.; Wang, F.; Wang, X.; Hu, W.; Zhang, X.; Zhao, P.; Xia, Q. Structural and Mechanical Properties of Silk from Different Instars of Bombyx Mori. *Biomacromolecules* **2019**, *20*, 1203–1216, doi:10.1021/acs.biomac.8b01576.

374. Wilson, D.; Valluzzi, R.; Kaplan, D. Conformational Transitions in Model Silk Peptides. *Biophys. J.* **2000**, *78*, 2690–2701, doi:10.1016/S0006-3495(00)76813-5.

375. Yang, Y.; Greco, G.; Maniglio, D.; Mazzolai, B.; Migliaresi, C.; Pugno, N.; Motta, A. Spider (Linothele Megatheloides) and Silkworm (Bombyx Mori) Silks: Comparative Physical and Biological Evaluation. *Mater. Sci. Eng. C* **2019**, *107*, 110197, doi:10.1016/j.msec.2019.110197.

376. Kai, D.; Prabhakaran, M.P.; Jin, G.; Ramakrishna, S. Biocompatibility Evaluation of Electrically Conductive Nanofibrous Scaffolds for Cardiac Tissue Engineering. *J. Mater. Chem. B* **2013**, *1*, 2305–2314, doi:10.1039/c3tb00151b.

377. Wang, S.; Sun, C.; Guan, S.; Li, W.; Xu, J.; Ge, D.; Zhuang, M.; Liu, T.; Ma, X. Chitosan/Gelatin Porous Scaffolds Assembled with Conductive Poly(3,4-Ethylenedioxythiophene) Nanoparticles for Neural Tissue Engineering. *J. Mater. Chem. B* **2017**, *5*, 4774–4788, doi:10.1039/c7tb00608j.

378. Tandon, B.; Kamble, P.; Olsson, R.T.; Blaker, J.J.; Cartmell, S.H. Fabrication and Characterisation of Stimuli Responsive Piezoelectric PVDF and Hydroxyapatite-Filled Pvdf Fibrous Membranes. *Molecules* **2019**, *24*, 1903, doi:10.3390/molecules24101903.

379. Huang, L.-K.; Wang, M.-J.J. Image Thresholding by Minimizing the Measures of Fuzziness. *Pattern Recognit.* **1995**, *28*, 41–51, doi:10.1016/0031-3203(94)E0043-k.

380. Ligorio, C.; Zhou, M.; Wychowaniec, J.K.; Zhu, X.; Bartlam, C.; Miller, A.F.; Vijayaraghavan, A.; Hoyland, J.A.; Saiani, A. Graphene Oxide Containing Self-Assembling Peptide Hybrid Hydrogels as a Potential 3D Injectable Cell Delivery Platform for Intervertebral Disc Repair Applications. *Acta Biomater.* **2019**, *92*, 92–103, doi:10.1016/j.actbio.2019.05.004.

381. Serth, J.; Kuczyk, M.A.; Paeslack, U.; Lichtinghagen, R.; Jonas, U. Quantitation of DNA Extracted after Micropreparation of Cells from Frozen and Formalin-Fixed Tissue Sections. *Am. J. Pathol.* **2000**, *156*, 1189–1196, doi:10.1016/S0002-9440(10)64989-9.

382. Cheng, G.; Wang, X.; Tao, S.; Xia, J.; Xu, S. Differences in Regenerated Silk Fibroin Prepared with Different Solvent Systems: From Structures to Conformational Changes. *J. Appl. Polym. Sci.* **2015**, *132*, 41959, doi:10.1002/app.41959.

383. Ye, S.; Feng, J. The Effect of Sonication Treatment of Graphene Oxide on the Mechanical Properties of the Assembled Films. *RSC Adv.* **2016**, *6*, 39681–39687, doi:10.1039/c6ra03996k.

384. Qi, X.; Zhou, T.; Deng, S.; Zong, G.; Yao, X.; Fu, Q. Size-Specified Graphene Oxide Sheets: Ultrasonication Assisted Preparation and Characterization. *J. Mater. Sci.* **2014**, *49*, 1785–1793, doi:10.1007/s10853-013-7866-8.

385. Cai, C.; Sang, N.; Shen, Z.; Zhao, X. Facile and Size-Controllable Preparation of Graphene Oxide Nanosheets Using High Shear Method and Ultrasonic Method. *J. Exp. Nanosci.* **2017**, *12*, 247–262, doi:10.1080/17458080.2017.1303853.

386. Zhou, T.; Li, G.; Lin, S.; Tian, T.; Ma, Q.; Zhang, Q.; Shi, S.; Xue, C.; Ma, W.; Cai, X.; et al. Electrospun Poly(3-Hydroxybutyrate-Co-4-Hydroxybutyrate)/Graphene Oxide Scaffold: Enhanced Properties and Promoted in Vivo Bone Repair in Rats. *ACS Appl. Mater. Interfaces* **2017**, *9*, 42589–42600, doi:10.1021/acsami.7b14267.

387. Wang, C.; Li, Y.; Ding, G.; Xie, X.; Jiang, M. Preparation and Characterization of Graphene Oxide/Poly(Vinyl Alcohol) Composite Nanofibers via Electrospinning. *J. Appl. Polym. Sci.* **2013**, *127*, 3026–3032, doi:10.1002/app.37656.

388. Huang, T.; Zheng, B.; Kou, L.; Gopalsamy, K.; Xu, Z.; Gao, C.; Meng, Y.; Wei, Z. Flexible High Performance Wet-Spun Graphene Fiber Supercapacitors. *RSC Adv.* **2013**, *3*, 23957–23962, doi:10.1039/c3ra44935a.

389. Ezra, M.; Bushman, J.; Shreiber, D.; Schachner, M.; Kohn, J. Porous and Nonporous Nerve Conduits: The Effects of a Hydrogel Luminal Filler with and without a Neurite-Promoting Moiety. *Tissue Eng. Part A* **2016**, *22*, 818–826, doi:10.1089/ten.tea.2015.0354.

390. Roshanbinfar, K.; Mohammadi, Z.; Mesgar, A.S.-M.; Dehghan, M.M.; Oommen, O.P.; Hilborn, J.; Engel, F.B. Carbon Nanotube Doped Pericardial Matrix Derived Electroconductive Biohybrid Hydrogel for Cardiac Tissue Engineering. *Biomater. Sci.* **2019**, *7*, 3906–3917, doi:10.1039/c9bm00434c.

391. Zhao, Y.; Gong, J.; Niu, C.; Wei, Z.; Shi, J.; Li, G.; Yang, Y.; Wang, H. A New Electrospun Graphene-Silk Fibroin Composite Scaffolds for Guiding Schwann Cells. *J. Biomater. Sci. Polym. Ed.* **2017**, *28*, 2171–2185, doi:10.1080/09205063.2017.1386835.

392. Tao, J.; Hu, Y.; Wang, S.; Zhang, J.; Liu, X.; Gou, Z.; Cheng, H.; Liu, Q.; Zhang, Q.; You, S.; et al. A 3D-Engineered Porous Conduit for Peripheral Nerve Repair. *Sci. Rep.* **2017**, *7*, 46038, doi:10.1038/srep46038.

393. Kucinska-Lipka, J.; Marzec, M.; Gubanska, I.; Janik, H. Porosity and Swelling Properties of Novel Polyurethane–Ascorbic Acid Scaffolds Prepared by Different Procedures for Potential Use in Bone Tissue Engineering. *J. Elastomers Plast.* **2017**, *49*, 440–456, doi:10.1177/0095244316672093.

394. Cheng, Y.; Koh, L.-D.; Li, D.; Ji, B.; Han, M.-Y.; Zhang, Y.-W. On the Strength of β-Sheet Crystallites of Bombyx Mori Silk Fibroin. *J. R. Soc. Interface* **2014**, *11*, 20140305, doi:10.1098/rsif.2014.0305.

395. Wang, W.; Caetano, G.; Ambler, W.S.; Blaker, J.J.; Frade, M.A.; Mandal, P.; Diver, C.; Bártolo, P. Enhancing the Hydrophilicity and Cell Attachment of 3D Printed PCL/Graphene Scaffolds for Bone Tissue Engineering. *Materials* **2016**, *9*, 992, doi:10.3390/ma9120992.

396. Belyaeva, L.A.; Deursen, P.M.G. van; Barbetsea, K.I.; Schneider, G.F. Hydrophilicity of Graphene in Water through Transparency to Polar and Dispersive Interactions. *Adv. Mater.* **2018**, *30*, 1703274, doi:10.1002/adma.201703274.

397. Zhang, C.; Zhang, Y.; Shao, H.; Hu, X. Hybrid Silk Fibers Dry-Spun from Regenerated Silk Fibroin/Graphene Oxide Aqueous Solutions. *ACS Appl. Mater. Interfaces* **2016**, *8*, 3349–3358, doi:10.1021/acsami.5b11245.

398. Izyan Syazana Mohd Yusoff, N.; Uzir Wahit, M.; Jaafar, J.; Wong, T.-W. Characterization of Graphene-Silk Fibroin Composites Film. *Mater. Today Proc.* **2018**, *5*, 21853–21860, doi:10.1016/j.matpr.2018.07.042.

399. Chen, X.; Shao, Z.; Marinkovic, N.S.; Miller, L.M.; Zhou, P.; Chance, M.R. Conformation Transition Kinetics of Regenerated Bombyx Mori Silk Fibroin Membrane Monitored by Time-Resolved FTIR Spectroscopy. *Biophys. Chem.* **2001**, *89*, 25–34, doi:10.1016/S0301-4622(00)00213-1.

400. Chen, X.; Knight, D.P.; Shao, Z. β-Turn Formation during the Conformation Transition in Silk Fibroin. *Soft Matter* **2009**, *5*, 2777–2781, doi:10.1039/b900908f.

401. Coh, S.; Tan, L.Z.; Louie, S.G.; Cohen, M.L. Theory of the Raman Spectrum of Rotated Double-Layer Graphene. *Phys. Rev. B* **2013**, *88*, 165431, doi:10.1103/PhysRevB.88.165431.

402. Angulo-Pineda, C.; Srirussamee, K.; Palma, P.; Fuenzalida, V.M.; Cartmell, S.H.; Palza, H. Electroactive 3D Printed Scaffolds Based on Percolated Composites of Polycaprolactone with Thermally Reduced Graphene Oxide for Antibacterial and Tissue Engineering Applications. *Nanomaterials* **2020**, *10*, 428, doi:10.3390/nano10030428.

403. Aguilar-Bolados, H.; Lopez-Manchado, M.A.; Brasero, J.; Avilés, F.; Yazdani-Pedram, M. Effect of the Morphology of Thermally Reduced Graphite Oxide on the Mechanical and Electrical Properties of Natural Rubber Nanocomposites. *Compos. Part B Eng.* **2016**, *87*, 350–356, doi:10.1016/j.compositesb.2015.08.079.

404. Wang, S.; Shi, L.; Zhang, S.; Wang, H.; Cheng, B.; Zhuang, X.; Li, Z. Proton-Conducting Amino Acid-Modified Chitosan Nanofibers for Nanocomposite Proton Exchange Membranes. *Eur. Polym. J.* **2019**, *119*, 327–334, doi:10.1016/j.eurpolymj.2019.07.041.

405. Roshanbinfar, K.; Vogt, L.; Greber, B.; Diecke, S.; Boccaccini, A.R.; Scheibel, T.; Engel, F.B. Electroconductive Biohybrid Hydrogel for Enhanced Maturation and Beating Properties of Engineered Cardiac Tissues. *Adv. Funct. Mater.* **2018**, *28*, 1803951, doi:10.1002/adfm.201803951.

406. Annabi, N.; Shin, S.R.; Tamayol, A.; Miscuglio, M.; Bakooshli, M.A.; Assmann, A.; Mostafalu, P.; Sun, J.-Y.; Mithieux, S.; Cheung, L.; et al. Highly Elastic and Conductive Human-Based Protein Hybrid Hydrogels. *Adv. Mater. Deerfield Beach Fla* **2016**, *28*, 40–49, doi:10.1002/adma.201503255.

407. Zhong, C.; Deng, Y.; Roudsari, A.F.; Kapetanovic, A.; Anantram, M.P.; Rolandi, M. A Polysaccharide Bioprotonic Field-Effect Transistor. *Nat. Commun.* **2011**, *2*, 476, doi:10.1038/ncomms1489.

408. Deng, Y.; Josberger, E.; Jin, J.; Roudsari, A.F.; Rousdari, A.F.; Helms, B.A.; Zhong, C.; Anantram, M.P.; Rolandi, M. H+-Type and OH- -Type Biological Protonic Semiconductors and Complementary Devices. *Sci. Rep.* **2013**, *3*, 2481, doi:10.1038/srep02481.

409. Pena-Francesch, A.; Jung, H.; Hickner, M.A.; Tyagi, M.; Allen, B.D.; Demirel, M.C. Programmable Proton Conduction in Stretchable and Self-Healing Proteins. *Chem. Mater.* **2018**, *30*, 898–905, doi:10.1021/acs.chemmater.7b04574.

410. Tulachan, B.; Meena, S.K.; Rai, R.K.; Mallick, C.; Kusurkar, T.S.; Teotia, A.K.; Sethy, N.K.; Bhargava, K.; Bhattacharya, S.; Kumar, A.; et al. Electricity from the Silk Cocoon Membrane. *Sci. Rep.* **2014**, *4*, 5434, doi:10.1038/srep05434.

411. Gabriel, C.; Gabriel, S.; Corthout, E. The Dielectric Properties of Biological Tissues: I. Literature Survey. *Phys. Med. Biol.* **1996**, *41*, 2231–2249, doi:10.1088/0031-9155/41/11/001.

412. Wu, Y.; Wang, L.; Guo, B.; Shao, Y.; Ma, P.X. Electroactive Biodegradable Polyurethane Significantly Enhanced Schwann Cells Myelin Gene Expression and Neurotrophin Secretion for Peripheral Nerve Tissue Engineering. *Biomaterials* **2016**, *87*, 18–31, doi:10.1016/j.biomaterials.2016.02.010.

413. Niple, J.C.; Daigle, J.P.; Zaffanella, L.E.; Sullivan, T.; Kavet, R. A Portable Meter for Measuring Low Frequency Currents in the Human Body. *Bioelectromagnetics* **2004**, *25*, 369–373, doi:10.1002/bem.20000.

414. Zamani, F.; Amani-Tehran, M.; Latifi, M.; Shokrgozar, M.A. The Influence of Surface Nanoroughness of Electrospun PLGA Nanofibrous Scaffold on Nerve Cell Adhesion and Proliferation. *J. Mater. Sci. Mater. Med.* **2013**, *24*, 1551–1560, doi:10.1007/s10856-013-4905-6.

415. Ryan, A.J.; Kearney, C.J.; Shen, N.; Khan, U.; Kelly, A.G.; Probst, C.; Brauchle, E.; Biccai, S.; Garciarena, C.D.; Vega-Mayoral, V.; et al. Electroconductive Biohybrid Collagen/Pristine Graphene Composite Biomaterials with Enhanced Biological Activity. *Adv. Mater.* **2018**, *30*, 1706442, doi:10.1002/adma.201706442.

416. Stout, D.A.; Yoo, J.; Santiago-Miranda, A.N.; Webster, T.J. Mechanisms of Greater Cardiomyocyte Functions on Conductive Nanoengineered Composites for Cardiovascular Application. *Int. J. Nanomedicine* **2012**, *7*, 5653–5669, doi:10.2147/ijn.s34574.

417. Zhou, Z.; Liu, X.; Wu, W.; Park, S.; Ii, A.L.M.; Terzic, A.; Lu, L. Effective Nerve Cell Modulation by Electrical Stimulation of Carbon Nanotube Embedded Conductive Polymeric Scaffolds. *Biomater. Sci.* **2018**, *6*, 2375–2385, doi:10.1039/c8bm00553b.

418. Akkas, T.; Citak, C.; Sirkecioglu, A.; Güner, F.S. Which Is More Effective for Protein Adsorption: Surface Roughness, Surface Wettability or Swelling? Case Study of Polyurethane Films Prepared from Castor Oil and Poly(Ethylene Glycol). *Polym. Int.* **2013**, *62*, 1202–1209, doi:10.1002/pi.4408.

419. Chong, Y.; Ge, C.; Yang, Z.; Garate, J.A.; Gu, Z.; Weber, J.K.; Liu, J.; Zhou, R. Reduced Cytotoxicity of Graphene Nanosheets Mediated by Blood-Protein Coating. *ACS Nano* **2015**, *9*, 5713–5724, doi:10.1021/nn5066606.

420. Kumar, S.; Parekh, S.H. Linking Graphene-Based Material Physicochemical Properties with Molecular Adsorption, Structure and Cell Fate. *Commun. Chem.* **2020**, *3*, 1–11, doi:10.1038/s42004-019-0254-9.

421. Shi, X.; Chang, H.; Chen, S.; Lai, C.; Khademhosseini, A.; Wu, H. Regulating Cellular Behavior on Few-Layer Reduced Graphene Oxide Films with Well-Controlled Reduction States. *Adv. Funct. Mater.* **2012**, *22*, 751–759, doi:10.1002/adfm.201102305.

422. Diez-Ahedo, R.; Mendibil, X.; Márquez-Posadas, M.C.; Quintana, I.; González, F.; Rodríguez, F.J.; Zilic, L.; Sherborne, C.; Glen, A.; Taylor, C.S.; et al. UV-Casting on Methacrylated PCL for the Production of a Peripheral Nerve Implant Containing an Array of Porous Aligned Microchannels. *Polymers* **2020**, *12*, 971, doi:10.3390/polym12040971.

423. Daud, M.F.B.; Pawar, K.C.; Claeyssens, F.; Ryan, A.J.; Haycock, J.W. An Aligned 3D Neuronal-Glial Co-Culture Model for Peripheral Nerve Studies. *Biomaterials* **2012**, *33*, 5901–5913, doi:10.1016/j.biomaterials.2012.05.008.

424. Mehrali, M.; Thakur, A.; Pennisi, C.P.; Talebian, S.; Arpanaei, A.; Nikkhah, M.; Dolatshahi-Pirouz, A. Nanoreinforced Hydrogels for Tissue Engineering: Biomaterials That Are Compatible with Load-Bearing and Electroactive Tissues. *Adv. Mater.* **2017**, *29*, 1603612, doi:10.1002/adma.201603612.

425. Tandon, B.; Magaz, A.; Balint, R.; Blaker, J.J.; Cartmell, S.H. Electroactive Biomaterials: Vehicles for Controlled Delivery of Therapeutic Agents for Drug Delivery and Tissue Regeneration. *Adv. Drug Deliv. Rev.* **2018**, *129*, 148–168, doi:10.1016/j.addr.2017.12.012.

426. Balint, R.; Cassidy, N.J.; Cartmell, S.H. Conductive Polymers: Towards a Smart Biomaterial for Tissue Engineering. *Acta Biomater.* **2014**, *10*, 2341–2353, doi:10.1016/j.actbio.2014.02.015.

427. Guimard, N.K.; Gomez, N.; Schmidt, C.E. Conducting Polymers in Biomedical Engineering. *Prog. Polym. Sci.* **2007**, *32*, 876–921, doi:10.1016/j.progpolymsci.2007.05.012.

428. Tseghai, G.B.; Mengistie, D.A.; Malengier, B.; Fante, K.A.; Van Langenhove, L. PEDOT:PSS-Based Conductive Textiles and Their Applications. *Sensors* **2020**, *20*, 1881, doi:10.3390/s20071881.

429. Thaning, E.M.; Asplund, M.L.M.; Nyberg, T.A.; Inganäs, O.W.; Holst, H. von Stability of Poly(3,4-Ethylene Dioxythiophene) Materials Intended for Implants. *J. Biomed. Mater. Res. B Appl. Biomater.* **2010**, *93B*, 407–415, doi:10.1002/jbm.b.31597.

430. Spencer, A.R.; Primbetova, A.; Koppes, A.N.; Koppes, R.A.; Fenniri, H.; Annabi, N. Electroconductive Gelatin Methacryloyl-PEDOT:PSS Composite Hydrogels: Design, Synthesis, and Properties. *ACS Biomater. Sci. Eng.* **2018**, *4*, 1558–1567, doi:10.1021/acsbiomaterials.8b00135.

431. Wang, S.; Guan, S.; Li, W.; Ge, D.; Xu, J.; Sun, C.; Liu, T.; Ma, X. 3D Culture of Neural Stem Cells within Conductive PEDOT Layer-Assembled Chitosan/Gelatin Scaffolds for Neural Tissue Engineering. *Mater. Sci. Eng. C* **2018**, *93*, 890–901, doi:10.1016/j.msec.2018.08.054.

432. Solazzo, M.; O’Brien, F.J.; Nicolosi, V.; Monaghan, M.G. The Rationale and Emergence of Electroconductive Biomaterial Scaffolds in Cardiac Tissue Engineering. *APL Bioeng.* **2019**, *3*, 041501, doi:10.1063/1.5116579.

433. Yildirim, E.; Wu, G.; Yong, X.; Tan, T.L.; Zhu, Q.; Xu, J.; Ouyang, J.; Wang, J.-S.; Yang, S.-W. A Theoretical Mechanistic Study on Electrical Conductivity Enhancement of DMSO Treated PEDOT:PSS. *J. Mater. Chem. C* **2018**, *6*, 5122–5131, doi:10.1039/c8tc00917a.

434. El Zein, A.; Huppé, C.; Cochrane, C. Development of a Flexible Strain Sensor Based on PEDOT:PSS for Thin Film Structures. *Sensors* **2017**, *17*, 1337, doi:10.3390/s17061337.

435. Pot, S.A.; Liliensiek, S.J.; Myrna, K.E.; Bentley, E.; Jester, J.V.; Nealey, P.F.; Murphy, C.J. Nanoscale Topography–Induced Modulation of Fundamental Cell Behaviors of Rabbit Corneal Keratocytes, Fibroblasts, and Myofibroblasts. *Invest. Ophthalmol. Vis. Sci.* **2010**, *51*, 1373–1381, doi:10.1167/iovs.09-4074.

436. Ahn, E.H.; Kim, Y.; Kshitiz; An, S.S.; Afzal, J.; Lee, S.; Kwak, M.; Suh, K.-Y.; Kim, D.-H.; Levchenko, A. Spatial Control of Adult Stem Cell Fate Using Nanotopographic Cues. *Biomaterials* **2014**, *35*, 2401–2410, doi:10.1016/j.biomaterials.2013.11.037.

437. Li, W.-J.; Cooper, J.A. Fibrous scaffolds for tissue engineering. In *Biomaterials for Tissue Engineering Applications*; Springer, Vienna, 2011; pp. 47–73 ISBN 978-3-7091-0384-5.

438. Shamsah, A.H.; Cartmell, S.H.; Richardson, S.M.; Bosworth, L.A. Tissue Engineering the Annulus Fibrosus Using 3D Rings of Electrospun PCL:PLLA Angle-Ply Nanofiber Sheets. *Front. Bioeng. Biotechnol.* **2020**, *7*, 437, doi:10.3389/fbioe.2019.00437.

439. Tsukada, S.; Nakashima, H.; Torimitsu, K. Conductive Polymer Combined Silk Fiber Bundle for Bioelectrical Signal Recording. *PloS One* **2012**, *7*, 33689, doi:10.1371/journal.pone.0033689.

440. Müller, C.; Hamedi, M.; Karlsson, R.; Jansson, R.; Marcilla, R.; Hedhammar, M.; Inganäs, O. Woven Electrochemical Transistors on Silk Fibers. *Adv. Mater.* **2011**, *23*, 898–901, doi:10.1002/adma.201003601.

441. Ryan, J.D.; Mengistie, D.A.; Gabrielsson, R.; Lund, A.; Müller, C. Machine-Washable PEDOT:PSS Dyed Silk Yarns for Electronic Textiles. *ACS Appl. Mater. Interfaces* **2017**, *9*, 9045–9050, doi:10.1021/acsami.7b00530.

442. Jiang, Y.; Xu, M.; Yadavalli, V.K. Silk Fibroin-Sheathed Conducting Polymer Wires as Organic Connectors for Biosensors. *Biosensors* **2019**, *9*, 103, doi:10.3390/bios9030103.

443. Severt, S.Y.; Ostrovsky-Snider, N.A.; Leger, J.M.; Murphy, A.R. Versatile Method for Producing 2D and 3D Conductive Biomaterial Composites Using Sequential Chemical and Electrochemical Polymerization. *ACS Appl. Mater. Interfaces* **2015**, *7*, 25281–25288, doi:10.1021/acsami.5b07332.

444. Teshima, T.; Nakashima, H.; Kasai, N.; Sasaki, S.; Tanaka, A.; Tsukada, S.; Sumitomo, K. Mobile Silk Fibroin Electrode for Manipulation and Electrical Stimulation of Adherent Cells. *Adv. Funct. Mater.* **2016**, *26*, 8185–8193, doi:10.1002/adfm.201603302.

445. Pal, R.K.; Farghaly, A.A.; Collinson, M.M.; Kundu, S.C.; Yadavalli, V.K. Photolithographic Micropatterning of Conducting Polymers on Flexible Silk Matrices. *Adv. Mater.* **2016**, *28*, 1406–1412, doi:10.1002/adma.201504736.

446. Dodel, M.; Hemmati Nejad, N.; Bahrami, S.H.; Soleimani, M.; Mohammadi Amirabad, L.; Hanaee-Ahvaz, H.; Atashi, A. Electrical Stimulation of Somatic Human Stem Cells Mediated by Composite Containing Conductive Nanofibers for Ligament Regeneration. *Biol. J. Int. Assoc. Biol. Stand.* **2017**, *46*, 99–107, doi:10.1016/j.biologicals.2017.01.007.

447. Shen, G.; Hu, X.; Guan, G.; Wang, L. Surface Modification and Characterisation of Silk Fibroin Fabric Produced by the Layer-by-Layer Self-Assembly of Multilayer Alginate/Regenerated Silk Fibroin. *PloS One* **2015**, *10*, 0124811, doi:10.1371/journal.pone.0124811.

448. Matsumoto, A.; Chen, J.; Collette, A.L.; Kim, U.-J.; Altman, G.H.; Cebe, P.; Kaplan, D.L. Mechanisms of Silk Fibroin Sol−gel Transitions. *J. Phys. Chem. B* **2006**, *110*, 21630–21638, doi:10.1021/jp056350v.

449. Regoutz, A.; Mascheck, M.; Wiell, T.; Eriksson, S.K.; Liljenberg, C.; Tetzner, K.; Williamson, B.A.D.; Scanlon, D.O.; Palmgren, P. A Novel Laboratory-Based Hard X-Ray Photoelectron Spectroscopy System. *Rev. Sci. Instrum.* **2018**, *89*, 073105, doi:10.1063/1.5039829.

450. Spencer, B.F.; Maniyarasu, S.; Reed, B.; Cant, D.J.H.; Ahumada-Lazo, R.; Thomas, A.G.; Muryn, C.A.; Maschek, M.; Eriksson, S.K.; Wiell, T.; et al. Dataset: Hard X-Rays and Inelastic Background Modelling Extend Photoelectron Spectroscopy below the Surface for the Detection of Buried Layers. *Appl. Surf. Sci.* **2020**, *[in peer review]*, doi:https://doi.org/10.17632/8d62nnf57b.1.

451. Alhummiany, H.; Rafique, S.; Sulaiman, K. XPS Analysis of the Improved Operational Stability of Organic Solar Cells Using a V2O5 and PEDOT:PSS Composite Layer: Effect of Varied Atmospheric Conditions. *J. Phys. Chem. C* **2017**, *121*, 7649–7658, doi:10.1021/acs.jpcc.6b13016.

452. Whitemarsh, R.C.M.; Pier, C.L.; Tepp, W.H.; Pellett, S.; Johnson, E.A. Model for Studying Clostridium Botulinum Neurotoxin Using Differentiated Motor Neuron-like NG108-15 Cells. *Biochem. Biophys. Res. Commun.* **2012**, *427*, 426–430, doi:10.1016/j.bbrc.2012.09.082.

453. Ouyang, J.; Xu, Q.; Chu, C.-W.; Yang, Y.; Li, G.; Shinar, J. On the Mechanism of Conductivity Enhancement in Poly(3,4-Ethylenedioxythiophene):Poly(Styrene Sulfonate) Film through Solvent Treatment. *Polymer* **2004**, *45*, 8443–8450, doi:10.1016/j.polymer.2004.10.001.

454. Gonzalez-Perez, F.; Udina, E.; Navarro, X. Chapter 10- Extracellular matrix components in peripheral nerve regeneration. In *International Review of Neurobiology*; Geuna, S., Perroteau, I., Tos, P., Battiston, B., Eds.; Tissue Engineering of the Peripheral Nerve: Stem Cells and Regeneration Promoting Factors; Academic Press, 2013; Vol. 108, pp. 257–275.

455. Lingstedt, L.V.; Ghittorelli, M.; Lu, H.; Koutsouras, D.A.; Marszalek, T.; Torricelli, F.; Crăciun, N.I.; Gkoupidenis, P.; Blom, P.W.M. Effect of DMSO Solvent Treatments on the Performance of PEDOT:PSS Based Organic Electrochemical Transistors. *Adv. Electron. Mater.* **2019**, *5*, 1800804, doi:10.1002/aelm.201800804.

456. Li, Q.; Yang, J.; Chen, S.; Zou, J.; Xie, W.; Zeng, X. Highly Conductive PEDOT:PSS Transparent Hole Transporting Layer with Solvent Treatment for High Performance Silicon/Organic Hybrid Solar Cells. *Nanoscale Res. Lett.* **2017**, *12*, 506, doi:10.1186/s11671-017-2276-5.

457. Ghasemi-Mobarakeh, L.; Prabhakaran, M.P.; Tian, L.; Shamirzaei-Jeshvaghani, E.; Dehghani, L.; Ramakrishna, S. Structural Properties of Scaffolds: Crucial Parameters towards Stem Cells Differentiation. *World J. Stem Cells* **2015**, *7*, 728–744, doi:10.4252/wjsc.v7.i4.728.

458. Rechendorff, K.; Hovgaard, M.B.; Foss, M.; Zhdanov, V.P.; Besenbacher, F. Enhancement of Protein Adsorption Induced by Surface Roughness. *Langmuir* **2006**, *22*, 10885–10888, doi:10.1021/la0621923.

459. Biazar, E.; Heidari, M.; Asefnezhad, A.; Montazeri, N. The Relationship between Cellular Adhesion and Surface Roughness in Polystyrene Modified by Microwave Plasma Radiation. *Int. J. Nanomedicine* **2011**, *6*, 631–639, doi:10.2147/IJN.S17218.

460. McUmber, A.C.; Randolph, T.W.; Schwartz, D.K. Electrostatic Interactions Influence Protein Adsorption (but Not Desorption) at the Silica–Aqueous Interface. *J. Phys. Chem. Lett.* **2015**, *6*, 2583–2587, doi:10.1021/acs.jpclett.5b00933.

461. van der Veen, M.; Norde, W.; Stuart, M.C. Electrostatic Interactions in Protein Adsorption Probed by Comparing Lysozyme and Succinylated Lysozyme. *Colloids Surf. B Biointerfaces* **2004**, *35*, 33–40, doi:10.1016/j.colsurfb.2004.02.005.

462. Medda, L.; Monduzzi, M.; Salis, A. The Molecular Motion of Bovine Serum Albumin under Physiological Conditions Is Ion Specific. *Chem. Commun.* **2015**, *51*, 6663–6666, doi:10.1039/c5cc01538c.

463. Ouyang, J. “Secondary Doping” Methods to Significantly Enhance the Conductivity of PEDOT:PSS for Its Application as Transparent Electrode of Optoelectronic Devices. *Displays* **2013**, *34*, 423–436, doi:10.1016/j.displa.2013.08.007.

464. Pathak, C.S.; Singh, J.P.; Singh, R. Effect of Dimethyl Sulfoxide on the Electrical Properties of PEDOT:PSS/n-Si Heterojunction Diodes. *Curr. Appl. Phys.* **2015**, *15*, 528–534, doi:10.1016/j.cap.2015.01.020.

465. Kwak, H.W.; Eom, J.; Cho, S.Y.; Lee, M.E.; Jin, H.-J. High-Toughness Natural Polymer Nonwoven Preforms Inspired by Silkworm Cocoon Structure. *Int. J. Biol. Macromol.* **2019**, *127*, 146–152, doi:10.1016/j.ijbiomac.2019.01.005.

466. Zhu, Z.; Song, H.; Xu, J.; Liu, C.; Jiang, Q.; Shi, H. Significant Conductivity Enhancement of PEDOT:PSS Films Treated with Lithium Salt Solutions. *J. Mater. Sci. Mater. Electron.* **2015**, *26*, 429–434, doi:10.1007/s10854-014-2417-x.

467. Döbbelin, M.; Marcilla, R.; Tollan, C.; A. Pomposo, J.; Sarasua, J.-R.; Mecerreyes, D. A New Approach to Hydrophobic and Water-Resistant Poly(3,4-Ethylenedioxythiophene):Poly(Styrenesulfonate) Films Using Ionic Liquids. *J. Mater. Chem.* **2008**, *18*, 5354–5358, doi:10.1039/B808723G.

468. Blau, A. Cell Adhesion Promotion Strategies for Signal Transduction Enhancement in Microelectrode Array in Vitro Electrophysiology: An Introductory Overview and Critical Discussion. *Curr. Opin. Colloid Interface Sci.* **2013**, *18*, 481–492, doi:10.1016/j.cocis.2013.07.005.

469. Wang, S.; Guan, S.; Zhu, Z.; Li, W.; Liu, T.; Ma, X. Hyaluronic Acid Doped-Poly(3,4-Ethylenedioxythiophene)/Chitosan/Gelatin (PEDOT-HA/Cs/Gel) Porous Conductive Scaffold for Nerve Regeneration. *Mater. Sci. Eng. C* **2017**, *71*, 308–316, doi:10.1016/j.msec.2016.10.029.

470. Zhang, C.; Deng, Y.; Dai, H.; Zhou, W.; Tian, J.; Bing, G.; Zhao, L. Effects of Dimethyl Sulfoxide on the Morphology and Viability of Primary Cultured Neurons and Astrocytes. *Brain Res. Bull.* **2017**, *128*, 34–39, doi:10.1016/j.brainresbull.2016.11.004.

471. Radio, N.M.; Breier, J.M.; Shafer, T.J.; Mundy, W.R. Assessment of Chemical Effects on Neurite Outgrowth in PC12 Cells Using High Content Screening. *Toxicol. Sci.* **2008**, *105*, 106–118, doi:10.1093/toxsci/kfn114.

472. O’Sullivan, A.; Lange, S.; Rotheneichner, P.; Bieler, L.; Aigner, L.; Rivera, F.J.; Couillard-Despres, S. Dimethylsulfoxide Inhibits Oligodendrocyte Fate Choice of Adult Neural Stem and Progenitor Cells. *Front. Neurosci.* **2019**, *13*, 1242, doi:10.3389/fnins.2019.01242.

473. Zhang, J.; Li, M.; Kang, E.-T.; Neoh, K.G. Electrical Stimulation of Adipose-Derived Mesenchymal Stem Cells in Conductive Scaffolds and the Roles of Voltage-Gated Ion Channels. *Acta Biomater.* **2016**, *32*, 46–56, doi:10.1016/j.actbio.2015.12.024.

474. Sheng, L.; Leshchyns’ka, I.; Sytnyk, V. Neural Cell Adhesion Molecule 2 Promotes the Formation of Filopodia and Neurite Branching by Inducing Submembrane Increases in Ca2+ Levels. *J. Neurosci. Off. J. Soc. Neurosci.* **2015**, *35*, 1739–1752, doi:10.1523/jneurosci.1714-14.2015.

475. Zamburlin, P.; Ruffinatti, F.A.; Gilardino, A.; Farcito, S.; Parrini, M.; Lovisolo, D. Calcium Signals and FGF-2 Induced Neurite Growth in Cultured Parasympathetic Neurons: Spatial Localization and Mechanisms of Activation. *Pflüg. Arch. - Eur. J. Physiol.* **2013**, *465*, 1355–1370, doi:10.1007/s00424-013-1257-5.

476. Zatkova, M.; Reichova, A.; Bacova, Z.; Strbak, V.; Kiss, A.; Bakos, J. Neurite Outgrowth Stimulated by Oxytocin Is Modulated by Inhibition of the Calcium Voltage-Gated Channels. *Cell. Mol. Neurobiol.* **2018**, *38*, 371–378, doi:10.1007/s10571-017-0503-3.

477. Crookes, W.J.; Ding, L.-L.; Huang, Q.L.; Kimbell, J.R.; Horwitz, J.; McFall-Ngai, M.J. Reflectins: The Unusual Proteins of Squid Reflective Tissues. *Science* **2004**, *303*, 235–238, doi:10.1126/science.1091288.

478. Roberts, A.D.; Finnigan, W.; Wolde-Michael, E.; Kelly, P.; Blaker, J.J.; Hay, S.; Breitling, R.; Takano, E.; Scrutton, N.S. Synthetic Biology for Fibers, Adhesives, and Active Camouflage Materials in Protection and Aerospace. *MRS Commun.* **2019**, *9*, 486–504, doi:10.1557/mrc.2019.35.

479. Hanlon, R. Cephalopod Dynamic Camouflage. *Curr. Biol. CB* **2007**, *17*, R400-404, doi:10.1016/j.cub.2007.03.034.

480. Mirow, S. Skin Color in the Squids Loligo Pealii and Loligo Opalescens. *Z. Für Zellforsch. Mikrosk. Anat.* **1972**, *125*, 143–175, doi:10.1007/bf00306786.

481. Tao, A.R.; DeMartini, D.G.; Izumi, M.; Sweeney, A.M.; Holt, A.L.; Morse, D.E. The Role of Protein Assembly in Dynamically Tunable Bio-Optical Tissues. *Biomaterials* **2010**, *31*, 793–801, doi:10.1016/j.biomaterials.2009.10.038.

482. Wolde-Michael, E.; Roberts, A.D.; Heyes, D.J.; Dumanli, A.G.; Blaker, J.J.; Takano, E.; Scrutton, N.S. Design and Fabrication of Recombinant Reflectin-Based Bragg Reflectors: Bio-Design Engineering and Photoisomerism Induced Wavelength Modulation. *bioRxiv* **2020**, 2020.02.11.942110, doi:10.1101/2020.02.11.942110.

483. Phan, L.; Walkup, W.G.; Ordinario, D.D.; Karshalev, E.; Jocson, J.-M.; Burke, A.M.; Gorodetsky, A.A. Reconfigurable Infrared Camouflage Coatings from a Cephalopod Protein. *Adv. Mater.* **2013**, *25*, 5621–5625, doi:10.1002/adma.201301472.

484. Levenson, R.; DeMartini, D.G.; Morse, D.E. Molecular Mechanism of Reflectin's Tunable Biophotonic Control: Opportunities and Limitations for New Optoelectronics. *APL Mater.* **2017**, *5*, 104801, doi:10.1063/1.4985758.

485. Levenson, R.; Bracken, C.; Sharma, C.; Santos, J.; Arata, C.; Malady, B.; Morse, D.E. Calibration between Trigger and Color: Neutralization of a Genetically Encoded Coulombic Switch and Dynamic Arrest Precisely Tune Reflectin Assembly. *J. Biol. Chem.* **2019**, *294*, 16804–16815, doi:10.1074/jbc.ra119.010339.

486. Andouche, A.; Bassaglia, Y.; Baratte, S.; Bonnaud, L. Reflectin Genes and Development of Iridophore Patterns in Sepia Officinalis Embryos (Mollusca, Cephalopoda). *Dev. Dyn. Off. Publ. Am. Assoc. Anat.* **2013**, *242*, 560–571, doi:10.1002/dvdy.23938.

487. Grant, P.; Zheng, Y.; Pant, H.C. Squid (Loligo Pealei) Giant Fiber System: A Model for Studying Neurodegeneration and Dementia? *Biol. Bull.* **2006**, *210*, 318–333, doi:10.2307/4134568.

488. Borrelli, L.; Fiorito, G. 1.31 - Behavioral analysis of learning and memory in cephalopods. In *Learning and Memory: A Comprehensive Reference*; Byrne, J.H., Ed.; Academic Press: Oxford, 2008; pp. 605–627 ISBN 978-0-12-370509-9.

489. Kautz, R.; Ordinario, D.D.; Tyagi, V.; Patel, P.; Nguyen, T.N.; Gorodetsky, A.A. Cephalopod-Derived Biopolymers for Ionic and Protonic Transistors. *Adv. Mater.* **2018**, *30*, 1704917, doi:10.1002/adma.201704917.

490. Selberg, J.; Jia, M.; Rolandi, M. Proton Conductivity of Glycosaminoglycans. *PloS One* **2019**, *14*, 0202713, doi:10.1371/journal.pone.0202713.

491. D. Ordinario, D.; Phan, L.; Iv, W.G.W.; Dyke, Y.V.; M. Leung, E.; Nguyen, M.; G. Smith, A.; Kerr, J.; Naeim, M.; Kymissis, I.; et al. Production and Electrical Characterization of the Reflectin A2 Isoform from Doryteuthis (Loligo) Pealeii. *RSC Adv.* **2016**, *6*, 57103–57107, doi:10.1039/c6ra05405f.

492. Prince, J.T.; McGrath, K.P.; DiGirolamo, C.M.; Kaplan, D.L. Construction, Cloning, and Expression of Synthetic Genes Encoding Spider Dragline Silk. *Biochemistry* **1995**, *34*, 10879–10885, doi:10.1021/bi00034a022.

493. Holland, C.; Numata, K.; Rnjak-Kovacina, J.; Seib, F.P. The Biomedical Use of Silk: Past, Present, Future. *Adv. Healthc. Mater. 0*, 1800465, doi:10.1002/adhm.201800465.

494. Sofia, S.; McCarthy, M.B.; Gronowicz, G.; Kaplan, D.L. Functionalized Silk-Based Biomaterials for Bone Formation. *J. Biomed. Mater. Res.* **2001**, *54*, 139–148, doi:10.1002/1097-4636(200101)54:1<139::aid-jbm17>3.0.cO;2-7.

495. Manchineella, S.; Thrivikraman, G.; Basu, B.; Govindaraju, T. Surface-Functionalized Silk Fibroin Films as a Platform to Guide Neuron-like Differentiation of Human Mesenchymal Stem Cells. *ACS Appl. Mater. Interfaces* **2016**, *8*, 22849–22859, doi:10.1021/acsami.6b06403.

496. Bai, L.; Zhu, L.; Min, S.; Liu, L.; Cai, Y.; Yao, J. Surface Modification and Properties of Bombyx Mori Silk Fibroin Films by Antimicrobial Peptide. *Appl. Surf. Sci.* **2008**, *254*, 2988–2995, doi:10.1016/j.apsusc.2007.10.049.

497. Li, X.; Zhang, Q.; Luo, Z.; Yan, S.; You, R. Biofunctionalized Silk Fibroin Nanofibers for Directional and Long Neurite Outgrowth. *Biointerphases* **2019**, *14*, 061001, doi:10.1063/1.5120738.

498. Murphy, A.R.; Kaplan, D.L. Biomedical Applications of Chemically-Modified Silk Fibroin. *J. Mater. Chem.* **2009**, *19*, 6443–6450, doi:10.1039/b905802h.

499. Ahmed, M.; Punshon, G.; Darbyshire, A.; Seifalian, A.M. Effects of Sterilization Treatments on Bulk and Surface Properties of Nanocomposite Biomaterials. *J. Biomed. Mater. Res. B Appl. Biomater.* **2013**, *101*, 1182–1190, doi:10.1002/jbm.b.32928.

500. DeMartini, D.G.; Izumi, M.; Weaver, A.T.; Pandolfi, E.; Morse, D.E. Structures, Organization, and Function of Reflectin Proteins in Dynamically Tunable Reflective Cells. *J. Biol. Chem.* **2015**, *290*, 15238–15249, doi:10.1074/jbc.M115.638254.

501. Levenson, R.; Bracken, C.; Bush, N.; Morse, D.E. Cyclable Condensation and Hierarchical Assembly of Metastable Reflectin Proteins, the Drivers of Tunable Biophotonics. *J. Biol. Chem.* **2016**, *291*, 4058–4068, doi:10.1074/jbc.m115.686014.

502. Yeo, I.-S.; Oh, J.-E.; Jeong, L.; Lee, T.S.; Lee, S.J.; Park, W.H.; Min, B.-M. Collagen-Based Biomimetic Nanofibrous Scaffolds: Preparation and Characterization of Collagen/Silk Fibroin Bicomponent Nanofibrous Structures. *Biomacromolecules* **2008**, *9*, 1106–1116, doi:10.1021/bm700875a.

503. Hu, X.; Park, S.-H.; Gil, E.S.; Xia, X.-X.; Weiss, A.S.; Kaplan, D.L. The Influence of Elasticity and Surface Roughness on Myogenic and Osteogenic-Differentiation of Cells on Silk-Elastin Biomaterials. *Biomaterials* **2011**, *32*, 8979–8989, doi:10.1016/j.biomaterials.2011.08.037.

504. Karageorgiou, V.; Meinel, L.; Hofmann, S.; Malhotra, A.; Volloch, V.; Kaplan, D. Bone Morphogenetic Protein-2 Decorated Silk Fibroin Films Induce Osteogenic Differentiation of Human Bone Marrow Stromal Cells. *J. Biomed. Mater. Res. A* **2004**, *71*, 528–537, doi:10.1002/jbm.a.30186.

505. Liu, R.; Ming, J.; Zhang, H.; Zuo, B. EDC/NHS Crosslinked Electrospun Regenerated Tussah Silk Fibroin Nanofiber Mats. *Fibers Polym.* **2012**, *13*, 613–617, doi:10.1007/s12221-012-0613-y.

506. Yang, X.; Wang, X.; Yu, F.; Ma, L.; Pan, X.; Luo, G.; Lin, S.; Mo, X.; He, C.; Wang, H. Hyaluronic Acid/EDC/NHS-Crosslinked Green Electrospun Silk Fibroin Nanofibrous Scaffolds for Tissue Engineering. *RSC Adv.* **2016**, *6*, 99720–99728, doi:10.1039/c6ra13713j.

507. Hsu, C.-C.; Serio, A.; Amdursky, N.; Besnard, C.; Stevens, M.M. Fabrication of Hemin-Doped Serum Albumin-Based Fibrous Scaffolds for Neural Tissue Engineering Applications. *ACS Appl. Mater. Interfaces* **2018**, *10*, 5305–5317, doi:10.1021/acsami.7b18179.

508. Kim, D.; Herr, A.E. Protein Immobilization Techniques for Microfluidic Assays. *Biomicrofluidics* **2013**, *7*, 041501, doi:10.1063/1.4816934.

509. Cai, S.; Singh, B.R. A Distinct Utility of the Amide III Infrared Band for Secondary Structure Estimation of Aqueous Protein Solutions Using Partial Least Squares Methods. *Biochemistry* **2004**, *43*, 2541–2549, doi:10.1021/bi030149y.

510. Ning, W.; Huang, J.; Ling, X.; Lin, H. Modification of Electrospun Silk Fibroin Nanofiber Mats: Using an EDC/NHS Ethanol Solvent. *IOP Conf. Ser. Mater. Sci. Eng.* **2018**, *423*, 012068, doi:10.1088/1757-899x/423/1/012068.

511. Schulten, Z.; Schulten, K. Proton conduction through proteins: An overview of theoretical principles and applications. In *Methods in Enzymology*; Biomembranes Part O: Protons and Water: Structure and Translocation; Academic Press, 1986; Vol. 127, pp. 419–438.

512. Liu, B.F.; Ma, J.; Xu, Q.Y.; Cui, F.Z. Regulation of Charged Groups and Laminin Patterns for Selective Neuronal Adhesion. *Colloids Surf. B Biointerfaces* **2006**, *53*, 175–178, doi:10.1016/j.colsurfb.2006.08.018.

513. Tonge, D.A.; de Burgh, H.T.; Docherty, R.; Humphries, M.J.; Craig, S.E.; Pizzey, J. Fibronectin Supports Neurite Outgrowth and Axonal Regeneration of Adult Brain Neurons in Vitro. *Brain Res.* **2012**, *1453*, 8–16, doi:10.1016/j.brainres.2012.03.024.

514. Patel, R.; Santhosh, M.; Dash, J.K.; Karpoormath, R.; Jha, A.; Kwak, J.; Patel, M.; Kim, J.H. Ile-Lys-Val-Ala-Val (IKVAV) Peptide for Neuronal Tissue Engineering. *Polym. Adv. Technol.* **2019**, *30*, 4–12, doi:10.1002/pat.4442.

515. Idini, M.; Wieringa, P.; Rocchiccioli, S.; Nieddu, G.; Ucciferri, N.; Formato, M.; Lepedda, A.; Moroni, L. Glycosaminoglycan Functionalization of Electrospun Scaffolds Enhances Schwann Cell Activity. *Acta Biomater.* **2019**, *96*, 188–202, doi:10.1016/j.actbio.2019.06.054.

516. Menezes, R.; Hashemi, S.; Vincent, R.; Collins, G.; Meyer, J.; Foston, M.; Arinzeh, T.L. Investigation of Glycosaminoglycan Mimetic Scaffolds for Neurite Growth. *Acta Biomater.* **2019**, *90*, 169–178, doi:10.1016/j.actbio.2019.03.024.

517. Li, Q.; Chow, K.L.; Chau, Y. Three-Dimensional Self-Assembling Peptide Matrix Enhances the Formation of Embryoid Bodies and Their Neuronal Differentiation. *J. Biomed. Mater. Res. A* **2014**, *102*, 1991–2000, doi:10.1002/jbm.a.34876.

518. Rivet, C.J.; Zhou, K.; Gilbert, R.J.; Finkelstein, D.I.; Forsythe, J.S. Cell Infiltration into a 3D Electrospun Fiber and Hydrogel Hybrid Scaffold Implanted in the Brain. *Biomatter* **2015**, *5*, 1005527, doi:10.1080/21592535.2015.1005527.

519. Saracino, G.A.A.; Cigognini, D.; Silva, D.; Caprini, A.; Gelain, F. Nanomaterials Design and Tests for Neural Tissue Engineering. *Chem. Soc. Rev.* **2012**, *42*, 225–262, doi:10.1039/c2CS35065c.

520. Silantyeva, E.A.; Nasir, W.; Carpenter, J.; Manahan, O.; Becker, M.L.; Willits, R.K. Accelerated Neural Differentiation of Mouse Embryonic Stem Cells on Aligned GYIGSR-Functionalized Nanofibers. *Acta Biomater.* **2018**, *75*, 129–139, doi:10.1016/j.actbio.2018.05.052.

521. Lin, R.; Rosahl, T.W.; Whiting, P.J.; Fawcett, J.W.; Kwok, J.C.F. 6-Sulphated Chondroitins Have a Positive Influence on Axonal Regeneration. *PloS One* **2011**, *6*, 21499, doi:10.1371/journal.pone.0021499.

522. George, J.; Dravid, S.M.; Prakash, A.; Xie, J.; Peterson, J.; Jabba, S.V.; Baden, D.G.; Murray, T.F. Sodium Channel Activation Augments NMDA Receptor Function and Promotes Neurite Outgrowth in Immature Cerebrocortical Neurons. *J. Neurosci.* **2009**, *29*, 3288–3301, doi:10.1523/jneurosci.6104-08.2009.

523. Yasuda, T.; Cuny, H.; Adams, D.J. Kv3.1 Channels Stimulate Adult Neural Precursor Cell Proliferation and Neuronal Differentiation. *J. Physiol.* **2013**, *591*, 2579–2591, doi:10.1113/jphysiol.2012.249151.

524. Vass, P.; Szabó, E.; Domokos, A.; Hirsch, E.; Galata, D.; Farkas, B.; Démuth, B.; Andersen, S.K.; Vigh, T.; Verreck, G.; et al. Scale-up of Electrospinning Technology:

Applications in the Pharmaceutical Industry. *Nanomedicine Nanobiotechnology* **2020**, *12*, 1611, doi:10.1002/wnan.1611.

525. Kolbasov, A.; Sinha-Ray, S.; Joijode, A.; Hassan, M.A.; Brown, D.; Maze, B.; Pourdeyhimi, B.; Yarin, A.L. Industrial-Scale Solution Blowing of Soy Protein Nanofibers. *Ind. Eng. Chem. Res.* **2016**, *55*, 323–333, doi:10.1021/acs.iecr.5b04277.
526. Espinosa Pérez, R.; Suárez, J.G.; Diaz, E.N.; Silva Rodríguez, R.; Caballero Menéndez, E.; Balaguer, H.D.; Musacchio Lasa, A. Scaling-up Fermentation of Escherichia Coli for Production of Recombinant P64k Protein from Neisseria Meningitidis. *Electron. J. Biotechnol.* **2018**, *33*, 29–35, doi:10.1016/j.ejbt.2018.03.004.
527. Tripathi, N.K. Production and Purification of Recombinant Proteins from Escherichia Coli. *ChemBioEng Rev.* **2016**, *3*, 116–133, doi:10.1002/cben.201600002.

Blank page

Appendix A

Note: A version of this Appendix has been published as Magaz *et al*. “Porous, aligned and biomimetic fibres of regenerated silk fibroin produced by solution blow spinning”. *Biomacromolecules*. 2018;19(12):4542–53

BIOMACROMOLECULES
Article
Cite This: Biomacromolecules 2018, 19, 4542−4553
pubs.acs.org/Biomac

Porous, Aligned, and Biomimetic Fibers of Regenerated Silk Fibroin Produced by Solution Blow Spinning

Adrián Magaz,[†,‡] Aled D. Roberts,[†] Sheida Faraji,[†] Tatiana R. L. Nascimento,[§] Eliton S. Medeiros,[§] Wenzhao Zhang,[†] Ryan D. Greenhalgh,[†] Andreas Mautner,[∥] Xu Li,[*,‡,⊥] and Jonny J. Blaker[*,†]

[†]Bio-Active Materials Group, School of Materials, The University of Manchester, Manchester, United Kingdom
[‡]Institute of Materials Research and Engineering (IMRE), Agency for Science, Technology and Research (A*STAR), Singapore
[§]Laboratory of Materials and Biosystems, Department of Materials Engineering, Universidade Federal da Paraíba, João Pessoa, Brazil
[∥]Polymer and Composite Engineering Group, Institute of Materials Chemistry and Research, University of Vienna, Vienna, Austria
[⊥]Department of Chemistry, National University of Singapore, Singapore

Supporting Information

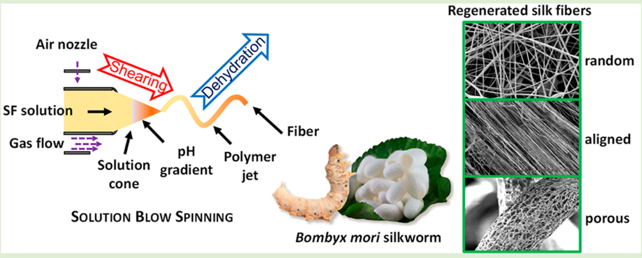

ABSTRACT: Solution blow spinning (SBS) has emerged as a rapid and scalable technique for the production of polymeric and ceramic materials into micro-/nanofibers. Here, SBS was employed to produce submicrometer fibers of regenerated silk fibroin (RSF) from *Bombyx mori* (silkworm) cocoons based on formic acid or aqueous systems. Spinning in the presence of vapor permitted the production of fibers from aqueous solutions, and high alignment could be obtained by modifying the SBS setup to give a concentrated channeled airflow. The combination of SBS and a thermally induced phase separation technique (TIPS) resulted in the production of macro-/microporous fibers with 3D interconnected pores. Furthermore, a coaxial SBS system enabled a pH gradient and kosmotropic salts to be applied at the point of fiber formation, mimicking some of the aspects of the natural spinning process, fostering fiber formation by self-assembly of the spinning dope. This scalable and fast production of various types of silk-based fibrous scaffolds could be suitable for a myriad of biomedical applications.

1. INTRODUCTION

Solution blow spinning (SBS) offers an efficient method to produce micro-/nanofibers at a significantly higher rate (about ×100 times faster[1,2]) compared to conventional electrospinning. By using pressurized gas as the driving force,[2−5] it overcomes some of the drawbacks of electrospinning including the use of electric fields and dense fibrous networks with low porosities;[6−9] in addition, fibers can be deposited *in situ* on virtually any surface.[4] To date, a myriad of polymers,[3−5] composites,[1,10,11] and ceramics[12,13] have been successfully processed into fibers by SBS. The use of micro-/nanofibers is of particular interest in the field of regenerative medicine due to their high surface area to volume ratio and morphological resemblance to the extracellular matrix of native tissues. Fibers can provide adequate topographical and mechanical cues to direct cell behavior, making them suitable for the fabrication of scaffolds for tissue regeneration.[14−16]

In its native state, *Bombyx mori* silk consists of fibrous protein filaments (silk fibroin) surrounded by a glue-like layer (sericin). Among the wide range of natural materials, silk fibroin has many attractive chemical, physical, and biological properties which make it convenient for regenerative medicine, tissue engineering, and therapeutic delivery applications.[17,18] Some of these properties include suitable cell−material interactions, tailored biodegradability, and oxygen/water permeability.[19−22]

Under natural spinning conditions, as the silk dope flows from the posterior to the anterior division of the silkworm gland, the dope is sheared, water content decreases from 80 to 77%, pH decreases from 6.9 to 4.8, and chaotropic ions are exchanged for kosmotropic ions,[23−29] contributing to fiber formation. Silk fibroin typically requires reprocessing from its native state to tune properties including fiber diameter and surface roughness/morphology to suit the intended application.[15,30] In particular, regenerated silk fibroin (RSF) from aqueous solutions has previously been electrospun by blending with high molecular weight poly(ethylene oxide) (PEO),[21,31,32] used as a temporary water-soluble spinning aid, and fully aqueous processes based on high molecular weight silk fibroin dopes have been successfully produced via electrospinning.[33,34] Recently, straining flow spinning (SFS) has been used to produce high performance RSF fibers by controlling the flow of the dope through its interaction with a coagulant bath,[35,36] mimicking the balanced mild aqueous chemical environment and moderate shear forces found in

Received: August 13, 2018
Revised: October 30, 2018
Published: November 2, 2018

Scheme 1. Schematic Representation of Conventional, Cryogenic, and Coaxial SBS Setups[a]

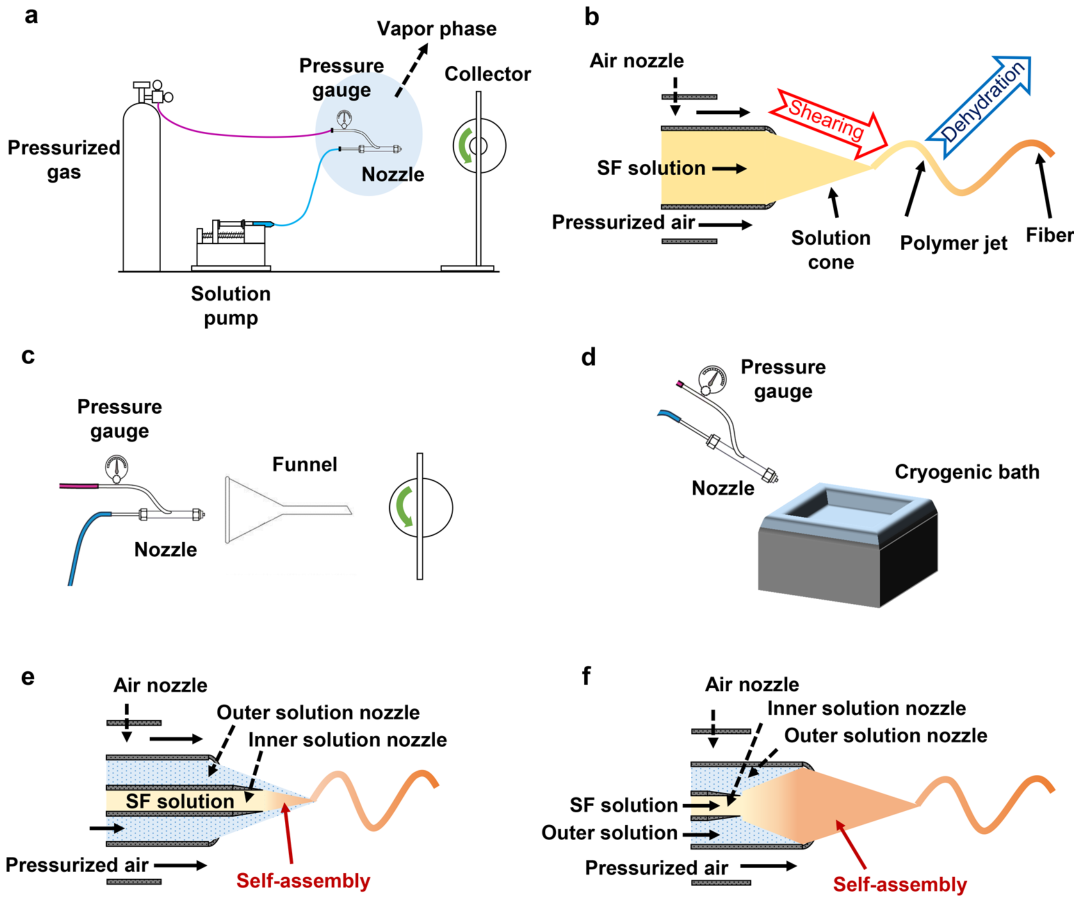

[a] (a, b) Conventional SBS setup (with/without vapor phase). (c) Modified SBS setup to channel the airflow and RSF fiber jet for spinning aligned nonporous fibers. (d) Cryo-SBS setup for the production of porous fibers. (e, f) Coaxial SBS setup to induce pH and ion gradients by (e) positive and (f) negative inner nozzle solution protrusion.

natural spinning glands.[35] While robust RSF fibers can be mass-produced by SFS, these range between 8 and 13 μm in diameter. SBS permits faster production rates (5 μL min^{-1} in SFS compared with >100 μL min^{-1} in SBS) and can even achieve sub-micron diameter fibers.

The aim of this study is not to produce high performance robust fibers nor retain the hierarchical structures of natural silks, but rather show that SBS is a suitable technique that could be used to mass-produce various types of RSF sub-micron diameter fibers with potential applications in regenerative medicine. Here, to the author's knowledge, we have for the first time employed SBS to process RSF into randomly aligned and aligned nonporous micro-/nanofibers, utilizing both organic (formic acid) and aqueous solvent systems, and by channeling the flow of air to the collector. Porous fibers from an aqueous system were obtained by using a modified SBS system based on a thermally induced phase-separation (TIPS) technique.[1,37] A coaxial SBS system was also employed to mimic a pH gradient as a means to replicate some of the physiological parameters of the natural spinning process[26] and drive secondary protein structure formation.

2. EXPERIMENTAL SECTION

2.1. Regenerated Silk Fibroin. RSF solutions from *Bombyx mori* silkworm cocoons (Wildfibers; Birmingham, UK) were prepared following a previously described protocol[38] with minor modifications. Briefly, cocoons were dewormed and degummed in a 0.02 M boiling Na_2CO_3 (Sigma-Aldrich, UK) aqueous solution for 30 min to remove the sericin. Degummed silk fibroin was thoroughly washed in deionized water (three water changes, 20 min each) and air-dried for 24 h. The dried degummed silk fibroin was dissolved in 7.9 M aqueous LiBr (Sigma-Aldrich, UK) to form a 16% w/v solution, with gentle continuous stirring at 60 °C for 4 h. The solution was centrifuged (10000*g*, 20 min) to remove any residual pupa and dialyzed (3.5 kDa MWCO SnakeSkin, ThermoScientific, UK) against 5 L of deionized water at 4 °C for 3 days, with regular water changes under continuous stirring. The concentration of the RSF solution after water dialysis was ~5−6% w/v. The solution was centrifuged again (10000*g*, 20 min) and either freeze-dried for 72 h (VirTis BenchTop Pro; New York) or concentrated for further use, described below.

2.2. Spinning Dope Formulations. Formic acid dopes as precursors of nonporous fibers were prepared by dissolving freeze-dried RSF in formic acid (95% v/v; Sigma-Aldrich, UK) at a concentration of 8−20% w/v at room temperature and stirred for 2 h prior to spinning.

Aqueous precursor dopes were prepared by means of reverse dialysis processes. Aqueous formulations as precursors for nonporous fibers were prepared by concentrating an RSF solution by reverse dialysis (10 kDa MWCO SnakeSkin dialysis tubing, Thermo-Scientific, UK) against a 15% w/v poly(ethylene glycol) (PEG 10000 M_w; Sigma-Aldrich, UK) aqueous solution at 4 °C. Note that some PEG likely diffused into the RSF solution and may have acted as a spinning aid. Prior to spinning, a 3 M $CaCl_2$ (Sigma-Aldrich, UK) solution was added into the RSF system to adjust the $[Ca]^{2+}$ to 0.3 M (pH ~7.5, 9:1 v/v ratio SF/$CaCl_2$). The role of $CaCl_2$ is to promote

RSF conformation from random coil/α-helix to β-sheet.[39−41] The pH was subsequently adjusted to 10.5 with a 5 M NaOH (Sigma-Aldrich, UK) solution, which was found to make the dope stable during the spinning process and promote fiber formation. Aqueous formulations as precursors of porous fibers and biomimetic fibers were prepared by concentrating an RSF solution by reverse dialysis (3.5 kDa MWCO SnakeSkin dialysis tubing, Thermo-Scientific, UK) against a 20% w/v PEG (10000 M_w; Sigma-Aldrich, UK) aqueous solution at 4 °C.

All solutions were stored in sealed glass vials at 4 °C and spun within 24 h.

2.3. Rheological Analysis of Regenerated Silk Fibroin Solutions. RSF formulations at increasing concentrations were loaded into an AR-G2 rheometer (TA Systems; UK), operated with a parallel plate geometry (20 mm diameter and gap set to 600 μm) at 25 °C and with an environmental case attached to prevent solvent evaporation. Each concentration (n = 2 replicates of the same solution) was subjected to a logarithmic steady shear rate increase from 0.01 to 1000 s^{-1}.[42]

2.4. Fiber Production by Conventional, Cryogenic, and Coaxial Solution Blow Spinning. All RSF dopes were spun via a custom-made SBS setup (Scheme 1), consisting of a syringe pump, connective tubing, a concentric nozzle, and a compressed air source controlled by a pressure regulator. Solutions were injected to the inner nozzle of the SBS head using a precision syringe driver pump (N-300, New Era Pump Systems Inc.; USA). Compressed air was delivered to the outer nozzle via an oil-free and water-free air compressor (Bambi VT150D; Italy). The internal diameter (i.d.) of the SBS inner nozzle was 0.8 mm, and the outer diameter (o.d.) was 1.8 mm; the outer nozzle had an i.d. of 2 mm and an o.d. of 3 mm. The inner nozzle was set to protrude by ≥+2 mm from the outer nozzle into a conical-shaped end.

Random nonporous fibers from RSF formulations based on formic acid were spun directly with a conventional SBS apparatus (Scheme 1a,b): feed rate of 50−60 μL min^{-1}, air pressure of 30−40 psi (0.21−0.28 MPa), and working distance to the collector of 20−30 cm. Production of random nonporous fibers from RSF aqueous dopes was enhanced by spinning through a vapor immediately after the SBS nozzle. Vapor was generated using different solvents (water, absolute ethanol, or absolute methanol) in a beaker on a hot plate (100−200 °C) placed under the SBS nozzle. Ethanol and methanol are known to promote β-sheet formation. Spinning parameters in this case were feed rate of 100−110 μL min^{-1}, air pressure of 30−60 psi (0.21−0.41 MPa), and working distance of 30−40 cm to fiber collection.

Aligned nonporous fibers out of formic acid and aqueous systems were obtained by placing a funnel between the SBS head and collector (Scheme 1c). This served to channel the airflow and the fiber forming jet, aligning the fibers in flight prior to collection. The same spinning parameters as previously stated for nonporous fibers were used.

Porous fibers were obtained using RSF aqueous dopes based on a cryogenic SBS (cryo-SBS) setup (Scheme 1d).[1,37] As-produced RSF aqueous formulations were sprayed into fibers directly into a bath of liquid nitrogen. The feed rate was 100 μL min^{-1}, and the air pressure was 30 psi (0.21 MPa); a working distance of 15 cm and an angle of ∼45° to the cryogenic bath were selected to limit liquid nitrogen loss. The bath container was made from an expanded-polystyrene foam box. During cryo-SBS, the level of liquid nitrogen in the bath was constantly topped up to ensure that the working distance remained ±2 cm of the target value. Frozen fibers were then collected into 50 mL Falcon tubes, transferred to lyophilization flasks (precooled in liquid nitrogen), and subsequently lyophilized (VirTis BenchTop Pro; New York). The external glass portion of the lyophilization flask was kept under liquid nitrogen using the polystyrene foam box until a vacuum of ∼50 mTorr was reached, after which the outside of the flask was exposed to ambient conditions. Lyophilization was continued for a total of 72 h to ensure complete drying.

For biomimetic fibers, a coaxial SBS head, consisting of two concentric solution nozzles (inner solution nozzle, outer solution nozzle) within an outer pressurized air nozzle, was employed to induce changes to the chemical environment at the point of the solution cone (positive protrusion of inner solution nozzle, Scheme 1e) or prior to it (negative protrusion of inner solution nozzle, Scheme 1f) by flowing a secondary solution through the outer solution nozzle while flowing the RSF solution through the inner solution nozzle. The outer solution nozzle was set to protrude ≥2 mm from the outer pressurized air nozzle; the inner solution nozzle was set to protrude ±2 mm (positively or negatively) from the outer solution nozzle. A number of kosmotropic phosphate solutions adjusted to various acidic pH values (pH 2−7) and a commonly used coagulant in wet-spinning (ammonium sulfate)[22] were used to induce self-assembly of aqueous RSF solutions into fibers. Two precision syringe driver pumps were used for injecting the inner and outer solutions. Successful fiber spinning was achieved with the following set parameters. For the positive nozzle protrusion, inner and outer solutions were injected at feed rates 100 and 150 μL min^{-1}, respectively; for the negative nozzle protrusion, the inner and outer solutions were injected at feed rates of 190 and 100 μL min^{-1}, respectively. Air pressure and distance to collector were maintained in both cases at 40 psi (0.28 MPa) and 40 cm.

2.5. Insolubilization of Solution Blow Spun Regenerated Silk Fibroin Fibers. Nonwoven random fiber mats were immersed in 90% v/v ethanol (EtOH) or 90% v/v methanol (MeOH) baths for 10 min to further induce protein secondary structure transition from α-helix/random coils into β-sheets. The mats were then dried in an oven at 30 °C for 24 h.

2.6. Physicomechanical Characterization of the Fibers. *2.6.1. Fiber Morphology.* Fiber morphology was assessed using scanning electron microscopy (SEM) on a Hitachi S300 N (USA) and on a PhenomPro Generation 5 (USA) and field emission scanning electron microscopy on a Zeiss Supra 35VP FE-SEM (Germany). Briefly, fiber mats (1 cm × 1 cm) were mounted onto aluminum stubs with double-sided conductive carbon tape and sputter-coated with gold/palladium (Gatan Model 682 Precision Etching Coating System, USA) to an average thickness of 3 nm; images were captured at 2.5−5 kV. The average fiber diameter was determined using ImageJ (Fiji 1.28, USA) software by measuring a minimum of 50 fibers per sample type.

2.6.2. Protein Structure Quantification and Crystallinity Assessment. The conformational structure of nonwoven RSF fiber mats was investigated by wide-angle X-ray diffraction (WAXD; PANalytical X'Pert Pro, UK) with the following parameters: copper line focus X-ray tube with Ni Kβ absorber (0.02 mm; Kβ = 1.392250 Å) and Kα radiation (Kα_1 = 1.540598 Å, Kα_2 = 1.544426 Å, Kα ratio 0.5, Kα_{av} = 1.541874 Å), diffraction angle of 5°−45°, and scanning rate of 2° min^{-1}. In addition, a Fourier transform infrared spectrometer (FTIR Nicolet iS5; Thermo Scientific, UK) equipped with an iD5 attenuated total reflectance (ATR) attachment (diamond crystal) was used to examine the conformational changes of the secondary structure of RSF within the amide I region. For each measurement, 32 scans were recorded with a resolution of 4 cm^{-1} and wavenumbers from 500 to 4000 cm^{-1}. The amide I region ranging from 1600 to 1700 cm^{-1} was baseline corrected and deconvoluted by applying a second derivative algorithm, a signal smoothing algorithm, and a curve-fitting algorithm based on Fourier self-deconvolution (FSD) according to refs 43 and 44. The band positions were fixed at 1595 cm^{-1} (side chains), 1610 cm^{-1} (side chains), 1620 cm^{-1} (intermolecular β-sheets), 1630 cm^{-1} (intermolecular β-sheets), 1640 cm^{-1} (random coils), 1650 cm^{-1} (random coils), 1660 cm^{-1} (α-helices), 1670 cm^{-1} (β-turns), 1680 cm^{-1} (β-turns), 1690 cm^{-1} (β-turns), and 1700 cm^{-1} (intramolecular β-sheets) following ref 45. Samples were run in triplicate.

2.6.3. Mechanical Testing. Uniaxial tensile testing of as-spun RSF mats (cardboard window frame dimensions of 5 mm × 5 mm) of aligned nonporous fibers was performed with a mechanical tester (Instron 3344; Instron Ltd., USA). The ends of the fiber mats were embedded in epoxy and taped to avoid stress concentration at the clamps during mounting to the tensile test machine. Prior to testing, the sides of the window frame were cut through, enabling direct loading of the sample. Samples (n = 12 replicates) were subjected to uniaxial loads at 2 mm min^{-1}, and a 10 N load cell was used. The strain at break and ultimate tensile strength (UTS) were calculated from the maximum value of the stress−strain curve before breakage,

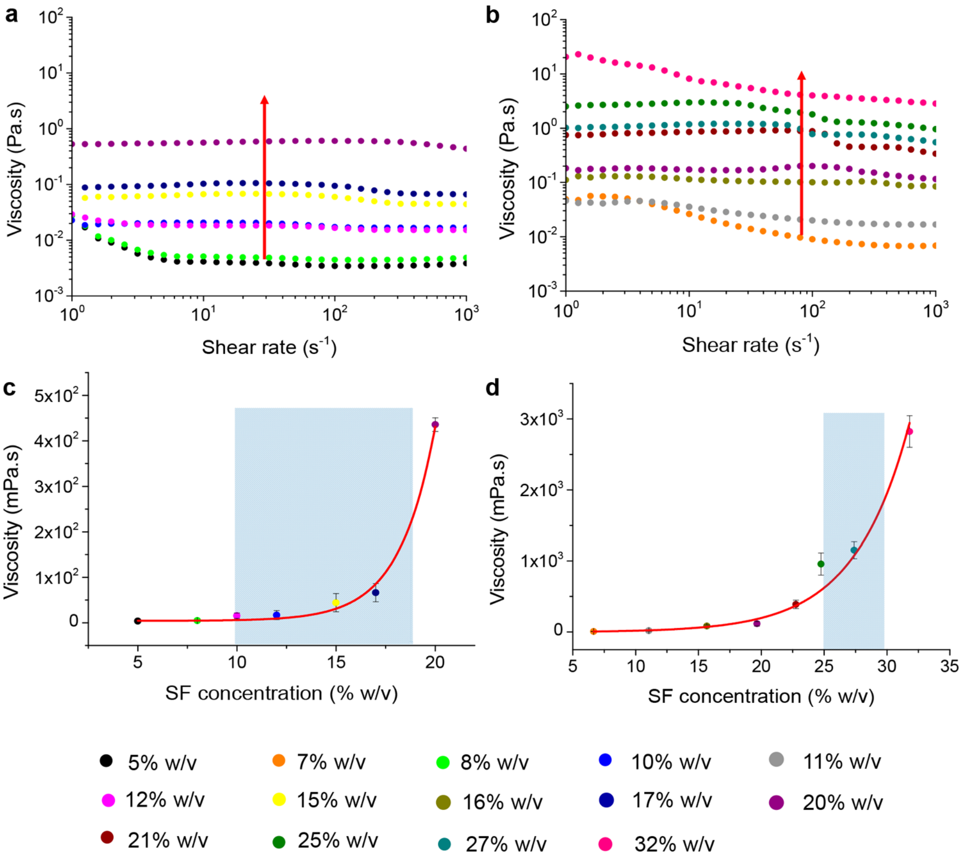

Figure 1. Rheology of RSF solutions. (a, b) Shear sweep measurements of (a) formic acid and (b) aqueous RSF solutions at increasing concentrations. Red arrows represent increase in concentration. (c, d) Relationship between viscosity (at 1000 s^{-1} shear rate) and concentration for (c) formic acid and (d) aqueous solutions, highlighting the spinnability window for SBS; error bars in SD (n = 2).

Young's modulus from the slope of the linear portion of the curve, and toughness from the area under the graph for each sample tested. The area occupied by the fibers was calculated by measuring the area of the mat and subtracting the void space of the fibers based on mass-density differences between the mat and single fibers.[46] Instruments were calibrated prior to use and all tests were performed at room temperature.

2.6.4. Surface Area Analysis and Fiber Pore Size. Brunauer–Emmett–Teller (BET) surface area measurements of porous fibers obtained by cryo-SBS were made using a surface area and porosity analyzer (TriStar II, Micromeritics, Neu-Purkersdorf, Austria). Prior to gas adsorption experiments, impurities were removed via a degassing step (FlowPrep 060, Micromeritics). Approximately 100 mg of sample was placed inside a glass chamber, purged with nitrogen at ambient temperature overnight. Nitrogen adsorption isotherms were then measured at 77 K.

The size of a minimum of 70 pores from SEM images of porous fibers was measured using by ImageJ (Fiji 1.28, USA); measurements were performed along the minor axis of the pores.

2.7. Data Analysis. Quantitative data are presented as standard deviation (SD) of the mean values. Statistical analysis of the results was performed using GraphPad Prism 7 (San Diego, CA).

3. RESULTS AND DISCUSSION

3.1. Nonporous RSF Fibers Obtained via SBS.

Analysis of the viscoelastic properties of RSF formulations is of interest since solution viscosity determines whether a droplet spray or continuous fibers are obtained, as it affects initial droplet shape and stability of the jet trajectory during SBS.[47] The viscosity measurements of RSF formulations of formic acid and the aqueous system at increasing concentrations are shown in Figure 1a,b. Both systems exhibited slightly different rheologies over the range of concentrations tested. For the case of RSF solutions in formic acid, the viscosities were almost independent of the shear rate exhibiting Newtonian-like behavior. This is consistent with work reported by Zhu et al. for RSF formulations in formic acid below 20% w/v.[48] Aqueous RSF formulations, on the other hand, exhibited non-Newtonian shear-thinning-like behavior, more evident at high solution concentrations. Shear thinning at increasing shear rate is characteristic of native silk dopes[49] and suggests more entanglement of the chain networks in the polymer solution,[50,51] which should aid spinning by SBS.

The solutions over the range of different concentrations were spun via conventional SBS. A systematic investigation found that nonporous fibers only formed for concentrations between 10 and 18% w/v for solutions based on the formic acid system and between 25 and 30% w/v for aqueous solutions in the presence of a water/ethanol/methanol vapor and pH-Ca^{2+} adjustment, as detailed in the Experimental Section. Solutions lower than 10% and above 18% w/v (formic acid system), or below 25% and above 30% w/v (aqueous system), did not have suitable rheological properties for processing into fibers by SBS: either the nozzle blocked frequently, or the solutions resulted exclusively in droplets and no fibers were formed. The spinnability windows (Figure 1c,d) for RSF solutions were established as 15−144 mPa·s (formic acid system) and 500−1500 mPa·s (aqueous system), identified as the target viscosities for blow spinning RSF

DOI: 10.1021/acs.biomac.8b01233

dopes into nonporous fibers based on formic acid and aqueous systems, respectively.

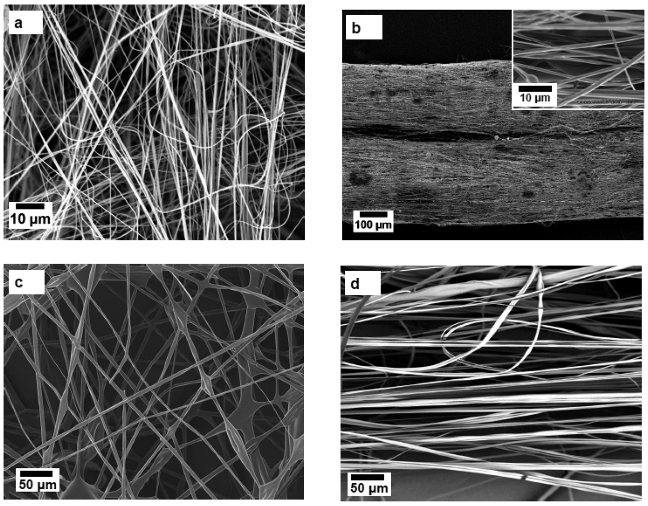

Figure 2. SEM images of RSF nonporous fibers from formic acid and aqueous solutions. (a, b) Fibers spun from formic acid at 12% w/v: (a) randomly aligned fibers; (b) aligned fiber bundle with inset at higher magnification. (c, d) Fibers spun from an aqueous system at 27% w/v through a water vapor: (c) randomly aligned fibers; (d) aligned fibers.

SEM images of RSF nonporous fibers spun from formic acid are shown at 12 and 15% w/v (Figure 2a,b and Figure S1). The most stable fiber mats were obtained at a flux of 50−60 μL min^{-1} at an air pressure of 30−40 psi (0.21−0.28 MPa) with a working distance of 20−30 cm to fiber collection. Increasing the concentration of the RSF formulation resulted in fibers with a greater diameter consistent with previously reported data of solution blow spinning of other polymers.[3,52,53] The mean diameter of randomly aligned fibers based on formic acid (Figure 2a and Figure S1a) was 290 ± 60 and 910 ± 300 nm for RSF solution concentrations at 12 and 15% w/v, respectively. Fiber morphology was relatively smooth in both cases. Aligned fiber bundles and mats were also produced at 12% w/v (Figure 2b and Figure S1b) by channeling the airflow toward the collector. Fibers were quickly formed as the RSF solution exited the nozzle and consolidated within less than 5 cm, meaning that by channeling the flow through greater distances fiber alignment could be achieved. Aligned nonporous fibers exhibited a similar mean fiber diameter (p-value nonsignificant) compared to that of randomly aligned nonporous fibers produced from RSF formulations at the same concentration. The mean fiber diameter in this case was 260 ± 150 nm, and fiber morphology was smooth and consistent, with no droplets/beads observed.

For aqueous RSF solutions, the most stable nonporous fibers were obtained at a flux of 100−110 μL min^{-1} at an air pressure 30−60 psi (0.21−0.41 MPa) and working distance of 30−40 cm. SEM images of RSF fibers spun at 27% w/v are shown in Figure 2c,d. The structure of the fiber mats consists of nonporous fibers interconnected into a 3D porous nonwoven network with some conglutination, with a mean diameter of 410 ± 130 nm for randomly aligned fibers (Figure 2c) and 465 ± 170 nm for aligned fibers (Figure 2d) (p-value nonsignificant between them). Compared to RSF fibers produced from formic acid dopes (Figure 2a,b), these fibers had poorer morphological homogeneity. Water has a relatively high boiling point and low volatility, resulting in residual moisture content prior to collection.[54]

It should be noted that some low molecular weight PEG likely diffused into the aqueous RSF solutions during reverse dialysis concentration and that this acted as a spinning aid during SBS promoting fiber formation. A plasticizing effect due to the presence of PEG in polylactide (PLA) blends has been reported,[55] considerably increasing the elongation at break, while the tensile strength remained unchanged. Low molecular weight PEG is difficult to spin on its own,[56,57] and only its high molecular weight form, PEO, is commonly used during electrospinning of aqueous biopolymer systems due to its higher viscosity aiding stabilization of the polymer jet.

PEG is water-soluble and can be easily removed after fiber spinning. RSF solutions for aqueous nonporous fiber spinning were also concentrated up to 30% w/v by forced airflow and by reverse dialysis in PEG using a 3.5 kDa membrane, yet none of the prepared solutions were able to form fibers, suggesting that concentrations >30% w/v may be required. However, this is disadvantageous for industrial processing due to the easy transition of highly concentrated solutions into gel and clogging of the nozzle.

The structure of nonporous fibers was further characterized by ATR-FTIR and WAXD (Figure 3a−c). Indeed, the conformation and structure of proteins are an important factor in both their physicochemical and mechanical properties, which ultimately affects their ability to interact with biological interfaces—an important consideration for tissue engineering and therapeutic delivery applications.

The ATR-FTIR spectra of the amide I (1700−1600 cm^{-1}) and amide II (1600−1450 cm^{-1}) bands of nonporous fibers spun from formic acid and aqueous solutions are shown in Figure 3a, indicating that the typical chemical composition of silk fibroin remained unaffected during SBS. A clear shift of the absorption peak of the amide I region (1700−1600 cm^{-1}) after post-treatment in ethanol and methanol can be observed.

A detailed quantification of the amide I band by curve fitting and deconvolution revealed changes in the chain structure (Figure 3c). While β-sheets make up the crystalline regions of silk fibroin, other more flexible structures such as β-turns or random coils and α-helices account for the more amorphous structures of silk.[58,59] Significantly greater ($p < 0.0001$) β-sheet and lower ($p < 0.01$) α-helix/random coil contents were quantified in untreated fibers spun from aqueous solutions (through a water vapor) compared to those spun from formic acid (Figure S2). As expected, the immersion of the as-spun RSF fibers into ethanol and methanol bath solutions increased the partial fraction of secondary structural components (β-sheets), while reducing the less-ordered structures (α-helixes and random coils) (Figure 3c). For the case of fibers spun from an aqueous system, the β-sheet content before or after post-treatment of fibers spun through a water vapor phase was higher compared to the other two vapor phases using either methanol or ethanol (Figure 3c). Only fibers spun in a methanol vapor phase and post-treated in methanol exhibited a similar high content in β-sheets. The added water content of the vapor phase may have acted as a plasticizer permitting fibroin to have more rotational and translational freedom during their rearrangement,[58,60−62] allowing more stable β-sheet structures to form, in addition to assisting in fiber formation. In fact, significantly higher ($p < 0.001$) contents of β-turns were quantified in fibers spun through an ethanol vapor

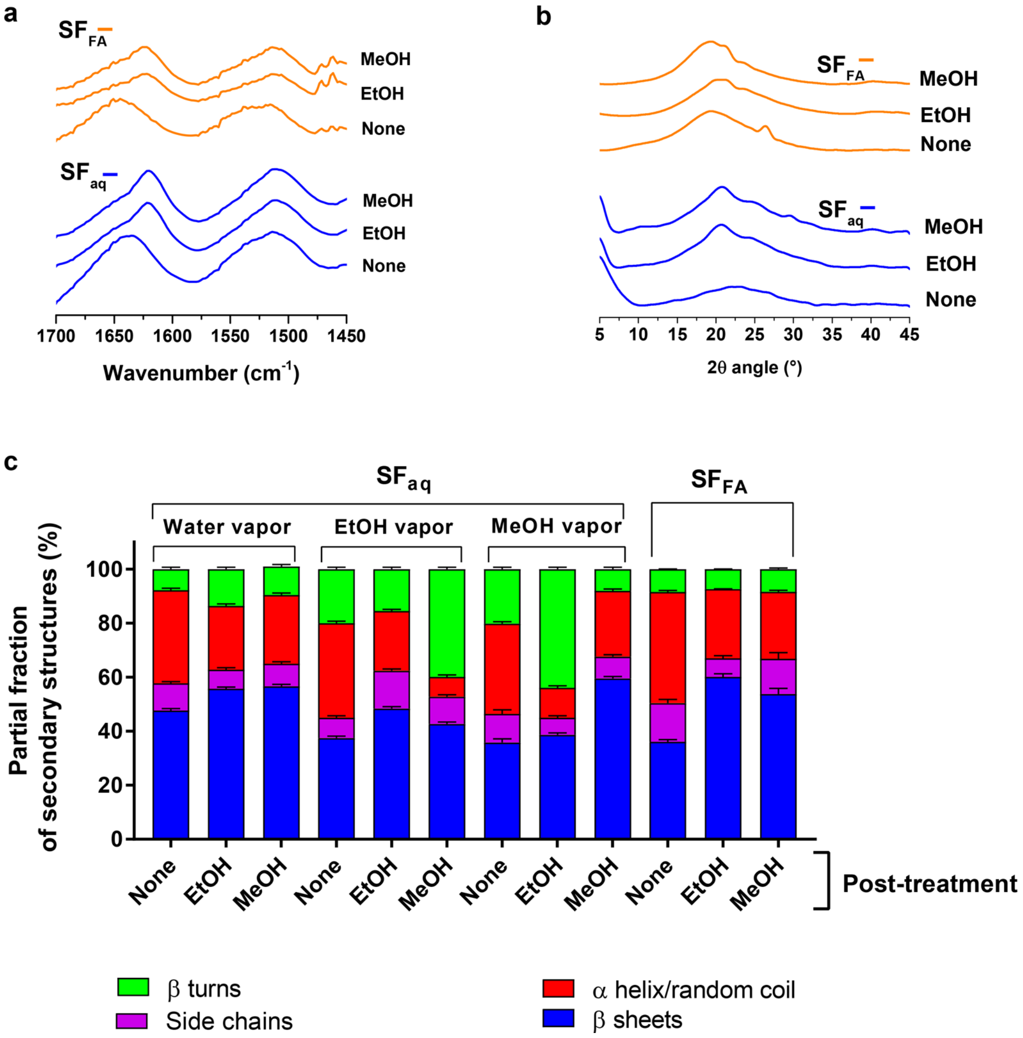

Figure 3. ATR-FTIR and WAXD of randomly aligned nonporous RSF fibers obtained from formic acid (SF_{FA}) and aqueous solutions (SF_{aq}). (a) Normalized ATR-FTIR spectrum showing the amide I (1700−1600 cm^{-1}) and amide II (1600−1450 cm^{-1}) bands of fibers spun from formic acid, and from an aqueous solution through a water vapor, comparing post-treatment. (b) Normalized WAXD spectrum of fibers spun from formic acid, and from an aqueous solution through a water vapor, comparing post-treatment. (c) Stacked bar chart depicting the partial fraction of secondary protein structures within the amide I band of fibers spun from formic acid, and from an aqueous solution through a water/ethanol/methanol vapor, comparing post-treatment; error bars in SD (n = 3).

phase and post-treated in methanol or spun through a methanol vapor phase and post-treated with ethanol.

WAXD (Figure 3b) was used to further assess the crystallinity conformation[63,64] of the nonporous fibers and complement the information provided by ATR-FTIR. The secondary structure of silk fibroin exhibits at least three crystalline conformations: random coil, silk I, and silk II. Among these, silk II is the most stable structure and is thought to be constituted by antiparallel β-sheets. Untreated fibers from aqueous solution spun through a water vapor exhibited a low-intensity broad halo with a peak around $2\theta = 22.68°$ (d-spacing 0.39 nm). Fibers spun through a water vapor and post-treated in methanol exhibited crystalline peaks at 2θ = 9.7°, 20.83°, 24.85°, and 29.50° (d-spacing of 0.91, 0.43, 0.36, and 0.31 nm), corresponding to a mixed silk II (0.91, 0.43, and 0.36 nm) and silk I (0.31 nm) structure.[65] Fibers spun through a water vapor and post-treated in ethanol exhibited crystalline peaks at 2θ = 20.67° and 25.11° (d-spacing 0.43 and 0.35 nm) corresponding to silk II conformation.[65] These results suggest that ethanol post-treatment of fibers spun through water vapor resulted in a higher component of silk II. For the case of formic acid solutions, fibers post-treated in ethanol and in methanol showed similar mixed silk type I and II conformations. In particular, fibers post-treated in ethanol exhibited peaks at 2θ = 20.60° and 23.48° (d-spacings of 0.43 and 0.38 nm) relating to silk II and silk I conformations, respectively.[65] Fibers post-treated in methanol exhibited peaks at 2θ = 19.30°, 21.03°, and 23.33° (d-spacings of 0.45, 0.42, and 0.38 nm) characteristic of silk II (0.45 and 0.42 nm) and silk I (0.38 nm) polymorphs.[65]

To elucidate any influence of in-flight fiber alignment on the protein structure, both aligned and randomly aligned nonporous fibers from formic acid were evaluated by ATR-FTIR and WAXD (Figure S3). No significant differences in terms of the quantification of the secondary structures within the amide I region were observed (Figure S3a), and similar peaks were retrieved by WAXD (Figure S3b), suggesting no increase in β-sheet conformation after fiber alignment.

A direct comparison of the mechanical properties of fibers is challenging due to differences in the reported literature concerning measurement and manufacture (i.e., spinning

Table 1. Mechanical Properties of As-Produced Aligned Nonporous Fiber Mats by SBS[a]

	Young's modulus [MPa]	ultimate tensile strength [MPa]	strain at break [%]	toughness [MJ m^{-3}]
27% w/v RSF, as-spun aqueous dope through water vapor	1.13 ± 0.50	0.30 ± 0.10	1.28 ± 0.36	0.007 ± 0.003
12% w/v RSF, as-spun formic acid dope	11.10 ± 2.70	3.50 ± 0.70	0.46 ± 0.10	0.05 ± 0.01

[a] Error in SD (n = 12).

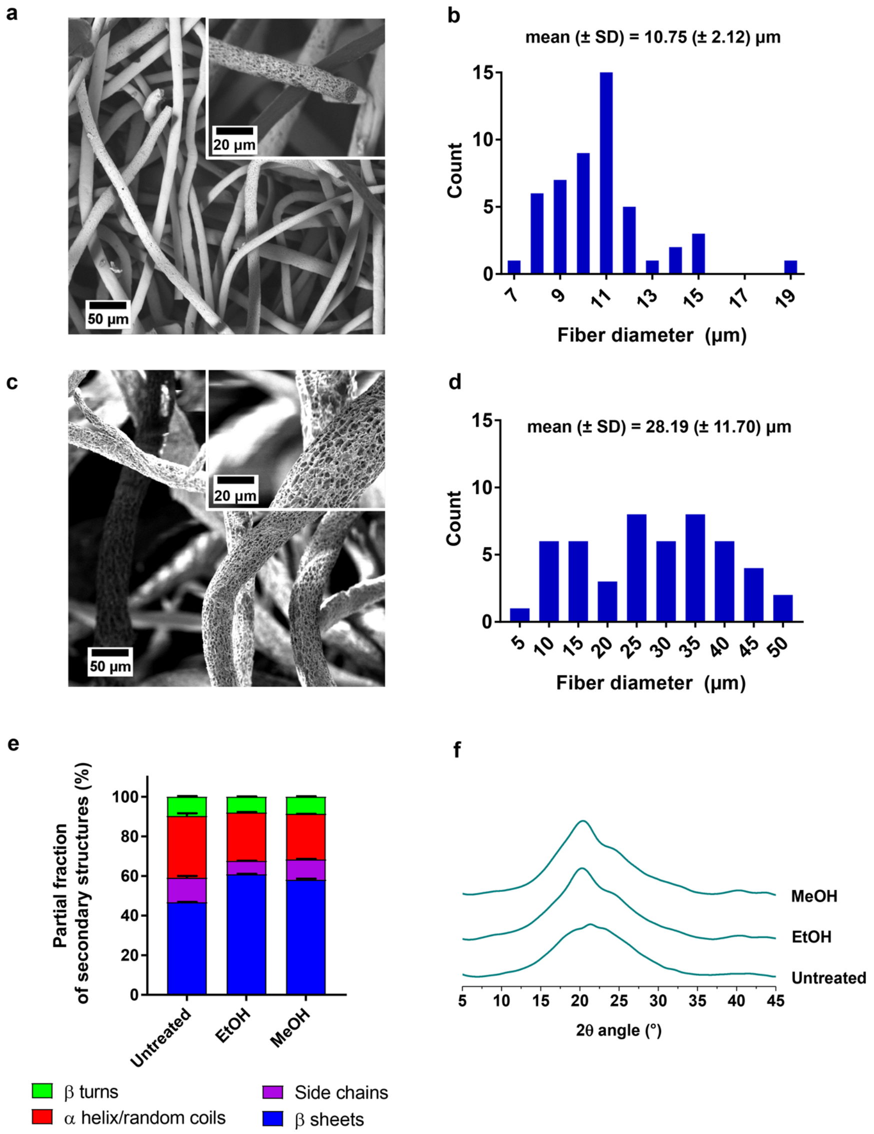

Figure 4. SEM, ATR-FTIR, and WAXD of porous RSF fibers spun from aqueous formulations by cryo-SBS. (a−d) SEM images showing porous fibers, along with their fiber diameter distribution, at (a, b) 27% w/v and (c, d) 30% w/v; error in SD (n = 50). (e) Stacked bar chart depicting the partial fraction of secondary protein structures within the amide I band, before and after post-treatment; error bars in SD (n = 3). (f) Normalized WAXD spectrum, before and after post-treatment.

technique used, fiber diameter produced, solvents and processing conditions, coagulantion baths, and drawing used during spinning). For instance, electrospun RSF fibers from aqueous solutions have been reported with tensile stress of 0.18−0.83 MPa and strain at break of 1.3−11.1%.[66] In other studies, the apparent stress and strain at break have been reported to be 11.7 MPa and 10.2% by Cao et al.[34] and 1.49 MPa and 1.6% by Chen et al.[67] Electrospun RSF fibers from formic acid solutions have been reported with tensile stress and strain at break of 7 MPa and 12% by Kishimoto et al.[68] or ranging between 11−18 MPa and 16−23% by Amiraliyan et al.[64] Koeppel and Holland recently published a comprehensive systematic review on the progress of artificial silk spinning,[22] including that of RSF solutions, where the mechanical properties of a wide range of these fibers obtained via different spinning techniques are reported.

The mechanical properties of as-produced nonporous aligned RSF fibers, out of aqueous and formic acid dopes, are shown in Table 1. Fiber mats spun from formic acid solutions exhibited higher Young's modulus, UTS, and toughness, yet lower strain at break compared to fibers spun from aqueous solutions. The values reported here, though, still

DOI: 10.1021/acs.biomac.8b01233
Biomacromolecules 2018, 19, 4542−4553

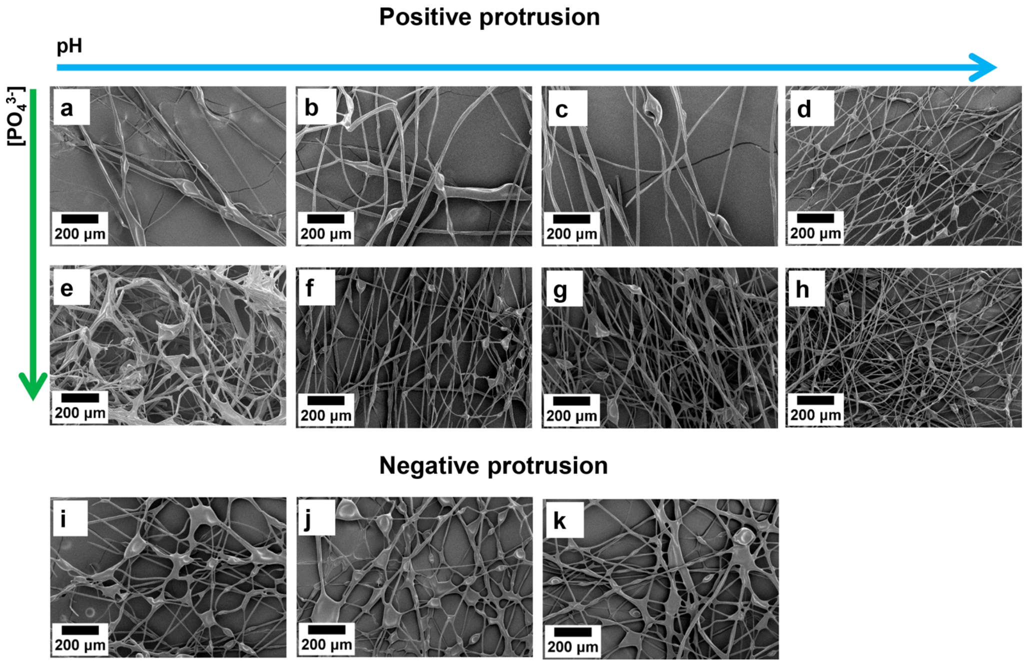

Figure 5. FESEM of RSF biomimetic fibers. Fibers spun at 27% w/v via coaxial SBS with (a–h) positive inner nozzle protrusion from basic toward acid pH values (blue arrow) and increasing phosphate concentration (green arrow) and (i–k) with negative inner nozzle protrusion with variances in pH and/or phosphate concentration: (a) 10 mM HCl, pH 2; (b) 1 mM HCl, pH 3; (c) 0.1 mM HCl, pH 4; (d) H_2O, pH 7; (e) 17 mM $[PO_4^{3-}]$, pH 2; (f) 17 mM $[PO_4^{3-}]$, pH 3; (g) 17 mM $[PO_4^{3-}]$, pH 4; (h) 17 mM $[PO_4^{3-}]$, pH 7; (i) 17 mM $[PO_4^{3-}]$, pH 4; (j) 0.1 mM HCl, pH 4; (k) H_2O, pH 7.

fall short of benchmarks such as that of *A. diadematus* spider dragline silk,[22,69] and further work is required for their optimization. While it remains challenging to retain the advantages of natural silks in terms of their structural hierarchy and excellent mechanical properties, promising advances have been made in recent years with respect to RSF fibers[70,71] mainly due to mimicking the structural hierarchy present in their native state. To this regard, developing highly stable nematic silk microfibril solutions[71] may be a step forward that could be implemented in SBS in the future.

3.2. Porous RSF Fibers Obtained via Cryogenic SBS.

Developing porous micro-/nanofibers is of particular interest in the field of regenerative medicine because of their enhanced surface area to volume ratio, roughness, and their potential to incorporate a wide range of growth factors and other molecules of biological interest. Highly porous composite fibers have been previously produced by SBS with PLA[1] and hybrid sol–gel inorganic/gelatin solutions[37] by spinning them directly into a cryogenic bath followed by lyophilization. The ability to produce porous RSF fibers from aqueous solutions is reported here (Figure 4). For cryogenic SBS, only solutions at 27–30% w/v RSF were able to form a stable stream of fibers (flux of 100 μL min^{-1}, air pressure of 30 psi (0.21 MPa)). Polymer solutions <25% w/v concentration resulted exclusively in droplets and micro-/macrosphere formation due to insufficient solution viscosity. A working distance of 15 cm (SBS nozzle to surface of cryogenic bath) was suitable to retain solvent during the SBS process to cause phase separation in the fibers upon exposure to liquid nitrogen. Fibers were observed to float on the surface of the cryogenic bath and formed a continuous 3D network of noninterconnected fibers, similar to our previous work with polylactide.[1]

SEM images of the lyophilized samples demonstrated porous fibers characterized by elongated micro-/macropores of various sizes along the fiber axis (Figures 4a–d). Compared to conventional SBS, fiber diameters of the as-spun porous fibers were higher, at the micrometer scale; this can be attributed to the porous fibers having higher water content upon solidification in liquid N_2, as opposed to conventional SBS fibers which dry out before reaching the collector. In addition, the viscosity is likely to have increased due to the lower local temperature of the solution cone proximal to the liquid nitrogen. The diameter of the porous fibers increased with increased polymer concentration, with mean fiber diameters of 10.75 ± 2.12 and 28.19 ± 11.70 μm for solutions spun at 27 and 30% w/v, respectively. The size of the elongated surface pores along the fibers' axes was also related to the fiber diameter: porous fibers exhibited pore lengths of 0.64 ± 0.20 and 1.02 ± 0.41 μm for fibers spun from solutions at 27 and 30% w/v, respectively. RSF fibers spun by cryo-SBS exhibited an average BET surface area of 34.7 m^2 g^{-1} (Figure S4), consistent with their macroporous nature. Surface areas of 43.5 m^2 g^{-1} have been reported for cryo-SBS produced PLA fibers; however, these were of lower diameter (~400 nm).[1] McCann et al. reported surface areas of ~9.5 m^2 g^{-1} for poly(acrylonitrile) (PAN) fibers with diameters of 1 μm using a cryogenic electrospinning process.[72]

The chemical composition of RSF remained unaffected after TIPS. The content of the secondary protein structures in the amide I region (Figure 4e) of untreated porous fibers was in line with that of nonporous fibers obtained from aqueous solutions. However, a broad halo of greater intensity was observed at around $2\theta = 21.25°$ (*d*-spacing of 0.42 nm) (Figure 4f) for untreated porous fibers. This may suggest slightly further crystallization or cryo-coagulation induced by the TIPS process. Both morphology and porosity were retained after post-treatment (Figure S4), which in turn induced higher crystallinity as determined by ATR-FTIR and WAXD (Figure 4e,f).

3.3. Toward Biomimetic Spinning with pH-Ion Induced Changes via Coaxial SBS.

In nature, silkworm silk is produced by passing a highly concentrated (∼30% w/v) aqueous silk fibroin solution through specialized glands (spinning ducts), wherein changes to the physiochemical environment induce crystallization of β-sheets and formation of strong, tough fibers.[24] These physiochemical changes are understood to include dehydration, a pH drop (6.9 to 4.8) and exchange of β-sheet disrupting chaotropic ions (e.g., Na^+, Cl^-) for β-sheet stabilizing kosmotropic ions (e.g., PO_4^{3-}), in addition to shearing and elongation.[23−28] Such complex processing has proven challenging to emulate *in vitro* via conventional fiber spinning techniques, yet are likely necessary to induce the hierarchical ordering of silk fibers which gives rise to their remarkable mechanical properties. Rising et al. recently employed a wet-spinning technique to produce recombinant spider silk fibers by extruding a concentrated protein solution into a low-pH (2.0−5.5) coagulation bath.[73] The use of a coaxial SBS head, not to promote core−shell fiber formation, but rather to implement pH-ion changes, could advance on this work in addition to enabling dehydration and shearing/elongational forces at the point of fiber formation to closer mimic biological silk spinning.

Here, we emulated some aspects of native *B. mori* silk spinning *in vitro* through the use of a coaxial SBS head (Scheme 1e,f), which changes the physiochemical conditions at the point of fiber formation. It was hypothesized that the elongation and shearing forces that occur during SBS fiber formation, in combination with the different ionic gradients and exposure to lower pH obtained by the nozzle protrusion, would drive secondary structure formation.

Due to the increased number of variables to consider for this coaxial SBS system, which included relative positioning of the inner and outer nozzles, coagulant flux and formulation (salt type and concentration, pH), as well as the standard variables for SBS spinning (air pressure, working distance to collector, RSF solution flux and concentration), a systematic parameter screening approach was adopted, and the conditions that resulted in the formation of fibers are detailed in Table S1.

Lower concentrations of RSF (9 and 17% w/v) were attempted as means to use less viscous solution concentrations (viscosity would be expected to increase in contact with coagulant); however, only highly concentrated aqueous RSF solutions (27% w/v) were able to form fibers. SEM images of the samples were taken to further assess fiber morphology and fiber quality. It was found that relatively low pH values (pH 4−7) in the outer solution nozzle resulted in the greatest number of fibers and better fiber morphology. Relatively low phosphate concentrations (17 mM) in the outer solution nozzle resulted in superior fibers compared to higher concentrations or no phosphate at all (Figure 5a−h). It was also found that a positive inner nozzle protrusion gave superior fibers in comparison to a negative inner nozzle protrusion, where conglutinated fibers tended to occur (Figure 5i−k).

Some of these fibers (Figure S7) were further analyzed by ATR-FTIR and WAXD. Quantification of the secondary protein structures within the amide I band is shown in Figure 6a. Greater β-sheet and lower α-helix/random coil content were observed with respect to untreated fibers spun via conventional SBS from formic acid and aqueous solutions (Figure 3c), demonstrating that the presence of an additional pH and ion gradient at the point of fiber formation can induce self-assembly and drive the formation of secondary protein structures during SBS spinning. Indeed, as-produced fibers that had been spun with variances in pH-ion partially retained their structure after rinsing with water (Figure S6).

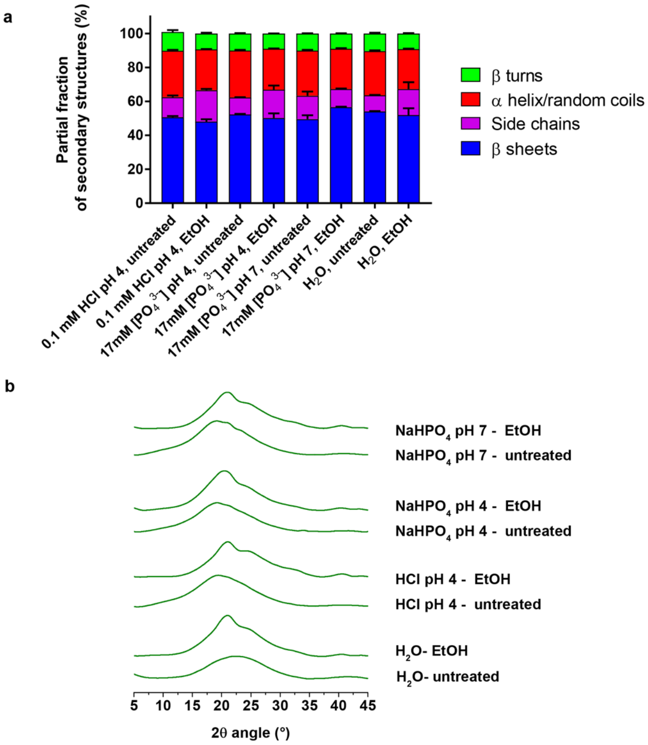

Figure 6. ATR-FTIR and WAXD of biomimetic fibers. Fibers were spun via coaxial SBS with variances in pH and/or phosphate concentration with a positive inner nozzle protrusion. (a) Stacked bar chart depicting the partial fraction of secondary protein structures within the amide I band before and after post-treatment; error bars in SD (n = 3). (b) Normalized WAXD spectrum, before and after post-treatment.

All tested conditions exhibited similar percentages, and while post-treatment with ethanol did not result in a major rearrangement of their secondary protein structures within the amide I region as observed by FTIR (Figure 6a), further conformational changes could be picked up by WAXD (Figure 6b).

Interestingly, while PEG served as spinning aid during conventional SBS spinning, a coaxial sheath of water was only needed here to drive fiber formation from aqueous solutions (Figure 5d and Figure S7a), suggesting that the requirement of a spinning aid can be overcome by the coaxial approach.

While the initial results provided here seem promising, further process development and formulation optimization are required to achieve high quality fibers with consistent morphology. These issues could likely be overcome by implementing a microfluidic chip nozzle device to drive the pH and ion gradients[74] and produce fibers with precise diameter control.[75]

4. CONCLUSION

We have shown here for the first time that the SBS technique is suitable to provide a simple and rapid route to produce a variety of RSF fibers from formic acid and aqueous systems.

Spinning in-line through vapor permitted the production of RSF nonporous fibers from aqueous solutions. In addition, fiber collection could be modified into a concentrated channeled airflow that resulted in highly aligned nonporous fibers being collected, with a more consistent morphology compared to randomly aligned fibers; aligned fibers may have applications in cardiac, muscle, and nerve tissue engineering. The combination of SBS and TIPS resulted in macroporous fibers with 3D interconnected pores, which may have potential applications in encapsulation and controlled release of a wide range of therapeutics in regenerative medicine. The use of a coaxial SBS system to induce a pH and ion gradient was implemented to induce self-assembly and drive formation of secondary protein structures simulating some of the aspects of the natural spinning process.

This study presented here with SBS contributes a new perspective on the way that silk-based fibrous scaffolds could potentially be manufactured extremely rapidly to a commercial level to suit a variety of potential biomedical applications.

■ ASSOCIATED CONTENT

Ⓢ Supporting Information

The Supporting Information is available free of charge on the ACS Publications website at DOI: 10.1021/acs.biomac.8b01233.

> Experimental data: SEM images of aligned and randomly aligned nonporous fibers from formic acid; comparison of the secondary protein structures of nonporous fibers from formic acid and aqueous systems; FTIR-ATR and WAXD spectra comparing the effect of alignment of nonporous fibers; BET surface area plot of porous RSF fibers; (FE)SEM imaging of porous RSF fibers after post-treatment; summarizing table of biomimetic fiber quality (PDF)

■ AUTHOR INFORMATION

Corresponding Authors

*(J.J.B.) Tel +44(0)161 3063578; e-mail jonny.blaker@manchester.ac.uk.
*(L.X.) Tel +65 64168933; e-mail x-li@imre.a-star.edu.sg.

ORCID

Xu Li: 0000-0001-5589-2905
Jonny J. Blaker: 0000-0003-1112-8619

Present Address

R.D.G.: Department of Physiology, Development and Neuroscience, University of Cambridge, Cambridge, UK.

Author Contributions

Adrián Magaz and Aled D. Roberts contributed equally to this work.

Notes

The authors declare no competing financial interest.

■ ACKNOWLEDGMENTS

Adrián Magaz acknowledges financial support from the University of Manchester EPSRC DTP (EP/N509565/1, 1786315) and A*STAR Institutes Singapore (A*STAR Research Attachment Programme). J.J.B., A.D.R., and S.F. acknowledge funding from the Defence, Science and Technology Laboratory (DSTL, UK Ministry of Defence, Project No. CDE100640).

■ REFERENCES

(1) Medeiros, E. L. G.; Braz, A. L.; Porto, I. J.; Menner, A.; Bismarck, A.; Boccaccini, A. R.; Lepry, W. C.; Nazhat, S. N.; Medeiros, E. S.; Blaker, J. J. Porous Bioactive Nanofibers via Cryogenic Solution Blow Spinning and Their Formation into 3D Macroporous Scaffolds. *ACS Biomater. Sci. Eng.* **2016**, *2*, 1442−1449.

(2) Medeiros, E. S.; Glenn, G. M.; Klamczynski, A. P.; Orts, W. J.; Mattoso, L. H. C. Solution Blow Spinning: A New Method to Produce Micro- and Nanofibers from Polymer Solutions. *J. Appl. Polym. Sci.* **2009**, *113*, 2322−2330.

(3) Santos, A. M. C.; Medeiros, E. L. G.; Blaker, J. J.; Medeiros, E. S. Aqueous Solution Blow Spinning of Poly(Vinyl Alcohol) Micro- and Nanofibers. *Mater. Lett.* **2016**, *176*, 122−126.

(4) Behrens, A. M.; Casey, B. J.; Sikorski, M. J.; Wu, K. L.; Tutak, W.; Sandler, A. D.; Kofinas, P. In Situ Deposition of PLGA Nanofibers via Solution Blow Spinning. *ACS Macro Lett.* **2014**, *3*, 249−254.

(5) Srinivasan, S.; Chhatre, S. S.; Mabry, J. M.; Cohen, R. E.; McKinley, G. H. Solution Spraying of Poly(Methyl Methacrylate) Blends to Fabricate Microtextured, Superoleophobic Surfaces. *Polymer* **2011**, *52*, 3209−3218.

(6) Stojanovska, E.; Canbay, E.; Pampal, E. S.; Calisir, M. D.; Agma, O.; Polat, Y.; Simsek, R.; Gundogdu, N. A. S.; Akgul, Y.; Kilic, A. A Review on Non-Electro Nanofibre Spinning Techniques. *RSC Adv.* **2016**, *6*, 83783−83801.

(7) Daristotle, J. L.; Behrens, A. M.; Sandler, A. D.; Kofinas, P. A Review of the Fundamental Principles and Applications of Solution Blow Spinning. *ACS Appl. Mater. Interfaces* **2016**, *8*, 34951−34963.

(8) Tutak, W.; Sarkar, S.; Lin-Gibson, S.; Farooque, T. M.; Jyotsnendu, G.; Wang, D.; Kohn, J.; Bolikal, D.; Simon, C. G. The Support of Bone Marrow Stromal Cell Differentiation by Airbrushed Nanofiber Scaffolds. *Biomaterials* **2013**, *34*, 2389−2398.

(9) Sohier, J.; Corre, P.; Perret, C.; Pilet, P.; Weiss, P. Novel and Simple Alternative to Create Nanofibrillar Matrices of Interest for Tissue Engineering. *Tissue Eng., Part C* **2014**, *20*, 285−296.

(10) Kuk, E.; Ha, Y.-M.; Yu, J.; Im, I.-T.; Kim, Y.; Jung, Y. C. Robust and Flexible Polyurethane Composite Nanofibers Incorporating Multi-Walled Carbon Nanotubes Produced by Solution Blow Spinning. *Macromol. Mater. Eng.* **2016**, *301*, 364−370.

(11) Kamyar, N.; Greenhalgh, R.; Nascimento, T.; Medeiros, E. S.; Matthews, P. D.; Nogueira, L.; Haugen, H. J.; Lewis, D. J.; Blaker, J. J. Exploiting Inherent Instability of 2D Black Phosphorus for Controlled Phosphate Release from Blow-Spun Poly(lactide-co-glycolide) Nanofibers. *ACS Appl. Nano Mater.* **2018**, *1*, 4190−4197.

(12) Li, L.; Kang, W.; Zhuang, X.; Shi, J.; Zhao, Y.; Cheng, B. A Comparative Study of Alumina Fibers Prepared by Electro-Blown Spinning (EBS) and Solution Blowing Spinning (SBS). *Mater. Lett.* **2015**, *160*, 533−536.

(13) Cena, C. R.; Behera, A. K.; Behera, B. Structural, Dielectric, and Electrical Properties of Lithium Niobate Microfibers. *J. Adv. Ceram.* **2016**, *5*, 84−92.

(14) Li, W.-J.; Cooper, J. A. Fibrous Scaffolds for Tissue Engineering. In *Biomaterials for Tissue Engineering Applications*; Springer: Vienna, 2011; pp 47−73.

(15) Jun, I.; Han, H.-S.; Edwards, J. R.; Jeon, H. Electrospun Fibrous Scaffolds for Tissue Engineering: Viewpoints on Architecture and Fabrication. *Int. J. Mol. Sci.* **2018**, *19*, 745.

(16) Magaz, A.; Faroni, A.; Gough, J. E.; Reid, A. J.; Li, X.; Blaker, J. J. Bioactive Silk-Based Nerve Guidance Conduits for Augmenting Peripheral Nerve Repair. *Adv. Healthcare Mater.* **2018**, 1800308.

(17) Altman, G. H.; Diaz, F.; Jakuba, C.; Calabro, T.; Horan, R. L.; Chen, J.; Lu, H.; Richmond, J.; Kaplan, D. L. Silk-Based Biomaterials. *Biomaterials* **2003**, *24*, 401−416.

(18) Holland, C.; Numata, K.; Rnjak-Kovacina, J.; Seib, F. P. The Biomedical Use of Silk: Past, Present, Future. *Adv. Healthcare Mater.* **2018**, 1800465.

(19) Zhu, J.; Shao, H.; Hu, X. Morphology and Structure of Electrospun Mats from Regenerated Silk Fibroin Aqueous Solutions with Adjusting PH. *Int. J. Biol. Macromol.* **2007**, *41*, 469−474.

(20) Zhang, X.; Reagan, M. R.; Kaplan, D. L. Electrospun Silk Biomaterial Scaffolds for Regenerative Medicine. *Adv. Drug Delivery Rev.* **2009**, *61*, 988−1006.

(21) Zhang, X.; Baughman, C. B.; Kaplan, D. L. In Vitro Evaluation of Electrospun Silk Fibroin Scaffolds for Vascular Cell Growth. *Biomaterials* **2008**, *29*, 2217−2227.

(22) Koeppel, A.; Holland, C. Progress and Trends in Artificial Silk Spinning: A Systematic Review. *ACS Biomater. Sci. Eng.* **2017**, *3*, 226−237.

(23) Tanaka, T.; Kobayashi, M.; Inoue, S.-I.; Tsuda, H.; Magoshi, J. Biospinning: Change of Water Contents in Drawn Silk. *J. Polym. Sci., Part B: Polym. Phys.* **2003**, *41*, 274−280.

(24) Jin, H.-J.; Kaplan, D. L. Mechanism of Silk Processing in Insects and Spiders. *Nature* **2003**, *424*, 1057−1061.

(25) Dicko, C.; Vollrath, F.; Kenney, J. M. Spider Silk Protein Refolding Is Controlled by Changing PH. *Biomacromolecules* **2004**, *5*, 704−710.

(26) Terry, A. E.; Knight, D. P.; Porter, D.; Vollrath, F. PH Induced Changes in the Rheology of Silk Fibroin Solution from the Middle Division of Bombyx Mori Silkworm. *Biomacromolecules* **2004**, *5*, 768−772.

(27) Rammensee, S.; Huemmerich, D.; Hermanson, K. D.; Scheibel, T.; Bausch, A. R. Rheological Characterization of Hydrogels Formed by Recombinantly Produced Spider Silk. *Appl. Phys. A: Mater. Sci. Process.* **2006**, *82*, 261.

(28) Moriya, M.; Ohgo, K.; Masubuchi, Y.; Asakura, T. Flow Analysis of Aqueous Solution of Silk Fibroin in the Spinneret of Bombyx Mori Silkworm by Combination of Viscosity Measurement and Finite Element Method Calculation. *Polymer* **2008**, *49*, 952−956.

(29) Andersson, M.; Johansson, J.; Rising, A. Silk Spinning in Silkworms and Spiders. *Int. J. Mol. Sci.* **2016**, *17*, 1290.

(30) Wang, X.; Ding, B.; Li, B. Biomimetic Electrospun Nanofibrous Structures for Tissue Engineering. *Mater. Today* **2013**, *16*, 229−241.

(31) Jin, H.-J.; Fridrikh, S. V.; Rutledge, G. C.; Kaplan, D. L. Electrospinning Bombyx Mori Silk with Poly(Ethylene Oxide). *Biomacromolecules* **2002**, *3*, 1233−1239.

(32) Meinel, A. J.; Kubow, K. E.; Klotzsch, E.; Garcia-Fuentes, M.; Smith, M. L.; Vogel, V.; Merkle, H. P.; Meinel, L. Optimization Strategies for Electrospun Silk Fibroin Tissue Engineering Scaffolds. *Biomaterials* **2009**, *30*, 3058−3067.

(33) Wang, H.; Shao, H.; Hu, X. Structure of Silk Fibroin Fibers Made by an Electrospinning Process from a Silk Fibroin Aqueous Solution. *J. Appl. Polym. Sci.* **2006**, *101*, 961−968.

(34) Cao, H.; Chen, X.; Huang, L.; Shao, Z. Electrospinning of Reconstituted Silk Fiber from Aqueous Silk Fibroin Solution. *Mater. Sci. Eng., C* **2009**, *29*, 2270−2274.

(35) Madurga, R.; Gañán-Calvo, A. M.; Plaza, G. R.; Guinea, G. V.; Elices, M.; Pérez-Rigueiro, J. Production of High Performance Bioinspired Silk Fibers by Straining Flow Spinning. *Biomacromolecules* **2017**, *18*, 1127−1133.

(36) Madurga, R.; Guinea, G. V.; Elices, M.; Pérez-Rigueiro, J.; Gañán-Calvo, A. M. Straining Flow Spinning: Simplified Model of a Bioinspired Process to Mass Produce Regenerated Silk Fibers Controllably. *Eur. Polym. J.* **2017**, *97*, 26−39.

(37) Greenhalgh, R. D.; Ambler, W. S.; Quinn, S. J.; Medeiros, E. S.; Anderson, M.; Gore, B.; Menner, A.; Bismarck, A.; Li, X.; Tirelli, N.; et al. Hybrid Sol−Gel Inorganic/Gelatin Porous Fibres via Solution Blow Spinning. *J. Mater. Sci.* **2017**, *52*, 9066−9081.

(38) Rockwood, D. N.; Preda, R. C.; Yücel, T.; Wang, X.; Lovett, M. L.; Kaplan, D. L. Materials Fabrication from Bombyx Mori Silk Fibroin. *Nat. Protoc.* **2011**, *6*, 1612−1631.

(39) Jin, Y.; Zhang, Y.; Hang, Y.; Shao, H.; Hu, X. A Simple Process for Dry Spinning of Regenerated Silk Fibroin Aqueous Solution. *J. Mater. Res.* **2013**, *28*, 2897−2902.

(40) Jin, Y.; Hang, Y. C.; Zhang, Y. P.; Shao, H. L.; Hu, X. C. Role of Ca^{2+} on Structures and Properties of Regenerated Silk Fibroin Aqueous Solutions and Fibres. *Mater. Res. Innovations* **2014**, *18*, 113−115.

(41) Wei, W.; Zhang, Y.; Zhao, Y.; Luo, J.; Shao, H.; Hu, X. Bio-Inspired Capillary Dry Spinning of Regenerated Silk Fibroin Aqueous Solution. *Mater. Sci. Eng., C* **2011**, *31*, 1602−1608.

(42) Hodgkinson, T.; Chen, Y.; Bayat, A.; Yuan, X.-F. Rheology and Electrospinning of Regenerated Bombyx Mori Silk Fibroin Aqueous Solutions. *Biomacromolecules* **2014**, *15*, 1288−1298.

(43) Byler, D. M.; Susi, H. Examination of the Secondary Structure of Proteins by Deconvolved FTIR Spectra. *Biopolymers* **1986**, *25*, 469−487.

(44) Litvinov, R. I.; Faizullin, D. A.; Zuev, Y. F.; Weisel, J. W. The α-Helix to β-Sheet Transition in Stretched and Compressed Hydrated Fibrin Clots. *Biophys. J.* **2012**, *103*, 1020−1027.

(45) Kasoju, N.; Hawkins, N.; Pop-Georgievski, O.; Kubies, D.; Vollrath, F. Silk Fibroin Gelation via Non-Solvent Induced Phase Separation. *Biomater. Sci.* **2016**, *4*, 460−473.

(46) Gonzalez, G. M.; MacQueen, L. A.; Lind, J. U.; Fitzgibbons, S. A.; Chantre, C. O.; Huggler, I.; Golecki, H. M.; Goss, J. A.; Parker, K. K. Production of Synthetic, Para-Aramid and Biopolymer Nanofibers by Immersion Rotary Jet-Spinning. *Macromol. Mater. Eng.* **2017**, *302*, 1600365.

(47) Liu, F.; Türker Saricaoglu, F.; Avena-Bustillos, R. J.; Bridges, D. F.; Takeoka, G. R.; Wu, V. C. H.; Chiou, B.-S.; Wood, D. F.; McHugh, T. H.; Zhong, F. Preparation of Fish Skin Gelatin-Based Nanofibers Incorporating Cinnamaldehyde by Solution Blow Spinning. *Int. J. Mol. Sci.* **2018**, *19*, 618.

(48) Zhu, J.; Zhang, Y.; Shao, H.; Hu, X. Electrospinning and Rheology of Regenerated Bombyx Mori Silk Fibroin Aqueous Solutions: The Effects of PH and Concentration. *Polymer* **2008**, *49*, 2880−2885.

(49) Holland, C.; Terry, A. E.; Porter, D.; Vollrath, F. Comparing the Rheology of Native Spider and Silkworm Spinning Dope. *Nat. Mater.* **2006**, *5*, 870−874.

(50) Kopperud, H. M.; Hansen, F. K.; Nyström, B. Effect of Surfactant and Temperature on the Rheological Properties of Aqueous Solutions of Unmodified and Hydrophobically Modified Polyacrylamide. *Macromol. Chem. Phys.* **1998**, *199*, 2385−2394.

(51) Um, I. C.; Kweon, H.; Park, Y. H.; Hudson, S. Structural Characteristics and Properties of the Regenerated Silk Fibroin Prepared from Formic Acid. *Int. J. Biol. Macromol.* **2001**, *29*, 91−97.

(52) da Silva Parize, D. D.; de Oliveira, J. E.; Foschini, M. M.; Marconcini, J. M.; Mattoso, L. H. C. Poly(Lactic Acid) Fibers Obtained by Solution Blow Spinning: Effect of a Greener Solvent on the Fiber Diameter. *J. Appl. Polym. Sci.* **2016**.

(53) Polat, Y.; Pampal, E. S.; Stojanovska, E.; Simsek, R.; Hassanin, A.; Kilic, A.; Demir, A.; Yilmaz, S. Solution Blowing of Thermoplastic Polyurethane Nanofibers: A Facile Method to Produce Flexible Porous Materials. *J. Appl. Polym. Sci.* **2016**.

(54) Meechaisue, C.; Dubin, R.; Supaphol, P.; Hoven, V. P.; Kohn, J. Electrospun Mat of Tyrosine-Derived Polycarbonate Fibers for Potential Use as Tissue Scaffolding Material. *J. Biomater. Sci., Polym. Ed.* **2006**, *17*, 1039−1056.

(55) Li, D.; Jiang, Y.; Lv, S.; Liu, X.; Gu, J.; Chen, Q.; Zhang, Y. Preparation of Plasticized Poly (Lactic Acid) and Its Influence on the Properties of Composite Materials. *PLoS One* **2018**, *13*, e0193520.

(56) Lin, L.; Dai, Y.; Cui, H. Antibacterial Poly(Ethylene Oxide) Electrospun Nanofibers Containing Cinnamon Essential Oil/Beta-Cyclodextrin Proteoliposomes. *Carbohydr. Polym.* **2017**, *178*, 131−140.

(57) Wan, Y.-Q.; He, J.-H.; Yu, J.-Y.; Wu, Y. Electrospinning of High-Molecule PEO Solution. *J. Appl. Polym. Sci.* **2007**, *103*, 3840−3843.

(58) Vasconcelos, A.; Freddi, G.; Cavaco-Paulo, A. Biodegradable Materials Based on Silk Fibroin and Keratin. *Biomacromolecules* **2008**, *9*, 1299−1305.

(59) He, S. J.; Valluzzi, R.; Gido, S. P. Silk I Structure in Bombyx Mori Silk Foams. *Int. J. Biol. Macromol.* **1999**, *24*, 187−195.

(60) Hu, X.; Shmelev, K.; Sun, L.; Gil, E.-S.; Park, S.-H.; Cebe, P.; Kaplan, D. L. Regulation of Silk Material Structure by Temperature-

Controlled Water Vapor Annealing. *Biomacromolecules* **2011**, *12*, 1686−1696.

(61) Agarwal, N.; Hoagland, D. A.; Farris, R. J. Effect of Moisture Absorption on the Thermal Properties of Bombyx Mori Silk Fibroin Films. *J. Appl. Polym. Sci.* **1997**, *63*, 401−410.

(62) Yazawa, K.; Ishida, K.; Masunaga, H.; Hikima, T.; Numata, K. Influence of Water Content on the β-Sheet Formation, Thermal Stability, Water Removal, and Mechanical Properties of Silk Materials. *Biomacromolecules* **2016**, *17*, 1057−1066.

(63) Zhang, H.; Li, L.-L.; Dai, F.-Y.; Zhang, H.-H.; Ni, B.; Zhou, W.; Yang, X.; Wu, Y.-Z. Preparation and Characterization of Silk Fibroin as a Biomaterial with Potential for Drug Delivery. *J. Transl. Med.* **2012**, *10*, 117.

(64) Amiraliyan, N.; Nouri, M.; Kish, M. H. Structural Characterization and Mechanical Properties of Electrospun Silk Fibroin Nanofiber Mats. *Polym. Sci., Ser. A* **2010**, *52*, 407−412.

(65) Cebe, P.; Partlow, B. P.; Kaplan, D. L.; Wurm, A.; Zhuravlev, E.; Schick, C. Silk I and Silk II Studied by Fast Scanning Calorimetry. *Acta Biomater.* **2017**, *55*, 323−332.

(66) Kishimoto, Y.; Morikawa, H.; Yamanaka, S.; Tamada, Y. Electrospinning of Silk Fibroin from All Aqueous Solution at Low Concentration. *Mater. Sci. Eng., C* **2017**, *73*, 498−506.

(67) Chen, C.; Chuanbao, C.; Xilan, M.; Yin, T.; Hesun, Z. Preparation of Non-Woven Mats from All-Aqueous Silk Fibroin Solution with Electrospinning Method. *Polymer* **2006**, *47*, 6322−6327.

(68) Kishimoto, Y.; Kobashi, T.; Yamanaka, S.; Morikawa, H.; Tamada, Y. Comparisons between Silk Fibroin Nonwoven Electrospun Fabrics Using Aqueous and Formic Acid Solutions. *Int. J. Polym. Mater.* **2018**, *67*, 462−467.

(69) Fu, C.; Shao, Z.; Vollrath, F. Animal Silks: Their Structures, Properties and Artificial Production. *Chem. Commun.* **2009**, No. 43, 6515−6529.

(70) Zhang, F.; Lu, Q.; Yue, X.; Zuo, B.; Qin, M.; Li, F.; Kaplan, D. L.; Zhang, X. Regeneration of High-Quality Silk Fibroin Fiber by Wet Spinning from $CaCl_2$−Formic Acid Solvent. *Acta Biomater.* **2015**, *12*, 139−145.

(71) Ling, S.; Qin, Z.; Li, C.; Huang, W.; Kaplan, D. L.; Buehler, M. J. Polymorphic Regenerated Silk Fibers Assembled through Bioinspired Spinning. *Nat. Commun.* **2017**, *8*, 1387.

(72) McCann, J. T.; Marquez, M.; Xia, Y. Highly Porous Fibers by Electrospinning into a Cryogenic Liquid. *J. Am. Chem. Soc.* **2006**, *128*, 1436−1437.

(73) Andersson, M.; Jia, Q.; Abella, A.; Lee, X.-Y.; Landreh, M.; Purhonen, P.; Hebert, H.; Tenje, M.; Robinson, C. V.; Meng, Q.; et al. Biomimetic Spinning of Artificial Spider Silk from a Chimeric Minispidroin. *Nat. Chem. Biol.* **2017**, *13*, 262−264.

(74) Peng, Q.; Zhang, Y.; Lu, L.; Shao, H.; Qin, K.; Hu, X.; Xia, X. Recombinant Spider Silk from Aqueous Solutions via a Bio-Inspired Microfluidic Chip. *Sci. Rep.* **2016**, *6*, 36473.

(75) Hofmann, E.; Krüger, K.; Haynl, C.; Scheibel, T.; Trebbin, M.; Förster, S. Microfluidic Nozzle Device for Ultrafine Fiber Solution Blow Spinning with Precise Diameter Control. *Lab Chip* **2018**, *18*, 2225−2234.

Blank page

Appendix B

Note: A version of this Appendix has been published as Magaz *et al*. "Electroresponsive silk-based biohybrid composites for electrochemically controlled growth factor delivery". *Pharmaceutics*. 2020;12(8):742

pharmaceutics

MDPI

Communication

Electroresponsive Silk-Based Biohybrid Composites for Electrochemically Controlled Growth Factor Delivery

Adrián Magaz [1,2,†], Mark D. Ashton [3,†], Rania M. Hathout [4], Xu Li [2,5,*], John G. Hardy [3,6,*] and Jonny J. Blaker [1,7,*]

[1] Department of Materials and Henry Royce Institute, The University of Manchester, Manchester M13 9PL, UK; adrian.magaz@postgrad.manchester.ac.uk
[2] Institute of Materials Research and Engineering (IMRE), Agency for Science, Technology and Research (A*STAR), Singapore 138634, Singapore
[3] Department of Chemistry, Lancaster University, Lancaster LA1 4YB, UK; m.ashton2@lancaster.ac.uk
[4] Department of Pharmaceutics and Industrial Pharmacy, Faculty of Pharmacy, Ain Shams University, Cairo 11566, Egypt; rania.hathout@pharma.asu.edu.eg
[5] Department of Chemistry, National University of Singapore, Singapore 117543, Singapore
[6] Materials Science Institute, Lancaster University, Lancaster LA1 4YB, UK
[7] Department of Biomaterials, Institute of Clinical Dentistry, University of Oslo, 0317 Oslo, Norway
* Correspondence: x-li@imre.a-star.edu.sg (X.L.); j.g.hardy@lancaster.ac.uk (J.G.H.); jonny.blaker@manchester.ac.uk (J.J.B.); Tel.: +44-(0)1613063587 (J.J.B.)
† These authors contributed equally to this work.

Received: 6 July 2020; Accepted: 1 August 2020; Published: 7 August 2020

Abstract: Stimuli-responsive materials are very attractive candidates for on-demand drug delivery applications. Precise control over therapeutic agents in a local area is particularly enticing to regulate the biological repair process and promote tissue regeneration. Macromolecular therapeutics are difficult to embed for delivery, and achieving controlled release over long-term periods, which is required for tissue repair and regeneration, is challenging. Biohybrid composites incorporating natural biopolymers and electroconductive/active moieties are emerging as functional materials to be used as coatings, implants or scaffolds in regenerative medicine. Here, we report the development of electroresponsive biohybrid composites based on *Bombyx mori* silkworm fibroin and reduced graphene oxide that are electrostatically loaded with a high-molecular-weight therapeutic (i.e., 26 kDa nerve growth factor-β (NGF-β)). NGF-β-loaded composite films were shown to control the release of the drug over a 10-day period in a pulsatile fashion upon the on/off application of an electrical stimulus. The results shown here pave the way for personalized and biologically responsive scaffolds, coatings and implantable devices to be used in neural tissue engineering applications, and could be translated to other electrically sensitive tissues as well.

Keywords: growth factor; stimuli-responsive delivery; nerve repair; conductivity; biohybrid; silk; reduced graphene oxide

---

1. Introduction

Drug delivery technologies are a multibillion-dollar global industry [1]. Driving the increase in research and development efforts [2] is the market need for devices and 'smart' implants or scaffolds capable of delivering active agents at specific rates. These systems can be controlled by either physical (e.g., electromagnetic fields, electrical stimulation, temperature) or (bio)chemical (e.g., enzymes, ions, pH) stimuli, in single or combined mechanisms. These technologies enable greater control over the delivery of drugs compared to traditional systems that rely on passive delivery, which cannot be modified in response to therapeutic demand [3].

Electrical stimulation in particular can offer control over drug delivery according to the strength, duration and frequency of the applied field. Consequently, electroconductive/active biomaterials have received great attention in recent years for wound healing and tissue engineering applications due to their potential to allow direct delivery of electrical signals, which are stimulatory to cells/tissues and further trigger a controlled/responsive release of therapeutics to the site of interest [4], potentially wirelessly [5]. Responsiveness to an electric field is an inherent feature of electroconductive/active materials, and their properties can be tailored to suit the delivery of various pharmacological agents and biomolecules. Conductive components used for biomaterial design range from conjugated polymers (e.g., polypyrrole (PPy), polyaniline (PANI), poly (3,4-ethylenedioxythiophene) (PEDOT) and their copolymers), to metallic nanoparticles and carbon-based materials (e.g., carbon nanotubes and graphene family materials) [6–11]. A mechanism of electrical conduction involves electron mobility along the backbone of the conjugated polymers and ionic groups appended to or complexed with the conjugated polymers and electrolytes in the medium [12]. High versatility and functionality can be achieved with carbon-based materials. Graphene derivatives in particular have shown advantageous properties for several electrically sensitive tissues, such as nerves [13], but their use as standalone materials is challenging. Biohybrid composites allow flexibility in manufacturing. Combining a protein found in nature as the matrix phase with a conductive component to provide additional functionality offers a multifunctional platform for developing coatings, implants or scaffolds for tissue engineering to match a variety of tissues in surgical reconstruction and regeneration [14].

The response achieved by releasing domain-sized macromolecular therapeutics (e.g., high-molecular-weight drugs >20 kDa, such as proteins, genes, growth factors or siRNA) is challenging due to their larger molecular dimensions and difficulties in their absorption or adsorption to the carrier system, which is limited by diffusion and surface area [15–17]. Most electroresponsive systems described for on-demand drug delivery make use of low-molecular-weight (LMW) drugs, which can be easily embedded in a scaffold. LMW drugs are good candidates for disease treatment as they easily transverse through organs and tissues, but they also impart non-specificity, increase the incidence of side effects and are rapidly eliminated from the body, therefore requiring frequent dosing [17]. Furthermore, most responsive systems suffer from short release duration (in the range of minutes to days) of the therapeutic [18–20], while tissue regeneration and repair often requires long-term drug release [21].

In particular, the lifelong disability related to peripheral nerve injury (PNI) continues to be a common condition occurring in about 3–10% of trauma patients, with an estimated one million surgical reconstruction procedures performed annually between Europe and the US [9,22,23]. Peripheral nerve axons can spontaneously regenerate to a certain extent after injury, but the probability of recovery decreases as the level of injury increases. Current therapeutic procedures are surgical, employing biomaterials to bridge nerve defects with varying degrees of success [24–26]. To enhance the probability of successful outcomes, the use of pharmacological agents and biomolecules, such as microRNAs or growth factors to promote nerve regeneration have gained attention over the last few years [27–29]. Neurotrophins are one of many examples of these, which regulate extracellular signaling, neuronal survival and differentiation and axonal regeneration [30]. Among the wide range of neurotrophins, nerve growth factor (NGF) plays a critical role in the development and phenotype maintenance of the peripheral nervous system [31], assisting the functional recovery of injured nerves (by contributing to maintaining the synaptic activity of neurons, preventing apoptosis or regulating the functions of other cell types [32]). However, the effective administration of a domain-sized macromolecular therapeutic such as NGF remains an issue.

With a view to treat nerve injuries and develop a combinatorial tissue engineered approach, we report here the development of electroresponsive biohybrid composites based on *Bombyx mori* silk fibroin (SF), which acts as the continuous phase, and reduced graphene oxide (rGO) as a conductive dispersed phase. These biohybrid composites enable the controlled release of nerve growth factor-β

(NGF-β, 26 kDa) over long-term periods upon the application of a pulsatile electrochemical stimulus (Scheme 1).

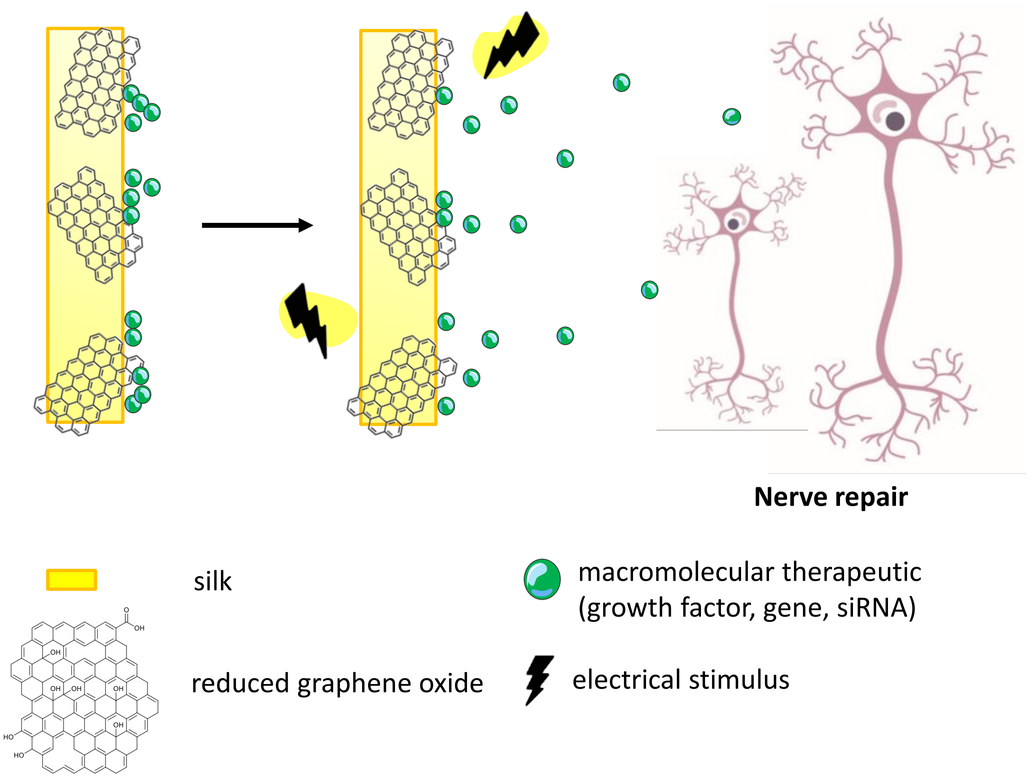

Scheme 1. Schematic representation of electroresponsive biohybrid composites based on silk fibroin and reduced graphene oxide for the controlled release of macromolecular therapeutics.

2. Materials and Methods

2.1. Preparation of Regenerated Silk Fibroin

Extraction and purification of silk fibroin (SF) from *Bombyx mori* silkworm cocoons was carried out as previously described [33]. In brief, cocoons (Wildfibres; Birmingham, UK) were dewormed, sliced into small pieces, and degummed in 0.02 M sodium carbonate (Sigma-Aldrich; Gillingham, UK) for 30 min. Degummed SF fibres were thoroughly washed in deionized (DI) water and air-dried overnight. The fibres were then dissolved in 7.9 M lithium bromide (Sigma-Aldrich, UK) solution at 60 °C for 4 h, then dialyzed against 5 L of DI water over the course of 3 days, with regular water changes. The regenerated SF solution was centrifuged, cast onto polystyrene dishes (Sigma-Aldrich, UK) and dried at 60 °C for 2 h in a forced air-circulation oven (Memmert Universal; Schwabach, Germany). The resulting films were subsequently peeled off and kept in sealed vials as stock material for further use.

2.2. Preparation of Electroconductive Biohybrid Composite Films

Graphene oxide (GO) flakes (2-DTech; Manchester, UK) (<4 μm lateral width and <2 layers, as quoted by the manufacturer) were dispersed in ≥95% v v^{-1} formic acid (Sigma-Aldrich, UK), sonicated at 80 Hz for 2 h (Elmasonic P60H) (Elma Schmidbauer; Singen, Germany) and homogenized with SF by mixing for 1 h at room temperature. Reduction of GO was performed in situ [34,35] following a previously described protocol [36,37], in which 1 μL of ≥98% v v^{-1} hydrazine monohydrate (Sigma-Aldrich, UK) was added for every 3 mg of GO and heated at 95 °C in an oil bath under constant stirring for a minimum period of 3 h. Film membranes were then prepared by solution casting and evaporation. The prepared silk-based solutions were cast onto polystyrene dishes (Sigma-Aldrich, UK) and the solvent was evaporated overnight in a fume hood, giving films at controlled rGO loadings (control 0, 10, 20, 30 and 40% wt. rGO/SF). The as-prepared films were annealed by immersion in a bath of 80% v v^{-1} ethanol for 20 min to induce β-sheet conformational transition, washed with DI water and dried for 24 h while sandwiched between filter paper (Whatman) (Sigma-Aldrich, UK) to prevent curling or folding. The resulting films were stored in a desiccator until further use.

2.3. Characterization of the Electroconductive Biohybrid Composites

The visual appearance of the top surface of the films were observed at room temperature using an optical DS microscope (Olympus) fitted with a digital camera, and the surface was further examined with a JEOL JSM6700F field emission scanning electron microscope (FESEM) (JEOL; Tokyo, Japan). For the latter, samples (n = 2 per type) were mounted on aluminum stubs with double-sided adhesive carbon tape and gold-coated prior to visualization at 5 kV, with a working distance of ~8 mm and ×1k magnification.

The chemical structures of the films (n = 2 per type) were analyzed with a Fourier transform infrared (FTIR) spectrometer (PerkinElmer 2000) equipped with a zinc selenide (ZnSe) crystal in attenuated total reflectance (ATR) mode. For each measurement, 32 scans were recorded with a resolution of 4 cm^{-1} and wavenumbers from 4000 to 600 cm^{-1}.

The swelling characteristics of the films (n = 3 per type) were investigated by weight differences between the hydrated and dry states. Samples (15 mm × 15 mm) were immersed in 10 mL of DI water and incubated at 37 °C in a water bath overnight. Excess water was removed by sandwiching the samples in filter paper and weighing immediately afterwards with a high-precision analytical balance. Three measurements were taken per sample. The swelling ratio was calculated according to Equation (1):

$$\text{Swelling ratio } (\%) = \frac{W_{\text{wet}} - W_{\text{dried}}}{W_{\text{dried}}} \times 100 \tag{1}$$

Electrical conductivity measurements were performed with a four-point probe automated electrical conductivity and resistivity system (A4P-200 MicroXACT, US) [38], using MicroXACT LabView-based automated software. Conductivity of the samples (n = 4 per type) was assessed in different locations across the surface in both the dry and hydrated states. To test the hydrated samples, films were immersed in 10 mL of phosphate buffered saline (PBS) overnight, with excess removed by blotting with tissue paper prior to testing.

2.4. In Vitro NGF-β Loading and Release Study

2.4.1. Electrochemical Loading

Recombinant rat nerve growth factor β (NGF-β) (Thermo Fisher Scientific; Altrincham, UK) was diluted into PBS to make a 1 nM solution. The material samples were then actively/electrochemically loaded with NGF-β (using 4 mL of a 1 nM NGF-β solution in PBS as the electrolyte bath). A three-electrode cell was composed of an Ag/AgCl reference electrode, an Au counter electrode and a glassy carbon electrode with the sample material on its surface [1]. Growth factor loading was achieved by applying a constant potential of 0.6 V for 30 min, after which the samples were rinsed in PBS to wash away any residual unincorporated agent.

2.4.2. NGF-β Release

Chronoamperometric studies were completed using a PalmSens EmStat 3+ potentiostat connected to a computer and PSTrace software (v. 7.4) supplied by Alvatek; Tetbury, UK). The cell comprised a three-electrode system with an Ag/AgCl reference electrode, an Au counter electrode and a glassy carbon working electrode with the sample material on its surface in PBS (0.01 M, 4 mL). Prior to each experiment, there was 'quiet time' for 10 s, the initial potential was 0 V, the high potential was 0.7 V, the low potential was −0.5 V, the initial scan was positive, the current was measured at 1 mV intervals, the scan rate used for all experiments was 50 mV s^{-1} and the stimulation lasted 62 s. After stimulation of the material, the cell was allowed to rest for 24 h to allow the released drug to equilibrate in the PBS solution. After allowing the drug to equilibrate in solution post stimulation, a 10 µL aliquot was taken from the electrolyte solution and diluted with 100 µL of PBS before being frozen prior to analysis. Passive release controls were run in parallel with the electrically stimulated samples.

2.4.3. NGF-β Quantification

Quantification of the released NGF-β was achieved by means of ELISA using a commercial kit (Thermo Fisher Scientific, UK). Absorbance measurements were taken in triplicate using a Molecular Devices FlexStation 3 plate reader at 450 nm. Data were reported as the cumulative release by the percentage of the total mass of the growth factor loaded on the films.

2.5. *In Silico Studies*

In silico toxicity screening was carried out using Derek Nexus (v. 6.0.1) (Lhasa Ltd.; Leeds, UK), and the selected structural, topological and physicochemical descriptors were calculated using Bioclipse® (v. 2.6) (Bioclipse project; Uppsala University, Sweden) and Molecular Operating Environment (MOE®; v. 2014.0901) (Chemical Computing Group Inc.; Montreal, Canada), with information related to NGF-β sourced from the protein data bank (.pdb) files obtained from the Research Collaboratory for Structural Bioinformatics (RSCB) Protein Data Bank.

2.6. *Data Analysis*

Statistical analysis was performed with GraphPad Prism 8 (San Diego, CA, USA) and checked for normality. Normally distributed data were presented as standard deviation (SD, error bars) of the mean values. For parametric data and multiple comparisons, significance was assessed by one-way ANOVA (one independent variable) or two-way ANOVA (two independent variables), with Tukey's post hoc analysis test. A value of $p < 0.05$ was considered statistically significant.

3. Results and Discussion

Graphene oxide (GO) flakes were homogenized with regenerated silk fibroin in formic acid at high loadings (10–40% wt. GO/SF) and reduced in situ with hydrazine, as detailed in the methodology, until a stable co-suspension was formed. The co-suspensions were cast and the volatiles allowed to evaporate, yielding thin film substrates (thickness < 80 µm) that were annealed in ethanol. The as-cast pristine silk sample was semitransparent to light and became opaque and black after incorporation of rGO (Figure 1(a1)). FE-SEM micrographs of the surface topography of the films (Figure 1(a2)) exhibited differences with rGO incorporation; pristine silk exhibited smooth topography whereas increased topographical features were evident with increased rGO content. *B. mori* silk fibroin-based materials produced from solutions in formic acid tend to be β-sheet rich [39] after evaporation of the formic acid, which renders them insoluble in water. Analysis of the films via attenuated total reflectance infrared spectroscopy (FTIR-ATR) (Figure S1) confirmed the presence of β-sheets in the ethanol-annealed films, exhibiting peaks in the amide I region between 1621 and 1637 cm^{-1} and a peak at 1520 cm^{-1} in the amide II region characteristic of β-sheets [39]. *B. mori* silk fibroin-based materials absorb water, however, we observed no major differences in the swelling ratio of the films with the inclusion of rGO (Figure 1b), with a swelling ratio of ~25% for all films, regardless of rGO content. The mechanism of drug loading and release from a scaffold varies upon the molecular weight of the drug and may be affected by swelling. LMW drugs effectively penetrate the polymer matrix, and their release is more affected by diffusion (e.g., swelling and matrix) and solute size/hydrodynamic radius [40]. A molecular weight cutoff does exist, above which the drug is too large to diffuse into the matrix (e.g., macromolecular therapeutics), so the quantity of the drug loaded is controlled by the surface area available for adsorption [16]. In the scenario of this work, we did not need to consider the influence of swelling on the release of the growth factor since it was electrostatically adsorbed on the surface.

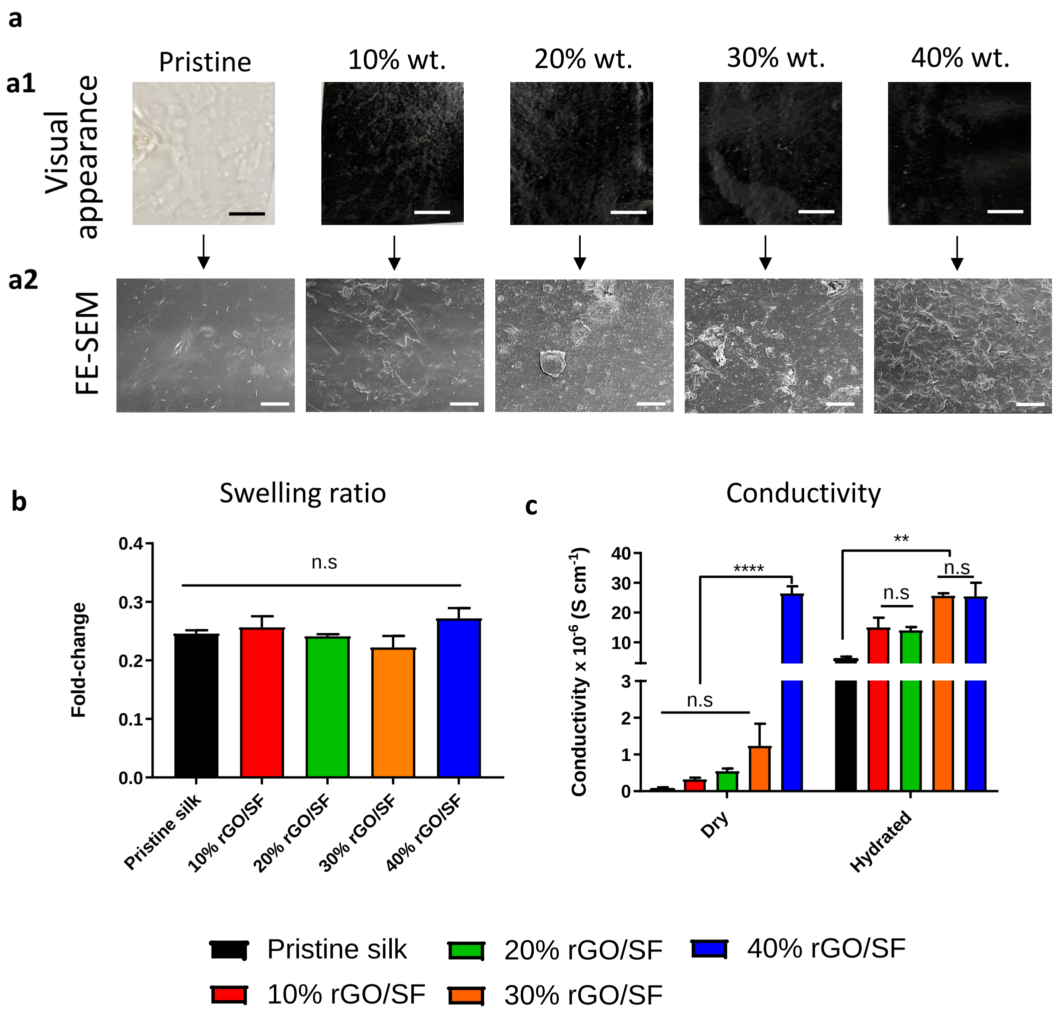

Figure 1. Electroconductive/active silk-based scaffolds. (**a**) Representative (**a1**) macroscopic visual appearance of silk-based films and (**a2**) FESEM micrographs at increasing rGO loading; scale bars at 5 mm and 10 µm respectively. (**b**) Swelling ratio ($n = 3$ per sample type). (**c**) Conductive properties ($n = 4$ per sample type) in the dry and hydrated states. The differences between the experimental groups were analyzed by one-way or two-way ANOVA using Tukey's post hoc test for multiple comparison. n.s, nonsignificant; ** $p < 0.01$, **** $p < 0.0001$.

The conductivity of the biohybrid composites was examined in the dry state as well as hydrated state, representing a more physiologically relevant environment (Figure 1c). Pristine silk films showed a conductivity of 9×10^{-8} S cm^{-1} in the dry state. The conductivity increased up to 3×10^{-5} S cm^{-1} as the content of the filler increased. After hydration, the conductance was dominated by the presence of both the substrate and the electrolytes from the buffered medium, with the conductivity increasing up to three orders of magnitude for the lower rGO loadings (10–30% wt.), analogous to other carbon-loaded materials [41]. The higher conductivity measured in the hydrated state of the samples could be further explained in terms of proton/ion conduction [42–45] by the *Grotthuss* mechanism, which describes the process of proton hopping across water networks from one water molecule to another across $H_9O_4^+$ or $H_5O_2^+$ cations, and could plausibly be enhanced by incorporating pristine graphene [14].

Myriad applications could be developed using stimuli-responsive drug delivery systems, which can control the chronopharmacology of the therapeutic of interest in line with the chronobiology of the condition to be treated. A variety of different therapeutics have been delivered using electroresponsive conductive scaffolds, as previously reviewed [46,47]. Most of these systems relied on the use of conductive polymers (e.g., PPy, PANI and PEDOT) as the electroconductive/active moiety [46,47]. For instance, electrically controlled drug delivery from GO-nanocomposite PPy and silk-PPy films have been previously reported [18,20]. However, the use of conjugated polymers tends to be limited due to their poor processability in aqueous solution, brittleness and tendency to crack [48]. GO is readily dispersible thanks to oxygen-containing functional groups on its surface, and it stands out for its ease of processability. Graphene-based scaffolds were previously reported as drug delivery systems based on the use of synthetic hydrogels and silk as the host materials [19,49], however, these systems relied on the use of LMW drugs for short-term release. In this work, the prepared film samples were loaded (doped) actively/electrostatically with a high-molecular-weight macromolecule - nerve growth factor-β (NGF-β), and its release profile was determined by means of an enzyme-linked immunosorbent assay (ELISA) which provides increased sensitivity and low limits of detection. The growth factor was released either passively by diffusion (Figure 2, zoomed-in version shown in Figure S2) or actively triggered upon the application of an electrical stimulus (Figure 3, stimulation paradigm depicted in Figure S3). Passive release from the composite films was observed (ca. 1–2% at each time-point tested), with a cumulative release of <10% over the course of the 10-day experiment. The application of a reducing potential to the NGF-β-doped films triggered the release of the growth factor.

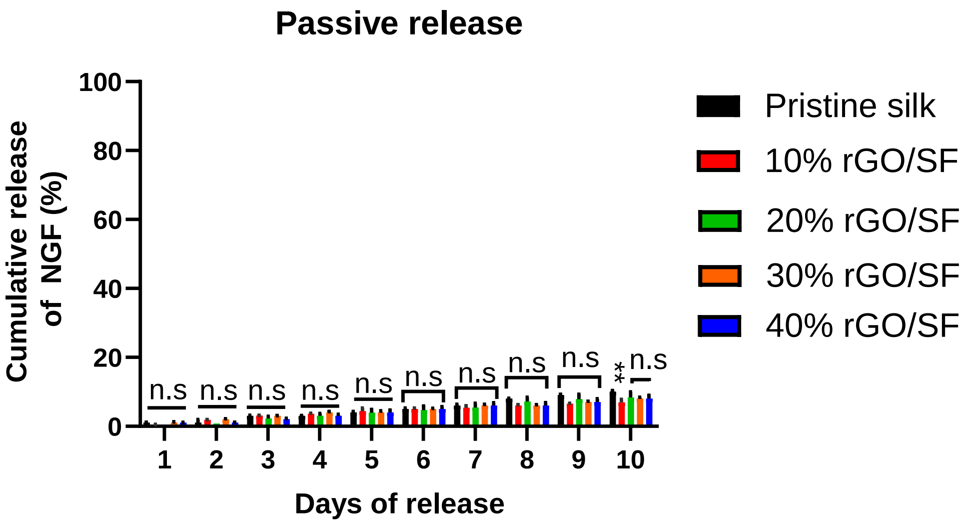

Figure 2. Delivery of nerve growth factor-β (NGF-β) from electroconductive/active silk-based scaffolds. Cumulative release percentage from the films ($n = 3$ per type) with passive release. The differences between the experimental groups were analyzed by two-way ANOVA using Tukey's post hoc test for multiple comparison (*p*-value with respect to pristine silk). n.s, nonsignificant; ** $p < 0.01$.

Notable differences were observed between the electrically stimulated samples and the non-stimulated ones. In particular, the amount of NGF-β released from the electrically stimulated films was significantly higher (five- to eight-fold increase) than for the non-stimulated films (i.e., passive release) at each time point tested, with an enhancement of up to 8–10% release at each time-point. By day 10, most of the loaded therapeutic had been released from the samples via electrical stimulation. The release of drugs over prolonged time periods is necessary for tissue repair and regeneration [21,50]; it obviates the need for repeated high dosing and improves the therapeutic index [17]. In addition to providing long-term release, the system described in this work could be further modulated in terms of the frequency pulse and duration used for stimulation. Notable differences were also observed for the pristine silk sample, for which electrical stimulation resulted in ca. <20% cumulative drug release over the course of 10 days, in comparison to the almost complete release of the growth factor from the composite films. This clearly demonstrated the benefit of the presence of a conductive carbon-based dispersed phase in the hybrid composites, which enhances the electrically triggered release of this therapeutic. However, no major differences in the drug release profiles were observed for the different rGO loadings, likely because the conductivities of the samples in the hydrated state were similar. The active delivery of NGF-β controlled in an on/off fashion is particularly interesting regarding the potential control of its chronopharmacology for nerve repair. A variety of other therapeutics or biological molecules (e.g., proteins, genes, siRNA molecules) could be delivered in a similar fashion when exposed to electrical fields, where the loading and release profiles of the bioactives could be correlated with their molecular descriptors (Tables S1 and S2).

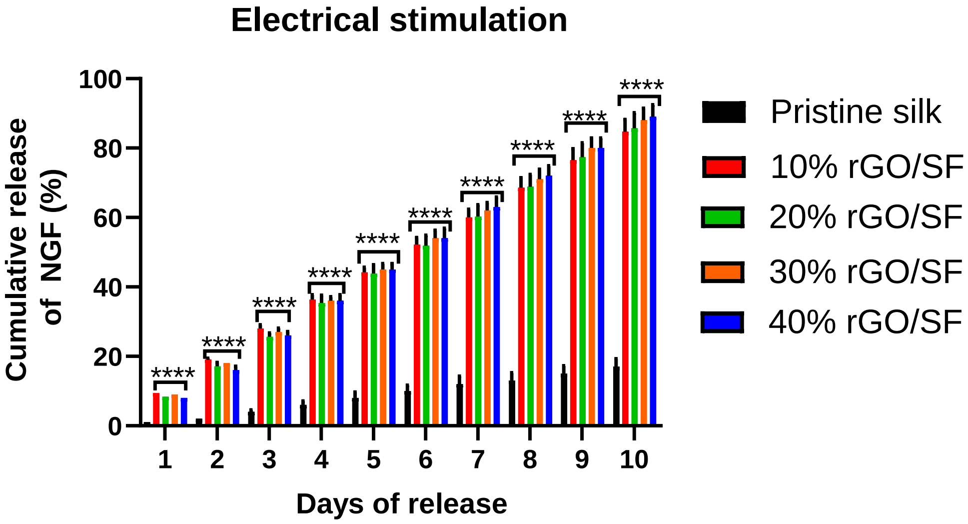

Figure 3. Electrically enhanced delivery of NGF-β from electroconductive/active silk-based scaffolds. Cumulative release percentage from the films ($n = 3$ per type) with electrical stimulation. The differences between the experimental groups were analyzed by two-way ANOVA using Tukey's post hoc test for multiple comparison (p-value with respect to pristine silk). **** $p < 0.0001$.

An important factor in the design of advanced composite biomaterials are material–tissue interactions, particularly the hazards that such materials present to the environment and life [51,52]. In vitro and in vivo tests showed that the choice of the specific graphene-based material incorporated in the composites and the method of use are of key importance regarding the risks associated with the application of such materials for biomedical applications [51,52]. Our in silico toxicity screening studies of these nanomaterials (Table S2) using Derek Nexus (Derek Nexus: 6.0.1, Nexus: 2.2.2) [53] confirmed some potential for graphene, GO and rGO to induce skin sensitization due to the presence of conjugated dienes in their structures, supported by observations in both in vitro and in vivo models [54–58]. Moreover, hydroxynaphthalene derivatives such as rGO were demonstrated as estrogen receptor modulators [59]. Our in silico mutagenicity screening studies of these nanomaterials (Table S2) using Sarah Nexus (Sarah Nexus: 3.0.0, Sarah Model: 2.0) also suggested that graphene, GO and rGO may be mutagenic, supported by in vitro and in vivo studies using graphene quantum dots [60], GO [61] and rGO [62]. Therefore, the specific method to use drug delivery devices based on these composites needs to be considered. In the case of the materials described in this work, it is possible to contemplate their use as microneedle patches or coatings on medical devices that would be removed after use and/or disposed of.

4. Conclusions

We report the development of electroresponsive biohybrid composites based on silk fibroin and reduced graphene oxide allowing the controlled release of a high-molecular-weight therapeutic over prolonged periods of time. NGF-β was loaded electrostatically and its release was facilitated over

10 days by electrical stimulation in an on/off mechanism, with a five- to eight-fold increase compared to the use of unmodified silk or the passive diffusion route. The conductivity of the system can be tuned as the ratio of its components changes, and the release profile can be controlled by triggering. These electroresponsive biohybrid composites based on silk could be manufactured in various other forms (e.g., sponges, aligned fibres or guidance conduits) to potentially regenerate nerve tissue. The concept of introducing electroconductive/active moieties into the network to impart conductive properties to protein-based systems could be readily applied to other polypeptides found in nature or recombinantly synthesized. The applications of the described system are numerous, from conductive scaffolds that can be implanted directly into electrically excited tissues other than nerve to in vitro platforms to grow electrically sensitive cells ex vivo. These findings represent a step forward in the generation of biohybrids easily tailorable to multiple biological applications, where different levels of conductivity may be desired.

Supplementary Materials: The following are available online at http://www.mdpi.com/1999-4923/12/8/742/s1, Figure S1: FTIR-ATR spectrum of the electroconductive/active silk-based films. Figure S2: Zoomed-in cumulative NGF-β release (passive release) from the films. Figure S3: Electrical stimulation paradigm. Table S1: Molecular descriptors. Table S2: Molecular-input line-entry system notations of the nanomaterials and molecules studied.

Author Contributions: Conceptualization, J.J.B., J.G.H., X.L., and A.M.; methodology, A.M., M.D.A. and R.M.H.; characterization and analysis, A.M., M.D.A. and R.M.H.; writing—original draft preparation, A.M.; writing—review and editing, all authors; supervision and project administration, J.J.B., X.L., and J.G.H.; funding acquisition, J.J.B., X.L., and J.G.H. All authors read and agreed to the published version of the manuscript.

Funding: This research was funded by a variety of sources. We thank the Engineering and Physical Sciences Research Council (EPSRC) Doctoral Training Partnership (DTP) via The University of Manchester (EP/N509565/1, 1786315) to fund A.M's research, as well as the Agency for Science, Technology and Research (A*STAR) via the A*STAR Research Attachment Programme (ARAP). An EPSRC National Productivity Investment Fund (NPIF) grant (EP/R512564/1, 2065445) to Lancaster University supported M.D.A. J.G.H was supported by an EPSRC First Grant (EP/R003823/1), a Biotechnology and Biological Sciences Research Council (BBSRC) Networks in Industrial Biotechnology and Bioenergy (NIBB) "FoodWasteNet" (FWN, grant BB/L0137971/1) Proof of Concept Grant and a Royal Society Research Grant (RG160449).

Conflicts of Interest: The authors declare no conflict of interest.

References

1. Shah, S.A.A.; Firlak, M.; Berrow, S.R.; Halcovitch, N.R.; Baldock, S.J.; Yousafzai, B.M.; Hathout, R.M.; Hardy, J.G. Electrochemically enhanced drug delivery using polypyrrole films. *Materials* **2018**, *11*, 1123. [CrossRef] [PubMed]
2. Tibbitt, M.W.; Rodell, C.B.; Burdick, J.A.; Anseth, K.S. Progress in material design for biomedical applications. *PNAS* **2015**, *112*, 14444–14451. [CrossRef] [PubMed]
3. Ashton, M.D.; Hardy, J.G. Progress in active ingredient formulations: Towards smart stimuli-responsive formulations. *Johnson Matthey Technol. Rev.* **2019**, *63*, 211–225. [CrossRef]
4. Tandon, B.; Magaz, A.; Balint, R.; Blaker, J.J.; Cartmell, S.H. Electroactive biomaterials: Vehicles for controlled delivery of therapeutic agents for drug delivery and tissue regeneration. *Adv. Drug Deliv. Rev.* **2018**, *129*, 148–168. [CrossRef]
5. Ashton, M.D.; Appen, I.C.; Firlak, M.; Stanhope, N.E.; Schmidt, C.E.; Eisenstadt, W.R.; Hur, B.; Hardy, J.G. Wirelessly triggered bioactive molecule delivery from degradable electroactive polymer films. *Polym. Int.* **2018**. [CrossRef]
6. Balint, R.; Cassidy, N.J.; Cartmell, S.H. Conductive polymers: Towards a smart biomaterial for tissue engineering. *Acta Biomater.* **2014**, *10*, 2341–2353. [CrossRef]
7. Guimard, N.K.; Gomez, N.; Schmidt, C.E. Conducting polymers in biomedical engineering. *Prog. Polym. Sci.* **2007**, *32*, 876–921. [CrossRef]
8. Tseghai, G.B.; Mengistie, D.A.; Malengier, B.; Fante, K.A.; Van Langenhove, L. PEDOT:PSS-based conductive textiles and their applications. *Sensors* **2020**, *20*, 1881. [CrossRef]
9. Magaz, A.; Faroni, A.; Gough, J.E.; Reid, A.J.; Li, X.; Blaker, J.J. Bioactive silk-based nerve guidance conduits for augmenting peripheral nerve repair. *Adv. Healthc. Mater.* **2018**, *7*, 1800308. [CrossRef]

10. Castro Neto, A.H.; Guinea, F.; Peres, N.M.R.; Novoselov, K.S.; Geim, A.K. The electronic properties of graphene. *Rev. Mod. Phys.* **2009**, *81*, 109–162. [CrossRef]
11. Burnstine-Townley, A.; Eshel, Y.; Amdursky, N. Conductive scaffolds for cardiac and neuronal tissue engineering: Governing factors and mechanisms. *Adv. Funct. Mater.* **2020**, *30*, 1901369. [CrossRef]
12. Palza, H.; Zapata, P.A.; Angulo-Pineda, C. Electroactive smart polymers for biomedical applications. *Materials* **2019**, *12*, 277. [CrossRef] [PubMed]
13. Guo, R.; Zhang, S.; Xiao, M.; Qian, F.; He, Z.; Li, D.; Zhang, X.; Li, H.; Yang, X.; Wang, M.; et al. Accelerating bioelectric functional development of neural stem cells by graphene coupling: Implications for neural interfacing with conductive materials. *Biomaterials* **2016**, *106*, 193–204. [CrossRef] [PubMed]
14. Ryan, A.J.; Kearney, C.J.; Shen, N.; Khan, U.; Kelly, A.G.; Probst, C.; Brauchle, E.; Biccai, S.; Garciarena, C.D.; Vega-Mayoral, V.; et al. Electroconductive biohybrid collagen/pristine graphene composite biomaterials with enhanced biological activity. *Adv. Mater.* **2018**, *30*, 1706442. [CrossRef] [PubMed]
15. Vazquez-Lombardi, R.; Phan, T.G.; Zimmermann, C.; Lowe, D.; Jermutus, L.; Christ, D. Challenges and opportunities for non-antibody scaffold drugs. *Drug Discov. Today* **2015**, *20*, 1271–1283. [CrossRef] [PubMed]
16. Carbinatto, F.M.; de Castro, A.D.; Evangelista, R.C.; Cury, B.S.F. Insights into the swelling process and drug release mechanisms from cross-linked pectin/high amylose starch matrices. *Asian J. Pharm. Sci.* **2014**, *9*, 27–34. [CrossRef]
17. Azad, N.; Rojanasakul, Y. Macromolecular Drug Delivery. In *Biopharmaceutical Drug Design and Development*; Wu-Pong, S., Rojanasakul, Y., Eds.; Humana Press: Totowa, NJ, USA, 2008; pp. 293–323, ISBN 978-1-59745-532-9.
18. Mousavi, S.T.; Harper, G.R.; Municoy, S.; Ashton, M.D.; Townsend, D.; Alsharif, G.H.K.; Oikonomou, V.K.; Firlak, M.; Au-Yong, S.; Murdock, B.E.; et al. Electroactive silk fibroin films for electrochemically enhanced delivery of drugs. *Macromol. Mater. Eng.* **2020**, *305*, 2000130. [CrossRef]
19. Servant, A.; Leon, V.; Jasim, D.; Methven, L.; Limousin, P.; Fernandez-Pacheco, E.V.; Prato, M.; Kostarelos, K. Graphene-based electroresponsive scaffolds as polymeric implants for on-demand drug delivery. *Adv. Healthc. Mater.* **2014**, *3*, 1334–1343. [CrossRef]
20. Weaver, C.L.; LaRosa, J.M.; Luo, X.; Cui, X.T. Electrically controlled drug delivery from graphene oxide nanocomposite films. *ACS Nano* **2014**, *8*, 1834–1843. [CrossRef]
21. Dang, M.; Saunders, L.; Niu, X.; Fan, Y.; Ma, P.X. Biomimetic delivery of signals for bone tissue engineering. *Bone Res.* **2018**, *6*, 1–12. [CrossRef]
22. Gaudin, R.; Knipfer, C.; Henningsen, A.; Smeets, R.; Heiland, M.; Hadlock, T. Approaches to peripheral nerve repair: Generations of biomaterial conduits yielding to replacing autologous nerve grafts in craniomaxillofacial surgery. *Biomed. Res. Int.* **2016**, *2016*. [CrossRef] [PubMed]
23. Kehoe, S.; Zhang, X.F.; Boyd, D. FDA approved guidance conduits and wraps for peripheral nerve injury: A review of materials and efficacy. *Injury* **2012**, *43*, 553–572. [CrossRef] [PubMed]
24. Du, J.; Chen, H.; Qing, L.; Yang, X.; Jia, X. Biomimetic neural scaffolds: A crucial step towards optimal peripheral nerve regeneration. *Biomater. Sci.* **2018**, *6*, 1299–1311. [CrossRef] [PubMed]
25. Lackington, W.A.; Ryan, A.J.; O'Brien, F.J. Advances in nerve guidance conduit-based therapeutics for peripheral nerve repair. *ACS Biomater. Sci. Eng.* **2017**, *3*, 1221–1235. [CrossRef]
26. Kasper, M.; Deister, C.; Beck, F.; Schmidt, C.E. Bench-to-bedside lessons learned: Commercialization of an acellular nerve graft. *Adv. Healthc. Mater.* **2020**, 2000174. [CrossRef]
27. Levi, M.S.; Brimble, M.A. A review of neuroprotective agents. *Curr. Med. Chem.* **2004**, *11*, 2383–2397. [CrossRef]
28. Mekaj, A.; Mekaj, Y. The role of pharmacological agents in nerve regeneration after peripheral nerve repair. *Peripher. Nerve Regen. Surg. New Ther. Approaches Incl. Biomater. Cell-Based Ther. Dev.* **2017**. [CrossRef]
29. Zhang, N.; Milbreta, U.; Chin, J.S.; Pinese, C.; Lin, J.; Shirahama, H.; Jiang, W.; Liu, H.; Mi, R.; Hoke, A.; et al. Biomimicking fiber scaffold as an effective in vitro and in vivo microrna screening platform for directing tissue regeneration. *Adv. Sci.* **2019**, *6*, 1800808. [CrossRef]
30. Liu, C.; Wang, C.; Zhao, Q.; Li, X.; Xu, F.; Yao, X.; Wang, M. Incorporation and release of dual growth factors for nerve tissue engineering using nanofibrous bicomponent scaffolds. *Biomed. Mater.* **2018**, *13*, 044107. [CrossRef]
31. Aloe, L.; Rocco, M.L.; Bianchi, P.; Manni, L. Nerve growth factor: From the early discoveries to the potential clinical use. *J. Transl. Med.* **2012**, *10*, 239. [CrossRef]

32. Lee, J.Y.; Lee, J.-W.; Schmidt, C.E. Neuroactive conducting scaffolds: Nerve growth factor conjugation on active ester-functionalized polypyrrole. *J. R. Soc. Interface* **2009**, *6*, 801–810. [CrossRef] [PubMed]
33. Magaz, A.; Roberts, A.D.; Faraji, S.; Nascimento, T.R.L.; Medeiros, E.S.; Zhang, W.; Greenhalgh, R.D.; Mautner, A.; Li, X.; Blaker, J.J. Porous, aligned, and biomimetic fibers of regenerated silk fibroin produced by solution blow spinning. *Biomacromolecules* **2018**, *19*, 4542–4553. [CrossRef] [PubMed]
34. Mitra, M.; Chatterjee, K.; Kargupta, K.; Ganguly, S.; Banerjee, D. Reduction of graphene oxide through a green and metal-free approach using formic acid. *Diam. Relat. Mater.* **2013**, *37*, 74–79. [CrossRef]
35. He, L.; Tjong, S.C. Low percolation threshold of graphene/polymer composites prepared by solvothermal reduction of graphene oxide in the polymer solution. *Nanoscale Res. Lett.* **2013**, *8*, 132. [CrossRef]
36. Ren, P.-G.; Yan, D.-X.; Ji, X.; Chen, T.; Li, Z.-M. Temperature dependence of graphene oxide reduced by hydrazine hydrate. *Nanotechnology* **2011**, *22*, 055705. [CrossRef]
37. Park, S.; An, J.; Potts, J.R.; Velamakanni, A.; Murali, S.; Ruoff, R.S. Hydrazine-reduction of graphite- and graphene oxide. *Carbon* **2011**, *49*, 3019–3023. [CrossRef]
38. Roshanbinfar, K.; Vogt, L.; Ruther, F.; Roether, J.A.; Boccaccini, A.R.; Engel, F.B. Nanofibrous composite with tailorable electrical and mechanical properties for cardiac tissue engineering. *Adv. Funct. Mater.* **2020**, *30*, 1908612. [CrossRef]
39. Um, I.C.; Kweon, H.; Park, Y.H.; Hudson, S. Structural characteristics and properties of the regenerated silk fibroin prepared from formic acid. *Int. J. Biol. Macromol.* **2001**, *29*, 91–97. [CrossRef]
40. Kucinska-Lipka, J.; Marzec, M.; Gubanska, I.; Janik, H. Porosity and swelling properties of novel polyurethane–ascorbic acid scaffolds prepared by different procedures for potential use in bone tissue engineering. *J. Elastom. Plast.* **2017**, *49*, 440–456. [CrossRef]
41. Martins, A.M.; Eng, G.; Caridade, S.G.; Mano, J.F.; Reis, R.L.; Vunjak-Novakovic, G. Electrically conductive chitosan/carbon scaffolds for cardiac tissue engineering. *Biomacromolecules* **2014**, *15*, 635–643. [CrossRef]
42. Amdursky, N.; Wang, X.; Meredith, P.; Bradley, D.D.C.; Stevens, M.M. Long-range proton conduction across free-standing serum albumin mats. *Adv. Mater.* **2016**, *28*, 2692–2698. [CrossRef] [PubMed]
43. Zhong, C.; Deng, Y.; Roudsari, A.F.; Kapetanovic, A.; Anantram, M.P.; Rolandi, M. A polysaccharide bioprotonic field-effect transistor. *Nat. Commun.* **2011**, *2*, 476. [CrossRef] [PubMed]
44. Ordinario, D.D.; Phan, L.; Walkup, W.G.; Jocson, J.-M.; Karshalev, E.; Hüsken, N.; Gorodetsky, A.A. Bulk protonic conductivity in a cephalopod structural protein. *Nat. Chem.* **2014**, *6*, 596–602. [CrossRef] [PubMed]
45. Deng, Y.; Josberger, E.; Jin, J.; Roudsari, A.F.; Rousdari, A.F.; Helms, B.A.; Zhong, C.; Anantram, M.P.; Rolandi, M. H+-type and OH- -type biological protonic semiconductors and complementary devices. *Sci. Rep.* **2013**, *3*, 2481. [CrossRef] [PubMed]
46. Pillay, V.; Tsai, T.-S.; Choonara, Y.E.; du Toit, L.C.; Kumar, P.; Modi, G.; Naidoo, D.; Tomar, L.K.; Tyagi, C.; Ndesendo, V.M.K. A review of integrating electroactive polymers as responsive systems for specialized drug delivery applications. *J. Biomed. Mater. Res. A* **2014**, *102*, 2039–2054. [CrossRef]
47. Vadlapatla, R.; Wong, E.Y.; Gayakwad, S.G. Electronic drug delivery systems: An overview. *J. Drug Deliv. Sci. Tec.* **2017**, *41*, 359–366. [CrossRef]
48. El Zein, A.; Huppé, C.; Cochrane, C. Development of a flexible strain sensor based on PEDOT:PSS for thin film structures. *Sensors* **2017**, *17*, 1337. [CrossRef]
49. Wang, L.; Lu, C.; Li, Y.; Wu, F.; Zhao, B.; Dong, X. Green fabrication of porous silk fibroin/graphene oxide hybrid scaffolds for bone tissue engineering. *RSC Adv.* **2015**, *5*, 78660–78668. [CrossRef]
50. Wu, J.; Zhang, Z.; Gu, J.; Zhou, W.; Liang, X.; Zhou, G.; Han, C.C.; Xu, S.; Liu, Y. Mechanism of a long-term controlled drug release system based on simple blended electrospun fibers. *J. Control. Release* **2020**, *320*, 337–346. [CrossRef]
51. Ou, L.; Song, B.; Liang, H.; Liu, J.; Feng, X.; Deng, B.; Sun, T.; Shao, L. Toxicity of graphene-family nanoparticles: A general review of the origins and mechanisms. *Part. Fibre Toxicol.* **2016**, *13*, 57. [CrossRef]
52. Fadeel, B.; Bussy, C.; Merino, S.; Vázquez, E.; Flahaut, E.; Mouchet, F.; Evariste, L.; Gauthier, L.; Koivisto, A.J.; Vogel, U.; et al. Safety assessment of graphene-based materials: Focus on human health and the environment. *ACS Nano* **2018**, *12*, 10582–10620. [CrossRef]
53. Macmillan, D.S.; Chilton, M.L. A defined approach for predicting skin sensitisation hazard and potency based on the guided integration of in silico, in chemico and in vitro data using exclusion criteria. *Regul. Toxicol. Pharmacol.* **2019**, *101*, 35–47. [CrossRef] [PubMed]

54. Mondal, S.; Thirupathi, R.; Rao, L.P.; Atreya, H.S. Unraveling the dynamic nature of protein–graphene oxide interactions. *RSC Adv.* **2016**, *6*, 52539–52548. [CrossRef]
55. Pelin, M.; Fusco, L.; León, V.; Martín, C.; Criado, A.; Sosa, S.; Vázquez, E.; Tubaro, A.; Prato, M. Differential cytotoxic effects of graphene and graphene oxide on skin keratinocytes. *Sci. Rep.* **2017**, *7*, 1–12. [CrossRef] [PubMed]
56. Pelin, M.; Fusco, L.; Martín, C.; Sosa, S.; Frontiñán-Rubio, J.; González-Domínguez, J.M.; Durán-Prado, M.; Vázquez, E.; Prato, M.; Tubaro, A. Graphene and graphene oxide induce ROS production in human HaCaT skin keratinocytes: The role of xanthine oxidase and NADH dehydrogenase. *Nanoscale* **2018**, *10*, 11820–11830. [CrossRef] [PubMed]
57. Fusco, L.; Garrido, M.; Martín, C.; Sosa, S.; Ponti, C.; Centeno, A.; Alonso, B.; Zurutuza, A.; Vázquez, E.; Tubaro, A.; et al. Skin irritation potential of graphene-based materials using a non-animal test. *Nanoscale* **2020**, *12*, 610–622. [CrossRef] [PubMed]
58. Shvedova, A.A.; Castranova, V.; Kisin, E.R.; Schwegler-Berry, D.; Murray, A.R.; Gandelsman, V.Z.; Maynard, A.; Baron, P. Exposure to carbon nanotube material: Assessment of nanotube cytotoxicity using human keratinocyte cells. *J. Toxicol. Environ. Health A* **2003**, *66*, 1909–1926. [CrossRef] [PubMed]
59. Surfraz, M.B.; Fowkes, A.; Plante, J.P. A semi-automated approach to create purposeful mechanistic datasets from heterogeneous data: Data mining towards the in silico predictions for oestrogen receptor modulation and teratogenicity. *Mol. Inform.* **2017**, *36*, 1600154. [CrossRef] [PubMed]
60. de Menezes, F.D.; dos Reis, S.R.R.; Pinto, S.R.; Portilho, F.L.; do Vale Chaves e Mello, F.; Helal-Neto, E.; da Silva de Barros, A.O.; Alencar, L.M.R.; de Menezes, A.S.; dos Santos, C.C.; et al. Graphene quantum dots unraveling: Green synthesis, characterization, radiolabeling with 99mTc, in vivo behavior and mutagenicity. *Mater. Sci. Eng. C* **2019**, *102*, 405–414. [CrossRef]
61. Evariste, L.; Lagier, L.; Gonzalez, P.; Mottier, A.; Mouchet, F.; Cadarsi, S.; Lonchambon, P.; Daffe, G.; Chimowa, G.; Sarrieu, C.; et al. Thermal reduction of graphene oxide mitigates its in vivo genotoxicity toward xenopus laevis tadpoles. *Nanomaterials* **2019**, *9*, 584. [CrossRef]
62. Bengtson, S.; Knudsen, K.B.; Kyjovska, Z.O.; Berthing, T.; Skaug, V.; Levin, M.; Koponen, I.K.; Shivayogimath, A.; Booth, T.J.; Alonso, B.; et al. Differences in inflammation and acute phase response but similar genotoxicity in mice following pulmonary exposure to graphene oxide and reduced graphene oxide. *PLoS ONE* **2017**, *12*, e0178355. [CrossRef] [PubMed]